UNIVERSITÀ
DEGLI STUDI
FIRENZE

INTERNATIONAL DOCTORATE IN
ATOMIC AND MOLECULAR PHOTONICS

CICLO XXVIII

COORDINATORE: Prof. Roberto Righini

Two-orbital quantum physics in Yb Fermi gases exploiting the $^1S_0 \rightarrow {}^3P_0$ clock transition

Settore Scientifico Disciplinare: FIS/03

Dottorando
Giacomo Cappellini

Tutor
Dr. Jacopo Catani

Coordinatore
Prof. Roberto Righini

Anni 2012/2015

Contents

Introduction

In the last decade, the development of extraordinary experimental techniques in the field of atomic physics, as well as in nanotechnology and photonics, allowed for a huge step in the understanding of complex fundamental problems of physics, especially in the field of condensed matter, where an extremely high number of variables is involved. Exploiting these techniques, fully tailored quantum systems can indeed be created, which guarantee an unparalleled control over their degrees of freedom. This realizes the idea of R. Feynman of a quantum simulator [1], i.e. a quantum system used to emulate another physical system by mimicking its evolution [2–6].

A fundamental field in this context is represented by ultracold atoms. With the development of laser cooling techniques [7] based on the interaction between matter and monochromatic light, it was possible to cool neutral atoms down to the quantum degenerate regime, where the effect of the Bose-Einstein [8, 9] and Fermi-Dirac [10] statistics plays a fundamental role. Such breakthroughs were followed by the introduction of a wealth of novel techniques devoted to efficiently manipulate and probe ultracold atomic gases [11]. Optical lattices in particular are a fundamental tool for the investigation of condensed matted systems, as they offer the opportunity to realize a lattice environment with fully controllable degrees of freedom, accurately implementing the Hubbard model [12]. This allowed for the observation of a wide array of phenomena, ranging from the superfluid to Mott insulator transition [13–15] and the Anderson localization [16] to fermionic superfluid pairing [17], correlated tunneling and superexchange processes [18–20], and reduced-dimensionality physics such as Tonks-Girardeau gases [21, 22].

Recently, a growing interest arose regarding the opportunities offered by alkali-earth(-like) (AEL) atoms. This class of atoms was initially considered for the realization of a new generation of frequency standards based on optical atomic clocks [23], but was soon realized that they also offered very promising opportunities for the implementation of new quantum simulation [24–26] and quantum information [27–30] schemes. AEL atoms possess indeed some peculiar properties that heavily differentiate them from alkali atoms, opening the possibility of a plethora of new applications. For instance, interaction between fermionic AEL isotopes with a high nuclear spin, such as ^{173}Yb, belong to a particular symmetry class called SU(N), which arises from the strong decoupling between orbital and nuclear degree of freedom. A remarkable consequence of this symmetry is that

interactions between atoms are independent from the specific nuclear spin states, a property which allows for the realization of multicomponent fermionic gases with tunable number of nuclear spin states [31–33] and heavily influences nearly any interacting fermionic many-body state [34].

Moreover, AEL atoms are characterized by a more complex electronic structure with respect to alkalis, which features a metastable state (or orbital, in analogy to electrons in solids) with an extremely long (> 10 s) radiative lifetime. This property provides a platform to the implementation of so far inaccessible many-body phenomena, based on orbital interactions [26, 35, 36], enlarged symmetries [26, 34] and strong effective gauge fields [37]. Moreover, the transition that connects the ground to the metastable state has been exploited for the realization of optical lattice clocks (hence the name "clock-transition") that reached a record stability and accuracy of the order of 10^{-18} [38–40], paving the way to the redefinition of the SI second.

This thesis covers several cross-disciplinary subjects related to two-orbital quantum physics of fermionic systems, and in particular of fermionic isotope ^{173}Yb of Ytterbium. In first place, the attention is focused on the basic properties of the interactions between atoms in different electronic states. In the experiment, we observe that such atoms feature a special type of interaction, the so-called interorbital spin-exchange interaction [41], which lies at the heart of a wide array of quantum phenomena in condensed matter, ranging from Kondo model [35, 42] to heavy-Fermi behaviour [36, 43, 44] and orbital quantum magnetism [45, 46]. In order to be implemented, all these schemes rely on the excitation of the clock transition. This requirement is fullfilled with the aid of ultranarrow laser systems [47–50], able to excite the clock transition without deteriorating its spectral characteristics. In order to reliably conduct experiments over long timescales, a high level of stability and accuracy are required from these devices, which is not easily attainable outside of metrology institutes. In this thesis, I also show that the necessary high degree of stability and accuracy can be reached by stabilizing the ultranarrow laser system, developed during the years of my PhD [50], to an absolute optical frequency reference disseminated from the Italian National Metrology Institute (INRIM, Turin) to our end-used laboratory (LENS, Florence) through a long-haul optical fiber link [51]. Optical fiber links have already proved to be a powerful tool for comparison between optical clocks and state-of-the-art frequency standards [52, 53], and their potential can be exploited in several other applications, ranging from geodesy [53, 54] to radioastronomy [55]. Optical fiber links could be exploited for the dissemination of a primary absolute frequency reference to remote non-metrological end-users, in such a way as to push the precision and accuracy of local measurements and applications beyond the GPS limit, nowadays the commonly used frequency reference. In this thesis, I provide the first demonstration of this capability: by disciplining our ultranarrow laser to the remote optical frequency reference, we perform spectroscopy on the Ytterbium clock transition, reaching an accuracy which goes beyond the limits of the GPS [56]. This high degree of accuracy and stability could allow for an effective excitation of the clock transition for

indefinitely long timescales, with great benefit for the experimental setup reliability and without any need of local metrologic infrastructure.

Finally, I also report on another experiment in which we observed that two-orbital interactions can be tuned exploiting a new type of Feschbach resonance [57], called Orbital Feshbach Resonance, very recently pointed out theoretically [58]. The possibility to tune interactions is lacking in ground state AEL atoms, due to the absence of hyperfine interaction and the existence of orbital Feshbach resonances opens totally new avenues in the investigation of two-orbital many-body physics, ranging from the BEC-BCS crossover in an ultracold gas of fermions with orbital degree of freedom and the realization of novel forms of topological superfluids with spin-orbit coupling [58], to the investigation of two-orbital Hubbard models [26] with tunable interactions.

This thesis is organized as follows.

- Chapter 1 introduces the basic concepts of the laser cooling and trapping techniques, including a review on optical lattices, and of interactions between ultracold atoms, introducing the concept of scattering length. The origin of the $SU(N)$ interaction symmetry is also briefly discussed. A final section is dedicated to the description of the basic properties of Ytterbium electronic and collisional properties.

- Chapter 2 contains a description of the fundamental parts of the experimental setup, including the vacuum apparatus and laser systems, and of the experimental procedures adopted to cool atoms down the atomic samples to the degenerate level and to trap and manipulate them.

- Chapter 3 is divided in two main sections. In the first the ultranarrow laser system at 578 nm, which I conspicuously contributed to devise and realize, is described in details, including the infrared laser source and the doubling cavity used to obtain visible radiation, the insulation of the reference ULE cavity, the locking technique and an analysis of the laser performances. In the second section, the optical fiber link that connects the italian metrological institute to LENS is described, followed by a discussion on the analysis of the our 578 nm laser long-term stability before and after the stabilization on the fiber link.

- In chapter 4 the properties of the metastable state and of the clock transition are discussed, followed by a description of Doppler-free spectroscopy experiments on spin-polarized samples. In the final part, the results of a high-accuracy spectroscopy experiment are discussed, enlightening the advantages offered by a long term stabilization of the optical fiber link for efficient frequency dissemination to non-metrological institutes.

- Chapter 5 is dedicated to the subject of interaction between atoms in different orbitals and different spin states. After a theoretical introduction, I discuss the

experimental results concerning a direct observation of the coherent nature of the interorbital interaction and for a full characterization of its properties as a function of the significant experimental parameters.

- Chapter 6 reports on the experimental study of orbital Feshbach resonances. After a general introduction to the basic concepts of Feshbach resonances, I briefly explain the mechanism at the basis of orbital Feshbach resonances. The final part of the chapter is dedicated to the experimental investigation of the resonance, including the determination of its approximate position for different spin mixtures and a study of the inelastic losses across the resonance.

- Finally, in chapter 7 I review additional experimental results which were achieved during the years of the PhD, but are not directly tied to two-orbital physics. In particular, I review the investigation of the effects of SU(N) symmetry in one-dimensional systems, and the observation of chiral edge states with neutral atoms in a synthetic gauge field.

Publications

The results shown in this thesis are reported in the following references (in chronological order):

- G. Pagano, M. Mancini, **G. Cappellini**, P. Lombardi, F. Schäfer, H. Hui, X. J. Liu, J. Catani, C. Sias, M. Inguscio and L. Fallani, *"A one dimensional liquid of fermions with tunable spin"*, Nature Physics **10**, 198 (2014).

- **G. Cappellini**, M. Mancini, G. Pagano, P. Lombardi, L. Livi, M. Siciliani de Cumis, P. Cancio, M. Pizzocaro, D. Calonico, F. Levi, C. Sias, J. Catani, M. Inguscio, and L. Fallani, *"Direct Observation of Coherent Interorbital Spin-Exchange Dynamics"*, Physical Review Letters **113**, 120402 (2014).

- **G. Cappellini**, P. Lombardi, M. Mancini, G. Pagano, M. Pizzocaro, L. Fallani, J. Catani, *"A compact ultranarrow high-power laser system for experiments with 578 nm Ytterbium clock transition"*, Rev. Sci. Instrum. **86**, 073111 (2015).

- M. Mancini, G. Pagano, **G. Cappellini**, L. Livi, M. Rider, J. Catani, C. Sias, P. Zoller, M. Inguscio, M. Dalmonte, L. Fallani, *"Observation of chiral edge states with neutral fermions in synthetic Hall ribbons"*, Science **349**, 1510 (2015).

- G. Pagano, M. Mancini, **G. Cappellini**, L. Livi, C. Sias, J. Catani, M. Inguscio, L. Fallani, *"A strongly interacting gas of two-electron fermions at an orbital Feshbach resonance"*, Physical Review Letters **115**, 265301 (2015).

- C. Clivati, **G. Cappellini**, L. Livi, F. Poggiali, M. Siciliani de Cumis, M. Mancini, G. Pagano, M. Frittelli, A. Mura, G. A. Costanzo, F. Levi, D. Calonico, L. Fallani, J. Catani, M. Inguscio, *"Measuring absolute frequencies beyond the GPS limit via long-haul optical frequency dissemination"*, arXiv:1511.08485 (2015).

Chapter 1

Ultracold atoms fundamentals

In this chapter we review some of the fundamental concepts of the field of ultracold atoms. We first discuss the basic concepts of laser cooling and trapping techniques, including a review of optical lattices. The fundamentals of atomic interaction are ultra-low temperature are then discusses, together with brief discussion on the origin of the SU(N) symmetry that characterize interactions between ground state Ytterbium atoms. Finally, we present the main electronic and collisional properties of the Ytterbium element.

1.1 Laser cooling and trapping

1.1.1 Laser cooling and optical potentials

The development of atomic cooling and trapping techniques is a directed consequence of light-matter interaction properties. These techniques rely on the mechanical action that lights exerts on atoms, which is of two kind, dissipative and conservative.

Dissipative force

In general, an atom interacting with light represents an *open quantum system* since it is always coupled with the electromagnetic vacuum field which acts as a thermal reservoir and causes spontaneous emission. Such a system can be described in the *master equation* formalism in which the time evolution of the density matrix $\hat{\rho}$ of the atomic system is given by[59]:

$$\frac{d\hat{\rho}}{dt} = \frac{1}{i\hbar}\left[\hat{H}, \hat{\rho}\right],\tag{1.1}$$

where $\hat{H}$ is the total Hamiltonian of the system and is given by:

$$\hat{H} = \hat{H}_A + \hat{H}_R + \hat{H}_I,\tag{1.2}$$

7

where $\hat{H}_A$ and $\hat{H}_R$ are, respectively, the atomic system and radiation field Hamiltonians and $\hat{H}_I$ is the Hamiltonian describing the interaction between atoms and the electromagnetic field:

$$\hat{H}_I = -\hat{\mathbf{d}} \cdot [\mathbf{E}(\mathbf{r}, t) + \mathbf{E}_{vac}(\mathbf{r}, t)] \tag{1.3}$$

where $\hat{\mathbf{d}}$ is the atomic dipole and the second term is the electromagnetic field which is given the sum of the vacuum electromagnetic field $\mathbf{E}_{vac}(\mathbf{r}, t)$ and of the laser field $\mathbf{E}(\mathbf{r}, t)$, assumed to be a plane wave with wavelength λ:

$$\mathbf{E}(\mathbf{r}, t) = \epsilon E_0 \cos(\mathbf{k} \cdot \mathbf{r} - \omega t) \tag{1.4}$$

where ϵ is the polarization vector and $|k| = 2\pi/\lambda$ is the wavevector. The dissipative force is the consequence of a series of cycles of absorption from the laser field and spontaneous emission in the reservoir vacuum field. With the absorption of a photon, the atom acquires a momentum $\hbar\mathbf{k}$ along the propagation direction of the laser beam and, since the spontaneous emission in the vacuum field is isotropic, the atomic motion can be damped out. This mechanism, often referred to as "radiation pressure", is at the basis of laser cooling techniques such as Zeeman slowing (section 2.2.1) and magneto-optical trapping (section 2.2.1). Considering a two-level $|g\rangle - |e\rangle$ atom, with $|g\rangle$ and $|e\rangle$ separated by an energy $\hbar\omega_0$, interacting with a laser field, the expression of the dissipative force can be derived within the master equations formalism (the so-called optical Bloch equations [59]). By assuming the Rotating Wave Approximation (RWA), in which the rapidly-oscillating components (at frequency $\omega_0 + \omega$) are neglected and only the slowly-oscillating terms (at frequency $\omega_0 - \omega$) are retained, the force exerted by a plane wave of intensity I, frequency ω and detuning $\Delta = \omega - \omega_0$ on an atom at rest is given by:

$$\mathbf{F}_{diss} = \hbar\mathbf{k}_L \frac{\Gamma}{2} \left(\frac{I/I_s}{1 + I/I_s + (2\Delta/\Gamma)^2} \right) \tag{1.5}$$

where $I_s = 4\pi^2\hbar c\Gamma/6\lambda^3$ is defined as the saturation intensity. In the so-called "saturation regime" at $I/I_s \gg 1, \Delta/\Gamma$, the dissipative force reduces to $\mathbf{F}_{diss} = \hbar\mathbf{k}\Gamma/2$. This last expression highlights that the dissipative force directly originates from the momentum transfer $\hbar\mathbf{k}$ induced by scattered photons at rate $\Gamma/2$. This holds for near resonant light ($\Delta \sim \Gamma$), where the RWA is a good approximation.

Conservative force

The origin of the conservative force can be well described with a classical approach, considering an electromagnetic $\mathbf{E}$ oscillating a frequency ω which induces in the atom an oscillating electric dipole $\mathbf{d} = \alpha(\omega)\mathbf{E}$, where $\alpha(\omega)$ is the atom polarizability. By time averaging the interaction between the induced dipole and the electromagnetic field itself, obtains the expression for the so-called AC-Stark shift (also called dipole potential or light shift) [60, 61]:

$$V_{dip}(\mathbf{r}, \omega) = -\frac{1}{2\epsilon_0 c} \text{Re}[\alpha(\omega)] I(\mathbf{r}), \qquad (1.6)$$

where $I(\mathbf{r}) = 2\epsilon_0 c |\mathbf{E}(\mathbf{r}|^2$ is the intensity of the electromagnetic field and where we have reintroduce the dependency on the spatial coordinates $\mathbf{r} = (x, y, z)$. The expression for the dipole force can then be straightforward derived as:

$$\mathbf{F}_{dip} = -\nabla V_{dip}(\mathbf{r}, \omega) = \frac{1}{2\epsilon_0 c} \text{Re}[\alpha(\omega)] \nabla I(\mathbf{r}). \qquad (1.7)$$

From this expression, it is evident how it is possible to confine atoms in potential minima using tailored intensity profile. Typical applications of this confining mechanism are dipole traps and optical lattices.

In general, in order to determine the exact polarizability, and hence the exact form of the light-shift, on a certain atomic level, all other atomic states must be considered [61], but a two-level approximation is enough to give the idea of the working principles of dipole traps and optical lattices. It can be shown that starting from the atom polarizability derived with a semi-classical approach [60], the AC-Stark shift of the ground state $|g\rangle$ is given in first approximation by:

$$V_{dip}(\mathbf{r}, \omega) = -\frac{3\pi c^2}{2\omega_0^3} \left(\frac{\Gamma}{\omega_0 - \omega} + \frac{\Gamma}{\omega_0 + \omega} \right) I(\mathbf{r}), \qquad (1.8)$$

where ω_0 is the frequency of the $|g\rangle \rightarrow |e\rangle$ transition and Γ its natural linewidth. This expression can be further simplified in RWA, giving:

$$V_{dip}(\mathbf{r}, \omega) = -\frac{3\pi c^2}{2\omega_0^3} \left(\frac{\Gamma}{\Delta} \right) I(\mathbf{r}). \qquad (1.9)$$

Form this expression, it is clear how the sign of the detuning Δ of the dominant transition influences the sign of the dipole potential: a positive or negative detuning would induce a repulsive or attracting potential, respectively. For this reason, red-detuned laser gaussian beams are typically used to realized nearly-harmonic traps [62, 63], but also blue-detuned beams can be used to engineer specific potentials, like quasi two-dimensional traps [64] or box potentials [65, 66].

As the dipole force still originates from the interaction between atoms and the electromagnetic field, processes of absorption and spontaneous emission may occur. It can be shown that the scattering rate associated to these kind of processes is proportional to the imaginary part of the polarizability [60, 61]:

$$\Gamma_{sc}(\mathbf{r}, \omega) = \frac{1}{\hbar\epsilon_0 c} \text{Im}[\alpha(\omega)] I(\mathbf{r}), \qquad (1.10)$$

which further simplifies in RWA, giving:

$$\Gamma_{sc}(\mathbf{r}, \omega) = \frac{3\pi c^2}{2\omega_0^3} \left(\frac{\Gamma}{\Delta} \right)^2 I(\mathbf{r}), \qquad (1.11)$$

Since the photon scattering transfers energy to the atomic sample, in order not to lose atoms from the trap is necessary to minimize the scattering rate, keeping at the same time a strong enough dipole potential. Since $\Gamma_{sc} \propto 1/\Delta^2$ and $V_{dip} \propto 1/\Delta$, this condition can be obtain choosing a detuning that is high enough to minimize the photon absorption but still small enough to exert a non-negligible dipole force.

For completeness sake, Eq. (1.8) and (1.9) for the dipole potential and the photon scattering rate can be easily generalized to take into account all the possible transitions from a certain state $|n\rangle$, giving in non-RWA:

$$
\begin{aligned}
V_{dip}^{(n)}(\mathbf{r}, \omega) &= -\sum_{m \neq m} \frac{3\pi c^2}{2\omega_{mn}^3} \left(\frac{\Gamma_{mn}}{\omega_{mn} - \omega} + \frac{\Gamma_{mn}}{\omega_{mn} + \omega} \right) I(\mathbf{r}), \\
\Gamma_{sc}^{(n)}(\mathbf{r}, \omega) &= \sum_{m \neq m} \frac{3\pi c^2}{2\hbar \omega_{mn}^3} \left(\frac{\omega}{\omega_{mn}} \right)^3 \left(\frac{\Gamma_{mn}}{\omega_{mn} - \omega} + \frac{\Gamma_{mn}}{\omega_{mn} + \omega} \right)^2 I(\mathbf{r}),
\end{aligned}
\tag{1.12}
$$

where ω_{nm} is the frequency of the transition $|n\rangle \to |m\rangle$ and Γ_{nm} its natural linewidth.

1.1.2 Optical lattices

Optical lattice represent a fundamental tool in quantum simulation of condensate matter systems [11], as it represents for neutral atoms the equivalent of the lattice potential experienced by electrons in solids. An optical lattice can experimentally be generated by superimposing two counter-propagating gaussian beams with wavevector $\pm \mathbf{k}_L$, waist w_0 and Rayleigh range z_R and with the same polarization. This creates a stationary interference pattern along the propagation direction z of the two beams, which generates a dipole potential (1.6) that is given by:

$$
V_{lat}(r, z) = V_0 e^{-2\frac{r^2}{w^2(z)}} \cos^2(k_L z) \simeq sE_r \cos^2(k_L z) + \underbrace{\frac{1}{2} m\omega_r^2 r^2 + \frac{1}{2} m\omega_z^2 z^2}_{V_{ext}}, \tag{1.13}
$$

where we have expressed the potential depth $V_0 = sE_r$ in terms of recoil energy $E_r = \hbar^2 k_L^2 / 2m$, with m the atomic mass, and the dimensionless parameter $s = V_0/E_r$. The potential (1.13) generated by the two gaussian beams is the sum of a periodic potential along the the beams propagation direction and of an external trapping potential V_{ext}. This trapping potential has two components, which can be approximated as harmonic confinements: a weak confinement along the longitudinal direction with harmonic frequency $\omega_z = \sqrt{\frac{2E_r}{mz_R^2}}\sqrt{s}$ and a stronger confinement along the radial direction with frequency $\omega_r = \sqrt{\frac{4E_r}{mw_0^2}}\sqrt{s}$. In presence of collimated beams, these trapping terms can be neglected in first approximation, and the potential simply reduces to the periodic term. This can be expanded around the minimum in $z = 0$, obtaining the harmonic frequency associated to the lattice site:

$$\omega = \sqrt{\frac{2k_L^2}{m}V_0} = \frac{2E_R}{\hbar}\sqrt{s}. \tag{1.14}$$

Adding additional laser beams along other directions, it is possible to create perfect lattice potentials with up to three dimensions. For example, the lattice potential created by three pairs of counter-propagating beams would be given by:

$$V_{lat}(x, y, z) = V_0 \cos^2(k_L x) + V_0 \cos^2(k_L y) + V_0 \cos^2(k_L z), \tag{1.15}$$

where we have assumed the same amplitude and wavevector for all the beams and we have neglected the external harmonic confinement. Moreover, more exotic optical lattice configuration, with a different translational symmetry than the simple cubic one, can be obtained through the interference of laser beams coming from different directions and possibly not orthogonally aligned to each other [67–70].

Optical lattices can also be used to tune the dimensionality of the investigated system. For example, in first approximation, a deep 1D lattice divides an atomic cloud into two-dimensional pancakes, while with deep 2D optical lattices it is possible to confine the atomic motion along a single directions, realizing one-dimensional systems. Indeed, a 2D optical lattice configuration allowed us to study the physics of one-dimensional systems [32] (see section 7.1), while 3D optical lattices have been used to perform interaction-free spectroscopy of the clock transition and to investigate two-body collisions between different electronic states in "zero-dimensional" traps [41] (see chapter 5).

Band structure and Bloch functions

The problem of a single particle in a periodic potential has been extensively studied in the last century in solid state physics [71]. The problem is simplified by the discrete translational symmetry of the systems, which implies, through the Bloch theorem, a specific form of the eigenfunctions $\psi_k^{(n)}(z)$:

$$\psi_k^{(n)}(z) = e^{ikz}u_k^{(n)}(z), \tag{1.16}$$

where $u_k^{(n)}(z)$ is a function with the same periodicity $d = \lambda_L/2$ of the potential, that is $u_k^{(n)}(z + d) = u_k^{(n)}(z)$. Bloch waves are characterized by their crystal momentum, or quasimomentum, k, which is restricted to the first Brillouin zone, i.e. $-k_L < k < k_L$ [71]. The Schrödinger equation for a perfect one-dimensional sinusoidal potential along z, can solved in terms of Mathieu functions, as it can be written as:

$$\left[\frac{d^2}{dw^2} + \left(\frac{E}{E_r} - \frac{s}{2}\right) - 2\left(\frac{s}{4}\right)\cos(2w)\right]\psi(w) = 0, \quad w = k_L z, \tag{1.17}$$

11
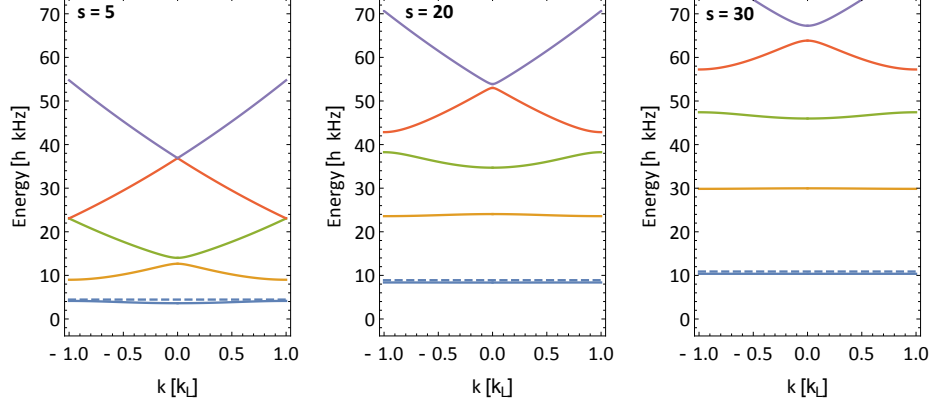
Figure 1.1: Energy bands of a 1D lattice for different lattice depth $V_0 = sE_r$. At higher lattice depth, the bands flatten and the energy gaps increase. The lowest band tends to harmonic oscillator frequency of Eq. (1.14).

which is the well-known Mathieu equation $y'' + [a - 2q \cos(2z)]y = 0$. with parameters $a = E/E_r - s/2$ and $q = s/4$. The eigenenergies of Eq. (1.17) is an infinite series of dispersion relations $E^{(n)}(k)$, where $k \in (-k_L, +k_L)$ and n is the band index, separated by energy gaps. The eigenenergies for different values of s are plotted in Fig. 1.1. Two main features of the energy bands appear clear from the figure: with increasing s the band gaps increase accordingly, while the energy bands gets narrower and approach the harmonic oscillator energy levels (dashed line in Fig. 1.1) at high values of s. In this regime, the band gap can be approximated as $\hbar\omega$, where ω is the harmonic frequency defined in Eq.(1.14). In the case of 3D lattices, the eigenenergies and the eigenfunctions can be computed easily since the problem is separable:

$$
\begin{aligned}
E^{(n_x, n_y, n_z)}(\mathbf{k}) &= E^{(n_x)}(k_x) + E^{(n_y)}(k_y) + E^{(n_z)}(k_z), \\
\Psi_{\mathbf{k}}(\mathbf{r}) &= \psi_{k_x}^{(n_x)}(x)\psi_{k_y}^{(n_y)}(y)\psi_{k_z}^{(n_z)}(z).
\end{aligned}
\tag{1.18}
$$

This fact has the peculiar consequence that in the 3D case, the gap between the energy bands do not open as soon as $s > 0$ as in the 1D case, but for $s \gtrsim 2.24$ (Fig. 1.2). This is caused by the fact that, in three dimensions, the first excited state, which corresponds to the eigenenergy $E^{(2,1,1)}(\mathbf{k})$, at low s and for some values of the quasi-momentum $\mathbf{k}$, can be smaller than the lowest band energy $E^{(1,1,1)}(\mathbf{k})$.

The Bloch eigenfunctions described above, are strongly delocalized functions which are not the suitable for the description of short-range interaction between particle pairs. For this reason, let us introduce a different basis composed by localised wave functions within each Bloch band, called Wannier functions [71]. In order to simplify the description, let us suppose that the tight binding approximation

12
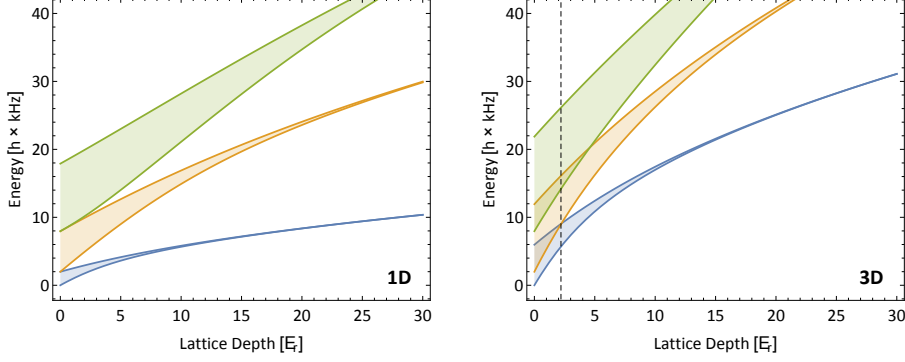
Figure 1.2: Bandwidth of lowest (blue), first (yellow) and second excited band (green) as a function of the lattice depth in units s of recoil energy. In a 1D lattice the gap opens as soon as $s \neq 0$, while in 3D the gaps opens only for $s \simeq 2.2$.

[11] is valid, which can be done in the Wannier basis. In this regime, the overlap between the Wannier functions centered on different lattice sites is non-negligible only for nearest-neighboring sites. Moreover, we assume that the lattice is deep enough that all energy scales are small compared to the energy gap to the first excited band and only the lowest energy band is populated. For the typical experimental condition, this situation holds for lattice sites with $s > 5$ [11, 12]. The usefulness of the Wannier function can be easily understood in the second quantization formalism, in which the wavefunction Ψ is replaced with field operators $\hat{\Psi}$. In particular the field operator related to a Bloch wavefunction $\psi_k^{(n)}(\mathbf{r})$ can be written as [11]:

$$\hat{\psi}_k^{(n)}(\mathbf{r}) = \sum_i w_i(\mathbf{r})\hat{a}_i, \qquad (1.19)$$

where $w_i(\mathbf{r})$ is the Wannier function centered in the site i and $\hat{a}_i^{\dagger}$ ($\hat{a}_i$) is the creation (annihilation) operator of an atom in the site i. Within the approximation discussed above, the Hamiltonian of non-interacting atoms in a lattice potential can be written as:

$$\hat{H} = -J \sum_{\langle i,j \rangle} \hat{a}_i^{\dagger}\hat{a}_j, \qquad (1.20)$$

where the notation $\langle \, \rangle$ indicates that the summation runs over nearest-neighboring lattice sites and the tunneling term J is given by:

$$J = \int d^3\mathbf{r}\, w_i^*(\mathbf{r}) \left[\frac{\hat{\mathbf{p}}^2}{2m} + V_{lat}(\mathbf{r}) \right] w_j(\mathbf{r}). \qquad (1.21)$$

The dependence of the tunneling J on the lattice depth expressed in units of recoil energy is nearly exponential [11], meaning that the tunneling parameter can be varied over a range spanning orders of magnitude simply changing the lattice beams intensity. In this way, it is possible to realize both very deep lattices, in
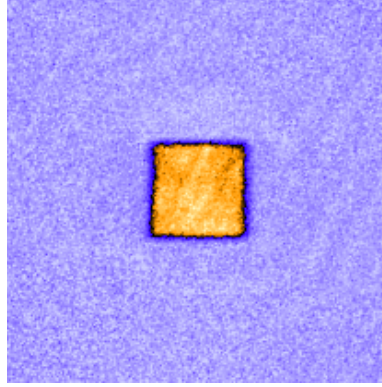
Figure 1.3: False-color time-of-flight image of the lattice momentum distribution of spin-polarized fermions in a s = 30 3D optical lattice. With a number of atoms $N = 2 \times 10^4$, only the lowest band is populated.

which the atoms are strongly localized since the tunneling to neighboring sites is negligible with respect to the experimental timescales, or shallow lattices, in which the atoms are delocalized over several lattice sites, due to a fast tunneling rate.

Above, the assumption that only the lowest lattice band is occupied is made. This condition is experimentally achieved by adiabatically ramping up the intensity of the lattice beams with an exponential ramp, to avoid atoms to Landau-Zener tunnel in the excited bands. In order to visualize the band population and check that the lattice loading procedure was executed successfully, a useful observable is the lattice momentum distribution of a Fermi gas in a optical lattice (Fig. 1.3). This is measured by means of band mapping technique [72, 73], which consists in switching off the lattice beams adiabatically with respect to the timescale $1/\omega$ (see Eq. 1.14), related to the lattice band gap, but faster than $1/\omega_{trap}$, associated to the trap frequencies of the external trapping potential. The lattice momentum is mapped onto the atomic velocity distribution, measured by absorption imaging after ballistic expansion.

1.1.3 Nearly resonant optical potentials

Up to now we assumed that the frequency ω of the laser used to generate the dipole potential is far-detuned from all the atomic transitions. A notable consequence of this condition is that all the sublevels of the state for which the dipole potential is calculated experience the same light shift. With a reference to Eq. (1.12), this is true if the detuning Δ_{mn} is greater that the energy separation between the sublevels of the final state m.

For example, in the case ^{173}Yb 1064 nm light is far detuned from the transitions (see section 4.1.2) and all the $m_F = -5/2, \cdots, +5/2$ states will experience the same light shift. If instead the detuning is of the order of the hyperfine splitting ΔE_{hfs}, for example of the $^3P_1$ state if 556 nm light, nearly-resonant with the

intercombination transition (see section 1.3.1), is used, then different nuclear spin states will experience different light shift. In such case, the expressions of Eq. (1.12) can be further generalized obtaining:

$$
\begin{aligned}
V_{dip}^{(n)}(\mathbf{r}, \omega) &= -\sum_{m \neq n} \frac{3\pi c^2}{2\omega_{mn}^3} |C_{mn}(q)|^2 \left(\frac{\alpha_{JJ'}\Gamma_{mn}}{\omega_{mn} - \omega} + \frac{\alpha_{JJ'}\Gamma_{mn}}{\omega_{mn} + \omega} \right) I(\mathbf{r}), \\
\Gamma_{sc}^{(n)}(\mathbf{r}, \omega) &= \sum_{m \neq n} \frac{3\pi c^2}{2\hbar\omega_{mn}^3} |C_{mn}(q)|^2 \left(\frac{\omega}{\omega_{mn}} \right)^3 \left(\frac{\alpha_{JJ'}\Gamma_{mn}}{\omega_{mn} - \omega} + \frac{\alpha_{JJ'}\Gamma_{mn}}{\omega_{mn} + \omega} \right)^2 I(\mathbf{r}),
\end{aligned}
$$

$$(1.22)$$

where $C_{mn}(q)$ is the Clebsch-Gordan coefficient of the transition from the initial state $|n\rangle |J, F, m_F\rangle$ to a final state $|m\rangle = \left| J', F', m_F' \right\rangle$ excited by a photon with polarization $q = (-1, 0, +1)$ (in spherical basis) and $\alpha_{JJ'} = \frac{2J'+1}{2J+1}$ is the multiplicity factor of a $J \rightarrow J'$ transition [60]. In particular, the Clebsch-Gordan coefficent $C_{mn}(q)$ can be written as:

$$
\begin{aligned}
C_{mn}(q) = \quad & (-1)^{2F'+J+I+m_F} \times \sqrt{(2f + 1)(2J + 1)(2F' + 1)} \times \\
& \times \left\{ \begin{array}{ccc} J & J' & 1 \\ F' & F & I \end{array} \right\} \left(\begin{array}{ccc} F' & 1 & F \\ m_F' & q & -m_F \end{array} \right)
\end{aligned}
$$

$$(1.23)$$

where the arrays enclosed in curly brackets and round brackets denote the 6j-symbol and the 3j-symbol respectively[60]. The dependence of the Clebsch-Gordan coefficients on m_F and the light polarization q is related to different line strengths between transitions from different magnetic sublevels of the initial state manifold excited by a certain polarization. This results in a different light shift for the different m_F states which is also dependent on the polarization of the incident light. These nuclear spin state-dependent optical potentials represent a very powerful tool for the manipulation of the atomic internal states. For example they are exploited in the Optical Stern-Gerlach (OSG) technique to realize a spin-dependent dipole force that splits the different spin components in the atomic cloud (see section 2.2.2).

1.2 Interactions at ultra-low temperatures

Atomic interactions play a crucial role in the field of quantum gases. First of all, interactions are fundamental to reach the incredibly low temperatures necessary to enter the degenerate regime since they are at the basis of evaporative cooling. Moreover, they are one of the building blocks of any many body phenomena that can be studied in experiment with quantum gases.

In this section, some basic, fundamental concepts regarding the interactions between neutral particles at very low temperature will be introduced. In this regime, the typical inter-particle distance is larger than the interaction range and the

system properties are substantially determined by two-body collisional processes. Since atoms are neutral particles, the interaction between them is not the long-range Coulomb interaction, but can be described by a central potential $V(r)$ arising from the atomic dipole-dipole interaction. Following the approach of ref[74], we chose a potential $V(r)$ given by a van der Waals potential at large distances and a repulsive hard core below a length scale r_c of the order of the atomic radius in order to take into account the repulsion between the two atoms electronic clouds:

$$V(r) = \begin{cases} -C_6/r^6 & \text{if } r > r_c \\ \infty & \text{if } r \leq r_c, \end{cases} \tag{1.24}$$

where C_6 is a constant and r_c is a length of the order of a few Bohr radii a_0. The range r_0 of the van der Waals interaction is given by [75]:

$$r_0 = \left(\frac{2\mu C_6}{\hbar^2}\right)^{1/4}, \tag{1.25}$$

where μ is the reduced mass of the two interacting particles. For two Ytterbium atoms in the ground state $C_6 \sim 2000$ a.u. (atomic units) [76], which implies an interaction range $r_0 \simeq 180\ a_0$. The De Broglie wavelength λ_{dB} becomes comparable with r_0 around 0.3 mK, meaning that for degenerate Ytterbium quantum gas both the De Broglie wavelength λ_{dB} and the inter-particle separation $n^{-1/3}$ are much larger than the effective range of interaction r_0. This is in general true in degenerate quantum gases. In this regime, the short-range details of the potential become irrelevant, implying that the collisional process can be parametrized by a single quantity, the scattering length, related to the phase shift acquired by the scattered wavefunction, and that the potential can be replaced by any other with the same associated scattering length.

In order to explicitly clarify the problem, let us consider the Hamiltonian describing two particles with mass m scattering through a spherically-symmetric potential $V(r)$ in the center of mass frame:

$$\hat{H} = \frac{\hat{p}_r^2}{2\mu} + \frac{\hat{L}^2}{2\mu\hat{r}^2} + V(\hat{r}), \tag{1.26}$$

where $\hat{p}_r$ is the relative radial momentum, $\hat{L}$ is the relative angular momentum and $\mu = m/2$ is the reduced mass. For two particles with relative motion energy of $E_k = \hbar^2 k^2/2\mu$, in the limit of $r \gg r_0$, the asymptotic wave function $\psi_{\mathbf{k}}(\mathbf{r})$ can be written as the sum of on incident plane wave and an outgoing scattered wave [75]:

$$\psi_{\mathbf{k}}(\mathbf{r}) \overset{r \to \infty}{\sim} e^{i\mathbf{k}\cdot\mathbf{r}} + f(\mathbf{k}, \mathbf{k}')\frac{e^{ikr}}{r}, \tag{1.27}$$

where $f(\mathbf{k}, \mathbf{k}')$ is called *scattering amplitude*, with $\mathbf{k}$ and $\mathbf{k}'$ the incoming and the scattered wavevectors respectively, and with $|\mathbf{k}| = |\mathbf{k}'| = k$ since the collision is elastic. Due to the spherical symmetry of the problem, the scattering amplitude only depends on the angle θ between the incoming and outgoing wave vectors, so

that $f(\mathbf{k}, \mathbf{k}') = f(k, \theta)$. Moreover, choosing the quantization axis z along $\mathbf{k}$, both the incident and scattered functions can be expanded in spherical partial waves with $m_z = 0$. In particular, The scattering amplitude will be given by [77]:

$$f(k, \theta) = \sum_{l=0}^{\infty} (2l + 1) \left(\frac{e^{2i\delta_l(k)} - 1}{2ik} \right) P_l (\cos \theta), \qquad (1.28)$$

where $P_l(\cos \theta)$ are the Legendre polynomials and $\delta_l(k)$ is the phase shift related to the l-th spherical wave. The total cross section σ_{tot} can be then obtained through the optical theorem [77]:

$$\sigma_{tot}(k) = \frac{4\pi}{k} Im[f(\theta = 0)] = \frac{4\pi}{k^2} \sum_{l=0}^{\infty} (2l + 1) \sin^2 \delta_l(k). \qquad (1.29)$$

In Eq. (1.26), the potential $V(r)$ is summed to the centrifugal potential giving a total potential $V_{tot}(r)$ which in partial waves assumes the form:

$$V_{tot}(r) = \frac{\hbar^2 l(l + 1)}{2\mu r^2} + V(r). \qquad (1.30)$$

In the low energy regime the energy of the relative particle E_k is not enough to overcome the centrifugal barrier and the potential $V(r)$ do not have any effect unless in case of $l = 0$ scattering, also called *s-wave scattering*, in which there is no centrifugal barrier and the atoms can effectively "feel" the presence of the potential. In particular it can be shown that [77]:

$$\delta_l(k) \sim k^{2l+1}. \qquad (1.31)$$

In case of *s*-wave scattering, the scattering amplitude in Eq. (1.28) is approximated by:

$$f(k) \simeq f_s = \frac{e^{i2\delta_0(k)} - 1}{2ik} = \frac{1}{k \cot \delta_0(k) - ik}, \qquad (1.32)$$

where f_s in the *s*-wave scattering amplitude. Time reversal symmetry implies that $\delta_0(k)$ must be an even function of k and therefore can be expanded to the order k^2, for $k \ll r_0^{-1}$, as [78]:

$$k \cot \delta_0 = -\frac{1}{a_s} + \frac{r_{\text{eff}} k^2}{2}, \qquad (1.33)$$

where a_s is the *s*-wave scattering length which can be defined as:

$$a_s = -\lim_{k \to 0} \frac{\tan \delta_0(k)}{k}, \qquad (1.34)$$

and r_{eff}, called *effective range*, is of the order of r_0 for Van der Waals potentials. Then the total cross-section (1.29) can be approximated as:

$$\sigma_{tot} \simeq 4\pi a_s^2. \tag{1.35}$$

All the results obtained are valid in case of scattering between two distinguishable particles. Quantum statistics plays a role in this, owing to the necessity to impose the symmetrization (antysimmetrization) of the bosonic (fermionic) wavefunction. This can be obtained imposing that $\Psi(\mathbf{r}_1, \mathbf{r}_2) = \varepsilon \Psi(\mathbf{r}_2, \mathbf{r}_1)$, with $\varepsilon = +1(-1)$ for bosons (fermions). The asymptotic scattering wavefunctions of Eq. (1.27) assumes the form:

$$\psi_{\mathbf{k}}(\mathbf{r}) \sim \frac{e^{ikz} + \varepsilon e^{-ikz}}{\sqrt{2}} + \frac{f(k,\theta) + \varepsilon f(k, \pi - \theta)}{\sqrt{2}} \frac{e^{ikr}}{r}. \tag{1.36}$$

Due to the parity $(1)^l$ of the spherical harmonic functions in Eq. (1.28) of the scattering amplitude, it follows that the bosonic (fermionic) particle statistics doubles the contribution of the even (odd) partial waves, canceling out the odd (even):

$$\sigma_{tot} = \frac{8\pi}{k^2} \sum_{l \text{ even}}^{\infty} (2l + 1) \sin^2 \delta_l(k) \quad \text{Bosons,}$$

$$\sigma_{tot} = \frac{8\pi}{k^2} \sum_{l \text{ odd}}^{\infty} (2l + 1) \sin^2 \delta_l(k) \quad \text{Fermions.} \tag{1.37}$$

A remarkable consequence of this fact, is that in the low energy regime (i.e. in most cases, with ultracold gases), where only s-wave scattering processing may occur, a sample of spin polarized, indistinguishable fermions would not interact because of the Pauli principle. This means that a spin polarized Fermi gas can be treated as an ideal, non-interacting gas in the very low temperature regime.

1.2.1 The pseudo-potential

As stated above, in diluted quantum degenerate gases at low temperatures the short-range details of the interaction potential are completely irrelevant to the scattering process, and it is possible to replace $V(r)$ with any other potential with the same scattering length. Here we introduce a very convenient interaction pseudo-potential, which has a very simple form and has the advantage to allow for a significant simplification of the calculations. This pseudo-potential is determined with a technique successfully borrowed from electrostatics [79], and takes the name of Huang's pseudopotential. Usually, in order to calculate the electrostatic potential generated by a charge distribution on a sphere, this is substituted by an equivalent series of point-like multipoles in the center of the sphere leading to the exact potential outside the sphere. Following the same approach, since short range details of the real potential are not important it is possible to replace the boundary conditions imposed by a hard-sphere potential with a series of point-like scatterers giving rise to s-wave, p-wave and so on. It was demonstrated [80] that

in case of s-wave scattering, the pseudo-potential that reproduces exactly a hard sphere-potential has the form:

$$U(r) = -\frac{\hbar^2}{m}\frac{4\pi}{k\cot(\delta_0)}\partial_r(r\cdot).$$ (1.38)

Using Eq.(1.33) in the limit $k \ll 1/r_{\text{eff}}$, we obtain the pseudo-potential:

$$U(r) = g\,\delta(\mathbf{r})\frac{\partial}{\partial r}(r\cdot),$$ (1.39)

with $g = 4\pi\hbar^2 a_s/m$. With this formulation of the interaction potential, a formula for the total cross section for bosons (or for distinguishable spin-1/2 fermions) can be easely derived [75]:

$$\sigma_{tot}(k) = \frac{8\pi a_s^2}{1 + k^2 a_s^2},$$ (1.40)

which leads to the asymptotic results:

$$\sigma_{tot} = \begin{cases} 8\pi a_s^2 & \text{if } ka_s \ll 1 \\ 8\pi/k^2 & \text{if } ka_s \gg 1. \end{cases}$$ (1.41)

The first is the same result already found in Eq. (1.35) for the total scattering cross-section, with a multiplicative factor of 2 to take into account the statistics, while the second expresses the fact that at high energy, or at high values of scattering length, the cross section depends only on the collisional energy, entering the so-called *unitary regime*.

1.2.2 Emergence of SU(N) symmetry

In this section we will extend the results obtained above to the case of spinful fermions and will briefly review the emergence of SU(N) symmetry in fermionic ^{173}Yb. SU(N) symmetry has important consequences on the properties of many interacting fermionic many-body systems [34]. Moreover, the consequences of SU(N) symmetry are remarkable in many fields of physics beyond many-body physics with ultracold gases, e.g. in quantum chromodynamics, where the interaction between quarks is mediated by SU(3) gauge bosons known as gluons [81, 82]. Since the physical implications of SU(N) symmetry are not the main focus of this work, only a brief review on the origin and consequences of this symmetry will be discussed below. A more detailed and rigorous discussion on the nature of SU(N) symmetry, as well as an extensive list of references on its consequences in different physical systems can be found in Ref. [83]. In the same reference, the theoretical treatment of the SU(N) symmetry is extended also to the metastable $^3P_0$ state (see also section 5.1.1), and its emergence in a mixture of fermionic Ytterbium atoms in different electronic and spin states is observed [84].

In the previous sections, no assumption has been made regarding the particle spin. Let us now consider the case of two interacting particles with total spin F_1 and F_2 colliding with relative orbital angular momentum L. In general, in presence of an atomic spin degree of freedom, the quantum mechanical exchange interaction causes the inter-atomic potential to depend strongly on the total spin of the colliding atomic pair [85, 86]. At small inter-particle distances, due to the non-negligible overlap of the electronic clouds, the individual F_i and m_i are no more good quantum numbers. In this case the total internal angular momentum $F_{pair} = F_1 + F_1$ of the pair of colliding atoms has to be considered. Supposing that the "spinor-gas collision" approximation [86] holds, we assume a rotationally invariant short-range interaction potential which implies that the the total angular momentum of the colliding pair, namely $F_{pair} + L$, is conserved during the collision. In case of ultracold s-wave scattering processes, the relative orbital angular momentum is zero, and the conserved quantity is the total internal angular momentum of the pair F_{pair}[1], as well as its projection M_{pair} along the quantization axis. A final constrain is given by the particles spin-statistics, which implies that for s-wave scattering F_{pair} has to be *even* [86] in order to have the correct symmetry of the total wavefunction, a results that surprisingly holds both for bosons and fermions.

The pseudo-potential of Eq. (1.39), which is valid for bosons and spin-1/2 fermions, can then be generalized to the case of spinor condensates or higher-spin fermionic gases [87, 88]. The pseudo-potential for a pair of spin-F atoms will be given by:

$$\hat{U}(\mathbf{r}) = \frac{4\pi\hbar^2}{m} \sum_{F_{pair} \text{ even}} a_{F_{pair}} \hat{P}_{F_{pair}} \delta(\mathbf{r}), \qquad (1.42)$$

where m is the atomic mass, and $a_{F_{pair}}$ and $\hat{P}_{F_{pair}}$ are the scattering length and the projector associated to the a colliding pair with total angular momentum F_{pair} respectively. Finally $\hat{P}_{F_{pair}}$ is the projection operator on the state $\left| F_{pair} \right\rangle$ and is given by:

$$\hat{P}_{F_{pair}} = \sum_{M_{pair}=-F_{pair}}^{+F_{pair}} \left| F_{pair}, M_{pair} \right\rangle \left\langle F_{pair}, M_{pair} \right|. \qquad (1.43)$$

Note that the summation in Eq. (1.42) runs over even values of F_{pair}, implying that all the scattering processes between two atoms with individual total angular momentum F can be described by $(2F + 1)$ scattering lengths (for example, binary collisions between ^{173}Yb atoms with $F_1 = F_2 = 5/2$ will have three possible scattering lengths a_0, a_2, a_4). In order to understand the effect of collisions on the spin degree of freedom of the individual atoms, we shall consider the the coupling between different single-atom spin orientations induced by the interaction. Let us

---

[1]Here we are also assuming that the spin-orbit coupling can be neglected through the short-range molecular potential so that F_{pair} and L are conserved individually during the collision

assume an initial state of the form $|F_1, m_1; F_2, m_2\rangle$. The coupling to a final state $|F_3, m_3; F_4, m_4\rangle$ will be given by:

$$\langle F_3, m_3; F_4, m_4| \hat{U}(\mathbf{r}) |F_1, m_1; F_2, m_2\rangle =$$
$$= \frac{4\pi\hbar^2}{m}\delta(\mathbf{r}) \sum_{F_{pair}} \sum_{M_{pair}} a_{F_{pair}} \langle F_3, m_3; F_4, m_4|F_{pair}, M_{pair}\rangle \times$$
$$\times \langle F_{pair}, M_{pair}|F_1, m_1; F_2, m_2\rangle . \quad (1.44)$$

From this equation, it is clear that in general after a collision between atoms with definite spin, different spin states may become populated due to the interference of the different scattering channels with total angular momentum F_{pair}. These collisional processes which populate different spin states (in which a non-zero electronic angular momentum J couples the different nuclear spin states of the interacting atoms) are called spin-changing collisions and have been observed in alkali atoms, as for example bosonic ^{87}Rb [89, 90] and fermionic ^{40}K [91, 92].

In case of fermionic Ytterbium instead, due to the absence of electronic angular momentum in the ground state, the nuclear spin is the only angular momentum degree of freedom of the atom, so the total angular momentum is simply $F = J+I = I$. In this situation, the nuclear spin is strongly decoupled from the electronic cloud: the spin degree of freedom is protected inside the nucleus, and it is substantially not affected by the physics happening at the electronic cloud distance scale. Since the scattering length is mainly determined by the electronic clouds of the two colliding atoms, the scattering lengths associated to collisional channels with different total angular momenta F are to a high degree all the same, due to the strong decoupling between nuclear and electronic degrees of freedom. For ^{173}Yb ground state it has been calculated theoretically [26] a relative variation between different scattering lengths of the order of $\delta a_s/a_s \sim 10^{-9}$, where $a_s = 199.4 \, a0$ [93]. Taking into account this equivalence between the different scattering lengths $a_{F_{pair}}$ and using the completeness relation $\sum_{F_{pair}} \sum_{M_{pair}} = \mathbb{1}$, for fermionic Ytterbium atoms in the ground state (and in the metastable state, see section 5.1.1), the matrix element in Eq. (1.44) reduces to:

$$\langle F_3, m_3; F_4, m_4| \hat{U}(\mathbf{r}) |F_1, m_1; F_2, m_2\rangle =$$
$$= \frac{4\pi\hbar^2}{m}\delta(\mathbf{r})a_{F_{pair}} \langle F_3, m_3; F_4, m_4|F_1, m_1; F_2, m_2\rangle , (1.45)$$

which is different from zero only if the final state coincides with the initial state. Under such conditions, the interaction Hamiltonian will be invariant under all transformations belonging to the SU($N = 2F + 1$) group. This means that not only F_{pair} and M_{pair} are conserved, but also the spin projection of each atom is now individually conserved, so that m_F becomes a good quantum number at any inter-atomic distance. Formally, the SU(N) symmetry can be extended to the total

Hamiltonian of the system, which is given, in the second-quantization formalism, by:

$$
\begin{aligned}
\hat{H} &= \sum_m \int \hat{\Psi}_m^\dagger(\mathbf{r}) \left(-\frac{\hbar^2}{2\mathrm{m}} \nabla^2 + V_{ext}(\mathbf{r}) \right) \hat{\Psi}_m(\mathbf{r}) d\mathbf{r} \\
&+ g \sum_{m<m'} \int \hat{\Psi}_m^\dagger(\mathbf{r}) \hat{\Psi}_{m'}^\dagger(\mathbf{r}) \hat{\Psi}_{m'}(\mathbf{r}) \hat{\Psi}_m(\mathbf{r}) d\mathbf{r},
\end{aligned}
\tag{1.46}
$$

where $\hat{\Psi}_\alpha(\mathbf{r})$ is the annihilation field operator of a particle with spin component α. More specifically, Hamiltonian (1.46) is invariant under the transformations:

$$
\hat{S}_n^m = \int \hat{\Psi}_n^\dagger(\mathbf{r}) \hat{\Psi}_m(\mathbf{r}) \, d\mathbf{r},
\tag{1.47}
$$

which replaces a particle of spin m with one of spin n. The most striking consequence of SU(N) symmetry is that no spin-changing collisions occur, which implies all the spin mixtures are stable. Therefore, by suitable optical pumping techniques (see section 2.2.2), it is possible to experimentally initialize atomic samples with an arbitrary number N of spin components, with $2 \leq N \leq 6$, which are stable on the experimental timescales, paving the way to the study of $SU(N)$-symmetric Hamiltonians with arbitrary N.

1.3 Ytterbium

Ytterbium (Yb) is a rare-earth element, the fourteenth in the lanthanide series with atomic number $Z = 70$. It is the last element in the f-block of the periodic table, meaning the 4f-shell is complete with 14 electrons. The full electronic configuration is thus [Xe] $4f^{14}\, 6s^2$. Due to this complete f-shell, its electronic structure is substantially determined by the two valence electrons in the shell 6s and its properties are therefore very similar to alkaline-earth atoms of the second group and quite different from other rare-earth elements like Erbium and Dysprosium.

Ytterbium was discovered in 1878, when the Swiss chemist Jean Charles Galissard de Marignac, while examining samples of gadolinite, found a new component in the earth then known as erbia, and he named it ytterbia [94]. Nevertheless, due to the difficulties in the separation process of Ytterbium, its physical and chemical properties of Ytterbium could not be determined with any precision until 1953, when the first almost pure sample of Ytterbium metal was obtained. Ytterbium is soft, malleable and ductile, and has a bright, silvery appearance in its pure form. Ytterbium metal slowly tarnishes reacting with moisture, and it quickly oxidizes when dispersed in air and under oxygen. Ytterbium has a density of 6.90 g/cm^3 near room temperature, lower than the typical $9 - 10$g/cm^3 of its neighbors in the periodic table, due to a different crystalline structure. Also, Ytterbium has a melting point of 824 °C and a boiling point of 1196 °C, significantly lower than those of

Isotope	Mass (a.m.u.)	Relative abundance (%)	Nuclear Spin
^{168}Yb	167.933894	0.13	0
^{170}Yb	169.934759	3.05	0
^{171}Yb	170.936323	14.3	1/2
^{172}Yb	171.936378	21.9	0
^{173}Yb	172.938208	16.12	5/2
^{174}Yb	173.938859	31.8	0
^{176}Yb	175.942564	12.7	0

Table 1.1: Summary of the properties of the seven stable isotopes of Ytterbium. Natural abundances are taken from [99], while the atomic mass is taken from [100].

other rare-earth elements. This is quite an advantage, because the vapor pressure necessary to obtain an acceptable atomic flux from the over (see section 2.1.1) is reached at a temperature of the order of $400 - 500$ °C, achievable by means of relatively uncomplicated oven setups and well below the temperatures needed for other rare-earth elements (e.g. ~ 1150 °C for Holmium [95] and around 1300 °C for Erbium [96] and Dysprosium [97]). In this temperature range, Ytterbium becomes highly reactive leading to rapid chemical deterioration of silica glass [98]. Ytterbium is also known to chemically bond to silica glass and (more weakly) to sapphire already at room temperature, so particular care has to be taken with vacuum viewports, which should not be exposed to the atomic vapor or to a direct flux without being heated.

Natural Ytterbium has seven stable isotopes: ^{168}Yb, ^{170}Yb, ^{171}Yb, ^{172}Yb, ^{173}Yb, ^{174}Yb and ^{176}Yb [99]. In table 1.1 the relative abundances and some fundamental properties of the different isotopes are reported. In Ytterbium many isotopes are present in relatively high natural abundance, differently from many alkali and alkaline-earth(-like) atoms. The two isotopes with non-zero nuclear spin, ^{171}Yb (with nuclear spin $I = 1/2$) and ^{173}Yb ($I = 5/2$), are fermionic, while all other isotopes, including ^{174}Yb which is the most abundant, are bosonic and have zero nuclear spin ($I = 0$). The results presented in this work are obtained using a fermionic isotope, the ^{173}Yb, characterized by a large nuclear spin $I = 5/2$, strong repulsive interactions in the ground state and by the possibility to directly excite the lower triplet state, the $^3P_0$.

1.3.1 Electronic states and transitions

Owing to its electronic configuration, which presents a full 4f shell and two electrons in the 6s, the electronic properties of Ytterbium are similar to those of Helium and alkali-earth atoms, like Strontium. Ytterbium level structure can be well described by the LS-coupling (Russel-Saunders coupling). The two valence electrons can couple in a spin singlet, in which the two electron spins are antiparallel, or a spin

triplet, in which the spins are instead parallel. These two possible arrangements divide the energy ladder in two different manifolds, which are completely separated in the LS-coupling scheme, as a dipole transition between a singlet ($S = 0$) and a triplet ($S = 1$) state would violate the spin selection rule $\Delta S = 0$.

Ytterbium ground state is the $^1S_0$. The total electronic momentum $J = 0$ implies that this state is completely insensitive to magnetic fields in bosonic isotopes, which have nuclear spin $I = 0$. In fermionic isotopes, which have nuclear spin different from zero, the ground state feels instead the presence of magnetic fields, but its sensitivity is ~ 3 orders of magnitude lower than in states with $J \neq 0$. Indeed, the total angular momentum F is simply the nuclear spin I and no hyperfine structure is present. In presence of magnetic field, the ground state of fermionic isotopes simply splits in a Zeeman manifold whose energy levels for a given magnetic field B are given by:

$$\Delta E_Z(B) = g_F m_F \mu_B B, \tag{1.48}$$

where μ_B is the Bohr magneton and m_F is the projection of the nuclear spin along the magnetic field direction in units of $\hbar$. The term g_F is the Landé factor, and is given by:

$$g_F = g_J \frac{F(F+1) - I(I+1) + J(J+1)}{2F(F+1)} + g_I \frac{F(F+1) + I(I+1) + J(J+1)}{2F(F+1)}. \tag{1.49}$$

If $J = 0$ the first term vanishes and it simply reduces to the nuclear g-factor:

$$g_F = g_I = \frac{\mu_I}{\mu_B |I|}, \tag{1.50}$$

where μ_I is the nuclear magnetic moment in units of the nuclear magneton μ_N. In particular the nuclear moment is $+0.4919\mu_N$ and $-0.6776\mu_N$ for ^{171}Yb and ^{173}Yb respectively [100]. Being the nuclear magneton ~ 2000 times lower than μ_B, hence the reduced sensitivity of fermionic Yb ground state to magnetic fields.

The ground state is connected to the $^1P_1$ state via a dipole allowed transition (see Fig. 1.4) of wavelength $\lambda = 398.8$ nm and natural linewidth $\Gamma = 2\pi \times 27.9$ MHz, corresponding to a lifetime of 5.7 ns and a saturation intensity of 57 mW/cm^2 [101]. In bosonic isotopes, only a single transition $F = 0 \rightarrow F' = 1$ is present, while in fermionic isotopes due to the non-zero nuclear magnetic moment, the hyperfine interaction generates additional structure in the $^1P_1$ state. The resulting hyperfine energy shifts are of the order of the GHz and are comparable to the isotope shifts of the blue transition, and the spectrum shows a succession of resonances from different isotopes. A complete characterization of the spectrum is given in Ref. [102]. This transition is exploited in the Zeeman slower (see section 2.2.1) and for the imaging of the atomic cloud.

Since the LS description is an approximation of the real atom, especially for atoms with high atomic number as Ytterbium, singlet and triplet states are connected
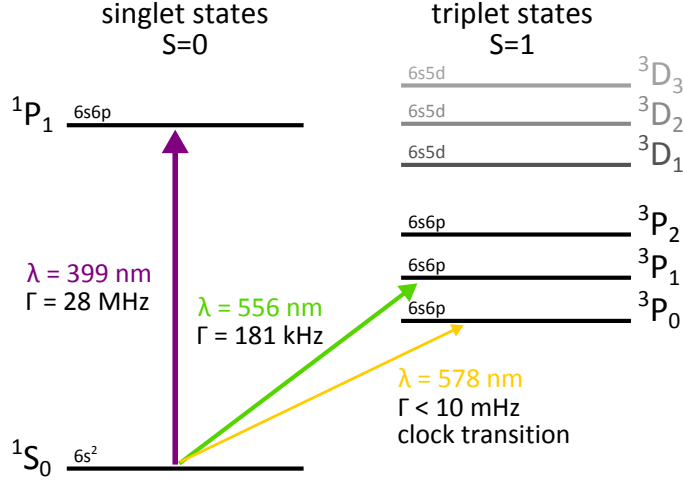
Figure 1.4: *Scheme of the main optical transitions of Ytterbium atoms used in this work.*

by narrow optical transition, which are called intercombination transitions. These transitions are allowed due to the presence of the spin-orbit interaction, which for instance partially mixes the $^1P_1$ and the $^3P_1$ states allowing for a direct excitation of the $^3P_1$. The green $^1S_0 \to {}^3P_1$ transition wavelength is 555.6 nm, with a natural linewidth of $\Gamma = 2\pi \times 181$ kHz [101]. Also in this case, in fermionic isotopes the $^3P_1$ state has a hyperfine structure with a separation energy between the levels of the order of the GHz, comparable to the isotope shifts. A detailed characterization of this transition for all isotopes was reported in Ref. [103]. Due to its narrow character, this intercombination transition is fundamental for both the magneto-optical trap cooling stage and for the manipulation of the atomic sample, as showed in section 2.2.2. Indeed, due to its non-zero angular momentum J, the coupling of the $^3P_1$ manifold to an external magnetic field is as large as in the alkali atoms ($g_{F'} = 0.425$ for the $^3P_1$ ($F' = 7/2$) state) and the magnetic field sensitivity is $g_{F'}\mu_B = 2\pi \times 595$ kHz/G that is of the order of 3Γ/G. This implies that already with a modest magnetic field of tens of Gauss the Zeeman splitting is enough to allow for the selective addressing of optical transitions of a specific nuclear spin component without affecting the others.

Ytterbium is also characterized by an extremely narrow optical transition that connects the ground state to the lowest triplet state, the $^3P_0$. This transition, which has a wavelength of 578.4 nm corresponding to a yellow color, is a doubly forbidden transition, as it violates not only the electric dipole selection rule $\Delta S = 0$, but is also a $J = 0 \to J' = 0$ transition. Nevertheless, in fermionic isotopes a very small dipole matrix element arises from the hyperfine interaction that mixes the $^3P_0$ state with the $^3P_1$, resulting in a natural linewidth of the order of 10 mHz. In bosons it can instead be induced by quenching of the $^3P_0$ state with the $^3P_1$ by a magnetic field (see section 4.1). In order to exploit such a narrow linewidth for precision measurements, an extremely pure laser source is necessary, which is described in

Isotope	^{168}Yb	^{170}Yb	^{171}Yb	^{172}Yb	^{173}Yb	^{174}Yb	^{176}Yb
^{168}Yb	**252.0**	117.0	89.2	65.0	38.6	2.5	359.2
^{170}Yb		**63.9**	36.5	-2.1	-81.3	-518.0	-209.5
^{171}Yb			**-2.8**	-84.3	-578	-429	141.6
^{172}Yb				**-599**	418	200.6	106.2
^{173}Yb					**199.4**	138.8	79.8
^{174}Yb						**104.9**	54.4
^{176}Yb							**-24.2**

Table 1.2: Summary of the s-wave scattering lengths between ground state Ytterbium atoms in units of a_0 [93].

details in Chapter 3. This transition is a fundamental element in the experiments reported in this work. For this reason, its properties will be described in details in Chapter 4, where a measurement of the absolute frequency of the $^1S_0 \rightarrow {}^3P_0$ transition in ^{173}Yb, which improves the known value by two orders of magnitude, is also reported.

1.3.2 Collisional properties

Ytterbium isotopes are characterized by a wide range of interaction strengths in the ground state. A complete characterization of the scattering properties between ground state atoms in the *s*-wave regime has been carried out in Ref. [93] by means of two-colour photoassociation spectroscopy on the $^1S_0 \rightarrow {}^3P_1$ transition. The measured s-wave scattering lengths, which are independent on the nuclear spin, as already mentioned in sec. 1.2.2, are summarized in Table 1.2, and they can be seen to vary from large negative to large positive values with a wide choice of intermediate conditions. For this reason, as well as for the non-negligible presence of both fermionic and bosonic isotopes, Ytterbium is an ideal candidate both for the production of mono-isotopic quantum gases and for the study of Bose-Bose, Bose-Fermi and Fermi-Fermi mixtures [104–107].

More recently, also the collisional properties between the $^1S_0$ and $^3P_0$ states in fermionic isotopes have been studied [41, 84, 108, 109]. The knowledge of these scattering properties is important due to the strong interest in exploiting the metastable $^3P_0$ state as tool in quantum simulation, as well as for the determination and characterization of collisional shifts in optical lattice clock [110]. In particular, in Chapter 5 an estimation of the scattering length relative to the spin-antisymmetric $|eg^+\rangle$ state is determined from the frequency of spin-exchange oscillations driven by the inter-orbital spin-exchange interaction [41]. This scattering length is remarkably large if compared to that of the spin-symmetric state $|eg^-\rangle$, which we also estimate to be in agreement with the value given in Ref. [84], giving rise to a strong spin-exchange interaction.

Chapter 2

Experimental setup and procedure

This chapter briefly illustrates the main features of the experimental apparatus and of the procedures adopted to trap, cool down an manipulate atomic Ytterbium. After a description of the main components of the vacuum and laser setups, we will describe the steps of the experimental procedure which produces degenerate atomic gases of Ytterbium. To conclude we will review the basic concepts of the techniques employed to realize ultracold samples of fermions with arbitrary number of spin components and to perform spin selective imaging. These subjects are described in detail in Ref. [111].

2.1 Experimental setup

2.1.1 Vacuum system

The vacuum apparatus is shown in Fig. 2.1. The atomic source of the experiment is an oven (**1**) containing 7 g of 99.9% pure Ytterbium chunks in natural isotopes composition. The oven operates at a temperature of 525 °C, corresponding to a vapor pressure of 10^{-2} Torr and to a most probable atomic velocity of $\sim$ 340 m/s [7]. A square array of $\sim$ 100 small tubes (with 1 cm length and 0.2 mm internal diameter) located at the exit of the oven allows for a collimation of the atomic beam and the implementation of a first differential pumping state, which is permed by a 20 l/s Varian Starcell ion pump (**3**) placed after the oven. The oven is connected to the rest of the setup by two small tubes (**6**) with lengths 8 and 10 cm, respectively, and with internal diameter 5 mm, which define two other differential pumping stage performed with a second 20 l/s ion pump (**3**) and a 55 l/s Varian Starcell ion pump (**14**). Between the two tubes is located a pneumatic shutter (**4**) which is used to block the atomic beam when the MOT is not loading in order to reduce the Ytterbium coating of the sapphire Zeeman slower beam input window (**17**).

An all-metal VAT-48124 UHV gate valve (**7**) connects this first section to the
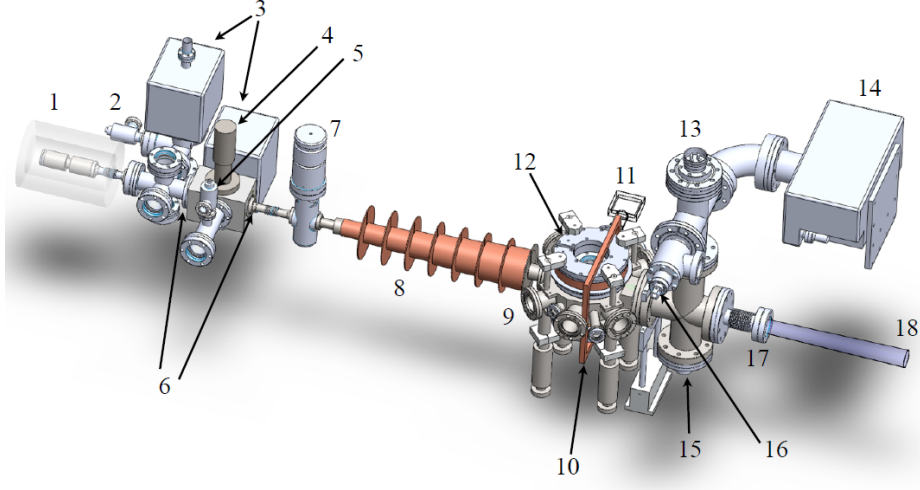
Figure 2.1: 1) Oven. 2) UHV valve. 3) Ion pumps for differential pumping (20 l/s each). 4) Compressed air shutter for atomic beam. 5) UHV valve. 6) Differential pumping tubes (not shown). 7) VAT UHV gate-valve. 8) Zeeman Slower. 9) MOT chamber. 10) Compensation coil. 11) Glass cell. 12) MOT coils. 13) Titanium sublimation pump (TSP). 14) Ion pump for MOT chamber (55 l/s). 15) UHV Gauge, mod. Bayard-Alpert, Varian UHV-24p. 16) UHV Valve. 17) Sapphire window with bellow. 18) Slowing beam at 399 nm.

UHV part of the apparatus, where the experiment takes place. The Zeeman Slower (**8**) slows down the atoms from thermal velocity to a few tens of m/s (see section 2.2.1) in order to be captured in a magneto-optical trap (MOT, see section 2.2.1). A compensation coil (**10**) is used to balance out the residual magnetic field of the Zeeman slower in the MOT chamber. The MOT is implemented with two water cooled anti-Helmholtz coils (**12**) (for details see Ref. [112]) mounted on a AISI L316 stainless steel octagonal chamber (**9**). On the horizontal plane, the chamber features seven CF40 flanges. One is used to connect the MOT chamber to the Zeeman slower and the four flanges at 45° degrees with respect to the atomic beam axis are used for the horizontal MOT beams. The two flanges orthogonal to the atomic beam axis are used as input window for the optical transport beam and as connector to the glass cell (**11**), respectively. All glass windows have broadband AR coating from 400 to 1100 nm. The MOT chamber also has two CF100 flanges on the vertical direction, both with a CF40 window in the center. The upper CF100 flange has two metallic mirror holders which are used to implement an in-vacuum optical cavity (see section 2.1.1) along the axis of two of the four CF16 windows in the horizontal plane of the MOT chamber (see Fig. 2.5). On the eighth side of the horizontal plane, opposite to the Zeeman slower and along the atomic beam axis, a CF63 flange connects the MOT chamber to a cross with a 55 l/s Varian Starcell ion pump (**14**), which helps to keep a pressure of the order of 10^{-11} Torr in the UHV part of the experiment. On top of the cross, we mounted a titanium sublimation pump (TSP) (**13**) for an optimal maintenance of the UHV environment.

The pressure is measured with a Ion Gauge UHV-24P Bayard-Alpert by Varian (**15**) mounted at the bottom of the cross. Finally, the cross is connected through a bellow to the sapphire input window (**17**) of the Zeeman slower beam (**18**), which is heated to 250 °C to avoid atoms coming from the atomic beam to stick on it.

In-vacuum resonator

This experimental apparatus is characterized by the presence of an in-vacuum optical cavity in the MOT chamber [113] to enhance the collection of atoms from the MOT and pre-cool them before their optical transport in the glass cell (see next section). The Fabry-Perot cavity is made up of two metallic mountings fixed to the CF100 upper flange of the MOT, which hold two spherical mirrors with a radius of curvature $r_c = 2$ m, diameter $d = 6.35$ mm and thickness 2.3 mm. The mirror reflectivity is $R = 99.98\%$, which results in a theoretical finesse of $\mathcal{F} \simeq 1600$. The cavity length is $L = 9$ cm, leading to a free spectral range (FSR) of 1.67 GHz. The cavity has been pre-aligned before evacuating the setup: the vertical degree of freedom was adjusted using the screws present on the mirror holders while the horizontal tilt was adjusted before tightening the holders to the flange. The cavity geometry has been designed to achieve the largest possible beam dimension in order to match the MOT size, compatibly with the trap depth which needs to be higher than the MOT temperature. With these constraints, the beam waist has been chosen as $w_0 = 300$ μm. The measured finesse is $\mathcal{F} \simeq 1850$, which results in a power enhancement factor of the approximately $4\mathcal{F}/\pi \sim 2350$ (neglecting the losses). These parameters correspond to a trap depth of $V_0/k_B \simeq 800$ μK $\simeq 8\,T_{MOT}$ with an incident power of only 1.8 W.

Glass science cell

The UHV chamber also features a high optical access glass cell, in which the atoms are transported from MOT chamber. In cold atoms experiments, it is becoming more and more common to perform the MOT in a separated vacuum chamber where the atoms are captured and pre-cooled and then optically or magnetically transport them in a separated science cell [114, 115]. This choice presents several advantages, first of all a very high optical access, not achievable in a metallic chamber, which is necessary to optical manipulation and high-resolution addressing of the quantum degenerate sample. Moreover, experiments performed in the glass cell are not influenced by the presence of residual magnetization of the metallic parts of the vacuum apparatus, as well as of Kovar glass-to-metal seal.

Our glass cell is manufactured by Hellma Analytics. The cell has external dimensions 60mm × 60mm × 18mm (see Fig. 2.2). The glass faces are 5 mm thick, hence the internal dimensions are 50mm × 50mm × 8mm. The cell has a reduced thickness in the vertical direction (9 mm between the center and the outer face) in order to allow for the possibility to implement single-atom resolution imaging using a high-NA (numerical aperture) objective with a small working distance. The
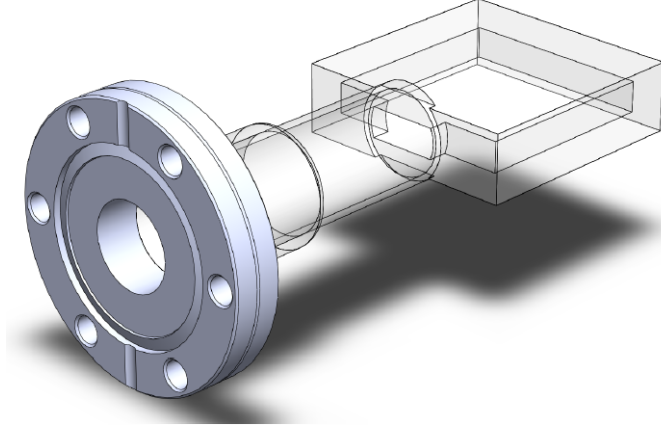
Figure 2.2: 3D model of the glass cell sealed to a CF40 flange.

glass cell is connected to the MOT chamber through a glass-metal junction and a CF40 flange. The geometric centers of the glass cell and of the MOT chamber are separated by 26 cm along which the atoms are optically transported (see section 2.2.1).

2.1.2   Laser setup

Here we briefly describe the laser systems used for the production and manipulation of degenerate Yb gases. Ytterbium lowest atomic transitions lay in the visible range (399 nm, 556 nm and 578 nm, see section 1.3.1). Since at the time of construction of the apparatus high-power sources with narrow linewidth were not available at these wavelengths, we adopted a scheme based on cavity-enhanced second harmonic generation (SHG) which produces visible light starting from the radiation emitted by commercial infrared lasers. Far-off-resonance lasers at 1064 nm and 759 nm are also used to produce dipole traps and optical lattices, which are necessary to reach the quantum degeneracy and perform experiments. Additional details on the 399 nm and 556 nm laser systems, as well as for the 1064 nm and 759 nm systems, can be found in [111, 112, 116, 117]. A separate section (3.1) is instead dedicated to a detailed description of the 578 nm ultranarrow laser system, which is one of the main topic of this work.

399 nm and 556 nm laser systems

Laser radiation at 399 nm is generated starting from a fiber-coupled tapered-amplifier laser-diode system Toptica TA PRO laser delivering 1.1 W at 798 nm. This radiation is then frequency doubled with a 15 mm long Lithium-Triborate (LBO) non-linear crystal, cut for type-I phase matching and stabilized at a temperature of 55 °C. In order to increase the conversion efficiency of the SHG process and
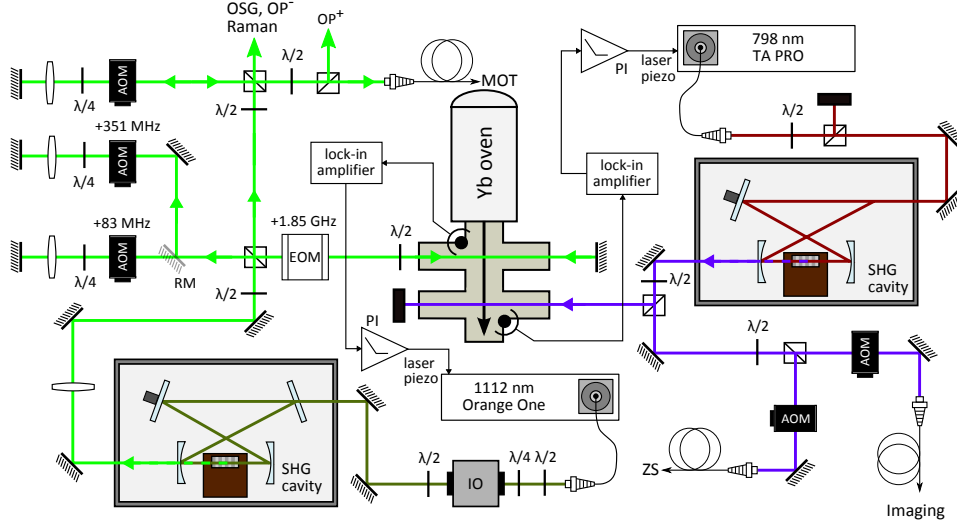
Figure 2.3: Scheme of the laser systems at 399 nm and 556 nm. The visible light is generated by means of cavity-enhanced SHG starting from the radiation of two infrared laser respectively at 798 nm and 1112 nm. For both lasers, part of the light is used to perform spectroscopy on a atomic beam generated in an oven. The removable mirror RM enables the switch of the 556 nm laser between bosons and fermions (see text and Ref. [111] for details). The rest of the light of two laser is divided in different paths with multiple purposes.

enhance the 399 nm output power, the LBO crystal is placed in a bow-tie optical cavity. The cavity, formed by two plane mirrors and two concave mirrors, is based on the same design of the 578 nm laser doubling cavity, which is discussed in detail in section 3.1.2, with the exception of the optical components (crystal and mirrors). It has a FSR of 749 MHz and the finesse is $\mathcal{F} \sim 100$. Similarly to the 578 nm laser case, in order to deliver a stable laser output the cavity resonant frequency can be locked to the TA PRO laser frequency with a piezo (PZT) by means of Hänsch-Couillaud locking technique [118]. The cavity is located in an aluminum box under low vacuum in order to increase thermal and acoustic insulation and achieve a better lock stability. This results in a stable output of 550 mW of 399 nm radiation out of 1 W of 798 nm pumping light. After the doubling cavity, a fraction of the laser radiation at 399 nm is withdrawn (see Fig. 2.3) to perform spectroscopy on an Yb atomic sample in order to lock the laser frequency on the $^1S_0 \rightarrow {}^1P_1$ transition (see sec. 1.3.1). The rest of the light is used to slow down atoms in the Zeeman Slower (section 2.2.1) and to perform absorption imaging (section 2.2.2).

The same technique described above is used for the generation of 556 nm light. The infrared source is a fiber laser at 1112 nm (Menlo Systems Orange One) whose radiation is frequency doubled by a 10 mm long Lithium Tantalate (LiTaO$_3$) periodically-poled (9.12 μm poling period) non-linear crystal placed inside a bow-tie cavity. The cavity free spectral range is FSR = 567 MHz and the measured finesse is $\mathcal{F}$ = 67. When locked using Haensch-Couillaud technique, the cavity

outputs 1.050 W of 556 nm light with 2 W of 1112 nm pumping light. Also in this case, a fraction of the visible light is power-stabilized and used for atomic spectroscopy (see Fig. 2.3) in order to lock the laser to the $^1S_0 \to {^3P_1}$ intercombination transition. The rest of the 556 nm light is used for the MOT (section 2.2.1), for the OSG (see section 2.2.2) and optical pumping beams (section 2.2.2) and for the Raman beams (see section 7.2).

The 399 nm and 556 nm laser frequencies are respectively locked on the $^1S_0 \to {^1P_1}$ and $^3S_0 \to {^3P_1}$ atomic transitions with standard fluorescence spectroscopy techniques and electronic feedback on the lasers piezos. Transverse spectroscopy is performed on an atomic beam generated in an additional oven with the same characteristics as the one in the main setup. No Doppler-free saturation spectroscopy is needed for the $^1S_0 \to {^1P_1}$ transition, due to its large natural linewidth of $2\pi \times 28$ MHz. On the other hand, the $^3S_0 \to {^3P_1}$ intercombination transition has a natural linewidth $\Gamma = 2\pi \times 182$ kHz hence, it is necessary to perform a Doppler-free saturation spectroscopy. With this technique, the best signal-to-noise ratio (SNR) is obtained for ^{174}Yb, which is the most abundant isotope and has no hyperfine structure, due to the zero nuclear spin. For experiments using bosonic ^{174}Yb, the 556 nm light is shifted by 83 MHz with an Acousto-Optic Modulator (AOM) in double passage configuration, so that the laser frequency is detuned by -166 MHz from the ^{174}Yb resonance. It is convenient to lock on this transition also for fermionic ^{173}Yb, which on the contrary has a worse SNR, due to the lower isotopic abundance and to the hyperfine structure which splits the error signal in six dispersive features. To achieve this, the laser frequency on the spectroscopy path is shifted by a double-passage AOM at 351 MHz, then it is further shifted with a resonant Electro-Optic Modulator (EOM) which adds a blue sideband at 1.85 GHz to the carrier. The total shift is exactly the isotopic shift $\Delta_{174-173} = 2386$ MHz, and in this way the laser can be locked to the ^{174}Yb transition while being still detuned by -166 MHz from the ^{173}Yb transition. This approach has the advantage that the laser configuration is the same both for bosons and fermions, with the exception of the spectroscopy part, which can be switched in a few minutes with a removable mirror on a magnetic mount and turning on or off the EOM (see Fig. 2.3). Additional details on this locking scheme can be found in Ref. [111].

1064 nm laser system

Laser radiation at 1064 nm is used to trap the atoms in the in-vacuum resonator (section 2.1.1) and to perform optical transport from the MOT chamber to the glass cell (section 2.2.1). The employed laser is a Nd:Yag Mephisto MOPA 25 (Innolight/Coherent) characterized by a maximum output power of 25 W and a linewidth below 100 kHz. The 1064 nm laser setup in showed in Fig.2.4). After an optical isolator, the beam is split in two paths, one for the resonator and one for the optical transport, which are delivered to the experimental setup with high-power photonic crystal fibers. In order not to damage the fibers due to high power involved, the AOMs used to ramp the beams intensity are driven using a dual-frequency driver
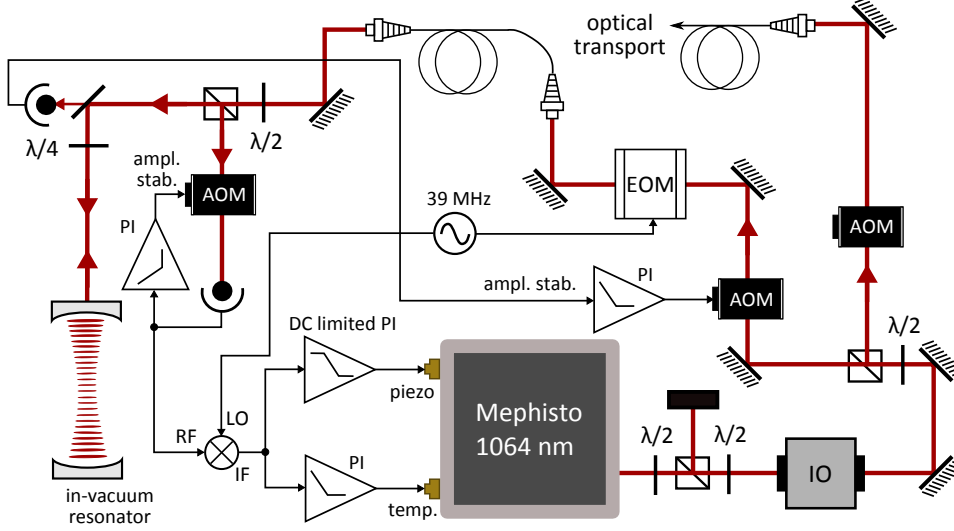
Figure 2.4: Scheme of the 1064 nm laser setup. The light is divided in two branches delivered to the experimental table through optical fibers to perform optical transport as well as to feed into the in-vacuum resonator. The resonator light power is stabilized after the optical fibers and also the reflected light is stabilized with a dedicated AOM in order not to burn the PDH photodiode during the evaporation ramps. The laser is locked to the resonator with two PI controllers which act on the laser piezo and temperature.

[119], which prevents thermal-induced misalignment of the diffracted beams. In order to lock the laser frequency to the in-vacuum resonator, a 37 MHz resonant EOM is used to generate a Pound-Drever-Hall (PDH) [120] error signal, which is processed by two PI (proportional-integral) controllers. One of them acts on the laser piezo and is responsible for the fast corrections over a bandwidth of approximately $\leq$ 10 kHz, while the seconds acts on the laser seed temperature, which allows for large range (3 GHz/°C) slow (1 Hz bandwidth) corrections. Since the piezo PI has a limited DC gain, only the temperature is used to compensate for the laser slow drifts. Moreover, since the resonator power is ramped during the experimental cycle to perform evaporative cooling (see section 2.2.1), we actively stabilize the power impinging on the PDH photodiode with an additional AOM, which allows us to have the same error signal amplitude over a wide range of resonator powers (from 100 μW to 2 W). Additional details on the locking scheme can be found in [111].

759 nm laser system

The optical lattice light is generated using a standard commercial setup consisting in a Coherent Verdi V18 laser emitting in single mode at 532 nm which acts as a pump for a Titanium-Sapphire laser (Coherent MBR 110). The MBR is tuned to lase at 759 nm, the so-called "magic wavelength" that induces the same light shift on both the $^1S_0$ and the $^3P_0$ states. At this wavelength, the lattice light does not

influence the frequency of the $^1S_0 \to {}^3P_1$ transition, as will be discussed further in section 4.1.2. The laser setup routinely outputs 3.5 W of 759 nm light, which is split in three different optical paths, each featuring a dual-frequency AOM and an optical fiber that deliver the light to the experimental table where the optical lattices along three orthogonal directions are implemented. The three AOMs are driven with three different frequencies, separated by tens of MHz to avoid cross-interference terms. Finally, a small fraction of the laser light is coupled into a Fabry-Perot cavity to monitor single-mode emission of the MBR.

2.2 Overview of experimental procedure

In this section we review the fundamentals of the experimental procedures employed to obtain quantum degenerate gases of both bosonic and fermionic Ytterbium and to manipulate the atomic samples. Additional details on the experimental procedure can be found in Ref. [111].

2.2.1 Cooling to the degenerate state

Zeeman slower

The Zeeman Slower (ZS) represents the first stage of the experimental cycle, which is responsible for the slowing of the atomic beam coming out of the oven. It should be noted, however, that the Zeeman slower is not the only suitable choice as first slowing state, as alternative techniques has been successfully employed [121]. The Zeeman slower uses the radiation pressure exerted on the atomic beam by a counter-propagating laser beam in resonance with the $^1S_0 \to {}^1P_1$ transition at 399 nm in order to reduce the velocity of the atomic beam and allow for the capture of atoms in the magneto-optical trap. A series of coils generates an inhomogeneous magnetic field $B_{ZS}(z)$ which induces a Zeeman shift which compensates for the decreasing atomic velocity during their travel through the Zeeman slower. In this way, the atoms are always resonant with the counter-propagating laser beam along the entire path from the oven to the MOT chamber and the effective detuning from resonance is null in every point in space [122]. The 399 nm light is particularly suited for this purpose due to its large natural linewidth $\Gamma = 2\pi \times 28$ MHz, which implies a larger maximum atomic deceleration $a_{max} = \hbar k_L \Gamma / 2m$ (see Eq. (1.5)). In particular for ^{173}Yb we use σ^--polarized light red-detuned by 983 MHz from the optically closed $F = 5/2 \to F' = 7/2$ transition, realizing a slowing scheme in which the light is resonant with the atoms coming out of the oven at ~ 330 m/s where there magnetic field is null [123]. With this design, the magnetic field $B_{ZS}(z)$ is maximum at the end of the Zeeman slower, so a compensation coil is used to cancel out the residual magnetic field in the MOT region.

Magneto-optical trap

After the Zeeman slower, the atoms are loaded in a magneto-optical trap which traps and cools down the atoms using 556 nm light resonant with the $^1S_0 \rightarrow {}^3P_1$ intercombination transition (also in this case, the optically closed hyperfine $F = 5/2 \rightarrow F' = 7/2$ transition is chosen for ^{173}Yb). Due to its narrow linewidth ($\Gamma = 2\pi \times 182$ kHz), using this transition allows for a much lower Doppler temperature ($k_B T_D = \hbar\Gamma/2$) at the expense of a reduced capture velocity[1] around 10 m/s for our parameters, namely a beam waist $w_0 \simeq 1.3$ cm, a magnetic field gradient $b \sim 1.6$ Gauss/cm and a saturation parameter of $I/I_s = 80$ for each of the six beams ($P_{tot} = 180$ mW). Since the atomic velocity after the ZS is about 20 m/s [112, 125], in order to increase its capture velocity and the MOT loading efficiency, the MOT beams are frequency modulated, adding $N_{sb} = 18$ equally-spaced sidebands [126], red-detuned with respect to the atomic transition, which result in a broadened effective linewidth of the transition. With this method, we can routinely trap $N_{at} = 7 \times 10^7$ ^{173}Yb atoms and $N_{at} = 1 \times 10^9$ ^{174}Yb atoms. After a 20 s MOT loading time the sidebands are switched off and the single frequency light is adjusted to minimize the temperature of the cloud. With the optimal parameters we achieve $T \simeq 25 \,\mu$K for the fermionic ^{173}Yb and $T \simeq 80 \,\mu$K for the bosonic ^{174}Yb isotope. These temperatures are significantly higher than the Doppler temperature ($T_D = 4.3 \,\mu$K) since the MOT density is large enough to let collisional heating mechanisms [127, 128] prevent the Doppler limit to be reached. In any case these temperatures are low enough to yield an efficient transfer inside the resonator optical dipole trap (see section 2.2.1). For further details on the multi-frequency setup and the MOT optimization, we refer to Ref. [112].

Resonator loading and evaporation

As explained in section 2.1.1, the laser at 1064 nm is locked in resonance with the in-vacuum optical cavity (from now on referred to as "resonator") forming a 1D optical lattice. In order to efficiently load the atoms into the lattice, after an adiabatic switch-off of the ZS beam, the in-cavity power is ramped up using an exponential ramp from idle level ($P_{idle} = 100 \,\mu$W) to an input power of $P_{in} = 1.8$ W, which corresponds to a trap depth $V_0/k_B \simeq 800 \,\mu$K, much higher than the MOT temperature ($\sim 25 \,\mu$K for ^{173}Yb, see previous section). In addition, the MOT is compressed raising the magnetic gradient from $b_i = 1.6$ to $b_f = 4.4$ G/cm and the center of mass of the atomic cloud is shifted with the aid of three compensation coils in order to match the beam waist position and dimension. In this way, roughly

---

[1] The capture velocity is the maximum velocity class that is possible to trap using a MOT and it is defined as [124]:

$$v_c = \left(\frac{\hbar^2 k_L^2}{m \, g_{F'} M_{F'} \mu_B b} \right) \frac{\Gamma}{2} \frac{I/I_s}{1 + I/I_s},$$

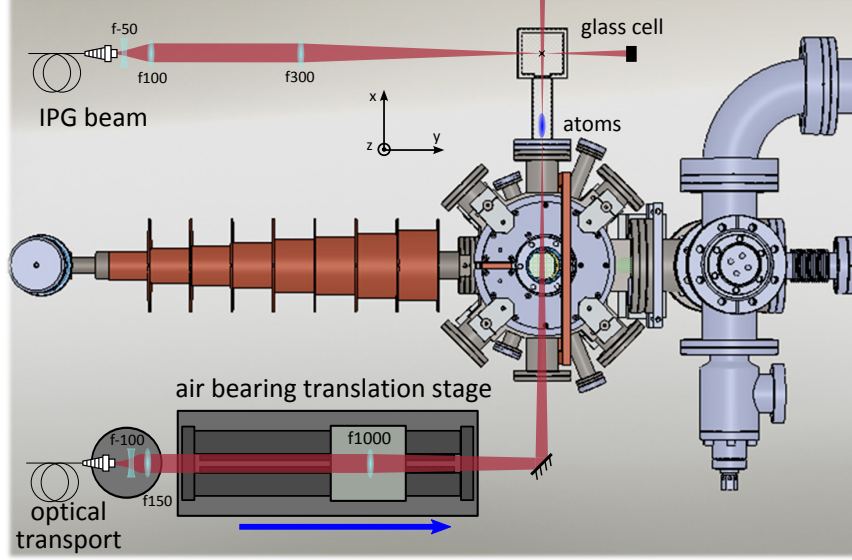where b is the MOT magnetic gradient, k_L is the laser beam wavevector and I_s the saturation intensity.

Figure 2.5: Representation of the optical transport procedure. The transport beam is focused in the MOT chamber with a lens with focal length f = 1000 mm. The lens is mounted in an air-bearing translation stage, so that its focal point can be moved of 26 cm in order to transport the atoms in the glass cell, where the evaporative cooling process takes place.

80% of the atoms are transferred from the fermionic MOT to the resonator trap in 300 ms.

After the loading stage, the MOT beams and magnetic fields are switched off and the atoms undergo evaporative cooling in the resonator, by lowering the trap optical depth to $P_{in} \sim 250$ mW using two consecutive exponential ramps. After this pre-cooling stage, we obtain a spin-unpolarized sample of $N_{at} \sim 1 \times 10^7$ atoms at approximately $T \simeq 5$ μK.

Optical transport and crossed dipole trap

In order to transport the atoms in the high optical access glass cell, we initially load the atoms in an Optical dipole Trap (ODT) formed by a tightly-focused transport beam at 1064 nm. The transport beam power is increased using a 200 ms-long exponential ramp and right afterwards, the resonator power is ramped down to the idle level (i.e. the minimum level), high enough to keep the 1064 nm laser locked to resonator but too low to hold the atoms, which are then transferred to the transport beam ODT. The transport beam is tightly-focused on a waist $w_0 = 30$ μm and has an initial power of 3.4 W, which correspond to a trap depth $V_0/k_B \simeq 90$ μK. Approximately 30% of the atoms are loaded from the resonator to the transport trap. The 30 μm beam waist is obtained by focusing a collimated beam with a waist of ~ 1 cm using a lens with focal length $f = 1$ m mounted on an air-bearing,

magnetically-driven translation stage Aerotech ABL 1500b (see Fig. 2.5) which moves the beam focus and performs optical transport [114, 115]. In this way, the atoms are transferred to center of the science cell along the 26 cm long path that separates it from the MOT cell center in 2.5 s. This time is much longer then the timescale of the longitudinal trapping frequency of the transport ODT ($\omega_z \simeq 2\pi \times 5$ Hz) in order to avoid heating during the transport process. With an optimization of the transport parameters [129], we obtained a transport efficiency of 66% with a final temperature only 30% higher than the initial one.

Once the atoms have been transported in the glass cell, an additional beam of $w_0 = 60$ μm and $P = 3$ W is focused onto the atoms. This beam is generated by an IPG Fibertech multimode laser at 1070 nm and is orthogonal to the transport beam in order to create a crossed dipole trap configuration (see Fig. 2.5), where the final evaporative cooling is performed.

^{173}Yb degenerate Fermi gas

In order to achieve Fermi degeneracy of the atomic cloud trapped in the crossed ODT, the atoms undergo an final evaporative cooling stage. In this final cooling stage, due to the fermionic character of the atoms, it is necessary to employ more the one spin component, otherwise evaporating cooling would not be effective at low temperature, since the s-wave scattering is inhibited by Pauli principle (see section 1.2). The evaporation process is composed by two different exponential ramps, the second of which is less efficient since the more the gas enters the degenerate regime, the more the thermalization process is inefficient, due to the Pauli suppression of collisional rate. At the end of the evaporation we routinely

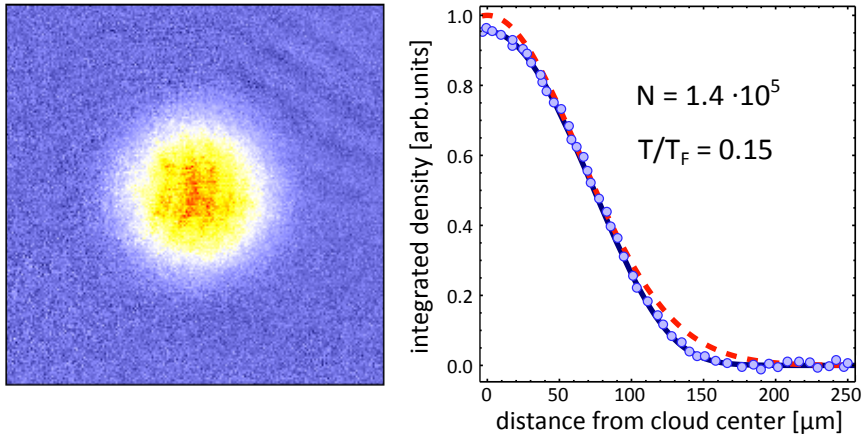Figure 2.6: **a.** False-color time of flight image of the expanding Fermi gas. **b.** The points are the integrated column density along the horizontal direction, while the red dashed and blue solid lines represent respectively the result of a fitting procedure with a Gaussian and with a Fermi gas Polylogarithmic distribution. At $T/T_F = 0.15$ the deviation from the Gaussian profile is clearly visible.

obtain six-spin-components Fermi gases with $N \simeq 1.4 \times 10^5$ atoms at a temperature $T \simeq 0.15 T_F$ where the Fermi temperature T_F is of the order of 200 nK. The trapping angular frequencies of the final crossed ODT are $\vec{\omega} = 2\pi \times (54, 100, 90)$ Hz, resulting in a geometric mean trapping frequency $\omega_{\mathrm{geom}} \simeq 2\pi \times 79$ Hz.

Optical lattices

The optical lattices (OL) setup consists of three, linearly polarized retroreflected beams, one along the vertical direction and two orthogonal beams in the horizontal plane, one of which forms an angle of 35 °with respect to the transport axis. The power of all three lattice beams is actively stabilized by feedback loops that act on the AOMs before the fibers (see section 2.1.2). The lattice depth $s = V_0/E_R$, in unit of recoil energy (see section 1.1.2), can be calibrated using two independent methods with ^{174}Yb BEC: the Raman-Nath diffraction [130] and the amplitude modulation of the lattice beams (AM) [131]. This allows us to determine the beam waists and the radial trapping frequencies of the OL beams, comparing the measured lattice depths with the theoretical values. The results of this calibration are reported in Table 2.1. During the experiments, the atoms are adiabatically loaded from the crossed-ODT to the optical lattice increase the lattice beam intensity with an exponential ramp. With the waists reported in Table 2.1, the optical lattices in the horizontal plane cannot hold the atoms against gravity and the crossed-ODT and/or the vertical lattice are needed.

	OL_1	OL_2	OL_3
waist (μm)	96.1	111.3	102.3
$\omega_z(s)$ [$2\pi \times$Hz]	$7.1\sqrt{s}$	$6.2\sqrt{s}$	$6.8\sqrt{s}$

Table 2.1: Waist and radial trap frequencies of the three optical lattice beams.

2.2.2 Detection and manupulation of the degenerate Fermi gas

Imaging

The imaging of the atomic cloud is performed with standard absorption imaging [132]. This technique consists in the detection with a CCD camera of the shadow cast by the atomic cloud when illuminated by a resonant laser beam. In order to reduce the interrogation time, we employ 399 nm light resonant with cycling $F = 5/2 \rightarrow F' = 7/2$ hyperfine component of the $^1S_0 \rightarrow {}^1P_1$ transition. Starting from the transmitted intensity profile $I_t(x, y)$ of the resonant light probe through the atomic cloud, it is possible to extract the column density of the cloud $n_c(x, y) = \int n(x, y, z)dz$ integrated along the imaging direction z according to the relation:

$$I_t(x, y) = I_0(x, y)e^{-\sigma n_c(x,y)} \longrightarrow n_c(x, y) = -\frac{1}{\sigma} \log\left(\frac{I_t(x, y)}{I_0(x, y)}\right), \qquad (2.1)$$

where $I_0(x, y)$ is the beam intensity profile without the atoms and $\sigma = 3\lambda^2/2\pi$ is the resonant scattering cross section of the atoms with λ being the wavelength of the imaging laser. Taking into account the pixelated nature of the CCD camera, the relation (2.1) will be given by:

$$n_c(i, j) = -\frac{S}{\sigma} \log\left(\frac{P_{ij} - B_{ij}}{F_{ij} - B_{ij}}\right), \qquad (2.2)$$

where S is the pixel area including the magnification and P_{ij}, F_{ij}, B_{ij} are the intensities detected by the pixel (i, j) corresponding to the imaging beam with atoms, without the atoms and with the probe laser off, respectively. Several imaging setups have been implemented to monitor the different stages of the experimental cycle [111]. The main imaging setup in the glass cell is performed with a single $f = 150$ mm lens providing a 3.2x magnification and a CCD camera (Andor iXon^{EM}+DU885KCSO). The camera has a CCD sensor with 1002×1004 pixels of size 8×8 μm and a resolution of 14 bit, and is used in fast kinetics mode in order to minimize the effects of fluctuations of laser power and airflows.

Spin distribution initialization

In order to prepare atomic sample with a specific number of spin components, we developed a spin-selective optical pumping (OP) protocol based on laser pulses resonant with the $^1S_0$ ($F = 5/2$) $\rightarrow$ $^3P_1$ ($F' = 7/2$) transition. As already mentioned in section 1.3.1, since this is a narrow transition ($\Gamma = 2\pi \times 181$ kHz), it is possible to selectively address only one single Zeeman component of the excited state manifold.

The initial atomic spin distribution coming from the MOT is approximately thermal with six equally populated spin components. In order to separate the Zeeman sublevels of the $^3P_1$ ($F' = 7/2$) state, we apply a homogeneous magnetic field of $B = 22.7$ gauss, generated by a pair of coils in Helmholtz configuration located above and below the glass cell. The resulting relative Zeeman splitting between adjacent m_F levels is $\Delta_Z = 2\pi \times 13.6$ MHz $\simeq 75\,\Gamma$. The pumping procedure is executed right after the transport in the glass cell, before the evaporation, in order to limit the effects of near-resonant light light scattering on the temperature of the sample. Two independent beams OP$^+$ and OP$^-$, with circular polarization σ^+ and σ^- respectively, are used so that only the transitions $m_F \rightarrow m_F \pm 1$ are resonantly excited. After the pumping, whose efficiency approaches 100%, the evaporative cooling takes place. Depending on the protocol, after the evaporation, the unwanted spin components are blasted away with resonant pulses, that heat the atoms, which are expelled from the shallower final crossed ODT. By properly combining pumping and blast pulses, it is possible to produce balanced mixtures
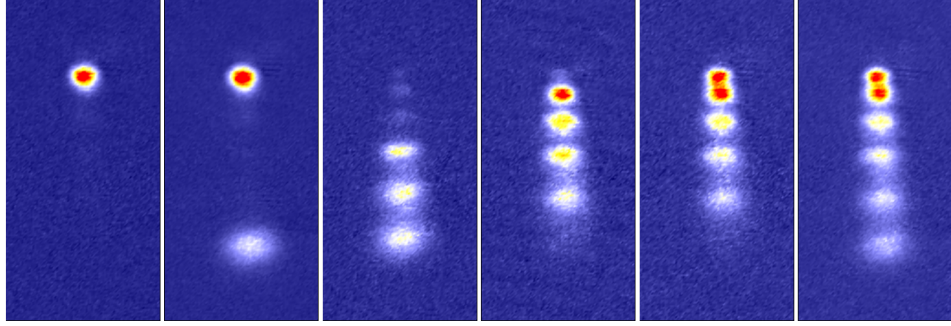
Figure 2.7: Spin-resolved images of atomic samples with different numbers of spin components, form 1 up to 6. The imagines are obtained by means of OSG technique described in section 2.2.2.

with one up to six components, interacting within different $SU(N)$ symmetry classes, where N ranges from 1 to 6. The specific optical pumping protocols to obtain the different mixtures are described in Ref. [111].

Optical Stern-Gerlach

The "optical Stern-Gerlach" (OSG) technique [107, 133] relies on the state dependent light shift discussed in section 1.1.3 in order to separate the different spin components of the atomic sample and perform spin-selective imaging. As shown in section 1.3, Ytterbium is a strongly diamagnetic atom which only has the nuclear spin component in its ground state, resulting in a ~ 2000 lower magnetic field sensitivity than alkali atoms. In this case, an effective separation of the different spin components via magnetic Stern-Gerlach is unfeasible due to the necessity of an extremely high magnetic field gradient. The OSG technique is instead feasible, since it relies on the optical dipole force and not on the atomic magnetic sensitivity.

In case of ^{173}Yb ($F = 5/2$), 556 nm light near-resonant with the $1S_0 \rightarrow {}^3P_1$ transition can be used to implement optical Stern-Gerlach. Atoms will be subject to a m_F-dependent light shift which is given by the sum over the contribution of the three hyperfine sublevels F' of the $^3P_1$ state, namely $F' = 7/2, 5/2, 3/2$. According to Eq. (1.22), the dipole force will be given by:

$$\mathbf{F}_{m_F}(\mathbf{r}, \omega, q) = \frac{3\pi c^2}{2\omega_{mn}^3}\Gamma\left(\frac{|C_{7/2,m_F}(q)|^2}{\Delta_{7/2}} + \frac{|C_{5/2,m_F}(q)|^2}{\Delta_{5/2}} + \frac{|C_{3/2,m_F}(q)|^2}{\Delta_{3/2}}\right)\nabla I(\mathbf{r}),$$
(2.3)

where q refers to light polarization, $\Delta_{F'} = \omega - \omega_{F'}$ are the detunings from the F' states, $\Gamma = 2\pi \times 182$ kHz is the decay rate of the $^3P_1$ state and $\omega_0 = 2\pi c/\lambda$, with $\lambda = 556$ nm. The principle of operation of the OSG technique is reported in Fig. 2.8. Employing σ^--polarized laser light with a detuning $\Delta_{7/2} = -566$ MHz $\simeq 3100\Gamma$, a dipole potential which is maximum for the $m_F = -5/2$ component is obtained.
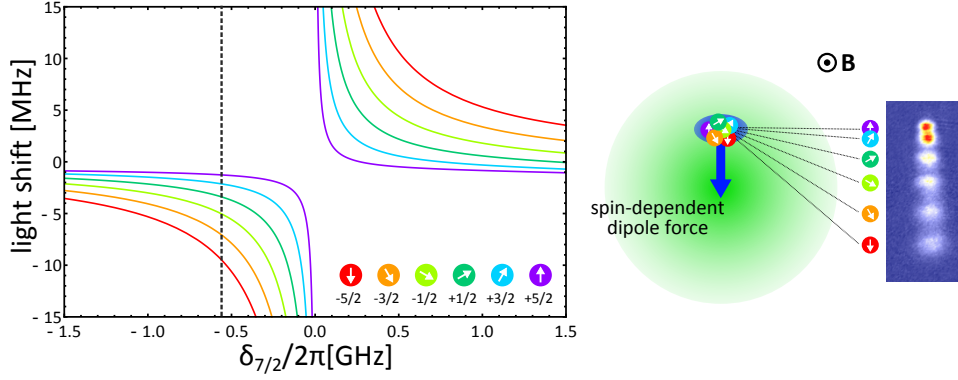
Figure 2.8: Working principle of the Optical Stern-Gerlach technique. The dipole potential generated by near-resonant 556 nm light depends on the nuclear spin compontent m_F. As a consequence, a gaussian beam positioned so that the atoms are located in the maximum intensity gradient exerts a spin-dependent dipole force on the atomic cloud. The different spin components of the could can then be resolved in the imaging process after a time of flight.

Experimentally, the dipole force is obtained with a laser beam with a power of 10 mW focused on a waist $w_0 = 60 \ \mu$m, which is aligned in such a way that the position of the atoms corresponds to the point of maximum intensity gradient of the laser beam. The spin-selective imaging of the atomic cloud is obtained performing a 1.25 μs square pulse of OSG light, followed by a 4.5 ms time of flight before the imaging. A magnetic field of 2.5 G is applied along the OSG beam direction to fix the quantization axis. The population in the different nuclear spin states can then be measured by means of absorption imaging.

Optical pumping and OSG setup

In the experiment, the OP$^+$ beam is generated using a fraction of the MOT beam, while the OP$^-$ and the OSG beams are generated by a dedicated beam (see Fig. 2.9). The OP$^+$ is superimposed on the OSG beam with a polarizing beam splitter (PBS) and are injected in the same fiber. An independent fiber is dedicated to the OP$^-$ beam. The two fibers deliver the beam to a vertical breadboard mounted above the glass cell. A PBS placed immediately after the OSG and OP$^+$ common fiber, separates the two lights, combining at the same time the two OP$^\pm$ beams. The horizontal and vertical polarizations of the two OP beams are then turned into σ^+ and σ^- respectively with two wave-plates. (see Fig. 2.9). On the now independent OSG beam path, a $f = 400$ mm lens focuses the beam on a 60 μm waist in order to maximize the optical gradient on atoms and a $\lambda/4$ waveplate adjusts the OSG polarization. Two beam splitters combine the OP and OSG beams and the imaging beam, which are then superimposed to the vertical optical lattice beam (OL$_3$) with a long-pass dichroic mirror. And all the four beams are directed towards the atomic sample into the glass cell.
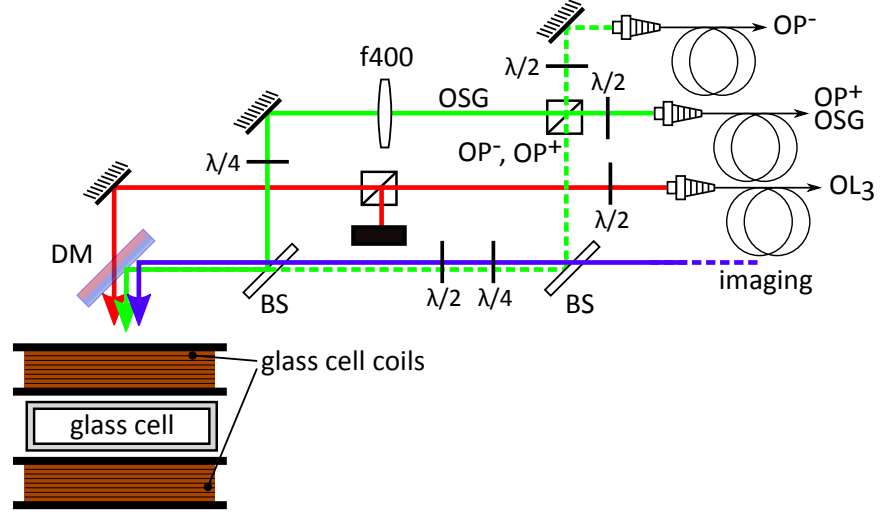
Figure 2.9: Schematics of the vertical breadboard laser setup. The OP^+ and the OSG beam are delivered by the same optical fiber with orthogonal polarizations and are separated by a PBS, which also recombines together the OP^+ with the OP^- beam which is carried by a separated optical fiber. The two OP beams are superimposed to the imaging beam with a beam sampler (BS) and with the OSG beam with a second BS. Finally the four beams are superimposed to the vertical optical lattice OL_3 with a dichroic mirror.

Chapter 3

Ultranarrow 578 nm laser stabilized on a remote frequency reference

The heart of every experimental setup which relies on the excitation an optical clock transition is a laser characterized by extremely pure spectral properties. For the realization of this kind of devices, the Pound-Drever-Hall [120, 134] technique is pushed to its limits in order to tightly lock the laser to a very stable reference [135], which usually consists in a high-finesse optical cavity realized in Ultra-Low-Expasion (ULE) glass. With a proper PDH lock loop, the laser frequency noise spectrum substantially reproduces that of the reference cavity. The very high finesse allows for a very sharp error signal which, together with a carefully designed shape and positioning of the cavity, opens the possibility to narrow the laser linewidth well below the Hz level on short timescales [47, 48]. Moreover, the very low thermal sensitivity of the ULE glass along with a proper stabilization of the cavity around its zero CTE (coefficient of thermal expansion) temperature minimize the cavity long term drift reducing it to the cavity intrinsic limit represented by the glass aging drift [48, 136].

This chapter contains a detailed description of the narrow laser system at 578 nm which is used to excite the $^1S_0 \rightarrow {}^3P_0$ clock transition in ^{173}Yb. The first part is dedicated to the laser source, which consists in an infrared solid state laser, frequency doubled to obtain 578 nm light and stabilized on an ULE glass cavity [50]. The second part of the chapter is focused on the description of an optical fiber link that is used to transfer to LENS in Florence an optical reference at 1542 nm, generated at the Italian National Metrology institute (INRIM) in Turin. By exploiting this remote optical reference, we determined the laser performances and, through a digital feedback system, stabilized its long-term frequency fluctuations allowing us to operate the laser on the clock transition with ease for weeks without any need of hour to hour calibration through spectroscopy measurements.
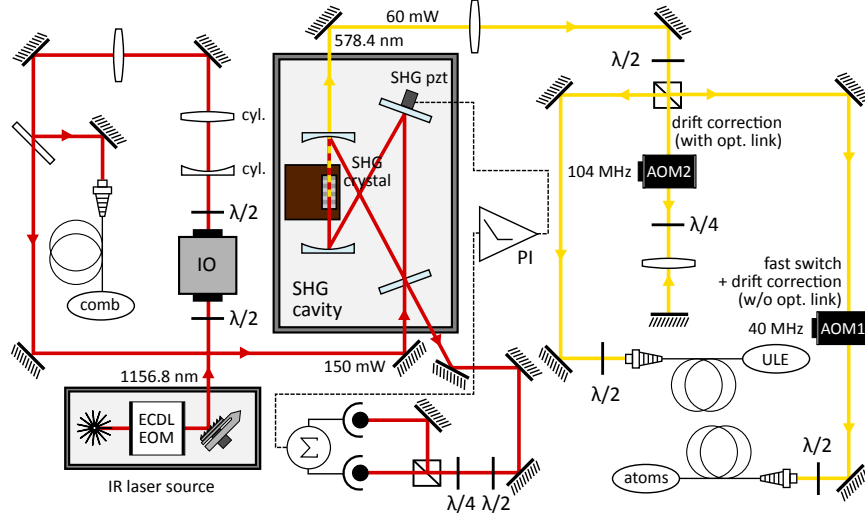
Figure 3.1: Scheme of the 578 nm laser system. The light is generated by an infrared ECDL and is collimated by a pair of cylindric lenses. Before the doubling cavity, a small part of the IR radiation is withdrawn and sent to an optical frequency comb (see sections 3.1.3 and 3.2.2). The 578 nm light is generated by a non linear crystal located in a bow-tie cavity, frequency locked to the ECDL by means of Hänsch-Couillaud technique. A small part of the visible light is delivered to the ULE cavity, after a double passage AOM at 104 MHz (AOM2), while the rest is delivered to the experiment table after passing through a 40 MHz AOM (AOM1). The two AOMs cover the frequency difference between the ULE resonant mode and the clock transition. AOM1 and AOM2 are also used to correct the ULE drift, respectively when the optical fiber link (see section 3.2.4) is or is not available.

3.1 Ultranarrow laser system

As of today, the only available laser sources emitting directly at 578 nm are dye lasers, which are expensive and difficult to maintain. For this reason, we opted for a cheaper and more reliable solid state laser. Differently from other experiments, in which the light at 578 nm is generated via sum frequency generation [137, 138], we employ a cavity-enhanced Second Harmonic Generation (SHG) scheme in order to obtain visible light at 578 nm from the 1156 nm infrared (IR) radiation emitted by a solid state gain chip in external cavity configuration (ECDL) (section 3.1.1). Before the injection of the doubling cavity, a small fraction of the ECDL infrared radiation is withdrawn with a beam sampler and delivered to an optical frequency comb. The light is coupled in a bow-tie optical cavity (section 3.1.2), where a nonlinear crystal converts ∼ 150 mW of infrared light into ∼ 60 mW of visible light. The cavity is frequency locked to the ECDL by means of Hänsch-Couillaud technique with a piezo acting on one of the cavity mirrors.

After the doubling cavity, the beam is split in two paths (ULE path and atoms path), as reported in fig 3.1. The light following the ULE path travels through an AOM (AOM2) in double passage configuration and is then delivered to the

ULE cavity through a 2 m long polarization maintaining optical fiber. As will be explained in section 3.2.4, AOM2 is used to compensate for the ULE cavity drift when the optical fiber link is available. The ULE cavity, placed in a vacuum chamber, is located in a thermally stabilized insulation enclosure that provides acoustic and thermal insulation from the environment lab, allowing for a laser linewidth reduction below 50 Hz over 5 minutes [50]. The ULE insulation system and the frequency narrowing procedure are described in detail in sections 3.1.3 and 3.1.4. The light in the atomic path is delivered to the experiment table through a second PM optical fiber, after passing through an AOM (AOM1) acting as fast switch and used to finely tune the light frequency. Additionally AOM1 is used to compensate the ULE cavity linear drift with a feed-forward when the optical fiber link is not available.

The good spectral properties and the high output power make this laser system a very versatile tool. On one hand, its narrow linewidth makes its perfectly suitable in precision measurements, where a high spectral purity is mandatory (see section 4.3). On the other hand, the high power allows for Rabi frequencies up to of a few kHz in ^{173}Yb atomic samples (see section 4.2.2), enabling the possibility to perform sub-ms π-pulses. For this reason our laser is suitable also in short timescales applications, where a fast manipulation of the metastable state is necessary.

3.1.1 Infrared laser source

The IR source of our laser system is a quantum dot gain chip Innolume GC-1156-TO-200, capable of up to $\sim$ 250 mW out of an ECDL configuration. This chip is characterized by a frequency-to-current response which shows a continuous phase slip from 0 to 180° between 10 and 100 kHz of current modulation frequency, making current a poor actuator for laser frequency locking to a stable reference with a > 100 kHz bandwidth. In order to obtain a robust and high-bandwidth frequency stabilization, we chose an ECDL configuration with an intra-cavity broadband electro-optic modulator (EOM) as fast cavity length actuator [139]. A schematic drawing and a picture of the ECDL are reported in Fig. 3.2. This design presents several advantages. First, the cavity length of 12 cm reduces the ECDL linewidth to approximately 20 kHz (estimated using the frequency doubling cavity as a diagnostic Fabry-Pérot), one order of magnitude smaller than standard ECDLs [140]. This value is obtained at the expense of a reduced mode-hopping-free interval. In our case this is not a major drawback, as we are able to cover more than one Free Spectral Range (FSR) of the reference ULE cavity without mode-hops (see section 3.1.3). The second advantage relies on the possibility of using the intra-cavity EOM as fast frequency actuator effective from DC up to the MHz level, due to its nearly flat modulation depth and phase response. The EOM, manifactured by Qubig GmbH (model EO-DC5M-BREWSTER), relies on a Brewster-cut (in order to avoid reflections and Etalon effect) Magnesium doped LiNbO$_3$ crystal. Its laser frequency-to-voltage transduction is of the order of 1 MHz/V, hence no high voltage amplifier is required to drive the EOM and a standard servo amplifier output can
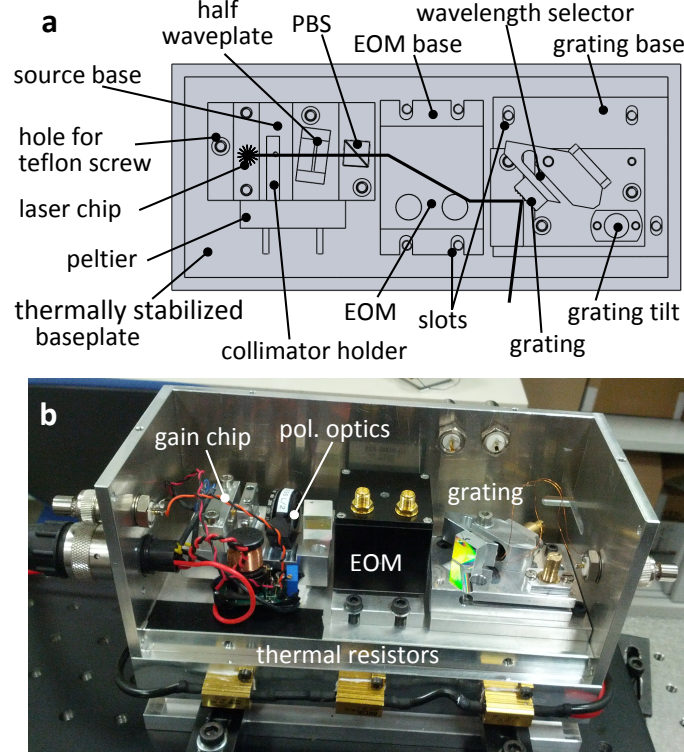
Figure 3.2: **a** *Top view of the long cavity ECDL laser source at 1156 nm, with labeling of the main components. Intracavity PBS and waveplate are tilted in order to avoid backreflections.* **b** *Picture of the* 1156 *nm ECDL. Between the laser (on the left) and the grating (on the right) the intra-cavity EOM is visible. On the laser baseplate the resistor used for temperature stabilization are visible.*

be used with benefits to the total bandwidth of the system. The EOM has two floating electrodes which are connected in differential configuration to SMA-type connectors so that two independent modulation signals can be used to drive the EOM.

The cavity also houses a $\lambda/2$ waveplate and a polarizing beamsplitter (PBS) in order to precisely tune and clean the polarization of the radiation. Their presence contrasts a marked tendency of the ECDL to lase on different linear polarization modes (with an angle of $\sim 15°$ between the two). The origin of this behavior is still unknown, but we exclude temperature fluctuations and current surges as possible causes since the laser temperature is stabilized and the supply current is accurately filtered. These intra-cavity polarizing elements also minimize the Residual Amplitude Modulation (RAM) due to the mismatch between the polarization of the light and the axes of the EOM crystal.

The optical feedback is provided by a diffraction grating optimized for UV (Thorlabs GH13-12U) that reinjects $\sim 10\%$ of the light into the laser chip and forms the Littrow external cavity. A piezoelectric stack (Piezomechanik PSt 150/4/7)

enables the tuning of the laser frequency over a span of about 1 GHz. In this configuration, the laser is able to deliver up to 200 mW of radiation at 1156 nm with a 500 mA supply current, which is the maximum output of our current driver (ILX Lightwave LDX-3620 Ultra-Low Noise). The chip is actually capable to sustain supply currents up to 700 mA in external cavity, further increasing the ECDL output power up to 250 mW.

The quantum dot chip and the grating are mounted on holders machined from Ergal aluminium alloy screwed to a monolithic massive Anticorodal baseplate, allowing for precise collimation of the laser beam and reinjection of the first diffraction order. A home-made Arduino-based digital temperature controller (described in details is section 3.1.3) stabilizes at 26.80 ± 0.01 °C the temperature of the laser baseplate (and of the ULE reference cavity, see section 3.1.3). Also the EOM is in direct thermal contact with the stabilized baseplate through an improved ceramic thermalization mount. A Peltier stage between the baseplate and the laser diode holder keeps the gain chip temperature fixed at 27 °C with 1 mK precision. Moreover, the ECDL is placed in a box providing thermal and mechanical insulation. The full temperature stabilization system limits the ECDL frequency drift within a few tens of MHz during one day of operation when not locked to the ULE cavity frequency reference.

3.1.2 Second harmonic generation

In our setup, the visible light at 578 nm is generated via SHG realized through a periodically poled $LiNbO_3$ nonlinear crystal placed into a symmetrical bow-tie optical cavity. The crystal, manufactured by HC Photonics, is doped with 5% of MgO to raise its damage threshold and has a poling period of 8.9 μm. A copper oven thermally stabilizes the crystal at the temperature of maximum conversion efficiency of 65 °C and is mounted on a four-axis translation stage (New Focus Model 9071) to adjust the crystal position with respect to the cavity optical axis.

The bow-tie optical cavity consists of two concave mirror with 100 mm radius of curvature and two plane mirrors. The two concave mirrors (M1 and M2 in Fig. 3.3) focus the beam in the non-linear crystal with a waist of ~ 50 μm in order to maximize the conversion efficiency. One of the two plane mirrors (M4) serves as input coupler while the other (M3) is mounted on a low capacity piezoelectric stack (Piezomechanik PSt 150/2x3/7, 170 nF) allowing the lock of the cavity length to the infrared laser source. The cavity has a 545 MHz FSR and a finesse ~ 100. The mirror holders are fixed to a monolithic Anticorodal base that rests upon four small 1/4 inch-thick Sorbothane dampers to decouple the whole cavity from acoustic noise delivered through the table top. The cavity is placed inside an aluminum enclosure that is evacuated to 10^{-2} bar to further reduce its sensitivity to air-delivered noise (see Fig. 3.3). The vacuum environment also suppresses bistability effects caused by a non-linear dispersive effect induced by the presence of water vapor resonances around 1156 nm.

The error signal used to keep the SHG cavity resonant frequency locked to the
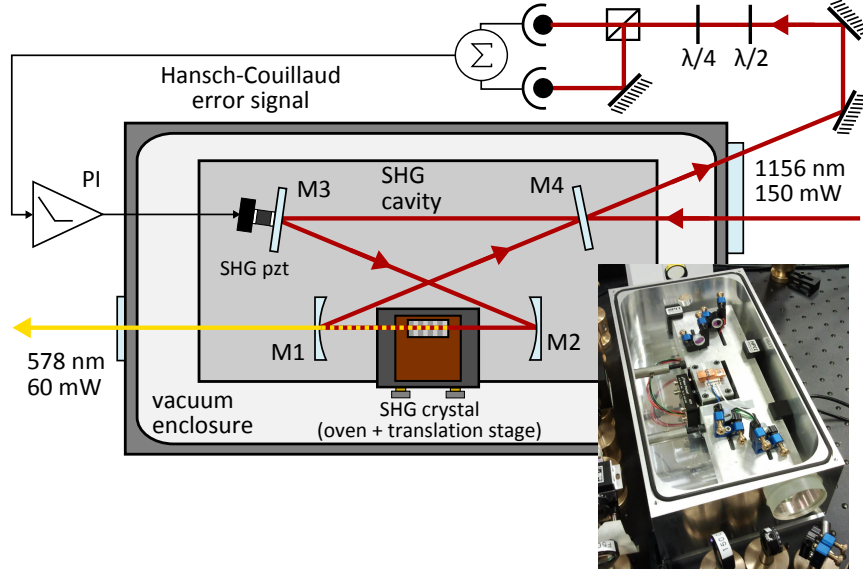
Figure 3.3: Schematic representation of the doubling cavity. The 1156 nm light is converted in 578 nm radiation with an efficiency of ~ 40%. The cavity resonant frequency is locked to the 1156 nm laser frequency by means of Hänsch-Couillaud technique acting on a piezo-mounted mirror (M3).

IR laser frequency is obtained employing the Hänsch-Couillaud technique [118]. This technique does not require any external modulation and exploits the strong birefringence of the non-linear crystal to generate the error signal. It is generated from the heterodyne detection of the two orthogonal polarizations, which experience different optical paths due to the crystal birefringence. This signal is fed to a single proportional-integral (PI) servo amplifier stage that provides the feedback on the cavity piezo with a −3 dB bandwidth of 300 Hz. With this system, we are able to obtain up to 60 mW of 578 nm light from 150 mW of 1156 nm radiation (40% conversion efficiency), which to our knowledge is the highest power at this wavelength reported in literature for a non-dye laser. A small fraction of the produced visible light (~ 1 mW) is sent to the reference ULE cavity for frequency stabilization of the laser source while the majority is delivered to the experiment table through a polarization maintaining (PM) optical fiber. The high output power of the doubling cavity represents a major advantage for spectroscopy and manipulation of the atomic sample. For example, in fermionic isotopes, the $^1S_0 \rightarrow {}^3P_0$ transition can be power broadened up to a few kHz with a 1 mm beam waist, and Rabi frequencies of the order of the transition linewidth can be driven. In bosonic isotopes instead, where the $^1S_0 \rightarrow {}^3P_0$ transition has to be induced via magnetic quenching with the $^3P_1$ state (see section 4.1) and is much weaker than in fermions, a high power allows for an easier observation and exploitation of the clock transition. Moreover, such high power could allow for off-resonant manipulation of ultracold fermionic ytterbium, e.g. for the realization of spin selective optical

dressing or for optical control of atom-atom scattering [141].

3.1.3 ULE reference cavity

Since with a properly executed feedback loop a laser noise reproduces that of its frequency reference, in order to reduce the laser linewidth to the Hz level, it is required to lock the source to a very stable reference. A few Hz linewidth for an optical transition means a stability of the order of 10^{-14}. Since $\Delta\nu/\nu = \Delta l/l$, where ν is the optical frequency and l the cavity length, for a reference cavity of 10 cm, its length is not allowed to fluctuate more than a proton radius. For this reason, it is fundamental to minimize the cavity sensitivity to all those perturbations that would lead to a length fluctuation. Mechanical vibrations, for instance, would result in laser frequency noise at acoustic frequencies increasing the laser fast linewidth. As a consequence, the geometry of the cavity is studied so that it is minimally influenced by vibrations and proper countermeasures are needed to insulate the cavity from them. On the other hand, thermal fluctuations would induce long term frequency drifts. ULE glass is then chosen since its linear coefficient of thermal expansion (CTE) has a zero around room temperature and the temperature dependence of the cavity length only retains its quadratic component:

$$\frac{\Delta\nu}{\nu} = \alpha^{(2)}\,(T - T_0) \tag{3.1}$$

where $\alpha^{(2)}$ is the quadratic CTE and is of the order 10^{-9}. In order to minimize the thermal sensitivity of the cavity it is crucial to determine its zero CTE temperature and to thermally insulate the cavity.

The ULE system employed in our setup, manufactured by Advanced Thin Films, was fully characterized in a previous experiment [138]. Both the mirrors substrates and the spacer are fabricated in ULE glass. The cavity FSR is 1.5 GHz and its finesse, measured by means of ring-down technique [142], results ~ 150000. In order to minimize sensitivity to external vibrations, the cavity, shaped as a notched cylinder, is suspended horizontally on viton pads at its Airy points, over an aluminum holder. The position of these points has been previously determined with a finite element analysis [138]. For a better acoustic and thermal insulation, the cavity, surrounded by a cylindrical thermal copper shield, is positioned in a 25 cm long horizontal stainless steel CF200 vacuum vessel and kept at 10^{-7} mbar by a 2 L/s ion pump. The vacuum chamber is placed on a passive vibration-insulation platform (MinusK BM-8) which grants a reduction between 10 and 20 dB of the acoustic noise in the Fourier frequency range from 1 to 100 Hz [138]. As a final thermal and acoustic insulation stage from the lab environment, the whole system is located inside an 80 cm $\times$ 80 cm $\times$ 80 cm home-made enclosure, of relatively low weight ($\sim$ 30 kg), made of joint layers of PVC and extruded polystyrene. A sketch of the structure is reported in Fig. 3.4a. Extruded polystyrene is one of the best commercially available thermal insulator (specific thermal resistivity $\lambda_{EP}^{-1} \sim 30$ m·K/W), while PVC is able to provide the mechanical support for the structure,
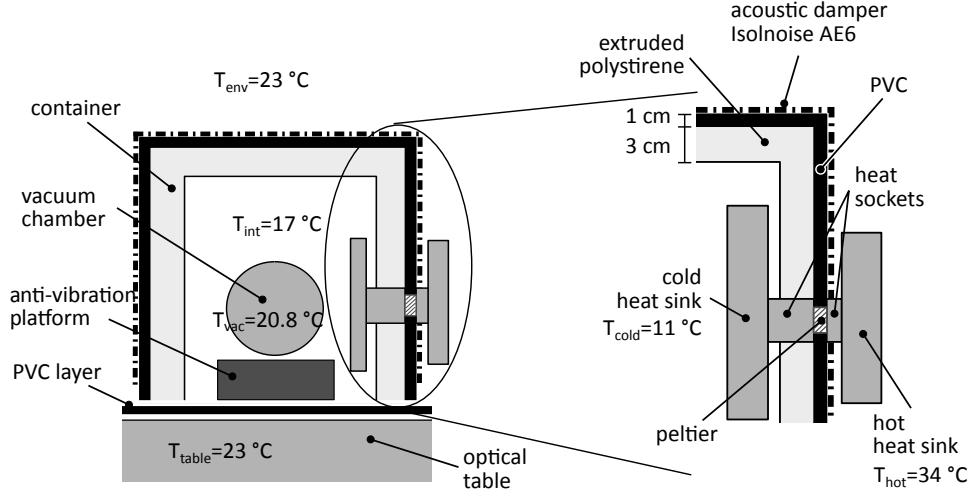
Figure 3.4: Sketch of the insulation system of the ULE cavity and detail of one of the four elements of the enclosure Peltier-based cooling stage.

and is a fair thermal insulator ($\lambda_{PVC}^{-1} \sim 5$ m·K/W). We also applied on the external surface of the enclosure a resilient mat (Aetolia Isolnoise AE6) as an additional low-frequency acoustic damper. We used commercial glue for linoleum floors to stick together all the layers. The box can be opened to grant access to the optics needed to couple the light to the ULE cavity, including the PDH EOM and other polarization optics that benefit from a thermally stable environment in terms of lock performances (see section 3.1.4).

The temperature of the ULE cavity (and of the ECDL baseplate, see section 3.1.1) is stabilized by the aforementioned Arduino-based digital temperature controller, which is described in the following section (3.1.3). The controller acts on two flat ribbon resistive heaters placed on the external surface of the vacuum chamber with an heating power of around 1.2 W at regime. The system handles up to 2.5 W during transients. The thermistor is placed on the copper shield and not directly on the cavity in order not to break its symmetry thus increasing vibration sensitivity. Due to the high vacuum environment, the ULE cavity thermalizes at the temperature of the copper shield via irradiation since all of the other heat exchange mechanisms are negligible.

A first measurement of the cavity zero CTE temperature T_0 was performed in Ref. [138], obtaining a value around 21 °C. This temperature is lower than our working environment (23 ± 1 °C), so cooling is required in order to stabilize the cavity at its zero CTE temperature. An optimal Peltier cooling system would require two vacuum thermal shields for an ideal heat exchange [48], while in our system a single thermal shield is present. On the other hand, cooling the vacuum chamber with Peltier cells coupled to standard heat sinks would create thermal gradients due to the low thermal conductivity of stainless steel. We also excluded the possibility
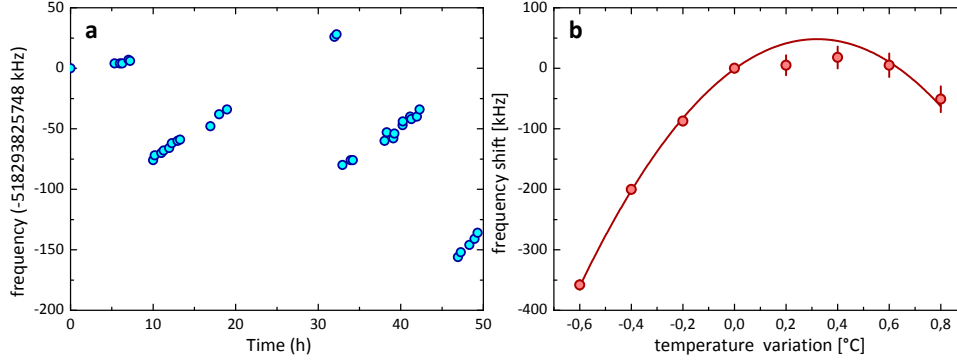
Figure 3.5: ***a.*** *Raw data of the ULE cavity thermal characterization. As a consequence of a* 0.2 °C *temperature variation of the ULE cavity, the laser frequency shifts of some tens of kHz due to the cavity length variation. After a temperature variation, the laser frequency is monitored for some days. The discontinuity in the frequency measurement is due to comb availability.* ***b.*** *Measured cavity resonant frequency as a function of temperature with a parabolic fit to the data. The stationary point of the fit curve is the zero CTE temperature.*

to cool the vacuum vessel with liquid and air flows as this would induce mechanical vibration on the structure. The required cooling is provided by a low-cost Peltier-based heat transfer stage, consisting in a set of four Peltier elements (Global Component Sourcing ET-127-14-11) in thermal contact with internal and external heat sinks through aluminum sockets (Fig. 3.4a). The Peltier cells maintain the internal temperature around 17.5 °C ($\sim$ 5 °C lower than lab temperature) stabilizing the internal heatsinks temperature at 12 °C with a total power consumption of 20 W. The effectiveness of this cooling stage is further increased with the addition of two slow speed fans ($\sim$ 100 rpm) on the external heat sinks with no visible effect on the laser system noise. Thermal stabilization of the internal heat sinks is implemented with a stand-alone digital temperature controller based on the scheme of sec. 3.1.3, which also adjusts its setpoint depending on the external temperature in order to compensate for different heat flows through the enclosure at different environmental temperatures. This allows us to stabilize the inner air temperature below the 0.1 °C level and keep it lower than the estimated zero CTE (see Fig. 3.4a). In this way the vacuum system can be stabilized around 21 °C without the need of an in-vacuum Peltier. The thermalization time of the entire system (ULE cavity and external enclosure) is of the order of 2-3 days, still adequately manageable through the digital thermal stabilization system. This scheme, in which both the reference cavity and its insulation enclosure are temperature controlled, could also allow for an easier stabilization of the cavity at high temperatures, heating the enclosure to an intermediate value between room temperature and the cavity target temperature.

In order to determine the cavity zero CTE temperature we measured the frequency of the infrared ECDL locked to the ULE reference resonator for temperature values spanning between 19.9 °C and 21.3 °C. The laser absolute frequency is deter-

mined with 1 kHz uncertainty by measuring the beat-note of the infrared light with a MenloSystems FC-1500 frequency comb with repetition rate and carrier-envelope offset (CEO) both referenced to a GPS-stabilized 10 MHz signal with a $5 * 10^{-13}$ stability at 1 s, by means of RF lock technique (see appendix B). For each temperature value, after a settling time of 2-3 days, the laser frequency is measured for a few days in order to estimate a value of the aging linear drift, as shown in Fig. 3.5a. For every temperature, the extrapolated linear drift is subtracted from the data and a single frequency value can be determined. The obtained frequency values are plotted versus the cavity temperature in Fig. 3.5b. The zero CTE temperature T_C can be found by fitting the points with a parabolic curve and determining the stationary point of the curve. The value for T_C has been measured as $(+0.32 \pm 0.03)$ °C in a relative scale centered around 20.5 °C, corresponding to an absolute temperature of 20.8 °C. The estimated linear aging drift of the ULE cavity for temperatures near T_C is of the order of 5 kHz/day, comparable with other values reported in literature [48, 136].

Multi-channel digital temperature controller

In order to stabilize the temperature of the laser baseplate and of the ULE cavity we developed a multi-channel, low-cost digital temperature controller based on Arduino UNO® architecture. The controller consists in three main blocks. The first block is a front-end responsible for the generation of the error signal that is fed to second block containing the Arduino which computes the correction. The third block is substantially constituted by a power supply and a thermal actuator (a set of resistors or a Peltier element) with a series MOSFET transistor that regulates the current flow through the actuator. Multiple front-ends and thermal actuators can be connected to the Arduino block allowing for an easy and centralized management of the temperature stabilization of the laser system key elements. A scheme of the controller is reported in figure Fig. 3.6b. Every front-end measures the temperature as the output of a voltage divider formed by a thermistor and a precision resistor. The measured temperature voltage is compared to the setpoint voltage, obtained with a simple 10 kΩ potentiometer, by a differential amplifier and an error signal centered around 0 V is generated at the amplifier output. This error signal is amplified and offset by 2.5 V by a second amplifier in order to obtain a $0 - 5$ V signal that is fed to one of the Arduino 10 bit analog inputs. The amplification stage is used to "zoom-in" around the setpoint, overcoming the limitation represented by the Arduino ADC resolution so that the desired controller precision can be achieved simply tuning its gain. The algorithm running on Arduino computes a PI correction for every error signal and the outputs are generated at the pulse-width-modulation (PWM) pins. Every PWM channel controls the gate of a MOSFET transistor acting as a switch to regulate the current flow through the thermal actuator, allowing for temperature stabilization with minimal power dissipation on the MOSFET transistor. The PWM signal and current wires are tightly twisted in order to avoid irradiated noise at the PWM frequency (480 Hz). At the moment, only two front-ends are used, but their
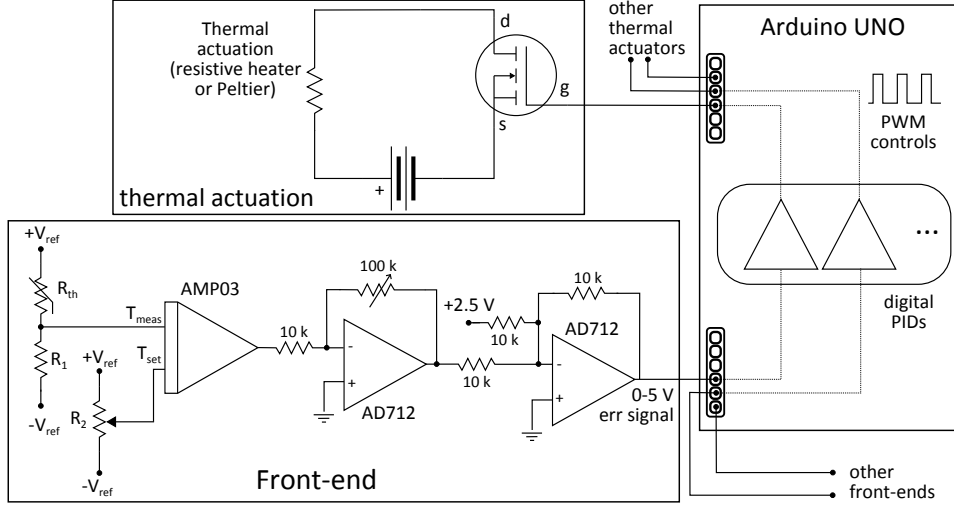
Figure 3.6: **a.** *Essential schematics of the Arduino-based digital temperature controller. The analog front-end performs the temperature reading, (the output of a voltage divider between a thermistor (R_{th}) and a precision resistor (R_1)) and compares it to the setpoint temperature (controlled by R_2). The error signal is translated into the $(0 - 5)$ V range and amplified so that it can be fed to the Arduino 10-bit ADC without loss of precision. Arduino computes and generates the correction at the PWM outputs and drives a MOSFET gate to regulate the mean current flow in a thermal actuation element (a set of resistors for the ULE cavity and laser baseplate or a Peltier for the enclosure, see sections 3.1.1 and 3.1.3).*

number can be increased up to six.

3.1.4 Laser frequency stabilization

In order to stabilize the laser frequency on the ULE reference cavity, a small fraction (~ 1 mW) of the 578 nm radiation is withdrawn after the doubling cavity. This light passes through an acousto-optic modulator (AOM1), operating at 104 MHz, in double passage configuration and is then delivered inside the ULE insulation enclosure via a 2 m long PM optical fiber. The 7 MHz EOM (Thorlabs EO-PM-NR-C4) used for the generation of the PDH signal is placed inside the enclosure, in order to minimize the RAM induced by temperature fluctuations of the EOM crystal. A Glan-Thompson polarizer on a tilt mount is used to carefully adjust the polarization of the incoming light to match the EOM crystal axis. Moreover, in order to minimize multiple internal reflections that would result in a low frequency residual modulation of the PDH signal, the EOM is tilted with respect to the light propagation axis.

A photodiode collects the incident light and drives a PI servo amplifier acting on AOM1 to stabilize the power at 60 μW in order to minimize power induced cavity resonance fluctuations. Such fluctuations may be caused both by coating absorption (photo-thermal effect) or by radiation pressure [143]. For the cavity in
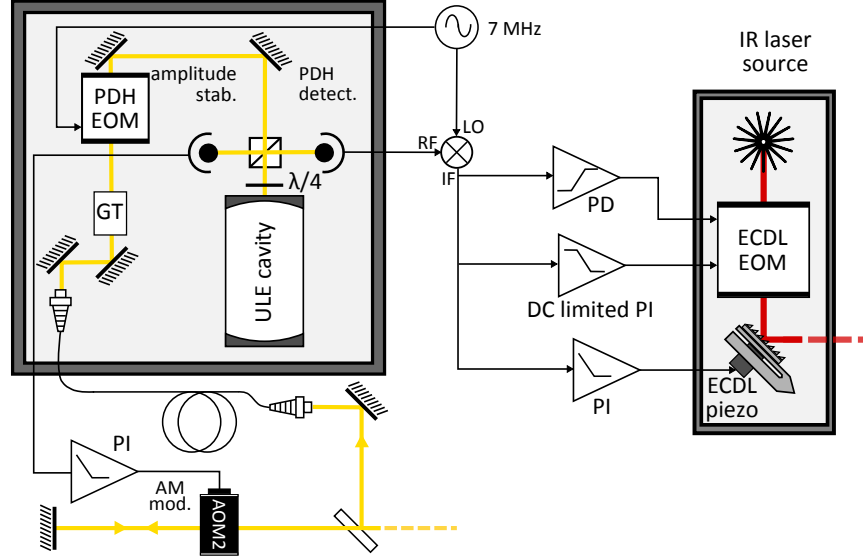
Figure 3.7: Scheme of the ULE cavity optical setup and of the feedback system. After passing through AOM2 (in double passage) the light is delivered in the ULE insulation enclosure. The Glan-Thompson polarizer (GT) cleans the light polarization to match the EOM crystal axis. Before the cavity, a polarizing beam splitter and a λ/4 waveplate build the PDH error signal, while the direct reflection of the PBS (note that the polarization is fixed by the GT polarizer) is used to stabilize the impinging light power acting on AOM2 RF amplitude.

use the fluctuations have been estimated in [138] of the order of 75 Hz/μW so a power stability of 10^{-3} is required to maintain frequency fluctuations below 10 Hz. We independently measured the power induced frequency shift with the aid of the fiber link, as will be described in section 3.2.3.

The PDH error signal is obtained by demodulating and low-pass filtering the output of a fast photodiode which collects the back-reflected light of the ULE glass cavity. The signal is fed in parallel to three servo amplifier stages which act on the ECDL piezo transducer and on the two intra-cavity EOM electrodes, as shown in Fig. 3.7. The piezo servo only works in the very low frequency range (DC-200 Hz), and its transfer function is enhanced in the very low frequency range with an additional integrator stage below 16 Hz. The intra-cavity EOM is driven by two independent servos, acting each on a single electrode with the ground as common reference. The first is a PI, with limited DC gain in order to avoid conflicts with the piezo loop. It provides corrections up to 200 kHz. The second servo consists of a minimal circuit, AC coupled above 16 kHz, with a single fast operational amplifier (AD818AN, 100 MHz bandwidth at unity gain). It provides a proportional correction up to $\sim$ 1 MHz, with a derivative stage which helps in lowering the PI servo bump and shifts its frequency up to $\simeq$ 0.5 MHz. All the elements of the feedback loops are battery powered in order to reduce the electronic noise. We also carefully arranged a "star-like" topology for the ground circuit to
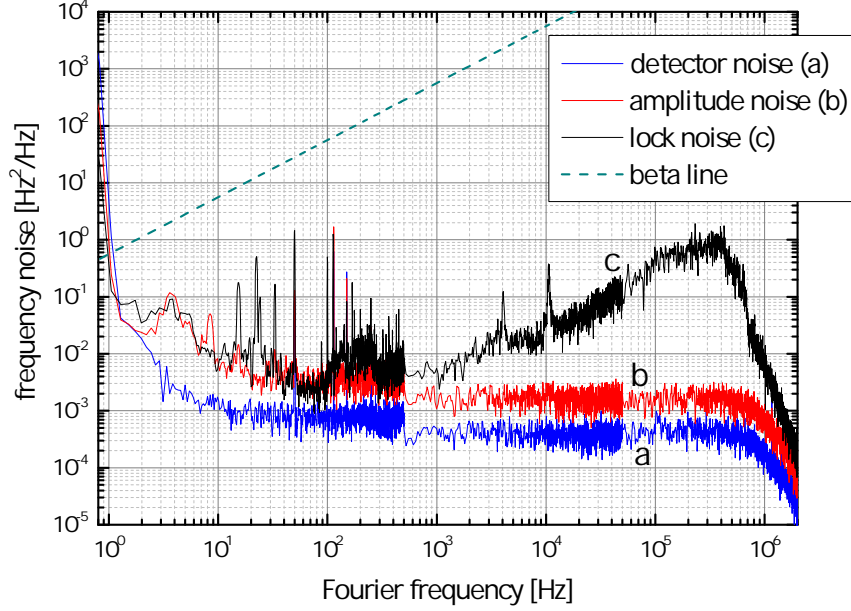
Figure 3.8: Frequency noise spectrum of the locked laser compared to electronic noise and amplitude noise of the out of resonance error signal. The black trace (c) is the frequency noise of the laser locked to the ULE cavity. The red trace (b) is the amplitude noise of the out-of-resonance backreflected light. The blue trace (a) is the electronic noise of the photodiode and locking electronics. The Beta Line [144] is a limit above which the frequency noise of the lock contributes to the laser linewidth.

minimize the noise induced by ground loops.

As we do not have a second system with comparable spectral characteristics to check the laser performances, we optimized the lock using for diagnostic the spectrum of the demodulated in-loop PDH error signal measured by a (battery powered) floating FFT spectrum analyzer. The spectrum, obtained after optimization of the lock performances, is reported in Fig. 3.8 (black trace, c). The red trace (trace b) is the spectrum of the error signal when the laser is not resonant with cavity modes and represents our sensitivity limit. It is generated by the amplitude noise of the light and the main contribution to it is due to RAM of the PDH EOM. The blue trace (trace a) is the spectrum obtained with no light, that is the intrinsic noise of the detector and the electronic chain of the feedback loop. The traces are composed by three spectra for different Fourier frequency ranges normalized by their resolution bandwidth and the volt-to-hertz conversion factor is estimated from the PDH signal amplitude. Substantially for all frequencies above 1 Hz, the frequency noise is reduced under the Beta Line [144], that discriminates whether the noise spectral components either contribute (if above) or not (if below) to the laser linewidth. In the low frequency region, which is the most critical in ultranarrow laser systems, the frequency noise of the locked laser is reduced to the amplitude noise level. At higher frequencies the lock noise grows up to a maximum around 500 kHz, which
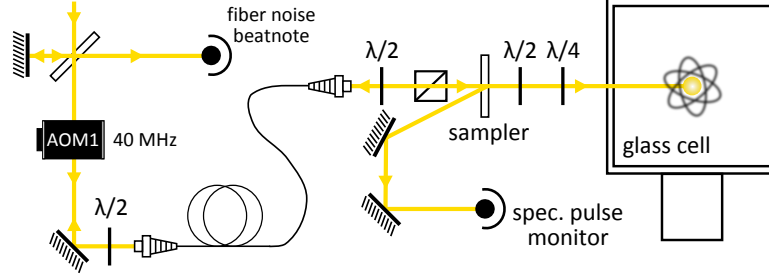
Figure 3.9: Scheme of the spectroscopy optical path. Before the optical fiber, AOM1 is used to finely tune the laser frequency and to shape spectroscopy pulses. AOM1 is responsible also for the drift compensation when the optical fiber link is not available. After the fiber the light polarization is cleaned and adjusted so that it has π polarization on the atomic sample. A sampler retroreflects part of the light to obtain a beatnote between the light before and after the optical fiber.

is our lock bandwidth, but still stays between 30 and 40 dB below the Beta Line level. In these in-loop spectra, the contribution of the cavity noise is not taken into account and the real laser linewidth can be determined only by observing atomic transitions.

3.1.5 Atomic spectroscopy

In order to perform spectroscopy on the atomic sample, the 578 nm probe light is delivered to the experimental setup through a 10 m long PM optical fiber contained in a protective tubing that provides insulation from air flows. Before the fiber, an AOM (AOM1, see figures 3.1 and 3.9) operating at 40 MHz, driven by a PC controlled synthesizer (Agilent 33522B), is used to finely tune the laser frequency (adding an offset to the AOM central frequency) and to rapidly switch light on and off (in cooperation with a fast mechanical shutter). In addition, in the case in which the optical fiber link is not available for long-term stabilization of the laser system (see section 3.2.4), the algorithm that drivers AOM1 can be configured to compensate with a feed-forward the ULE aging drift measured in sec. 3.1.3. Before the AOM, a beam sampler withdraws a small fraction of the light which is collected by a photodiode. After the fiber, a polarizing beam splitter cleans the light polarization and a $\lambda/2$ and a $\lambda/4$ waveplates compensate for polarization variation induced by the glass cell. After the PBS a beam sampler retroreflects part of the light into the fiber in order to obtain a beatnote between the light before and after the fiber (Fig. 3.9). This beatnote could be used to realize a fiber noise cancellation scheme [145] which at the moment is not implemented. In order to determine the effective linewidth of the laser system, we performed spectroscopy on a spin polarized sample of ^{173}Yb. The details of the spectroscopy procedure and conditions will be outlined in chapter 4, at the moment only the results of the measurement will be shown. A typical spectrum of the $^1S_0 \rightarrow {}^3P_0$ transition for a degenerate spin-polarized Fermi gas of ^{173}Yb loaded in a deep 3D optical lattice
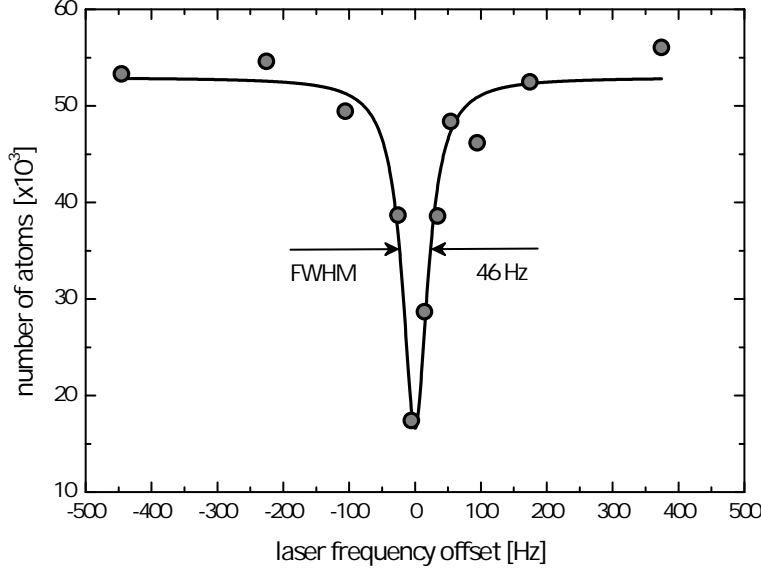
Figure 3.10: Clock transition observed with a 0.3 $\mu W/mm^2$ intensity and with 100 ms probe time. Every point is acquired at the end of a 30 s long experimental cycle for a final acquisition time of 5 minutes. The FWHM linewidth is 46 Hz.

probed with a $\sim 10\ \mu W/cm^2$ is reported in Fig. 3.10. During the data acquisition, the feed-forward compensation of the ULE cavity aging drift has been used. The linewidth is 46 Hz over a total acquisition time of 5 minutes. The observed linewidth on these timescales is substantially determined by a residual drift of the laser, which is present even operating the feed-forward to cancel the cavity linear aging drift. This residual drift varies in a range of a few 0.1 Hz/s during the day and we ascribe it to an imperfect thermal stabilization of the ULE cavity. The presence of this residual drift induces non-negligible shifts of the laser frequency between different experimental cycles (an experimental cycle lasts $\sim$ 35 s). For this reason, the shape of the spectrum will be altered depending on the relative orientation between the drift and scan directions, as will be also shown in section 4.3. Moreover, if the laser frequency is kept at a fixed value, initially in resonance with the atomic transition, after a certain number of experimental cycles, depending on the transition linewidth, the laser will no longer be resonant with the transition. Such residual drift represents the main limitation of the system and is studied in detail in section 3.2.3. Improving the thermal stabilization of the cavity could enhance the laser performances, however in order to perform experiments over timescales of some hours it is necessary to improve the laser long-term stability. For this reason, after the characterization of the laser performances, we stabilized the laser on an optical frequency reference, generated at INRIM (Italian National Metrology Institute) and delivered to our laboratory through a long-haul optical fiber link, which is described in the next section.

57

3.2 Optical fiber link to a remote metrology institute

As discussed in the previous sections, the main limitation of our system is a residual drift of the order of 0.1 Hz/s that compromises its long term performances. The short term stability of the laser allows for linewidths $\leq$ 100 Hz, which are suitable for the purposes of our experiments, however the residual drift prevents to effectively employ the laser over long timescales ($> 20 - 30$ minutes) without a calibration. In order to eliminate the residual drift, we exploit the existence of an optical fiber link that connects the Italian Metrological Institure (INRIM) to the LENS in Florence. This link disseminates the INRIM primary standards to the LENS laboratories as well as to several other institutes along the fiber link path.

This section is dedicated to a brief description of the optical fiber link. A detailed analysis of the link is can be found in Ref. [146]. After a general introduction to optical links, the attention is focused to the description of the specific fiber link, describing the three main components that allowed us to compare and lock our laser system to INRIM's remote optical reference. After a characterization of the performances of our ultranarrow laser system, we realized a digital feed-back protocol which transfers the long term stability of the remote optical reference to our laser system.

3.2.1 Introduction to optical fiber links

Currently, the most common technique employed for remote comparison of atomic clocks and frequency standards is represented by microwave satellite links. These links rely on a very well developed and extremely robust technology, that allows for the realization of the International Atomic Time (TAI) and the Universal Co-ordinated Time (UTC) [147, 148] averaging the signal of more than 250 atomic clocks located all around the world. Presently, microwave satellites links relying on the US Global Positioning System (GPS) are also the most widespread dissemination method, which allows for traceability to the second in the International System (SI) of units with a typical fractional frequency uncertainty of 10^{-13} on one day average [149]. However, GPS dissemination severely degrades the accuracy of current state of the art frequency standards (2×10^{-16} [150]) and even more that of the optical atomic clocks, which have already shown fractional accuracy capabilities of 10^{-18} in few hours of measurement [38–40]. For this reason, the development and characterization of long-haul optical fiber links, recently featured a substantial thrust [51, 151, 152]. In the last years, optical fiber links have shown undoubted effectiveness in comparing remote atomic clocks, beyond the ultimate limit of GPS-based comparisons ($> 10^{-16}$ [153]), attaining precision levels not limited by the frequency transfer method [52, 53, 154, 155], and short-range OFLs have recently been exploited in order to increase the spectral performances of a local laser and to allow for precision molecular spectroscopy [156]. In Chapter 4, we provide the first demonstration that optical fiber links can also be exploited for the dissemination of a primary absolute frequency reference to remote laboratories,
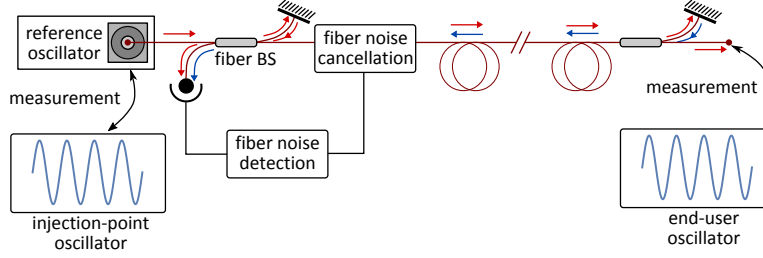
Figure 3.11: Conceptual scheme of an optical fiber link. The light of an ultrastable laser (reference oscillator) is sent through an optical fiber to a remote receiver. At the fiber end, part of the light is reflected back to the original station and heterodyne detected beating it with the original light, allowing for the realization of a fiber noise cancellation scheme. The reference oscillator is measured by two local oscillator at both ends, allowing for a comparison of the two which is not limited by the link noise.

in such a way as to push the precision and accuracy of local measurements and applications beyond the GPS limit.

A great advantage of optical fiber links is that they can be developed using the existing telecom fiber infrastructure and are compatible with Dense Wavelength Division Multiplexing (DWDM). This means that the a single channel of the International Telecommunication Union (ITU) Grid can be dedicated to frequency dissemination while Internet data are simultaneously transferred in other channels [157, 158]. While in telecommunication the information is encoded via phase or amplitude modulation of the optical carrier, in optical fiber links for metrological applications the information is represented by the frequency of a non-modulated continuous wave optical carrier. While other frequency dissemination techniques through optical links have been developed, the delivery of a phase-stabilized optical carrier represents the most common choice and is particularly suitable for the comparison between optical atomic clocks.

The realization of a metrological fiber link requires the employment of a reference CW laser with peculiar spectral properties. It is indeed necessary that the coherence time t_c of the laser source is greater than the round-trip time along the fiber, in order not to deteriorate the transmitted signal quality. This means that the laser linewidth needs to be:

$$\Delta \nu \sim \frac{1}{2\pi t_c} < \frac{1}{2\pi} \frac{c}{2nL}, \tag{3.2}$$

where L is the fiber length, n the refractive index and c the speed of light in vacuum. This ultrastable laser works as a reference oscillator between two different laboratories, where, typically, optical frequency combs are used to bridge the gap between the reference oscillator and the local oscillators, being microwave or optical.

While the adoption of an ultrastable laser source as reference oscillator prevents the phase detection at the fiber ends to be degraded by laser noise, other noise sources are present. Acoustic and seismic noise leads to variations of the fiber

59

length and mechanical stresses and thermal fluctuations can cause local variations of the refractive index, thus inducing a phase noise on the optical carrier. In order to suppress such noise, a fraction of the transmitted light at the far end of the link is withdrawn and sent back along the fiber. The heterodyne beatnote between the back-reflected and the original signals enables the detection of the phase noise induced by a double pass through the optical fiber and can be used as input of a feedback loop that actively compensates the fiber-induced phase noise, typically using an acousto-optic modulator, realizing a fiber noise cancellation (FNC) scheme [145]. It is important to note that with this technique the noise is actively compensated at the injection side, while a null phase noise would be desirable at the end-user. This condition is actually not achievable since the noise compensation bandwidth is limited by the round-trip time along the fiber link at a value lower than the typical acoustic frequencies, impliying that not all the noise is corrected. It has been demonstrated [159] that the phase noise Power Spectral Density (PSD) $S_{\phi,FE}(f)$ at the far end of the fiber link is given by:

$$S_{\phi,FE}(f) = \frac{1}{3} (2\pi\tau f)^2 \, S_{\phi,FR}(f) \tag{3.3}$$

where $\tau = nL/c$ is the time needed by the optical signal to travel through a fiber of length L and refractive index n and $S_{\phi,FR}(f)$ is the phase noise PSD of the free running optical link that is proportional to L. Equation 3.3 shows that the phase noise at the remote end of a compensated link is proportional to L^3 posing practical limitations to the realization of extremely long links.

It is important to remark that several factors have to be kept under control in a fiber link, ranging from Bragg reflection of the fiber to issues arising from the complex structure of a link with intermediate stations, which are beyond the scope of this introductory section. Reference [146] contains a detailed analysis of these issues, as well as an exhaustive list of references.

3.2.2 The INRIM-LENS optical fiber link

The optical link that connects INRIM and LENS is 642 km long, for a total 171 dB of optical losses along the entire path. The link is named LIFT (Italian Link for Frequency and Time) [160] and has been implemented on a dark fiber of the Italian National Research and Education Network (NREN), provided by Consortium GARR, that administrates the network. Nine dedicated Erbium Doped Fiber Amplifiers have been installed along the path (see Figure 3.12), for a total amplification of 156 dB [146]. The amplifiers are bidirectional, allowing for the transmission along the fiber link of the optical reference oscillator and of the retrorfletcted signal used for the fiber noise compensation. In the following sections the attention will be focused on the three main parts that substantially form the link infrastucture, i.e. the injection point at INRIM in Turin, the 642 km-long fiber link and the LENS end-user in Florence.

Figure 3.12: Optical fiber link between Turin (Torino) and Florence (Firenze) infrastucture with the Erbium Doped Fiber Amplifiers locations. Image taken from [146].

The INRIM injection point

The optical reference oscillator and the primary frequency standards are located at INRIM. The reference laser is an ultranarrow laser at 1542.14 nm. The laser source is a single-frequency Distributed-Feedback (DFB) fiber laser (Koheras-Adjustik by NKT Photonics), centered on the channel 44 of the ITU grid (1542.14 nm). The laser frequency can be coarsely tuned adjusting the laser temperature, while the fine tuning is achieved with a 100 kHz bandwidth piezo-stretcher. Similarly to the 578 nm laser of section 3.1, the 1542 nm laser is locked to an ULE reference cavity. Due to the low bandwidth of the low-noise high-voltage amplifier used to drive the piezo, its effectiveness is limited below 100 Hz, so an AOM is used as fast actuator, for a total locking bandwidth on the ULE cavity of 100 kHz. The ULE cavity is stabilized around 22 °C. Due to technical reasons, this temperature is far from the estimated zero CTE temperature (between 0 and 10 °C), resulting in a thermal sensitivity of ~ 6 MHz/K and a drift of the laser of the order of 1 Hz/s.

As the reference laser is locked on an ULE cavity, it shows a good short-term stability, but it is dominated by thermal induced fluctuations of the reference cavity on a long-term scale. In order to deliver a optical signal which is stable in time, the laser is referenced to the INRIM HM1 hydrongen maser and this is done through an optical fiber comb (MenloSystems model FC1500-250-WG). HM1 has two outputs in the RF domain, one at 10 MHz and one at 100 MHz. The former is used to stabilize the CEO frequency of the comb, while the latter is frequency multiplied to 1 GHz and used to stabilize the 4th harmonic of the comb repetition rate. Since the comb is located in another floor of the INRIM building, the reference laser is split and a fraction of the 1.5 μm light is delivered to the frequency comb via 100 m long optical fiber. Also the phase noise introduced by this relatively short
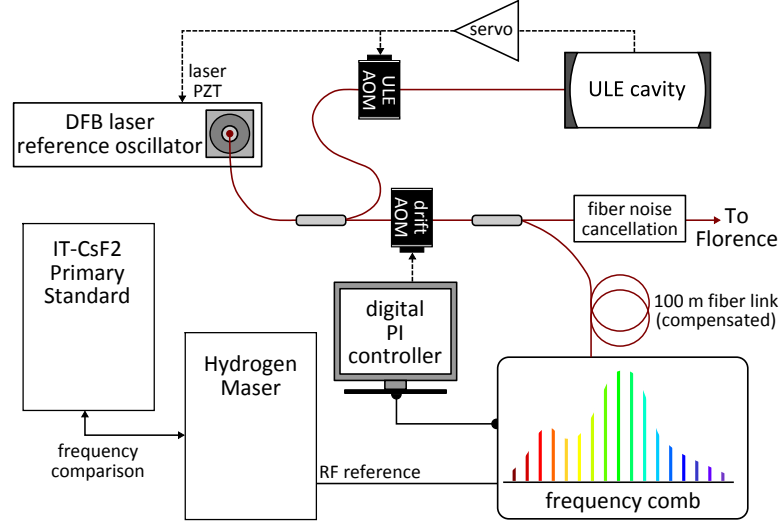
Figure 3.13: Scheme of the metrological chain at INRIM station. The reference oscillator is a distributed-feedback (DFB) laser locked to an ULE cavity with the laser piezo and a fiber-couled AOM (ULE AOM). The drift of the reference laser is measured with an optical frequency comb stabilized on an hydrogen maser and compensated by a digital PI servo acting on an AOM (drift AOM). The maser is calibrated against the IT-CsF2 cesium fountain clock.

fiber span is canceled with a FNC scheme analogous to that of the INRIM-LENS link. The reference laser frequency is then measured by the frequency comb, and a digital PI algorithm is used to correct and compensate for the ULE reference cavity drift by acting on an fiber-coupled AOM placed at the laser output. This allows the reference laser to inherit the hydrogen maser long-term stability and a drift-free (or "dedrifted") frequency is distributed through the optical fiber link. The HM1 frequency is continuously compared against the INRIM's Cs fountain clock IT-CsF2, in order to measure the maser frequency fluctuations and drifts, typically below of few parts in 10^{-15} for several days of operation.

The INRIM side also hosts all the optical and electronic apparatuses responsible for the fiber noise cancellation of the optical link. The scheme is relatively simple and is reported in Fig. 3.14. Before the injection of the fiber link, a fiber-coupled splitter delivers a fraction of the light to Faraday mirror[1], which reflects it towards a photodiode (PD). The light travels through a fiber-coupled AOM (AOM1 operating around 40 MHz) and then enters the fiber link. In Florence, after a second 40 MHz AOM (AOM2), another splitter withdraws a part of the incoming light and a Faraday mirror reflect it back to INRIM side. At INRIM, the back-reflected signal is also delivered to the photodiode PD and the beatnote between the original and

---

[1]Faraday mirrors are adopted at both ends in order to avoid polarization fluctuations of the signal induced by the fiber birifrangence: Faraday mirrors non only reflect the light but also rotate the light polarization by 90 °C, so that the back-reflected light experiences polarization fluctuations which are opposite to those experienced by incoming light.
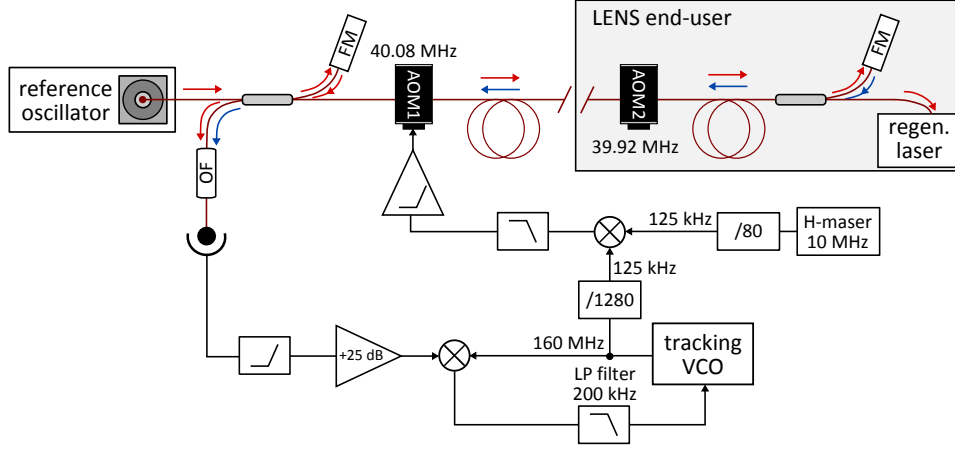
Figure 3.14: Schematic of the Fiber Noise Cancellation scheme implemented at the INRIM side of the fiber link. The 160 MHz beatnote between the original and back-reflected light is detected by a fiber coupled photodiode, high pass filtered and amplified. A tracking VCO with a 200 kHz bandwidth cleans and regenerate the beatnote signal which is divided by a factor 1280 and fed to a mixer working a phase detector. The mixer compares the beatnote with a 125 kHz stable signal, and its output is used as error signal for an analog PI servo amplifier that corrects the fiber link phase noise acting on AOM1.

the reflected light is detected. An optical filer before the photodiode filters out part the noise induced by spurious back-reflections along the fiber and ASE (amplified spontaneous emission, see next section). The 160 MHz beatnote is further cleaned by a tracking VCO (Voltage-Controlled Oscillator) with a 200 kHz bandwidth, whose output is a perfect copy of the beatnote within the bandwidth. The VCO output is divided by 1280^2 and compared through quadrature mixing with a 125 kHz stable reference (the H-maser 10 MHz divided by 80), in order to obtain a phase error. The mixer output is fed to PI stage whose output is used to modulate the frequency of AOM1 in order to correct the fiber phase noise. The bandwidth of this PLL (Phase-Lock Loop) is ~ 50 Hz, limited by the round-trip time.

As a final note, it should be mentioned that, as a consequence of shocks or fluctuations of the beatnote SNR, the FNC scheme may experience phase-slips, i.e. sudden relocks of the PLL in different working points, that induce undesired offsets of the delivered frequency. The occurrence of phase-slips is detected with a second, independent VCO, not shown in Fig. 3.14, that tracks the round-trip beatnote. The outputs of the this VCO and of the FNC VCO are synchronously counted and all measurements differing by more than 0.4 Hz identify the occurrence of phase jumps. This threshold is chosen according to the minimum slips amplitude, i.e. 1 cycle, that is detected as a 1-Hz frequency outlier on a gate time of 1 s. With this redundant

---

[2]The beatnote is divided by this large factor in order to increase the dynamic range of the mixer. In long fiber links, due to the low correction bandwidth, the uncompensated high frequency noise can induce phase jumps if the dynamic range of the phase detector is limited. An exhaustive discussion about this subject can be found in [146].

beatnote tracking, the occurrence of phase-slips is continuously monitored during measurements, so that it is possible to assign an uncertainty to the disseminated frequency.

The fiber Link

As stated above, the transmission of the optical reference oscillator from Turin to Florence would not be possible without a stepwise amplification of the signal due to the attenuation of the 640 km long fiber. For this reason, a total of 9 Erbium Doped Fiber Amplifiers (EDFA) have been installed along the path. EDFA are widely used in long-haul optical telecommunications and have been optimized during the years to achieve high gain, large bandwidth, and an adequate SNR. An EDFA is basically nothing else than a fiber laser without feedback, which amplifies the original signal maintaining its coherence properties. Typically these devices are unidirectional, but in coherent optical links there is a further requirement: the optical amplifier must be symmetrical, i. e. the optical path must be the same in the two directions. This is requested in order to effectively cancel the fiber phase noise. The development and proper operation of symmetrical EDFA in the fiber link needed an additional effort, in order to overcome the difficulties given by the amplifiers noise sources.

Optical amplifiers, as well as lasers, are indeed affected by spontaneous emission since not all the electrons decay from the excited level to the ground state through stimulated emission: some of them decay by spontaneous emission, and therefore are no longer coherent with the input signal. The spontaneously emitted photons may in turn be amplified, resulting in a degradation of the SNR. This process is usually referred to as Amplified Spontaneous Emission (ASE). ASE optical power forms a pedestal around the frequency peak, which may be several nanometers wide and is the most important source of wideband noise in optical amplifiers. The presence of ASE is even more problematic in a chain of EFDA, as the ASE produced by every amplifier saturates the gain of the next amplification stage and decreases the signal-to-noise ratio at detection. To mitigate the effect of ASE, the radiation is optically filtered at most sites with standard telecom filters with FWHM ~ 0.8 nm. Nevertheless, the amplifiers ASE still represents a source of noise in the optical fiber link. In addition to this, other phenomena related to the propagation along the fiber, such as double Rayleigh backscattering [146], contribute to the deterioration of the spectral properties of the fiber noise beatnote, compromising its effectiveness. Also these effects were taken into account in the implementation of the fiber link and an exhaustive discussion on their nature and the countermeasures adopted to minimize them can be found in Ref. [146].

The analysis of the fiber link performances is reported in [51]. Figure 3.15a shows the noise spectrum of the full 1284 km round-trip, with and without compensation of the fiber noise. It can be seen that the adoption of the FNC scheme is effective to cancel the fiber phase noise up to 20 Hz with nearly 40 dB of noise suppression at 1 Hz and an even higher 70 dB suppression on 100 s timescale. Figure 3.15b shows instead the frequency stability of the 1284 km fiber link, ex-
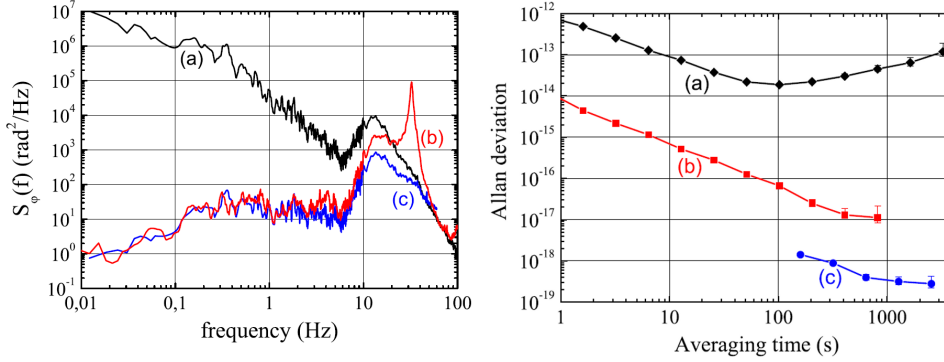
Figure 3.15: a) Phase noise PSD of the uncompensated (black) and compensated (red) link. A significant noise reduction is clearly visible up to the 10 Hz level, especially effective in the very low frequency region (up to 70 dB on 100 s timescales). The blue curve is the predicted noise of the theoretical model [51]. b) Frequency stability of the uncompensated and compensated link with the same color code. The blue points are the frequency stability at long times obtained applying a stronger data filtering (5 mHz). Figures taken from [51].

pressed in terms of Allan deviation (see appendix C) of the time series filtered with different bandwidths [51, 146]. From the graph it is evident how the noise cancellation allows for an improvement of the frequency stability at 1 second by two orders of magnitude, from 10^{-12} to 1×10^{-14} on a 1 Hz bandwidth. An ultimate frequency stability of the compensated link of 5×10^{-19} can be reached after 1000 s of integration time, with a 5 mHz bandwidth data filtering.

The LENS end-user

At LENS, the light of the reference laser is compared with the light of the 578 nm laser in order to stabilize the long term drift of the latter on the former. This goal can be achieved by optically locking a frequency comb (see appendix B) to the optical reference at 1542 nm and using it to measure the local 578 nm laser. Unfortunately, the optical power of the reference laser at the LENS end of the fiber link is of the order of 40 nW, too low for a proper optical lock of the frequency comb. In order to increase the optical power, a regeneration laser has been installed in the laboratory where the end of the fiber link is located.

The regeneration laser is a high-performance and cost effective diode laser module built by Redfern Integrated Optics (RIO). The module contains a Planar External Cavity Laser, with an integrated Bragg grating forming a laser cavity, as well as the electronics for current modulation. Coarse frequency and optical power adjustments are made by acting on the diode temperature, while fine tuning of the diode frequency is provided by current modulation. The heterodyne beatnote beatnote between the regeneration laser and the reference laser is detected and compared with a stable 100 MHz RF reference with a phase comparator. The output of the comparator acts on the RIO current in order to obtain a PLL with the
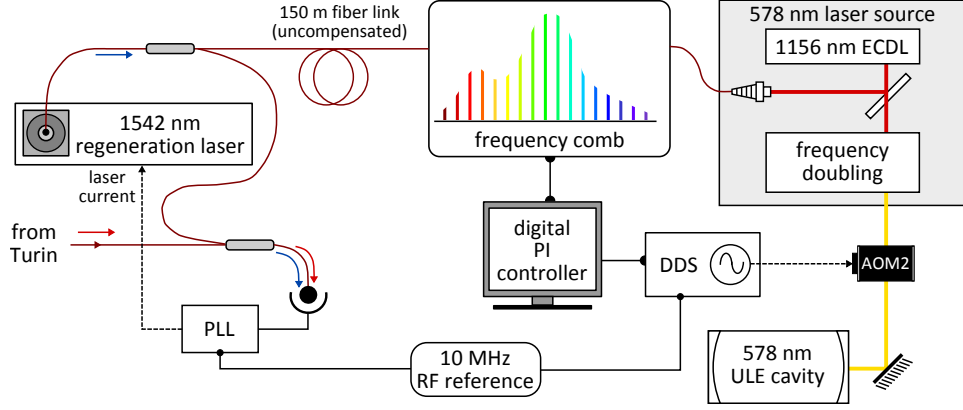
Figure 3.16: Scheme of the Florence side of the optical fiber link. The heterodyne beatnote between the incoming light and a local 1542 nm laser is detected with a photodiode and is used to phase-lock it to the optical fiber link light with a PLL. The phase-locked regeneration laser is then delivered to Ytterbium lab with a 150 m long uncompensated fiber. There it serves as optical reference to lock a frequency comb, which is used to measure the 1156 nm laser frequency.
This enables the stabilization of the ultranarrow laser on the fiber link with a digital PI controller acting on the 578 nm laser ULE cavity AOM, as explained in the next section.

reference laser with a 100 kHz bandwidth. The regeneration laser output power is of a few mW, and is delivered to the Ytterbium laboratory via a 150 m long optical fiber. This fiber span introduces a frequency instability below 10^{-15}, which is beyond our stability goal, so no fiber noise cancellation has been implemented up to now. In the Ytterbium lab, an optical frequency comb is stabilized on the regenerated optical reference by means of optical lock technique (see appendix B), thus inheriting the 10^{-14} stability at 1 s of the 1542 nm reference laser at the end-point of the optical fiber link. A dedicated all-fiber Beat Detection Unit (BDU) detects the beatnote between the 1156 nm infrared light of our ultranarrow laser, withdrawn before the frequency doubling (see section 3.1) and delivered to the comb's BDU with a 10 m-long, uncompensated optical fiber, and the closest tooth of the frequency comb. This allowed us first to characterize our ultranarrow laser long-term stability against the H-maser-stabilized 1542 nm reference laser, subsequently to develop a digital PI feedback algorithm to cancel the laser drift.

3.2.3 Ultranarrow laser characterization

As already mentioned in section 3.1.5, the main limitation of our laser system stability is a residual erratic drift of the order of 0.1 Hz/s, which is present despite the adoption of a feed-forward system to cancel the measured ULE cavity linear aging drift. As a consequence, our laser system is not suitable for experiments which rely on the interrogation of the clock transition over timescales of the hour or longer, since it requires periodic recalibration with spectroscopic measurements.
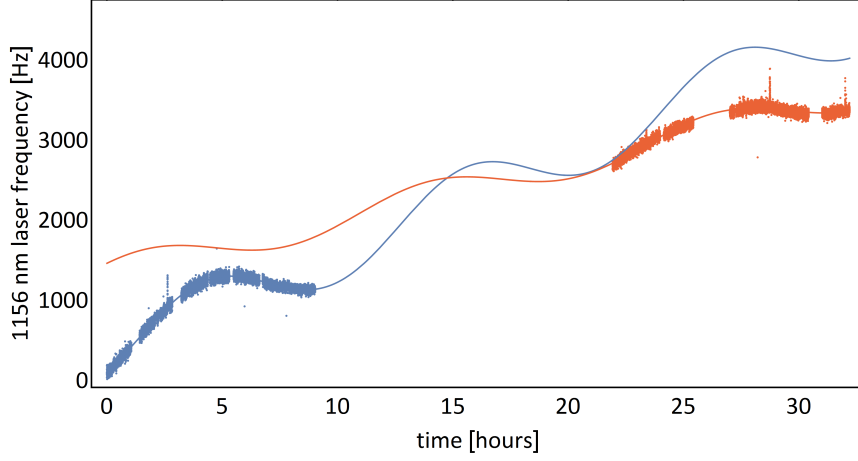
Figure 3.17: The points represent the measured beatnote between the 1156 *nm laser and the comb locked to the* 1542 *nm optical reference for two consecutive days (blue and orange). The lines represent the fit of the single days data with the simple model of Eq. (3.4). The two curves are not compatible, evidencing an underlying more complex behavior.*

Exploiting the optical fiber link described in the previous section, we measured the frequency of the 1156 nm laser locked to the ULE cavity for two consecutive days against the 1542 nm optical reference, in order to analyze the behavior of the ULE cavity drift. The results are reported in Fig. 3.17. In the figure, the data of two consecutive days of measurements are represented by the blue and orange points. We fit the two single-day datasets with a simple model:

$$y_0 + mx + A\sin(2\pi\omega x + \phi) \tag{3.4}$$

given by the sum of a linear (aging) drift and an oscillation, introduced, for example, a residual oscillation of the temperature stabilization. Both datasets show an oscillation on several hours timescale ($\sim$ 11.5 hours and $\sim$ 12.5 hours from the first and second day respectively) with an amplitude of the order of a few hundreds Hz (370 Hz and 190 Hz). These oscillations can be ascribed to imperfections in the thermal stabilization systems, like an excessive loop gain or thermal voltages and/or ground loops that slightly shift the setpoint of the analog frontend (see section 3.1.3). On the other hand, the data suggest that other phenomena may induce frequency fluctuations on longer timescales, since it is evident that the two fits are not compatible. This means that the simple model of Eq. (3.4) is not suitable to reliably forecast the underlying behavior of the system, which could be in principle used to improve the feed-forward. For this reason an active correction of the laser frequency has been implemented exploiting the optical frequency dissemination.

Exploiting the optical fiber link we also measured the power-induced deformations of the ULE cavity and the laser frequency sensitivity to residual amplitude modulation of the PDH signal. For the former, we measured the 1156 nm laser frequency with the frequency comb stabilized on the 1542 nm optical reference for

different power values of the light coupled in the ULE cavity, obtaining a sensitivity of 24 Hz/μW. This value is approximately three times lower than the estimation of Ref. [138]. Regarding the RAM, we observed that the offset of our Pound-Drever-Hall error signal monitored on an oscilloscope fluctuates approximately within a range of approximately ± 5 mV on a daily basis. In order to measure the corresponding laser frequency variation we manually changed the PDH signal offset up to ± 30 mV and measured the laser frequency shift. The measured sensitivity is 2.9 Hz/mV, hence the observed RAM could induce frequency fluctuations of the order of approximately ± 14.5 Hz.

These measurements show that several improvements can be made on the laser system to enhance its performances, for example improvements in the ULE temperature controller, an active stabilization of the PDH EOM temperature to reduce RAM and lowering the power coupled into the ULE cavity. Nevertheless, the exact origin of the residual day-to-day fluctuations remains as of today unknown.

3.2.4   Long-term stabilization on the optical fiber link

In order to eliminate the observed long-term fluctuations, the 1156 nm laser frequency is disciplined to the H-maser-stabilized optical fiber link. This is implemented with a digital PI servo-controller algorithm running on the comb control PC, which essentially acts on the ULE AOM (AOM2 in Fig. 3.7) frequency in order to stabilize the beatnote between the 1156 nm laser and the H-maser-stabilized frequency comb. The beatnote is read in λ-mode (i.e. a 1 s gate time reading is the result of an average over multiple sub-second readings [161]) by the comb counter software FXQE80 and recorded in a log file. The PI algorithm reads the log file and averages over the last 20 counter readings, meaning a $\tau_{av} = 20$ s averaging time, which is the timescale below which no correction is needed since the 578 nm laser has a better stability than the 1542 nm optical reference (see below). This averaged beatnote frequency is compared with a setpoint frequency to obtain an error signal ε and the PI correction is computed by the algorithm as:

$$f_{out} = f_0 + K_P \varepsilon + K_I \sum \varepsilon \tag{3.5}$$

where K_P and K_I are the proportional and integral constants, respectively, and f_0 is the ULE AOM initial frequency. The new frequency f_{out} is directly loaded by the PI algorithm on a DDS (Direct-Digital-Synthesizer, model AD9910 mounted on an UG-207 evaluation board) that drives the ULE AOM. Additional details on this subject can be found in Ref. [162], which contains an exhaustive description of the setup and the software. In this way our laser systems benefits from the improved long-term stability of the 1542 nm optical reference, retaining at the same time its own short-term frequency stability for timescales below the averaging time τ_{av}. On these timescale, the 1156 nm stability is higher that the 1542 nm reference. This can be clearly seen in Fig. 3.18a. The blue curve represents the frequency noise of the 1542 nm optical frequency measured at INRIM with an independent ultrastable laser. The dark grey curve represents the spectrum of the frequency
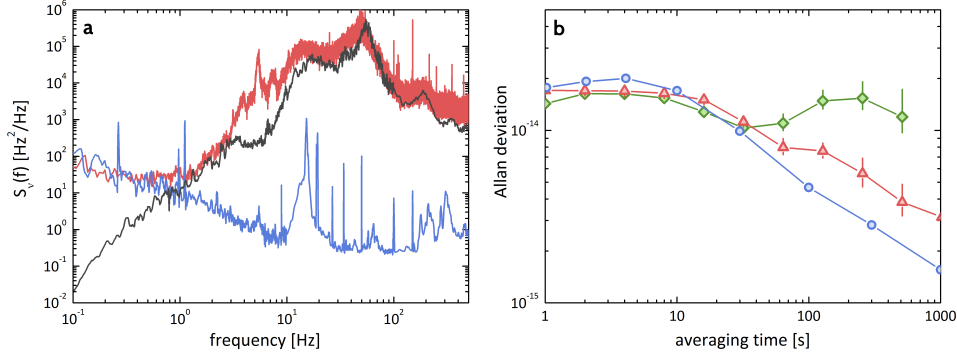
Figure 3.18: ***a.*** *Red line: frequency noise of the beatnote between the* 1156 *nm laser and the reference laser at* 1542 *nm; blue line: frequency noise of the HM-disciplined* 1542 *nm laser measured at INRIM; black line: expected contribution of the optical link. All the spectra are referred to the 1156-nm spectral region.* ***b.*** *Blue line (circles): fractional frequency instability (Allan deviation) of the HM-disciplined* 1542 *nm laser measured at INRIM; red line (triangles): Allan deviation of the beatnote between the reference laser at* 1542 *nm and the* 1156 *nm laser, locked to it; green line (diamonds): Allan deviation of the beatnote between the* 1542 *nm reference laser and the* 1156 *nm laser when a linear drift of* 0.1 *Hz/s is removed off-line. All measurements are taken with* 0.5 *Hz measurement bandwidth.*

noise introduced by the fiber link. The ∼ 30 Hz bandwidth of the fiber noise cancellation is clearly visible. The red trace is the noise spectrum of the beatnote between the 1156 nm laser and the 1542 nm optical reference. All the curves are referred to the 1156 nm spectral region. The red curve coincides with the worse between the 1542 nm and the link noise for all Fourier frequencies down to 0.1 Hz, with the exception of the spectral region between 1 and 30 Hz. However, in this spectral region the effectiveness of the FNC (and so the noise level) is dependent on the environmental conditions, so the discrepancy between the red and dark gray curves can be ascribed to different conditions in different acquisition periods. In conclusion, Fig. 3.18a shows that the 1156 nm laser has a better frequency stability than the 1542 nm reference for Fourier frequencies higher than 0.1 Hz.

The situation is different at longer timescales, as shown in Fig. 3.18b. The green curve is the Allan deviation of the drifting 1156 nm laser measured against the 1542 nm optical reference and the blue curve is the Allan deviation of the 1542 nm optical reference. The two curves coincide up to 30 s, meaning that up to this timescale the stability of the 1156 is better than the 1542 nm. For this reason we choose a similar timescale averaging time τ_{av} (20 s) of our digital feedback. The Allan deviation of the 1156 nm laser disciplined to the 1542 optical reference is represented by the red curve. The long-term drift and fluctuations of the 1156 laser are suppressed, and its stability reaches the 10^{-15} level at 1000 s integration time.

In chapter 4, it will be demonstrated that also the excellent accuracy of the 1542 nm optical reference, when referred to a primary Cs frequency standard, can

be transferred from a metrological institute to a remote, non-metrological research laboratory. This will be proved performing long-term, high-accuracy spectroscopy of the $^1S_0 \rightarrow {}^3P_0$ transition in a quantum degenerate gas of ^{173}Yb.

Chapter 4

Addressing the ^{173}Yb clock transition beyond the GPS limit

At the end of the previous chapter (see section 3.2), we described the technique employed to refer our ultranarrow 578 nm laser to an optical frequency reference at 1542 nm generated in the Italian National Metrology Institute (INRIM) and traced to the SI second in order to improve its long-term stability. In this chapter we show that, through this metrological chain, typical accuracies of the order 10^{-15} can be transferred from primary standards to non-metrological end-users in short timescales below 10^4 s, whereas the GPS dissemination method would only grant an accuracy of 10^{-13} [149]. Exploiting this absolute reference, we perform high-accuracy spectroscopy of the ^{173}Yb $^1S_0 \rightarrow {}^3P_0$ clock transition, determining its absolute frequency with an accuracy of 10^{-14} [56], limited by the systematic uncertainty of our end-user laboratory. Noticeably, this value exceeds by 20 times the uncertainty attainable with a GPS-based frequency transfer on the same timescale [149]. With this measurement we demonstrate the effectiveness of a long-haul optical for frequency dissemination beyond the GPS limit. This features a potential fallout on a wealth of applications ranging from scientific research to industrial development and production processes. Furthermore, our results could readily be exploited for the investigation of true many-body quantum physics in AEL atomic systems [26], and for the application of novel promising quantum information schemes [28–30] where the frequency precision and the coherence of a manipulation laser on typical experimental timescales are of the highest importance.

In the first part of this chapter, the properties of the $^1S_0 \rightarrow {}^3P_0$ and of the metastable $^3P_0$ state are described, in particular it will be shown the mechanism that enables the excitation of this doubly forbidden transition in fermions and bosons. We will then review how to perform Doppler-free spectroscopy of the clock transition, in which the observed linewidth is only limited by the power broadening of the transition, and show some basic experimental results. The last part is instead dedicated to the description of the high-accuracy measurement of the absolute frequency of the clock transition, including a discussion on the main

71

sources of uncertainty.

4.1 The $^1S_0 \to {}^3P_0$ clock transition

The doubly-forbidden $^1S_0 \to {}^3P_0$ represents one of the distinctive features of the Ytterbium atom and of AEL atoms in general. Indeed, several schemes of quantum simulation [26] and quantum information [28–30] with AEL atoms rely on the possibility to excite the atoms to the metastable level $^3P_0$, which represents an additional degree of freedom that alkali atoms are lacking. The direct excitation of the clock transition has so far been achieved in three isotopes, ^{174}Yb, ^{171}Yb and ^{173}Yb [163–165]. Its absolute frequency is know with great accuracy for two isotopes, ^{174}Yb and ^{171}Yb, and are respectively 518 294 025 309 217.8 (0.9) Hz [163] and 518 295 836 590 865.2 (0.7) Hz [164]. The clock transition frequency in ^{173}Yb is know only with a 4.4 kHz uncertainty, substantially because no optical atomic clock is based on such isotope as of today. Its numerical value is 518 294 576 847.6 (4.4) kHz [165] and in the last part of this chapter we give the results of our independent measurement which improves this result by two orders of magnitude.

The excitation of the $^1S_0 \to {}^3P_0$ is in principle doubly forbidden, since it violates both the total spin selection rule $\Delta S = 0$ and the total eletronic angular momentum selection rule which forbids $J = 0 \to J' = 0$ transitions. Nevertheless, the total spin selection rule is strict only in the LS approximation and can by violated due to the presence of spin-orbit interaction which mixes spin-singlet ($S = 0$) and spin-triplet states ($S = 1$), so that S is no longer a good quantum number. For example, the real $\left|{}^3P_1\right\rangle$ state will be a mixing between the pure LS eigenstates $\left|{}^1P_1^0\right\rangle$ and $\left|{}^3P_1^0\right\rangle$ [166]:

$$\left|{}^3P_1\right\rangle = \alpha \left|{}^3P_1^0\right\rangle + \beta \left|{}^1P_1^0\right\rangle. \tag{4.1}$$

Since the $\left|{}^1P_1^0\right\rangle$ state is coupled to the ground state by an electric dipole transition, the $\left|{}^3P_1\right\rangle$ state will inherits a dipole coupling with the ground state because of $\beta \neq 0$. In Ytterbium, the $^1S_0 \to {}^3P_0$ intercombination transition has a natural linewidth of $\Gamma = 2\pi \times 181$ kHz, and is exploited for the MOT cooling stage, as already mentioned in section 2.2.1.

The fermionic isotopes of Ytterbium are also characterized by a non zero nuclear spin I ($I = 1/2$ for ^{171}Yb and $I = 5/2$ for ^{173}Yb) that gives rise to a non zero nuclear magnetic moment μ_N. This magnetic moment interacts by the magnetic field generated by the electrons. This interaction provides an additional state-mixing mechanism between states having the same total spin $F = J + I$, so J is no longer a good quantum number. As a result, the $^3P_0$ ($F = 5/2$ in ^{173}Yb) state will be mixed with the $^3P_1$ ($F = 5/2$) state [166]:

$$\left|{}^3P_0\right\rangle = \left|{}^3P_0^0\right\rangle + \alpha_0 \left|{}^3P_1\right\rangle, \tag{4.2}$$

where α_0 is very small (i.e. 10^{-4} for ^{87}Sr [166]) and the state $\left|^3P_1\right\rangle$ was defined in Eq. (4.1)[1]. Since a small admixture of the pure $\left|^1P_1\right\rangle$ state is present in $\left|^3P_1\right\rangle$, also in this case a very tiny electric dipole matrix element is inherited by the $\left|^3P_1\right\rangle$ state. The exact mixing and the consequent matrix element of the transition can be accurately estimated by relativistic many-body calculations [167, 168], obtaining a natural linewidths of the clock $\Gamma = 2\pi \times 7$ mHz and $\Gamma = 2\pi \times 6$ mHz for ^{173}Yb and ^{171}Yb respectively. Such a small linewidth implies a saturation intensity of the order of 10^{-9} mW/cm^2, which is an extremely low value in typical experimental setups. As shown in section 4.2.2, due to this property, even with a relatively modest intensity it is possible to drive coherent Rabi oscillation at frequencies of a few kHz.

For sake of completeness, let us consider the case of bosonic isotopes, which have zero nuclear spin and show no hyperfine interaction. For this reason, J is a good quantum number and the clock transition is in principle strictly forbidden. In this case the mixing between the $^3P_0$ and the $^3P_1$ state is induced by the application of a static magnetic field [169, 170]. By labeling the states $\left|^1S_0\right\rangle$, $\left|^3P_0\right\rangle$ and $\left|^3P_1\right\rangle$ respectively as $|1\rangle$, $|2\rangle$ and $|3\rangle$, with the application of a static magnetic field $\mathbf{B}$, the state $|2\rangle$ will be mixed with the state $|3\rangle$, forming the state:

$$|2'\rangle = |2\rangle + \frac{\omega_B}{\Delta_{32}}|3\rangle, \tag{4.3}$$

where $\omega_B = \langle 2|\,\hat{\boldsymbol{\mu}} \cdot \mathbf{B}\,|3\rangle$, with $\hat{\boldsymbol{\mu}}$ being the magnetic dipole operator, is the coupling and Δ_{32} is the energy difference between the states $|2\rangle$ and $|3\rangle$. Since the ground state $|1\rangle$ is coupled to the state $|3\rangle$ by the Rabi frequency $\Omega_L = \langle 3|\,\hat{\boldsymbol{d}} \cdot \mathbf{E}\,|1\rangle$, with $\hat{\boldsymbol{d}}$ being the electric dipole operator and $\mathbf{E}$ the laser electric field, the Rabi frequency and the broadening associated to the $|1\rangle \rightarrow |2'\rangle$ transition will be given by:

$$\Omega_{12'} = \frac{\Omega_B \Omega_L}{\Delta_{32}}, \qquad \Gamma_{12'} = \Gamma_{13}\frac{\Omega_L^2/4 + \Omega_B^2}{\Delta_{32}^2}, \tag{4.4}$$

where Γ_{13} is the natural linewidth of the $|1\rangle \rightarrow |3\rangle$ transition which implies a natural broadening Γ of the order of the μHz [169]. In particular it can be shown that:

$$\Omega_{12'} = \alpha\sqrt{I}|\mathbf{B}|, \tag{4.5}$$

where I is the intensity of the probe (clock) laser and $\alpha = 186$ Hz/(T$\sqrt{\text{mW/cm}^2}$) for Ytterbium. According to this relation, a probe beam of 20 mW focused on a 100 μm waist with a field of 20 G would induce a Rabi frequency $\Omega_{12'}/(2\pi) \simeq 15$ Hz. It is worth noticing that the excitation of the clock transition in bosonic isotopes requires a much higher power with respect to the case of fermions.

---

[1] Other terms with the same F are also mixed in the $\left|^3P_0\right\rangle$ state, but with much lower coefficients, so they have been neglected for sake of clarity. See Ref. [166] for details.
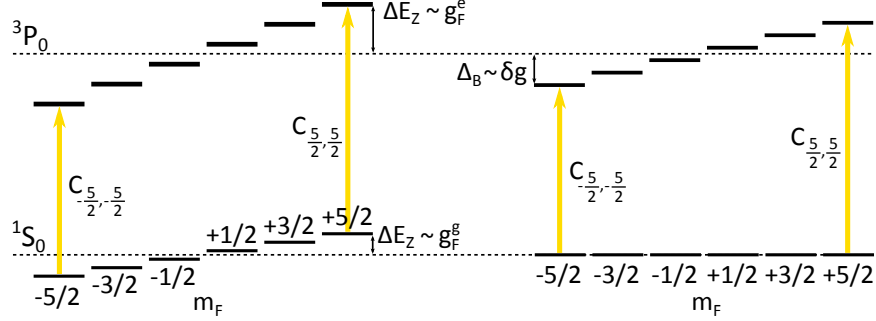
Figure 4.1: Due to the hyperfine interaction that mixes the $^3P_0$ state with the $^3P_1$, the excited state Lande g-factor g_F^e is different than in the ground state g_F^g, implying a different Zeeman splitting Δ_B at finite magnetic field. The effect is that the clock transition is shifted by a factor proportional to δg and to the nuclear spin m_F. The Clebsch-Gordan coefficients $C_{m_F,m_F'}$ of the different transition are directly inherited from the $^1S_0$ $(F = 5/2) \rightarrow {}^3P_1$ $(F = 5/2)$ transition (see appendix A).

4.1.1 Magnetic field splitting

As already mentioned, the electronic angular momentum J of the metastable $^3P_0$ is zero, like in the ground state $^1S_0$, and therefore no hyperfine structure is present. In the fermionic isotopes with non-zero nuclear spin, a magnetic structure is present, and the Zeeman shift of each m_F state, as already discussed in section 1.3.1, is given by $\Delta E_Z(B) = g_F m_F \mu_B B$, where g_F is the Landé g-factor and μ_B the Bohr magneton. The Landé factor is given by Eqs. (1.49-1.50) and for the pure $^3P_0$ state it the same as for the $^1S_0$ state. In this ideal case, the clock transition, which is sensitive to the differential Zeeman shift between the $^1S_0$ and $^3P_0$ states, would not be influenced by the presence of the magnetic field. However, also in this case, due to the nuclear spin-induced mixing with the $^3P_1$ state, the electronic wavefunction of the $^3P_0$ is distorted and the Landé g-factor g_F will be slightly different with respect to the ground state. As a consequence, focusing of the case of ^{173}Yb, the different transitions $^1S_0$ $(F = 5/2, m_F) \rightarrow {}^3P_0$ $(F' = 5/2, m_F')$ will be subjected to a linear Zeeman shift given by [166]:

$$\Delta_B = \delta g m_F' \mu_B B, \tag{4.6}$$

where $\delta g = g_F^e - g_F^g$ is the differential Landè g-factor, with g_F^g and g_F^e being the Landè g-factors of the ground and metastable state respectively (see Fig. 4.1). The differential Landè g-factor has been theoretically determined in [168] and determines a Zeeman shift $\Delta_B \simeq m_F B \times 113$ Hz/G·h. The magnetic fields calculated from the atomic transition spectra (see section 4.3.2) are compatible with the values determined with other methods, so this value of the clock transition linear Zeeman shift will be assumed, in the following parts of this thesis. With typical clock transition linewidth of the order of 100 Hz, each nuclear spin state can be separately addressed with a magnetic field of just a few Gauss. As a final note it shall be

mentioned that the line strength of the individual $^1S_0$ $(F = 5/2, m_F) \to {^3P_0}$ $(F' = 5/2, m'_F)$ transitions are proportional to the Clebsch-Gordan coefficients C_{m_F, m'_F}, which are directly inherited from the $^1S_0$ $(F = 5/2, m_F) \to {^3P_1}$ $(F' = 5/2, m'_F)$ transitions (see appendix A).

4.1.2 The magic wavelength and orbital-dependent optical lattices

Typically, in experiments the excitation of the clock transition is performed on atomic samples confined in deep optical lattices, enabling the possibility to perform Doppler-free, recoil-free spectroscopy of the clock transition, as we will see in section 4.2.1. As discussed in section 1.1.1, dipole potentials are intrinsically state-dependent, meaning that they depend on frequency and natural linewidth of the transitions from the considered electronic state. Since the ground and the metastable state are connected to the excited states via different transitions, the two state will experience quite different dipole potentials. Considering the transitions reported in appendix A, the dipole potentials for the $^1S_0$ and $^3P_0$ states can be calculated using Eq. (1.12) and are plotted in Fig. 4.2 as a function of the wavelength. A more accurate evaluation of the exact dipole potential requires relativistic many-body calculations of the energies and matrix elements and has been carried out in Ref. [76], but this is beyond the scope of this work. Away from resonances, the light shift of the ground state is dominated by the presence of the $^1S_0 \to {^1P_1}$ electric dipole transition, while the narrow $^1S_0 \to {^3P_1}$ transition only have an effect at relatively small detuning. The dipole potential for the metastable state is instead dominated in the visible by the $^3P_0 \to {^3S_1}$ transition at 649 nm and the $^3P_0 \to {^3D_1}$ transition at 1389 nm in the infrared region (see appendix A).

From this plot it can be see that it is possible to obtain very different configurations of differential dipole potential between the two states. Particularly interesting are the so-called "magic wavelengths", for which the light shift for the two states is the same in both magnitude and sign. This condition is satisfied for three wavelength in the visible and near-infrared region, around 450 nm, 550 nm and 750 nm. The last wavelength is detuned from all the transitions, and is particularly suitable for the realization of optical lattices. A more accurate value of this wavelength is given in [76], namely 759 nm, and has been experimentally determined in ^{171}Yb and ^{174}Yb. This subject will be further discussed in section 4.3.1, where the measured valued for ^{173}Yb will be given. Performing experiments in optical lattices at the magic wavelength is advantageous, in particular in optical atomic clocks [23, 110], since operating at the magic wavelength minimizes the frequency shift and broadening of the clock transition, due to the fact that the differential light shift between the ground and metastable states is null.

Another noticeable wavelength value is the so-called "anti-magic wavelength", for which the light shift experienced by the ground and metastable state is equal in magnitude but opposite in sign. This transition is located around 1115 nm, and atoms in the ground and metastable state loaded in a lattice at this wavelength will localize in the intensity maxima and minima respectively. This spatial "dislocation"
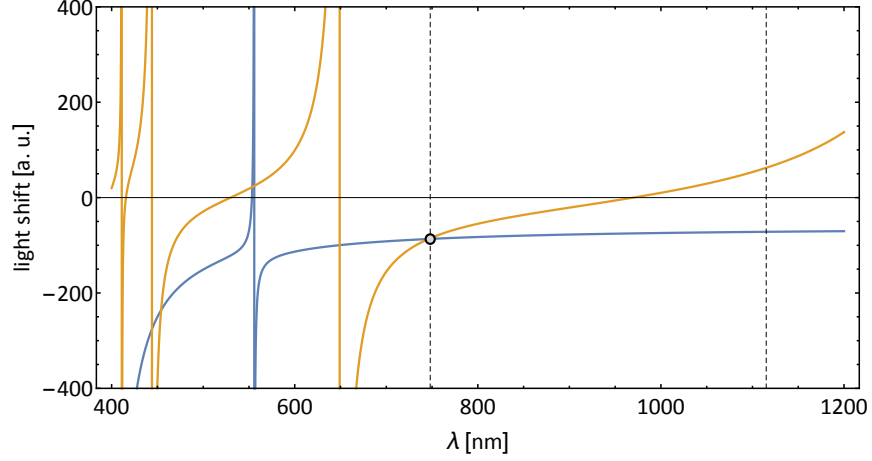
Figure 4.2: Approximate light shift for the ground state (in blue) and for the metastable state (in yellow) as a function of the wavelength in visible and near-IR region calculated using Eq. (1.12). The dashed lines mark the magic and antimagic wavelengths. The circle clearly identifies the location of the magic wavelength around 750 nm. This estimation is corrected in Ref. [76], obtaining a more accurate value of 759 nm.

of the two electronic states is particularly interesting for the implementation of artificial gauge fields [37].

Finally, it should be mentioned the case of lattice wavelengths for which the two states experience different magnitude of light shift. Atoms loaded in a lattice operating at such wavelength, would be almost free or tightly localized depending on their electronic state, realizing a state-dependent optical lattice. For example, for $\lambda = 670$ nm, near the 649 nm $^3P_0 \rightarrow ^3S_1$, the ratio between the light shift for the metastable and ground state is approximately 3.6, so a shallow $s =$ optical lattice for the $^1S_0$ would be a rather deep $s = 18$ optical lattice for atoms in the metastable state. This condition is particularly interesting for the implementation of the Kondo lattice model [35, 42], in which the mobile ground state atoms will represent the electrons and the localized metastable state atoms play the role of the magnetic impurities. Moreover, a state dependent optical lattice could represent a valuable tool to study the structure of the lowest lattice band in exotic lattice configurations, simply performing clock transition spectroscopy. Indeed, the $^3P_0$ state would show a very flat lowest lattice band, as further discussed in the Conclusions.

4.2 Clock transition spectroscopy

As mentioned before, the most important peculiarity of the clock transition is represented by its extremely narrow natural linewidth. In order to exploit it, it is necessary to minimize all the effects that may lead to a broadening of the transition. The main limitation in this sense is represented by the Doppler broadening of the transition. If probed in free space, the clock transition has a Gaussian profile with

FWHM given by:

$$\Delta \nu_D = \frac{1}{\lambda_0} \sqrt{\frac{8\ln(2) k_B T}{m}}, \tag{4.7}$$

where k_B is the Boltzmann constant, T the temperature and m the atomic mass. Due to weak dependence on T, even at very low temperatures this broadening is the dominant term, being still approximately 3 kHz at 10 nK. Standard Doppler-free techniques, like saturation spectroscopy, are not feasible since the signal is provided by only that fraction of atoms with velocity $\mathbf{v}$ slow enough to satisfy the relations $\mathbf{k} \cdot \mathbf{v} < \Gamma$, with $\mathbf{k}$ being the probe laser wavevector, resulting in an extremely low SNR. Moreover, during the spectroscopic process, the atoms acquire a recoil energy, which shifts the resonance frequency. For this reason, clock transition spectroscopy is typically performed in deep optical lattices, which freeze the motional degree of freedom allowing for Doppler-free, recoil-free spectroscopy. This is the so-called Lamb-Dicke regime, which will be discussed below.

4.2.1 The Lamb-Dicke regime

For simplicity, let us consider the case of a two-level $|g\rangle - |e\rangle$ atom, with energy levels $\hbar\omega_g$ and $\hbar\omega_e$, in a 1D harmonic potential with harmonic frequency ω_{ho}, interacting with a laser field of frequency ω_L and wavevector k. It can be shown [171] that the total Hamiltonian of the system in the frame rotating with the laser field is given by:

$$\hat{H} = -\hbar\Delta \, |e\rangle\langle e| + \hbar\omega_{ho} \left(\hat{a}^\dagger \hat{a} + \frac{1}{2} \right) + \frac{\hbar\Omega}{2} \left[e^{i\eta(\hat{a}+\hat{a}^\dagger)} \, |e\rangle\langle g| + e^{-i\eta(\hat{a}+\hat{a}^\dagger)} \, |g\rangle\langle e| \right], \tag{4.8}$$

where $\Delta = \omega_L - (\omega_e - \omega_g)$ is the detuning, Ω is the Rabi frequency for the unconfined atom at rest, $\hat{a}^\dagger$ and $\hat{a}$ are the creation and annihilation operators of the harmonic oscillator and the parameter η is known as Lamb-Dicke parameter and is defined as:

$$\eta = \frac{k x_{ho}}{\sqrt{2}} = k \sqrt{\frac{\hbar}{2m\omega_{ho}}} = \sqrt{\frac{\omega_{rec}}{\omega_{ho}}}, \tag{4.9}$$

where x_{ho} is the harmonic oscillator length and $\hbar\omega_{rec} = \hbar^2 k^2/(2m)$ is the recoil energy. The eigenstates of this Hamiltonian will be given by a linear superposition of product states of electronic and harmonic oscillator degrees of freedom:

$$\psi = \sum_{n=0}^{\infty} (c_{gn} \, |g\rangle \, |n\rangle + c_{en} \, |e\rangle \, |n\rangle). \tag{4.10}$$

Solving the Schrödinger equation for this state and the Hamiltonian (4.8), one can obtain a set of differential equations for c_{gn} and c_{en}, in which the Rabi frequency
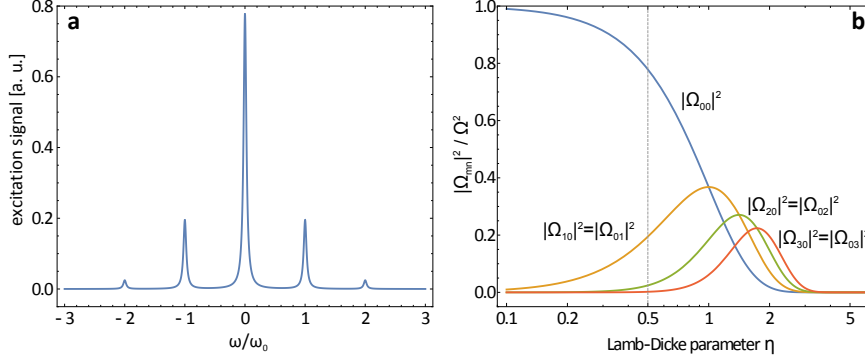
Figure 4.3: ***a.*** *Excitation spectrum for a Lamb-Dicke parameter $\eta = 0.5$. The central peak is the carrier, which corresponds to a purely electronic excitation from $|g\rangle$ to $|e\rangle$. The blue and red sidebands, at distance $l\omega_0$, correspond to the excitation and de-excitation, respectively, of l states of the harmonic oscillator in addition to the electronic excitation.* ***b.*** *Plot of the squared Rabi freqiencies $|\Omega_{mn}|^2$ as a function of the Lamd-Dicke parameter η for the lowest harmonic oscillator states ($n, m = 0, \ldots, 3$). At very high confinement ($\eta \ll 1$), substantially only the carrier is excited. For lower confinements, the sidebands start to rise, until they are comparable with the carrier. The dashed line marks the value of $\eta = 0.5$ considered for the spectrum in panel **a**.*

Ω, that couples the electronic states $|g\rangle$ and $|e\rangle$ of the atom at rest, is replaced by [171]:

$$\Omega_{mn} = \Omega \langle m| e^{i\eta(\hat{a}+\hat{a}^{\dagger})} |n\rangle . \tag{4.11}$$

This Rabi frequency not only couples the electronic states $|g\rangle$ and $|e\rangle$ at resonant frequency $\omega_0 = \omega_e - \omega_g$, but at the same time can induce $|n\rangle \rightarrow |m\rangle$ transitions between different states $|n\rangle$ and $|m\rangle$ of the harmonic oscillator at resonant frequencies $\omega_0 + \hbar(m - n)$. By expanding the exponential term in Eq. (4.11), one can find the explicit dependence of Ω_{mn} on the Lamb-Dicke parameter η [171, 172]:

$$\frac{\Omega_{mn}}{\Omega} = \begin{cases} e^{-\eta^2/2} \sqrt{\frac{n!}{m!}} \eta^{m-n} \mathcal{L}_n^{m-n}(\eta^2) & \text{if } m \geq n \\ e^{-\eta^2/2} \sqrt{\frac{m!}{n!}} \eta^{n-m} \mathcal{L}_n^{n-m}(\eta^2) & \text{if } m < n, \end{cases} \tag{4.12}$$

where $\mathcal{L}_n^{\alpha}(x)$ are the Laguerre polynomials. These Rabi frequencies correspond to a transition spectra with a purely electronic transition at frequency ω_0, namely the carrier, and a series of blue(red)-sidebands at frequency $\omega_0 + (m - n)\omega_{ho}$ from the carrier, which correspond to an excitation (de-excitation) of the harmonic oscillator states (see Fig. 4.3a). The relative amplitudes of these transitions are given by the square of the Rabi frequencies in Eq. (4.12) and depend heavily on the Lamb-Dicke parameter. In Fig. 4.3b, the transition amplitudes $|\Omega_{mn}|^2$ for the carrier and the lowest harmonic oscillator states sidebands are plotted as a function of η. It can be seen that for very high confinement, in the so-called Lamb-Dicke regime ($\eta \ll 1$),

the excitation probability is not-negligible only for the carrier and the first blue and red sidebands. In this case, if the natural linewidth of the transition Γ is much lower than ω_{ho}, the carrier and the sidebands will be individually addressable, leading to the so-called sideband-resolved regime. Furthermore, in this regime a Boltzmann-distributed atomic sample would tend to occupy the harmonic oscillator ground state, so the red-sideband amplitude will be reduced with the respect to the blue-sideband one. As the confinement ω_{ho} decreases, η increases and more sidebands appear at decreasing frequency distance between themselves, with an amplitude which becomes more and more comparable with the carrier as η grows. When the separation ω_{ho} becomes smaller the the natural linewidth Γ, carrier and sidebands are no longer resolvable, and the usual Doppler gaussian profile is recovered, if a Boltzmann thermal population of the atoms in the harmonic oscillator states is considered (see Ref. [171]).

In conclusion, operating in a deep Lamb-Dicke regime has the remarkable advantage that the carrier resonance clearly occurs at ω_0 and the sidebands at $\omega_0 \pm l\omega_{ho}$, being the recoil energy and momentum of the probe laser taken up by the confining potential. It should be noted that in typical experimental configurations, the confining potential is not an harmonic potential but an optical lattice, which shows non-flat energy bands. If the bandwidth is greater than Γ, which for a clock transition is typically limited by the larger between the laser linewidth and the Fourier broadening due to the finite interrogation time, then the excitation will be momentum selective. Considering the excitation of the carrier with a probe laser with ~ 100 Hz linewidth, this condition typically occurs employing optical lattices with depth $s \lesssim 12$. Higher lattice depths are instead necessary to probe momentum-independent sidebands.

4.2.2 Sideband-resolved spectroscopy of the clock transition

In order to perform spectroscopy of the clock transition, we load a degenerate Fermi gas of ^{173}Yb atoms in a three-dimensional deep optical lattice with typical depth of 20 to 30 E_{rec}, so that the Lamb-Dicke condition is satisfied ($0.30 \leq \eta \leq 0.33$). The optical lattice wavelength is tuned at the magic value of ^{174}Yb [173], in order to minimize the differential light shift of the clock transition, assuming that the isotope shift between ^{174}Yb and ^{173}Yb is small. A measurement of the magic wavelength for ^{173}Yb will be determined in section 4.3.1. Moreover, before the excitation pulse is shone on the atomic sample, the 1064 nm crossed dipole trap (see section 2.2.1) is switched off, so that the only trapping potential is the optical lattice.

The clock probe beam is π-polarized (see section 3.1.5) and is overlapped with the 1064 nm dipole trap beam perpendicular to the dipole trap beam (see section 2.2.1). The probe beam is angled with respect to all lattice beams, implying that a 3D lattice is mandatory to be in the Lamb-Dicke regime. The beam is collimated with 1 mm waist on the atomic sample, in order to minimize the intensity inhomogeneity that may lead to a broadening of the transition. In these preliminar experiments, only the 578 nm laser average linear drift (see section 3.1.3) is compensated via
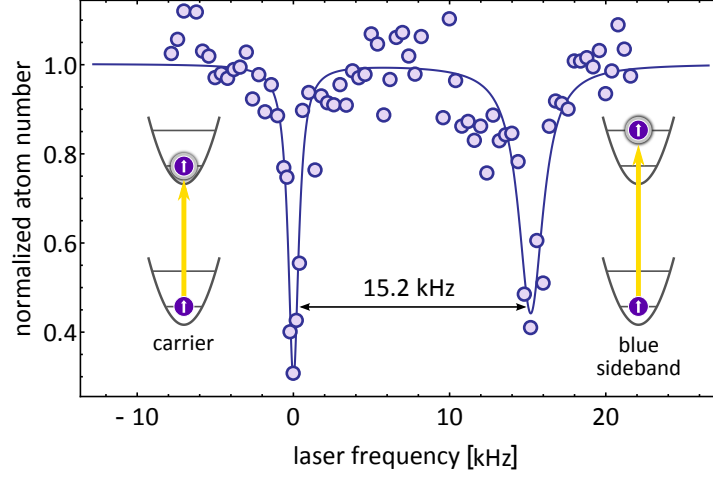
Figure 4.4: Sideband-resolved spectroscopy of a spin polarized $m_F = +5/2$ sample. The separation between the carrier and the blue-sideband is 15.2 ± 0.4 kHz, compatible with a $s \simeq 20$ lattice depth.

the feed-forward described in section 3.1.5). Due to the extremely small saturation intensity $I_s \sim 10^{-9}$ mW/cm^2 (see section 4.1), the transition linewidth is typically determined by the power broadening:

$$\Gamma_s = \Gamma\sqrt{1 + \frac{I}{I_s}} \simeq \Gamma\sqrt{\frac{I}{I_s}} \qquad (4.13)$$

where Γ is the natural linewidth (< 10 mHz) and I is the probe beam intensity. With a maximum power of the order of 10 mW on the atomic sample, it is possible to broaden the transition linewidth to a few kHz, which greatly eases the identification of the clock transition when the laser frequency is only approximately known (typically within a few tens of kHz from the atomic transition using the method described in section 3.1.3). The linewidth can then be narrowed simply by reducing the probe power, until the ultimate limit represented by the laser linewidth is reached. As already mentioned in section 3.1.5, we could observe transition with a linewidth as small as ~ 50 Hz also without the stabilization on the optical fiber link, but in this configuration the transition cannot be probed for long times (~ 5 minutes, see section 3.1.5), due to the residual drift of our laser. For applications where the spectroscopic limit is not required, we can increase the power in order to broaden the transition linewidth and operate for longer times in between subsequent laser frequency calibrations (of the order of 30 minutes to a maximum of one hour with a linewidth of ~ 150 Hz).

A typical spectrum for a spin-polarized $m_F = +5/2$ Fermi gas is reported in Fig. 4.4. The atoms are probed with 100 ms long pulses, then the remaining ground atoms are detected by absorption spectroscopy, so that the transition signature is a dip in the number of atoms. As discussed below, a 100 ms interrogation time is longer than the system coherence time (~ 30 ms, most probably limited
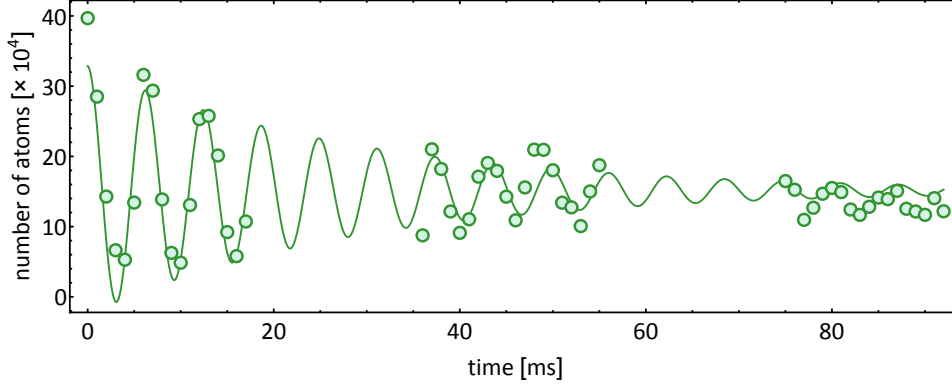
Figure 4.5: Coherent Rabi oscillation of the ground state population driven with a ultra-narrow laser intensity of ~ 2.5 mW/cm². The frequency is 160 Hz, leading to a pi-pulse time of ≃ 3 ms. The oscillation shows a damping on a timescale of 30 ms, compatible with a laser short-term linewidth of ~ 40 Hz.

by the ultranarrow laser coherence time), so the excitation is performed in the incoherent regime, in which only 50% of the ground state population is excited to the metastable state. With a probe beam power of ~ 20 μW, corresponding to an intensity of ~ 0.6 mW/cm², the carrier and the lattice blue-sideband are easily resolved. It should be noted that despite the fact that the sideband excitation probability is smaller than that of the carrier, the two features have approximately the same contrast, owing to the high saturation of the transition. We could not observe any red-sideband, indicating the that atomic sample substantially occupies only the lower lattice band. The separation between the two peaks is 15.2 ± 0.4 kHz, compatible with a $s \simeq 20$ deep lattice bandgap (15.8 kHz at $s = 20$). With such separation the carrier can be easily resolved even with a few kHz power broadening, enabling the possibility to perform fast Rabi oscillation and sub-ms π and $\pi/2$ pulses.

Coherent excitation of the clock transition

The possibility to coherently excite the $^1S_0 \rightarrow {}^3P_0$ transition is a key feature for the quantum simulation of many-body phenomena [26, 35] as well as for the implementation of quantum information schemes [28–30], since it enables the possibility to manipulate the ground and mestastable state population in a controllable way, without inducing decoherence in the atomic sample. For this reason, we also perform Rabi oscillation on the atomic samples to verify the coherent nature of the excitation process. An example of Rabi oscillation is reported in Fig. 4.5. With a probe beam intensity of ~ 2.5 mW/cm², it is possible to drive a coherent oscillation of 160 Hz for several cycles. The oscillation is damped on a timescale of ~ 30 s ($\tau^{-1} \sim 40$ Hz). This damping can be ascribed to the finite coherence time of the excitation laser, as it is compatible with the ≤ 50 Hz value estimated in section 3.1.5. The figure shows a π-pulse of ~ 3 ms, but it should be noted that the oscillation is performed with a probe beam power of 80 μW. Thanks to the high power at our disposal, this value

81

can be increased by a factor > 100, increasing the Rabi frequency by a factor > 10 (due to the well-know square root scale with the intensity [60]), thus shortening the π-pulse by an equivalent factor. A possible general constrain in this sense is represented by the sideband-resolved condition: a too high-intensity would cause the carrier and the sideband to overlap, with a consequent loss of coherence of the excitation process.

4.3 Beyond-GPS absolute frequency measurement of ^{173}Yb clock transition

While the presence of the long-term stochastic fluctuations of the ultranarrow 578 nm laser frequency (see section 3.2.3) is still acceptable for medium-precision measurements as those described in section 4.2.2, in order to perform high-precision measurements, the probe laser frequency has to be stabilized also on the long-term. As discussed in section 3.2.4, this is obtained by disciplining our 578 nm ultranarrow laser to an optical frequency reference at 1542 nm, generated at INRIM and traced to the SI second and transferred to LENS via a long-haul fiber link. By exploiting the high degree of stability of the remotely-referenced 578 nm laser, we measured the absolute frequency of the $^1S_0 \rightarrow {}^3P_0$ clock transition in ^{173}Yb with a uncertainty of 10 Hz, reaching an accuracy of 2×10^{-14} in a timescale of 10^4 s [56]. This accuracy level, which is limited by the systematic uncertainty of the experimental apparatus and not by the remote primary frequency reference, could not be achieved by stabilizing our laser on the GPS, since it only allows for an accuracy of 10^{-13} in one day of measurements [149]. This measurement represents a demonstration that optical fiber links can be exploited as primary frequency dissemination method, which features a potential outcome on a wealth of applications where achieving an ultra-high precision level is mandatory.

The advantages in terms of stability offered by referencing our ultranarrow laser to the 1542 nm optical reference appear evident in Fig. 4.6. Here, we compare two spectroscopic experiments carried out with and without the stabilization of our probe laser on the 1542 nm optical reference. Spectroscopy is performed by shining 100 ms long pulses of 578 nm light with an intensity of $\sim 10~\mu$W/cm^2 on a spin-polarized ^{173}Yb Fermi gas at $T \simeq 0.2 T_F$ in a 3D $s = 30$ optical lattice at the magic wavelength. In particular, the transition spectra in Fig. 4.6a have been acquired with the 578 nm laser simply locked to the ULE cavity, without any drift compensation. Nine different datasets have been acquired in about 3 hours and 30 minutes. Each scan takes typically 20 minutes, because of the characteristics of our setup, which is optimized for experiments with ultracold quantum gases lasting more than 30 s per run. In the entire duration of the experiment, the transition frequency shifted by approximately 1300 Hz. Moreover, despite the fact that the power broadening (~ 50 Hz) did not change during the whole experiment, the different lines show different widths (and/or shapes), varying between 30 and 100 Hz. This is caused by the relative direction of frequency scan and laser drift. If the scan direction follows
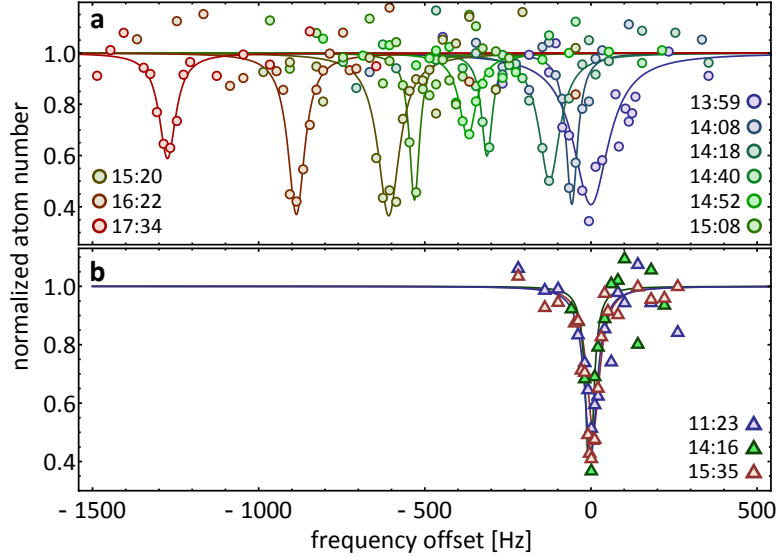
*Figure 4.6: Long-time spectroscopy of the clock transition performed with the 578 nm laser **a** not referenced and **b**. referenced to the 1542 nm optical frequency reference. In panel **a**. the different spectra show different shapes and widths depending on the relative scan and laser drift direction. In **b**. instead no fluctuations are visible and all the spectra linewidths are ∼ 50 Hz. The horizontal axis of both figures have been rescaled so that the zero frequency corresponds to the center of the earliest resonance.*

the drift, the resulting linewidth is larger, if instead the scan direction is opposite to the drift the lineshape features an "effective" reduced width. The spectra of Fig. 4.6b have instead been acquired after having stabilized our ultranarrow 578 nm laser to the 1542 nm frequency reference over similar timescales. The data points are averaged over 2-3 acquisitions. Here, no appreciable drift arises and the residual fluctuations are well below the observed ≤ 50 Hz linewidth. It should be noted that performing the same measurement with a lower power, the linewidth can be narrowed below 30 Hz but with a reduced SNR: at resonance, the ground state population decreases to about 70% of the out-of-resonance value instead of the 50% value expected in the incoherent excitation regime. This is an indication that the linewidth measured in section 3.1.5 is ultimately limited by the laser stability over the 100 ms pulse timescale. The remote long-term stabilization of the interrogation laser represents a keynote result for the vast majority of experimental setups that require a high degree of stability: the local sample can be employed as a "tool", rather than as a frequency reference (as happening, in optical clocks), and in turn the local laser can be used as a coherent manipulation device for the sample itself, rather than as a probe.

This high degree of stability and accuracy is exploited to measure the absolute frequency of the clock transition in ^{173}Yb improving by two orders of magnitude the literature value reported in Ref. [165]. Since ^{173}Yb is a fermionic isotope with
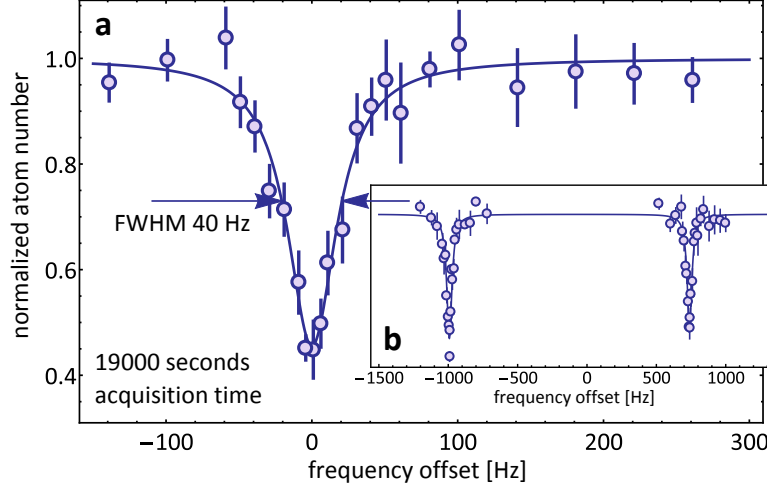
Figure 4.7: **a.** *Clock transition spectra of the* $m_F = +5/2$ *resonance acquired over* 19000 *s. The FWHM is* 40 *Hz. The horizontal axis has been centered at the resonance position.* **b.** *Full spectra of the two* $m_F = \pm 5/2$ *nuclear spin components. The zero frequency on the horizotal axis corresponds to a known arbitrary frequency of the probe laser.*

non-zero nuclear spin, the transition frequency depends on the nuclear spin state of the atomic sample at non-zero magnetic field. For this reason, in the following measurements we cancel the linear Zeeman shift of the clock transition by alternatively probing spin-polarized samples with opposite nuclear spin $m_F = \pm 5/2$ at every experimental cycle. The obtained spectra feature two resonances, corresponding to the two opposite nuclear spin states and are fitted with a double Lorentzian curve with centers $\nu_{-5/2}$ and $\nu_{+5/2}$. The transition center is then determined as $\nu_{fit} = (\nu_{-5/2} + \nu_{+5/2})/2$.

In order to determine the absolute frequency of the clock transition, we collected 6 measurements spread over a period of three months, each consisting of a complete scan of the transition, with typical linewidths between 40 Hz and 100 Hz FWHM (see Fig. 4.7a). All the measurements have been carried out with a bias magnetic field of 3.03(3) G, corresponding to a splitting of approximately 1700 Hz, which is high enough to clearly resolve the resonances relative to the two spin components (see Fig.4.7b). The lattice laser is tuned at the magic wavelength, and monitored for the whole acquisition time with a residual uncertainty of 2 GHz (see section 4.3.1). In these measurements we load in the 3D lattice spin-polarized Fermi gas with $\sim 2 \times 10^4$ atoms and a temperature of $T \simeq 0.2 T_F$, resulting in a negligible population of the lattice excited band. In this regime, only one atom per lattice site is present due to the Pauli exclusion principle, completely inhibiting the interaction-induced shift. The atoms are interrogated with 100 ms long pulses of π-polarized light at 578 nm. The runs had different duration, from 2000 s to 19000 s, for a total measurement time of 40000 s. The measured frequency of the $^1S_0 \rightarrow {}^3P_0$ clock transition for ^{173}Yb is:

$$\nu_{clock}^{173} = 518\,294\,576\,845\,268 \pm 10 \text{ Hz}.$$

This measurement improves the uncertainty of a previous direct measurement [165] by a factor 400, with an agreement between the two values. Consequently, combined with other previous measurements [3], we improve the knowledge of the isotope shifts of the $^{1}S_0 \to {}^{3}P_0$ transition, which are:

$$
\begin{aligned}
\nu_{clock}^{171} - \nu_{clock}^{173} &= 1\,259\,745\,597 \pm 10 \text{ Hz,} \\
\nu_{clock}^{173} - \nu_{clock}^{174} &= 551\,536\,050 \pm 10 \text{ Hz.}
\end{aligned}
$$

The total measurement uncertainty is a combination of statistical (Type A) and systematic (Type B) uncertainties.

The Type A uncertainty for each measurement is the quadratic sum of different contributions. The first is the error of the Lorentzian fit, which is given by $\sigma\nu_{fit} = (\sqrt{\sigma_{\nu-5/2}^2 + \sigma_{\nu+5/2}^2})/2$, where $\sigma_{\nu_{\pm 5/2}}$ are the fit errors on the peak centers. A second contribution is the error related to the instability of the frequency combs at INRIM and LENS (see section 3.2.2). Another contribution is represented by the instability of the Cesium fountain on which the maser-stabilized 1542 nm optical reference is referenced to. The total Type A uncertainty is given by the root-squared-sum of these four contributions and is different for each measurement, depending on the specific run acquisition time. For the final measurement, we consider a composed uncertainty of 2 Hz (4×10^{-15} fractional frequency uncertainty), where we considered a Student statistic for the data and a confidence level of 90%, due to the limited number of measurements.

The Type B uncertainty considers different sources: the Cs fountain accuracy and the phase-slips of the optical link (see section 3.2.2), which are related to the metrological chain, and the physical effects in the end-user laboratory at LENS which influence the clock transition frequency. The accuracy of the Cs fountain is 2×10^{-16} [174], corresponding to 0.1 Hz at 578 nm, whilst the contribution by the phase-slips on the fiber link was < 0.1 Hz (1.5×10^{-16}), measured by redundant beatnote tracking (see section 3.2.2). We then consider several physical effects in the experimental setup at LENS which influence the clock transition frequency. In particular two of them, the quadratic Zeeman effect and lattice "magicness", are discussed in more detail in the subsequent sections (4.3.2 and 4.3.1 respectively). The quadratic Zeeman effect yields a bias of $-0.59(3)$ Hz, while the lattice frequency introduces an uncertainty of 8 Hz. In addition to these, other effects are also considered. The blackbody radiation is accounted for by using the sensitivity reported in Ref. [175]. The atoms are probed in the glass science cell (see section 2.1.1) at thermal equilibrium with room temperature, resulting in a frequency bias of $-1.24(5)$ Hz for a room temperature of 298(3) K. Moreover, the SI second is defined at the geoid gravity potential, hence the frequency reference disseminated from INRIM is corrected for the gravitational redshift [176]. The

Table 4.1: Uncertainty budget of the ^{173}Yb $^1S_0 \rightarrow {}^3P_0$ transition.

Contribution	Bias (Hz)	Uncertainty (Hz)
Lorentzian fit (*)	-	$0.8 - 5$
Cs fountain statistical (*)	-	$0.9 - 2$
Comb INRIM statistical (*)	-	$0.4 - 1.2$
Comb LENS statistical (*)	-	$1 - 3$
Total Type A (**)	-	**2**
Quadratic Zeeman	-0.59	0.03
Lattice Stark	-	8
Blackbody radiation	-1.24	0.05
Probe laser light shift	-	0.00015
Gravitation redshift	2.277	0.005
Total end-user Type B	**0.5**	**8**
Cs fountain standard accuracy	-	0.1
Fiber link phase-slips (†)	-	0.1-5
Total Type B (†)	**0.5**	**9**
Total (†)	**0.5**	**10**

(*) Depending of the experimental run.
(**) Composed uncertainty with Student 90% confidence level.
(†) In some measurements the phase-slips uncertainty was 5 Hz for technical problems; in the total type B we considered the worst case scenario.

orthometric height on the geoid of the LENS laboratory was measured during a dedicated geodetic campaign[2], and the resulting gravitational redshift is $4.81(1) \times 10^{-15}$ or 2.277(5) Hz. Finally, the probe light induces a negligible light shift on the transition: according to the sensitivity of 15 mHz/(mW/cm^2) reported in Ref. [163] and to the laser intensity of 10 μWcm^2, the light shift is 0.15 mHz, kept as uncertainty contribution.

The uncertainty budget, together with the systematic biases, are reported in Table 4.1. In the table, all the contributions coming from physical effects in the LENS laboratory have been summed up in a single line, in order to clearly distinguish it from the uncertainty introduced by the metrological chain. It is clear that the final uncertainty of 10 Hz is by far dominated by the lattice AC-Stark shift, with an uncertainty of 8 Hz. The final accuracy of the measurement is 2×10^{-14} over a timescale of 10^4 s, exceeding by a factor 20 the standard GPS accuracy over the same timescale [149]. It should be noted that this measurement is limited by the systematic uncertainty of the end-user laboratory. The inherent uncertainty of the dissemination channel is limited to 2 Hz, corresponding to a relative uncertainty of
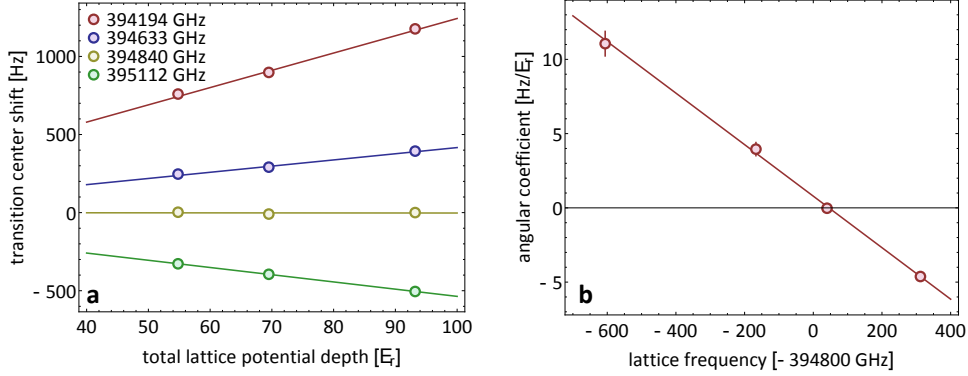
Figure 4.8: **a.** *Shift of the clock transition center as a function of the total lattice potential depth $V_0 = V_0^x + V_0^y + V_0^z$ for different optical lattice laser frequencies. All the points have been offset by the same amount to have zero shift at the magic wavelength.* **b.** *Slopes of the lines of panel* **a** *as a function of the lattice frequency. The zero-crossing represents the magic wavelength, corresponding to 759.27(1) nm (see text for details).*

4×10^{-15}. Noticeably, this beyond-GPS accuracy is achieved in timescales as short as few hours and can be reliably reproduced over time periods of several months in a non-metrological end-user laboratory.

4.3.1 Magic wavelength determination

As already mentioned in section 4.1.2, confining the atoms in a lattice at the magic wavelength is crucial to maximize the measurement accuracy, since the differential light shift induced by the trapping potential on the two involved levels is null at the leading order. However, the lattice light introduces also other systematic shifts due to higher-order AC-Stark shifts, like the hyperpolarizability [173, 177] and, in fermionic isotopes as ^{173}Yb, the vector and tensor Stark shifts [110, 164, 166]. While an accurate determination of these shifts is a fundamental concern in state-of-the-art lattice clocks [110], their contribution is typically sub-Hz if the lattice light is linearly polarized, as in our setup. As will be shown below, this value is beyond the level of accuracy that can be reached in our experimental setup, so we will consider these shifts negligible as long as the lattice laser operates at the magic wavelength.

The magic wavelength has been previously determined with 10^{-7} precision in optical lattice clock setups for ^{174}Yb [170, 173] and ^{171}Yb [164], with values $\lambda_m = 759.3537$ nm and $\lambda_m = 759.3559$ nm respectively. Also the sensitivity of differential light shift in the vicinity of the magic wavelength has been measured, obtaining for both isotopes $d\alpha/d\nu_{magic} = -22(2)$ mHz/(GHz·E_r), where E_r is the lattice recoil energy. In order to determine the ^{173}Yb magic wavelength, we follow the approach of Refs. [170, 173] and measure the shift of the transition center for different values of lattice depths and different lattice frequencies, stabilizing the 578 nm laser on the SI traced 1542 nm remote optical reference. The measurements

are performed at a fixed value of magnetic field $B \simeq 3$ G. The lattice frequency is measured with a wavelength meter (*Coherent WaveMaster*) with ~ 2 GHz accuracy[3] and the lattice depths $V_0^{x,y,z}$ along the directions $\hat{x}, \hat{y}, \hat{z}$ are measured by means of lattice amplitude modulation technique (see section 1.1.2). Fig. 4.8a reports the clock transition frequency shift as a function of the total lattice potential depth $V_0 = V_0^x + V_0^y + V_0^z$ in units of recoil energy E_r for four different values of lattice frequency (in four different colors). The three points of each lattice frequency are fitted with a linear model, and the four slopes are reported in Fig. 4.8b as a function of the lattice frequency. A weighted linear fit to the data determines the magic wavelength frequency as the zero-crossing of the curve, namely 394 845(5) GHz, corresponding to 759.27(1) nm. The slope determines instead the sensitivity of the differential light shift that is given by $-17(1)$ mHz/(GHz E_r). With a total lattice potential amplitude V_0 of 90 E_r, corresponding to a lattice depth of 30 E_r along the three directions, and the magic frequency uncertainty of 5 GHz, the lattice light yields a systematic uncertainty of ~ 8 Hz.

The values of the magic wavelength and of the differential light shift sensitivity are slightly different than those measured for ^{174}Yb and ^{171}Yb. This may be caused by the hyperfine interaction with different transition coupling strengths; further investigations and additional more accurate measurement are required in order to confirm and understand the origin of these differences. In any case, with our measurement we found a value of lattice wavelength for which the transition frequency do not depend on the lattice depth within ~ 10 Hz uncertainty, indicating a minimum of the differential light shift sensitivity.

4.3.2 Quadratic Zeeman effect

An effective method to cancel the magnetic linear shift of the clock transition is to measure the average frequency between two opposite nuclear spin states $\pm m_F$. This requires the application of a bias magnetic field to resolve the sublevels, giving rise to a second order Zeeman shift $\Delta_B^{(2)}$ that have to be taken into account. This shift arises from the coupling between fine-structure levels mediated by the Zeeman Hamiltonian [166] and is proportional to the square of the magnetic field:

$$\Delta_B^{(2)} = \beta B^2. \tag{4.14}$$

In order to determine the value of the parameter β, we measure the clock transition center frequency for different values of magnetic field, operating the optical lattice at the magic wavelength. For each measurement, the values of the magnetic field is calculated from the separation between the $\pm 5/2$ peaks and considering a linear Zeeman shift of $113 \times m_F$ Hz/G (see section 4.1). The results of this measurement are reported in Fig. 4.9a, in which the points are fitted with a quadratic curve. From the fit we obtain $\beta = -0.064(2)$ Hz/G^2, comparable with the values

---

[3]The wavelength meter accuracy was estimated by repeatedly measuring the ULE-locked 578 nm laser referenced to the optical fiber link.
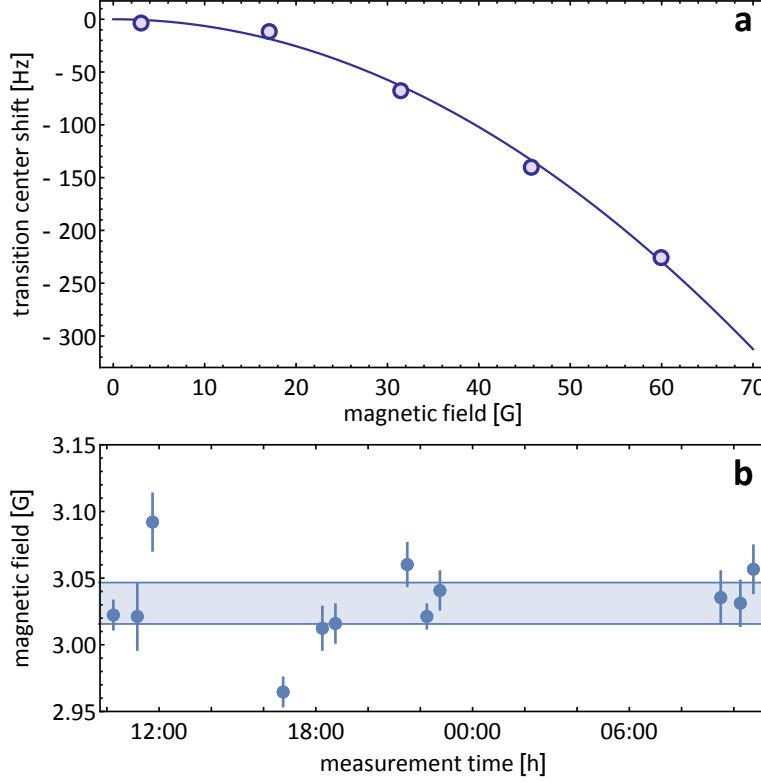
Figure 4.9: ***a.*** *Measurement of the quadratic Zeeman shift. The shift of the transition center is measured for increasing values of the magnetic field, which is determined from the separation between the $m_F \pm 5/2$ resonances. The points have been offset to have zero shift at $B = 0$. The value of the parameter $\beta = -0.064(2)$ Hz/G^2 is determined with a quadratic fit to the points.* ***b.*** *Magnetic field values for a fixed coils current determined from the separation of the $m_F = \pm 5/2$ resonances. The shaded area indicates the average and standard deviation of the points.*

$\beta = -0.07(1)$ Hz/G^2 and $\beta = -0.061(1)$ Hz/G^2 measured respectively for ^{171}Yb [164] and ^{174}Yb [163].

In order to determine the bias and the uncertainty introduced by the bias magnetic field, we precisely measure it from the distance between the $m_F = \pm 5/2$ peaks at the value of coil current used for the measurements in section 4.3.1. The measurement of the absolute frequency is then performed at the same value of coil current. Also in this case we use a linear Zeeman shift of $113 \times m_F$ Hz/G. The measured values of magnetic field are represented by the circles in Fig. 4.9b. The shaded area indicates the average and standard deviation of the data. Indeed, by averaging the data, we determine the value of magnetic field corresponding to the specific current value, namely $B = 3.03$, which leads to a frequency bias of 0.59 Hz in the measurement. The magnetic field stability is determined as the standard deviation of the data and is $\sigma_B = 0.03$ G. With this values it is possible to determine the systematic uncertainty due to the quadratic Zeeman shift, which

is given by $\sigma_{\Delta_B^{(2)}} = B^2 \sigma_\beta + 2B\beta\sigma_B = 0.03$ Hz.

Chapter 5

Two-orbital spin-exchange interactions

In this chapter we review the emergence of interorbital spin-exchange interactions between ultracold two-electron atoms in the two lowest electronic states. This kind of interaction represents one of the elementary building blocks of orbital quantum magnetism and is at the base of many strongly correlated quantum phenomena in condensed matter, ranging from heavy-Fermi behavior [36, 43, 44], to Kondo effect [35, 42] to magnetic ordering [45, 46].

Here, we present how spin-exchange interaction arises from the coupling of atoms in different electronic (meta)stable states and how this interaction has been experimentally revealed and characterized in ^{173}Yb atoms, paving the way towards the realization of orbital magnetism in atomic systems. In particular we directly measured the spin-exchange interaction by observing coherent oscillation driven by the interorbital spin exchange [41]. In the last years, similar coherent spin-changing dynamics have been observed in ground state atomic systems, arising from small differences between the scattering length values in different collisional channels in alkali atoms [89–92], or from second-order tunneling in an optical lattice [19]. In the case of ^{173}Yb, not only this coherent coupling is remarkably strong in a 3D optical lattice, giving rise to very fast oscillations, but it also entangles two stable internal degrees of freedom of the atom [178], the nuclear spin and stable electronic states, which can be independently and coherently manipulated, opening new realistic possibilities for both quantum information processing and quantum simulation.

5.1 Two-body interorbital interactions

In this section we see how the signature of the two-orbital interaction can be retrieved by performing spectroscopic experiments on a two-component Fermi gas in a three-dimensional optical lattice. We first detail a simple theoretical model which describes how a spin-exchange interaction arises in a pair of two-orbital

atoms, and how the energy levels are modified by the presence of a magnetic field. We then focus on the experimental spectrum show how the different visible peaks, can be attributed to the different interaction processes described by the model.

5.1.1 Direct and exchange interaction

Let us start from the situation of two interacting atoms in a potential well and in two different nuclear spin states $|\uparrow\rangle$ and $|\downarrow\rangle$, where the arrows are placeholders for two arbitrary nuclear spin states. Let us introduce the possibility to excite the atoms in the metastable $^3P_0$ state with π-polarized clock laser light in order to conserve the nuclear spin during the optical excitation. Let us also assume that the atoms are characterized by the same spatial wavefunction $\phi(\mathbf{r})$. Imposing a global anti-symmetrization of the wavefunction, the states that form the basis of the Hilbert space are the following:

$$
\begin{aligned}
\left|\psi_{gg}\right\rangle &= |gg\rangle \otimes |s\rangle \otimes \phi(\mathbf{r}_1)\phi(\mathbf{r}_2), \\
\left|\psi_{eg}\right\rangle_s &= \frac{|eg\rangle + |ge\rangle}{\sqrt{2}} \otimes |s\rangle \otimes \phi(\mathbf{r}_1)\phi(\mathbf{r}_2), \\
\left|\psi_{eg}\right\rangle_t &= \frac{|eg\rangle - |ge\rangle}{\sqrt{2}} \otimes |t\rangle \otimes \phi(\mathbf{r}_1)\phi(\mathbf{r}_2), \\
\left|\psi_{gg}\right\rangle &= |ee\rangle \otimes |s\rangle \otimes \phi(\mathbf{r}_1)\phi(\mathbf{r}_2),
\end{aligned}
\tag{5.1}
$$

where $|g\rangle$ and $|e\rangle$ denote an atom in the ground and excited (metastable) orbital state respectively and $|t\rangle$ and $|s\rangle$ are the symmetric (triplet) and anti-symmetric (singlet) two-particle nuclear spin states:

$$
\begin{aligned}
|s\rangle &= \frac{|\uparrow\downarrow\rangle - |\downarrow\uparrow\rangle}{\sqrt{2}}, \\
|t\rangle &= \frac{|\uparrow\downarrow\rangle + |\downarrow\uparrow\rangle}{\sqrt{2}}.
\end{aligned}
\tag{5.2}
$$

Omitting the radial part, let us now focus the attention on the states involving atoms in different electronic orbitals:

$$
\begin{aligned}
|eg^+\rangle &\equiv |s\rangle\frac{|eg\rangle + |ge\rangle}{\sqrt{2}} = \frac{1}{2}\left[\,|e\uparrow\rangle|g\downarrow\rangle - |g\downarrow\rangle|e\uparrow\rangle + |g\uparrow\rangle|e\downarrow\rangle - |e\downarrow\rangle|g\uparrow\rangle\,\right], \\
|eg^-\rangle &\equiv |t\rangle\frac{|eg\rangle - |ge\rangle}{\sqrt{2}} = \frac{1}{2}\left[\,|e\uparrow\rangle|g\downarrow\rangle - |g\downarrow\rangle|e\uparrow\rangle - |g\uparrow\rangle|e\downarrow\rangle + |e\downarrow\rangle|g\uparrow\rangle\,\right],
\end{aligned}
\tag{5.3}
$$

where, for simplicity, we have omitted the tensor product symbol. The explicit expression of these two states in quite cumbersome, so it is useful to find a more compact notation for $|eg^\pm\rangle$ states. Let us first introduce the following anti-symmetrized two particle states:

$$\begin{aligned}
|e\uparrow,g\downarrow\rangle &= \frac{|e\uparrow\rangle|g\downarrow\rangle - |g\downarrow\rangle|e\uparrow\rangle}{\sqrt{2}}, \\
|g\uparrow,e\downarrow\rangle &= \frac{|g\uparrow\rangle|e\downarrow\rangle - |e\downarrow\rangle|g\uparrow\rangle}{\sqrt{2}},
\end{aligned} \tag{5.4}$$

in which a defined nuclear spin is associated to a specific orbital state. It is then straightforward to see that the $|eg^{\pm}\rangle$ states can be rewritten in term of these two new states:

$$|eg^{\pm}\rangle = \frac{1}{\sqrt{2}}\left[|e\uparrow,g\downarrow\rangle \pm |g\uparrow,e\downarrow\rangle\right], \tag{5.5}$$

This formulation is useful in order to derive a formal expression and understand the effect of the two-body interaction potential for the states of Eq. (5.5). The interaction potential in the four states of Eq. (5.1) can be written in terms of pseudo-potential (sec. 1.2.1) and projector operators as [87]:

$$\hat{V}(\mathbf{r}_1 - \mathbf{r}_2) = \left(g_{gg}\hat{P}_{gg} + g_{eg^+}\hat{P}_{eg^+} + g_{eg^-}\hat{P}_{eg^-} + g_{ee}\hat{P}_{ee}\right)\delta(\mathbf{r}_1 - \mathbf{r}_2), \tag{5.6}$$

where $g_X = 4\pi\hbar^2 a_X/\mu$, with μ being the reduced mass of the two particles and a_X and $\hat{P}_X$ the scattering length and the projector, respectively, on the gg, eg^+, eg^- and ee channels. In particular, it is useful to write down the projector on the $|eg^{\pm}\rangle$ states:

$$\begin{aligned}
\hat{P}_{eg^{\pm}} &= |eg^{\pm}\rangle\langle eg^{\pm}| = \\
&= \left(|e\uparrow,g\downarrow\rangle\langle e\uparrow,g\downarrow| + |g\uparrow,e\downarrow\rangle\langle g\uparrow,e\downarrow|\right) \pm \\
&\quad \left(|e\uparrow,g\downarrow\rangle\langle g\uparrow,e\downarrow| + |g\uparrow,e\downarrow\rangle\langle e\uparrow,g\downarrow|\right).
\end{aligned} \tag{5.7}$$

In this expression it is possible to distinguish two different components of the projection operator. The first two terms are related to processes in which the spin of the ground state atom and of the excited state atom are not changed in the collision, and is called *direct* interaction. The last two terms are instead related to processes in which the interaction between a ground state and an excited state atom involves a spin-flip. This second part is called *exchange* interaction. Using Eq. (5.7), the interaction potentials for the $|eg^{\pm}\rangle$ states can then be written as:

$$\begin{aligned}
\hat{V}_{eg} &= g_0\delta(\mathbf{r}_1 - \mathbf{r}_2)\left[a_{eg}^+\hat{P}_{eg^+} + a_{eg}^-\hat{P}_{eg^-}\right] = \\
&= g_0\left[\left(\frac{a_{eg}^+ + a_{eg}^-}{2}\right)\hat{\mathcal{V}} + \left(\frac{a_{eg}^+ - a_{eg}^-}{2}\right)\hat{\mathcal{V}}_{ex}\right]\delta(\mathbf{r}_1 - \mathbf{r}_2), \tag{5.8}
\end{aligned}$$

where $g_0 = 4\pi\hbar^2/\mu$ and in which $\hat{\mathcal{V}} = |e\uparrow,g\downarrow\rangle\langle e\uparrow,g\downarrow| + |g\uparrow,e\downarrow\rangle\langle g\uparrow,e\downarrow|$ is the direct interaction term and $\hat{\mathcal{V}}_{ex} = |e\uparrow,g\downarrow\rangle\langle g\uparrow,e\downarrow| + |g\uparrow,e\downarrow\rangle\langle e\uparrow,g\downarrow|$ is the
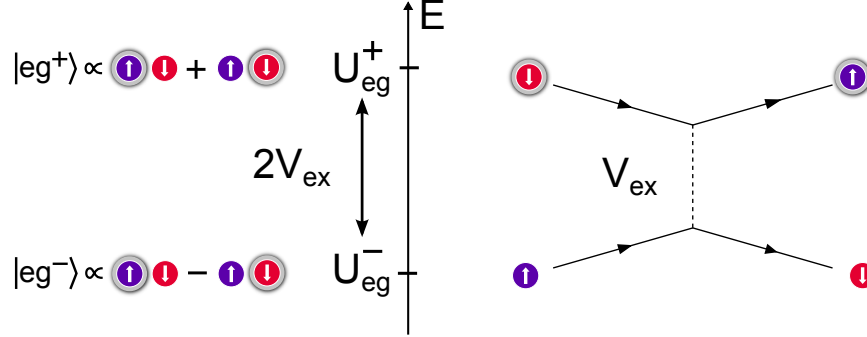
Figure 5.1: The spin-singlet $|eg^+\rangle$ and spin-triplet $|eg^-\rangle$ states have different interaction energies $U_{eg}^\pm$, that give rise to a non-zero interorbital spin-exchange interaction energy V_{ex}. Due to this finite spin-exchange energy, a pair of atoms with a defined nuclear spin linked to a specific electronic orbital will exchange their spin in a collision. Arrows and circles colors (blue and red) label the nuclear spin while the gray shaded area around the circle labels the excited electronic state.

exchange interaction term. The interaction in the $|eg^\pm\rangle$ channels is simply given by:

$$U_{eg}^\pm = \phi^*(\mathbf{r}_1)\phi^*(\mathbf{r}_2) \otimes \langle eg^\pm| V_{eg} |eg^\pm\rangle \otimes \phi(\mathbf{r}_1)\phi(\mathbf{r}_2) = g_0 a_{eg^\pm} \int d\mathbf{r}\, \phi(\mathbf{r})^4. \quad (5.9)$$

Due to the presence of the exchange term in Eq. 5.8), V_{eg} also describes interaction mechanisms in which the two particles exchange their spin. This exchange process takes place if the initial state is not an eigenstate of the system $|eg^\pm\rangle$, but a state with definite spin and orbital states, e.g. as $|g\uparrow, e\downarrow\rangle$ (see Fig. 5.1), and is described by an interaction energy of the form:

$$V_{ex} = \langle e\uparrow, g\downarrow| V_{eg} |g\uparrow, e\downarrow\rangle = g_0 \frac{a_{eg}^+ - a_{eg}^-}{2} \int d\mathbf{r}\, \phi(\mathbf{r})^4, \quad (5.10)$$

where we have omitted the radial part in the left-hand side of the equation. From this formula it is clear that this exchange process may happen only if the scattering lengths of the $|eg^+\rangle$ and $|eg^-\rangle$ states are different, otherwise no spin-exchange occurs. This condition is similar to the condition on spin-changing collisions [87, 92], in which two atoms with initial spin component m_{f_1} and m_{f_2} could change to new spin components m'_{f_1} and m'_{f_2}, with $m_{f_1} + m_{f_2} = m'_{f_1} + m'_{f_2}$, only if the scattering lengths associated to the two different pairs are different. Using Eqs. (5.9) and (5.10), the interaction energies $U_{eg}^\pm$ can be easily related to the exchange energy V_{ex}, as well as to the direct interaction V with a similar argument, obtaining (see Fig. 5.1):

$$V = \frac{U_{eg}^+ + U_{eg}^-}{2},$$

$$V_{\text{ex}} = \frac{U_{eg}^+ - U_{eg}^-}{2}. \tag{5.11}$$

These results can be generalized to the case of a two nuclear spin component degenerate Fermi gas in an optical lattice at the magic wavelength, for which the trapping potential in the same for atoms in the ground state g and the metastable state e. Since $J = 0$ for both g and e, the nuclear spin I is completely decoupled and an arbitrary couple between the $2I + 1$ nuclear spin components can be chosen (see section 1.2.2). Let us assume also in this case that all the atoms are in the lowest lattice band. We introduce three quantum numbers for the atoms: α, indicating the orbital degree of freedom (g or e), m indicating the nuclear spin projection, and j indicating the lattice site. In the second quantization formulation, the system can be described by a field operator given by:

$$\hat{\Psi}_{\alpha m}^\dagger(\mathbf{r}) = \sum_j w(\mathbf{r} - \mathbf{r}_j)\hat{a}_{j\alpha m}^\dagger, \tag{5.12}$$

where $w(\mathbf{r} - \mathbf{r}_j)$ is the Wannier function [11] centered in the lattice site j and $\hat{a}_{j\alpha m}$ is the creation operator of an atom with spin component m and electronic state α in lattice site j. Using an interaction of the form (5.6) it is possible to obtain the total Hamiltonian of the system operating the substitution $|g \uparrow, e \downarrow\rangle \rightarrow \hat{\Psi}_{g\uparrow}^\dagger(\mathbf{r})\hat{\Psi}_{e\downarrow}^\dagger(\mathbf{r}')$ and $|e \uparrow, g \downarrow\rangle \rightarrow \hat{\Psi}_{e\uparrow}^\dagger(\mathbf{r})\hat{\Psi}_{g\downarrow}^\dagger(\mathbf{r}')$, giving the following result[26]:

$$
\begin{aligned}
\hat{H} &= J \sum_{\alpha m \langle ij \rangle} (\hat{a}_{i\alpha m}^\dagger \hat{a}_{j\alpha m} + \text{h.c.}) + \sum_{\alpha, i} \frac{U_{\alpha\alpha}}{2} \hat{n}_{i\alpha}(\hat{n}_{i\alpha} - 1) \\
&+ V \sum_i \hat{n}_{ig}\hat{n}_{ie} + V_{\text{ex}} \sum_{m,m'} \hat{a}_{igm}^\dagger \hat{a}_{iem'}^\dagger \hat{a}_{igm'} \hat{a}_{iem},
\end{aligned} \tag{5.13}
$$

where $J = \int d\mathbf{r} \, w^*(\mathbf{r})(-\hbar^2\nabla^2/2\text{m}) \, w(\mathbf{r} + \mathbf{R})$ is the tunneling energy between nearest neighbors, which is the same for g and e due to the magic wavelength lattice, and $U_{\alpha\alpha} = g_{\alpha\alpha} \int d\mathbf{r}|w(\mathbf{r})|^4$ and $U_{eg}^\pm = g_{eg}^\pm \int d\mathbf{r}|w(\mathbf{r})|^4$ denote the on-site interaction energies.

As mentioned earlier, having $J = 0$, also the metastable state $|e\rangle = \left|{}^3P_0\right\rangle$ is decoupled from the nuclear spin and therefore its collisional properties do not depend on the nuclear spin state. For this reason, also interorbital $g - e$ interactions, as well as $e - e$ interactions within atoms in the $|e\rangle$ state, are expected to exhibit SU(N) symmetry, meaning that also the scattering lengths $a_{eg}^\pm$ and a_{ee} do not depend on the nuclear spin state. For this reason, the two-component formulation used so far can be easily generalized to the multi-component case $-5/2 \leq m \leq +5/2$ [26]. The Hamiltonian (5.13), which is the generalization to the case of two

95

electronic states of the Hamiltonian (1.46), will be invariant under transformations of the kind:

$$\hat{S}_n^m = \sum_j \hat{S}_n^m(j) = \sum_{j,\alpha} \hat{S}_n^m(j,\alpha) = \sum_{j,\alpha} \hat{a}_{j\alpha n}^\dagger \hat{a}_{j\alpha m}, \tag{5.14}$$

which are the generalization of the operators 1.47, obtained summing also over the two electronic states $\alpha = g, e$, which replace a particle with spin m with a particle with spin n. The SU(N) symmetry represents a very interesting features of this system, which offers interesting opportunities for quantum simulation of orbital magnetism. Nevertheless, it should be noted that, since the hyperfine interaction slightly mixes the $^3P_0$ with the $^3P_1$ state, the angular momentum decoupling is slightly broken [166]. This leads to a violation of the SU(N) symmetry and to a nuclear-spin-dependent variation δa of the scattering lengths, which is theoretically estimated to be $\delta a/a \sim 10^{-3}$ in ^{87}Sr [26]. The experimental investigation of this violation is reported in section 5.2.5.

5.1.2 Laser excitation of a two-particle state

In the previous section we considered the presence of a π-polarized laser field capable to promote atoms to the excited state without changing their nuclear spin. Here we want to study the interaction of the laser field with the two-particle system. Let us consider the case of two ground state atoms in a lattice site, with no external magnetic field so that the states of the Zeeman manifold are degenerate. Let us also suppose that the two atoms occupy only two spin state $|\uparrow\rangle$ and $|\downarrow\rangle$ and that the laser light is π-polarized. Following the treatment of Ref. [179], the Hamiltonian describing the coupling of the laser with the two atoms is given by:

$$\hat{H}_L = \hat{H}_1 + \hat{H}_2, \tag{5.15}$$

where $\hat{H}_1$ and $\hat{H}_2$ are the laser-atom Hamiltonians of the two atoms that are given by the sum of the transition processes that may occur for each spin state:

$$\hat{H}_i = \frac{\hbar}{2}\Omega \left(S_{i\uparrow} |e_{i\uparrow}\rangle \langle g_{i\uparrow}| + S_{i\downarrow} |e_{i\downarrow}\rangle \langle g_{i\downarrow}| \right) + h.c. \tag{5.16}$$

where $\Omega = d_{eg}E/\hbar$ (d_{eg} being the dipole matrix element and E the laser electric field), is the Rabi frequency and $S_{i\uparrow\downarrow}$ are coefficients that include the angular momentum contribution to the matrix element and the Clebsch-Gordan coefficients of the transition and [60]. We remind here that Clebsch-Gordan of the $F = 5/2$ $^1S_0 \rightarrow {}^3P_0$ transition are inherited from the $^1S_0 \rightarrow {}^3P_1$ transition due to the hyperfine mixing (see appendix A). The Hamiltonian (5.16) can be rewritten as:

$$\hat{H}_i = |e_i\rangle \langle g_i| \otimes \frac{\hbar}{2} \left(\Omega_\uparrow \hat{P}_{i\uparrow} + \Omega_\downarrow \hat{P}_{i\downarrow} \right) + h.c., \tag{5.17}$$

where the Clebsch-Gordan coefficients have been included in the Rabi frequency $\Omega_{\uparrow,\downarrow} = S_{\uparrow,\downarrow}\Omega$ and $\hat{P}_{i\uparrow}$ and $\hat{P}_{i\downarrow}$ are the projectors on the spin states $|\uparrow\rangle$ and $|\downarrow\rangle$

respectively. Adding and subtracting the terms $\Omega_\uparrow P_{i\downarrow}$ and $\Omega_\downarrow P_{i\uparrow}$, the Hamiltonian can be rewritten as:

$$\hat{H}_i = |e_i\rangle \langle g_i| \otimes \frac{\hbar}{2} \left(\Omega^+ \hat{\mathbb{1}}_i + \Omega^- \hat{\sigma}_{zi} \right) + h.c., \tag{5.18}$$

where $\hat{\mathbb{1}} = \hat{P}_{i\uparrow} + \hat{P}_{i\downarrow}$ is the identity operator, that does not act on the spin state of the atom, while $\hat{\sigma}_{zi} = \hat{P}_{i\uparrow} - \hat{P}_{i\downarrow}$ is the σ_z Pauli matrix, which acts on the states $|\uparrow\rangle$, $|\downarrow\rangle$ as $\hat{\sigma}_{zi}|\uparrow\rangle = |\uparrow\rangle$ and $\hat{\sigma}_{zi}|\downarrow\rangle = -|\downarrow\rangle$, and where we have introduced two new Rabi frequencies:

$$
\begin{aligned}
\Omega^+ &= \frac{\Omega_\uparrow + \Omega_\downarrow}{2}, \\
\Omega^- &= \frac{\Omega_\uparrow - \Omega_\downarrow}{2}.
\end{aligned}
\tag{5.19}
$$

The effect of the application of the laser field to a pair of atoms in the ground state can be determined by operating the Hamiltonian (5.15) on the state $|gg\rangle \otimes |s\rangle$, obtaining:

$$\hat{H}_L(|gg\rangle \otimes |s\rangle) = \frac{\hbar}{2} \left(\sqrt{2}\Omega^+ |eg^+\rangle + \sqrt{2}\Omega^- |eg^-\rangle \right). \tag{5.20}$$

From the definition (5.19) of $\Omega^\pm$ it is clear that for spin mixtures with opposite spin components, $\pm 5/2$, $\pm 3/2$ and $\pm 1/2$, the excitation to the $|eg^+\rangle$ state is inhibited because the Clebsch-Gordan coefficients have equal magnitude and opposite sign, hence Ω^+ is zero. In this case only the excitation to the $|eg^-\rangle$ state is possible. In all the non-symmetric spin mixtures instead the excitation to both the $|eg^+\rangle$ and $|eg^-\rangle$ states is possible.

5.1.3 Magnetic field mixing

The results obtained up to now are valid only with no external magnetic field. The introduction of a magnetic field modified the Hamiltonian of the system, introducing an additional term:

$$\hat{H}_Z = \hat{H}_{Z1} + \hat{H}_{Z2}, \tag{5.21}$$

where $\hat{H}_{Z1}$ and $\hat{H}_{Z2}$ are the Hamiltonians relative to the action of a magnetic field respectively on atoms 1 and 2 and are given by $\hat{H}_{Zi} = g_F^\alpha \mu_B I_{zi} B$, where g_F^α is the g-factor for the electronic state α, μ_B the Bohr magneton and I_{zi} the projection of the nuclear spin along the quantization axis z defined by the direction of the magnetic field B. We remind here that due to the hyperfine mixing of the $^3P_0$ state with the $^3P_1$ state, the difference between $\delta g = g_F^g - g_F^e$ is 113 Hz/G [168]. The matrix element of the Zeeman Hamiltonian (5.21) can be easily computed for the states defined in Eq. (5.1) and are given by:

$$\langle gg| \hat{H}_Z |gg\rangle = g_g(m + m')\mu_B B, \tag{5.22}$$

$$\langle ee| \hat{H}_Z |ee\rangle = g_e(m + m')\mu_B B,$$

$$\langle eg^\pm| \hat{H}_Z |eg^\mp\rangle = \frac{1}{2}(m - m')\delta g\, \mu_B B,$$

$$\langle eg^\pm| \hat{H}_Z |eg^\pm\rangle = \frac{1}{2}(m + m')(g_e + g_g)\, \mu_B B, \tag{5.23}$$

where m and m' are generic nuclear spin components. By restricting to the subspace $\{|eg^+\rangle, |eg^-\rangle\}$, the total Hamiltonian can be found adding the Zeeman Hamiltonian $\hat{H}_Z$ to the zero field Hamiltonian $\hat{H}_0$:

$$\hat{H}_0 = \begin{pmatrix} U_{eg}^+ & 0 \\ 0 & U_{eg}^- \end{pmatrix}. \tag{5.24}$$

In a spectroscopic experiment in which the initial state is $|gg\rangle$, the measured quantities will be the difference between the energies of the final and initial states, hence the total Hamiltonian directly related to the spectroscopic observables will be given by:

$$\hat{H}_{eg} = \begin{pmatrix} (U_{eg}^+ - U_{gg}) + \frac{1}{2}\delta g\,(m + m')\mu_B B & \frac{1}{2}(m - m')\delta g\, \mu_B B \\ \frac{1}{2}(m - m')\delta g\, \mu_B B & (U_{eg}^- - U_{gg}) + \frac{1}{2}\delta g\,(m + m')\mu_B B \end{pmatrix}, \tag{5.25}$$

in which the energy offset $\langle gg| (H_0 + H_Z) |gg\rangle$ has been subtracted along the diagonal. It is clear that in presence of a magnetic field B, the states $|eg^\pm\rangle$ are no longer the eigenstates of the Hamiltonian, and the new eigenstates can be found diagonalizing the Hamiltonian $\hat{H}_{eg}$. For a finite B, the zero field eigenenergies $U_{eg^\pm}$ become:

$$U_{eg}^{H,L}(B) = \frac{1}{2}(m + m')\delta g\, \mu_B B + V \pm \sqrt{V_{ex}^2 + \left(\frac{1}{2}(m - m')\delta g\, \mu_B B\right)^2}, \tag{5.26}$$

where the labels H and L stand respectively for high-energy and low-energy. In the particular case of two opposite nuclear spin components, $m = -m'$, the energies of Eq. (5.26) simply reduce to:

$$U_{eg}^{H,L}(B) = V \pm \sqrt{V_{ex}^2 + \left(\frac{1}{2}\Delta m \delta g\, \mu_B B\right)^2}, \tag{5.27}$$

with $\Delta m = m - m'$. These eigenenergies are plotted in Fig. 5.2 as a function of the magnetic field. In particular, the figure shows that for $B \to 0$, the low-energy branch
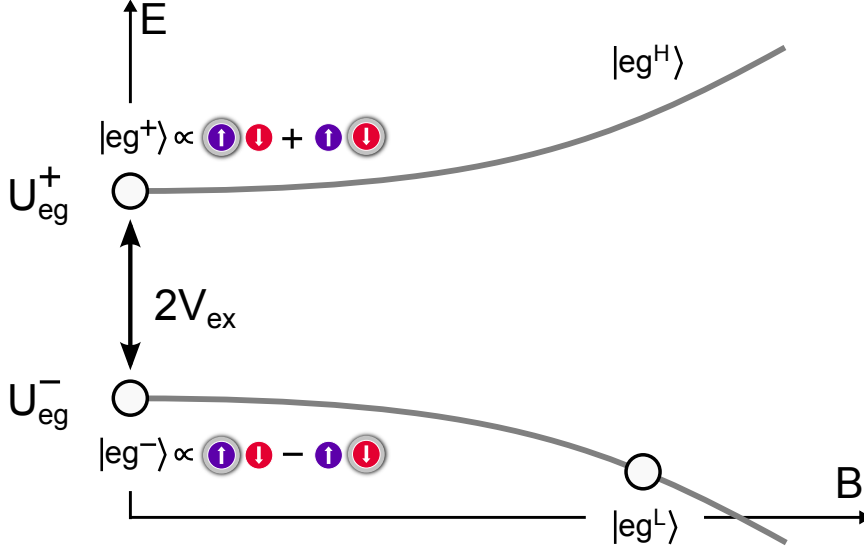
Figure 5.2: Qualitative plot of U^L and U^H eigenenergies of Eq. (5.26) as a function of the magnetic field B for a symmetric $m = -m'$ mixture.

tends to U_{eg}^-, implying a positive exchange interaction V_{ex}, as will be explained in the next section.

The presence of the magnetic field also modifies the eigenstates of the Hamiltonian, which are no longer $|eg^\pm\rangle$ but are given by:

$$\begin{aligned}
\left|eg^L\right\rangle &= \gamma(B)\left|eg^-\right\rangle + \delta(B)\left|eg^+\right\rangle \\
\left|eg^H\right\rangle &= -\delta(B)\left|eg^-\right\rangle + \gamma(B)\left|eg^+\right\rangle
\end{aligned} \tag{5.28}$$

where the coefficients $\gamma(B)$ and $\delta(B)$ depend on the magnetic field and satisfy the conditions $\gamma^2(B) + \delta^2(B) = 1$ and $\gamma(0) = 1$, $\delta(0) = 0$. The coefficients γ^2 and δ^2 are plotted in Fig. 5.3 as a function of the magnetic field. Since the mixing depends not only on the the strength of the magnetic field but also on the nuclear spin components m and m', for a given magnetic field value the value of γ and δ depends on the spin mixture. The maximum mixing is obtained for a $m = 5/2$, $m' = -5/2$ mixture. The exchange energy V_{ex} has been measured exactly in this configuration, as described in the following sections.

For very high magnetic field values, at which $\delta g \mu_B B \gg V_{ex}$, the Zeeman energy is the dominant energy scale and the the eigenstates of the Hamiltonian tend to a superposition of $|eg^-\rangle$ and $|eg^+\rangle$:

$$\begin{aligned}
\left|eg^L\right\rangle &\rightarrow \left(\frac{|eg^+\rangle - |eg^-\rangle}{\sqrt{2}}\right) = |g\uparrow, e\downarrow\rangle \\
\left|eg^H\right\rangle &\rightarrow \left(\frac{|eg^+\rangle + |eg^-\rangle}{\sqrt{2}}\right) = |e\uparrow, g\downarrow\rangle
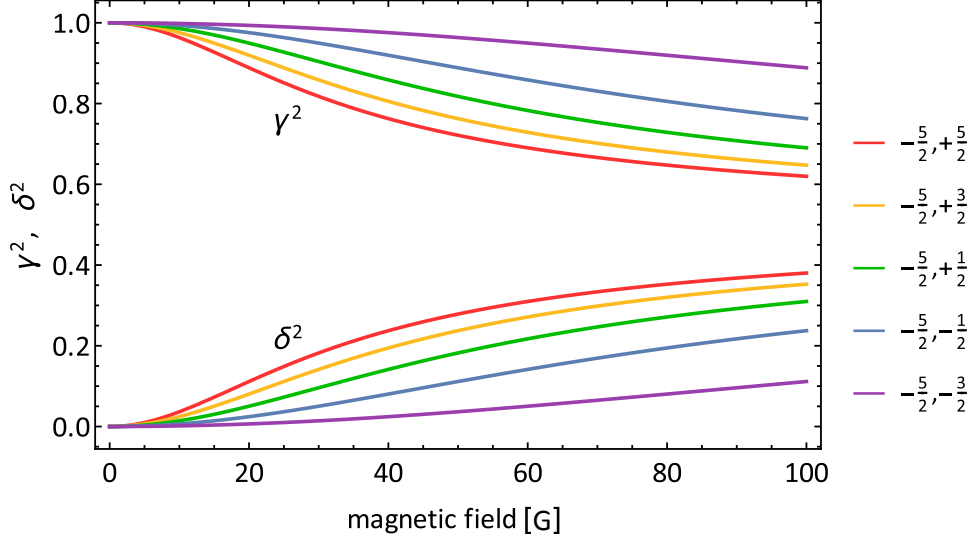\end{aligned} \tag{5.29}$$

Figure 5.3: Coefficients γ^2 and δ^2 as a function of the magnetic field for different spin mixtures m, m'. The mixing coefficients are maximal for the mixture $-5/2, +5/2$. This will be exploited in the initial state preparation for the observation of spin exchange oscillations (see sec. 5.2.2).

These two states are eigenstates of the Zeeman Hamiltonian $\hat{H}_Z$. Evaluating the total Hamiltonian $\hat{H}_{eg}$ of Eq. (5.25) on the basis $\{|e \uparrow, g \downarrow\rangle \ |g \uparrow, e \downarrow\rangle\}$ we obtain the following result:

$$\hat{H}_{eg} = \begin{pmatrix} (V - U_{gg}) + m\delta g \mu_B B & V_{ex} \\ V_{ex} & (V - U_{gg}) + m'\delta g \mu_B B \end{pmatrix}. \quad (5.30)$$

According to this Hamiltonian, at intermediate magnetic fields, the states $|e \uparrow, g \downarrow\rangle$ and $|g \uparrow, e \downarrow\rangle$ are mixed by exchange energy V_{ex}. This coupling represents the key mechanism giving rise to Orbital Feshbach Resonances, as will be shown in Chapter 6.

5.1.4 Spectroscopy of a two-spin states mixture

In this section a spectroscopy experiment on a sample of Ytterbium atoms in two opposite spin states is presented. While in the case of a polarized sample a single transition line was observed (with the exception of the blue lattice sidebands, which do not depend on the symmetrization properties of the sample), in case of a two spin mixture the full spectrum is not given by a single line (excluding sidebands), but is more complex (see Fig. 5.4). The experiment is performed on a sample of atoms loaded in a deep optical lattice, and in each lattice site it is possible to find or a single particle in a certain spin state, or two particles, one in the $|\uparrow\rangle$ state and one in the $|\downarrow\rangle$ state. Furthermore, due to the inhomogeneity given by the harmonic
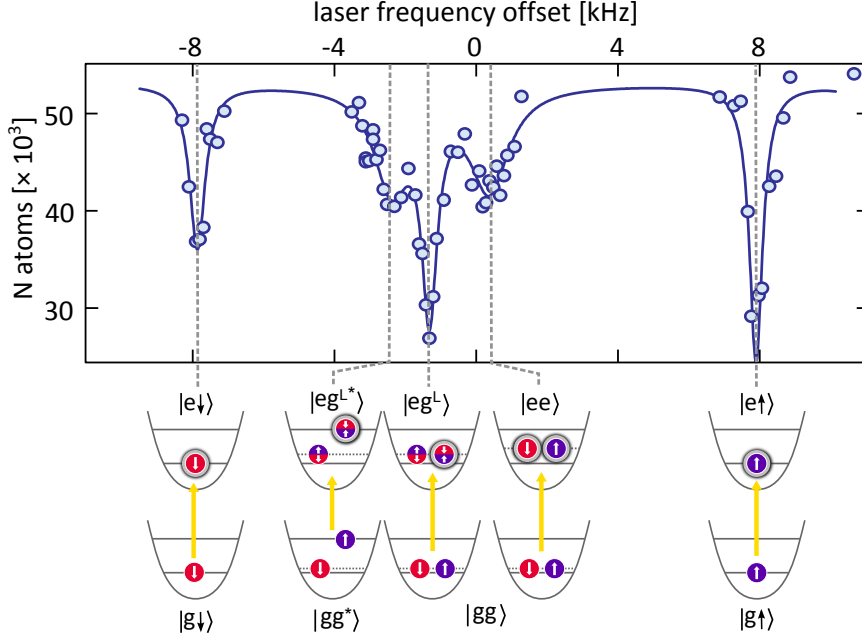
Figure 5.4: Spectrum of the clock transition for a mixture of $m_F = \pm 5/2$ spin components. The nature of the different excitation peaks is sketched in the lower panel. The extreme right and left peaks are relative to the single particle resonances, while the central peaks are relative to different excitation channels in doubly-occupied states. The different depth between the $|\downarrow\rangle$ and $|\uparrow\rangle$ single-particle transitions may be ascribed to an unbalance of the spin mixture due to an imperfect preparation of the initial state.

confinement, the doubly occupied sites will mostly accumulate into the core, whilst singly occupied sites will concentrate mostly into the surrounding shell. In the previous sections it was shown that doubly-occupied states are characterized by an interaction energy between the two atoms in the lattice site. For this reason, singly-occupied and doubly-occupied states will respond differently to the probe laser and several peaks will be visible, each corresponding to a specific state within the atomic sample. The transition frequency will be shifted by a quantity $\Delta\nu$, corresponding to the difference between the interaction energy of the final state U_f and the interaction energy of the initial state U_{gg}:

$$\Delta\nu = \frac{U_f - U_{gg}}{h}, \tag{5.31}$$

where h is the Planck constant. Provided a probe laser with a high enough frequency resolution is available, it is then possible to directly measure the interaction energy difference. Noticeably, as we will see in a while, the scattering length of the final state can also be determined from the measured frequency shift, assuming to know the spatial wavefunctions and the scattering length of the initial state.

Fig. 5.4 reports the spectrum of the $^1S_0 \rightarrow {}^3P_0$ transition obtained performing spectroscopy on an sample of $N_{at} = 5 \times 10^4$ Ytterbium atoms prepared at tem-

perature $T \simeq 0.2T_F$ in a mixture of $m_F = \pm 5/2$ nuclear spin states. The sample is confined in a 3D optical lattice at the magic wavelength with a depth of 30 E_r, where E_r is the recoil energy. In order to properly split the different peaks, a magnetic field $B \sim 28$ Gauss is applied. The π-polarized probe laser has an intensity of the order of 10^{-4} W/cm^2, resulting in linewidths of the order of 150 Hz, narrow enough to clearly distinguish the different excitation peaks. Fig. 5.4 shows a total of five different peaks, which are related to different excitation process. As pictorially shown in the lower panel of Fig. 5.4, the peaks at the extreme left and extreme right can be identified as resonances involving single atoms sitting in the external lattice sites and are related to the excitation of the $m_F = \pm 5/2$ states. This can be easily verified by performing spectroscopy at the same magnetic field on a spin-polarized atomic samples and observing that the resonances are in the same position as in the two-spin case. Since the differential g-factor $\delta g = 113$ Hz/G is positive, it is possible to assign the lowest energy peak to the $m_F = -5/2$ state. The three central peaks, which are not present in spectroscopy experiments on spin-polarized samples, are related to the excitation of two particles states. The attribution of each feature to a particular excitation channel is not trivial because the scattering lengths of the different interaction channels are substantially unknown, and is based on the analysis of displacement of the peaks position as a function of the magnetic field [84].

In Fig. 5.5 different spectra for different values of the magnetic field are reported. The central peaks can be identified as relative to the excitation of the $\left|eg^L\right\rangle$ state. Its energy decreases at high values of magnetic field following a square-root trend as expected from Eq. (5.26). In particular, since in the mixture $m_F = \pm 5/2$ has opposite spin components, the excitation to the $\left|eg^+\right\rangle$ is forbidden (see section 5.1.2), hence we can identify this peak as the one adiabatically connected to the $\left|eg^-\right\rangle$ state at $B = 0$. In particular, this implies that U_{eg}^- is lower than U_{eg}^+ and that the exchange energy $V_{ex} = (U_{eg}^+ - U_{eg}^-)/2$ is positive.

The peak at lower energy close to the central peak has the same dependence on the magnetic field as the $\left|eg^-\right\rangle$ state (see inset of Fig. 5.5), but its energy is systematically lower than that of the central peak. It can be identified as related to a process of the kind $\left|gg\right\rangle^* \rightarrow \left|eg^-\right\rangle^*$, in which both in the initial and final state one of the atoms is in an excited band. This is evident considering that the scattering length associated to this process would be the same as a_{eg}^-, and the difference in interaction energy ΔU between the two states would be given by:

$$\Delta U = U_{eg}^{-*} - U_{eg}^- = \frac{4\pi\hbar^2 a_{eg}^-}{2\mu} \int d\mathbf{r} \left(w_0^2(\mathbf{r})w_1^2(\mathbf{r}) - w_0^4(\mathbf{r}) \right), \qquad (5.32)$$

where $w_0(\mathbf{r})$ and $w_1(\mathbf{r})$ are the Wannier functions in the fundamental and the first excited bands, respectively. Since, in each lattice site, the overlap between the fundamental and first excited Wannier function is lower than the overlap between two fundamental Wannier functions, ΔU will then be lower than zero, meaning that the $\left|eg^-\right\rangle^*$ state has lower energy than $\left|eg^-\right\rangle$. Another evidence that this peak
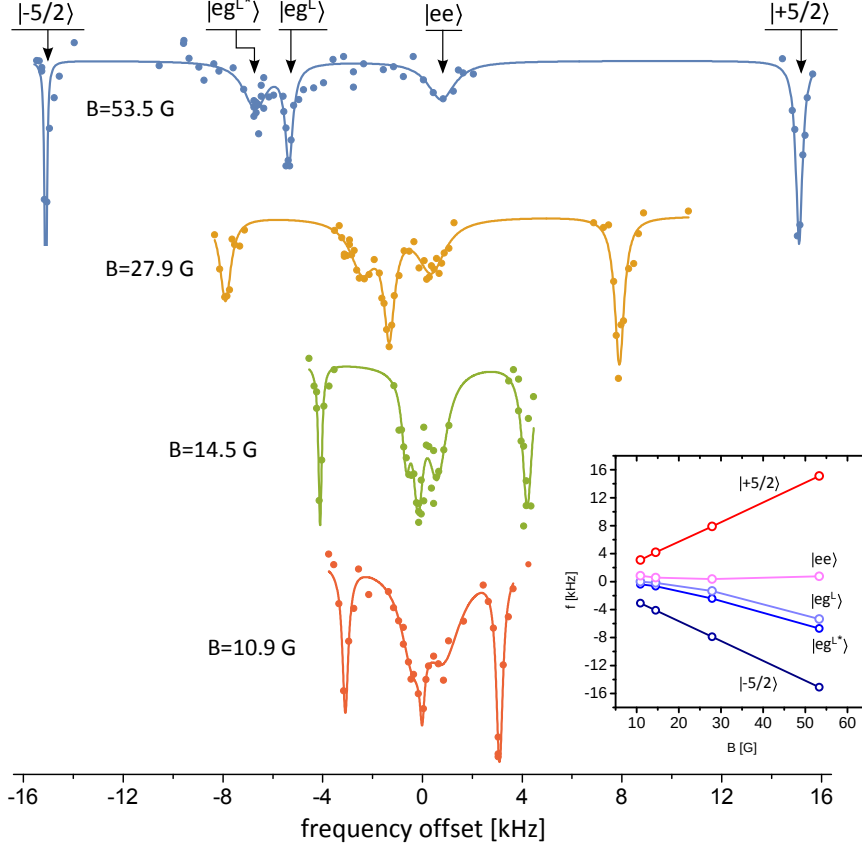
Figure 5.5: Clock transition spectroscopy of a two component sample for different values of external magnetic field. The inset shows the trend of the different peaks as a function of the magnetic field: the single particle peaks shift linearly with the magnetic field due to the Zeeman energy, while the displacement of the states $\left|eg^L\right\rangle$ and $\left|eg^L\right\rangle^*$ is not linear. Finalyl the $\left|ee\right\rangle$ position is independant on the magnetic field.

involves an excited state is that it gets stronger as the number of atoms populating the first excited band of the lattice is increased, by loading in the lattice atomic samples with a higher overall number of atoms.

Finally, the peak close to the central peak at higher frequency can be identified as the transition to the $\left|ee\right\rangle$ state, in which both the atoms are excited to the e state. Its identification is easy by noticing that the matrix element of the Zeeman Hamiltonian for the $\left|ee\right\rangle$ is given by $\left\langle ee\right| \hat{H}_Z \left|ee\right\rangle = g_e(m+m')\mu_B B$, which is identically zero for $m=-m'$. Then, the position of the peak should not be influenced by the magnetic field, that is actually the case in our observation (see inset of Fig. 5.4). Moreover, this peak is typically lower, due to the two-photon nature of the process which connects the $\left|gg\right\rangle$ state to the $\left|ee\right\rangle$ passing through the virtual state $\left|eg^L\right\rangle$.
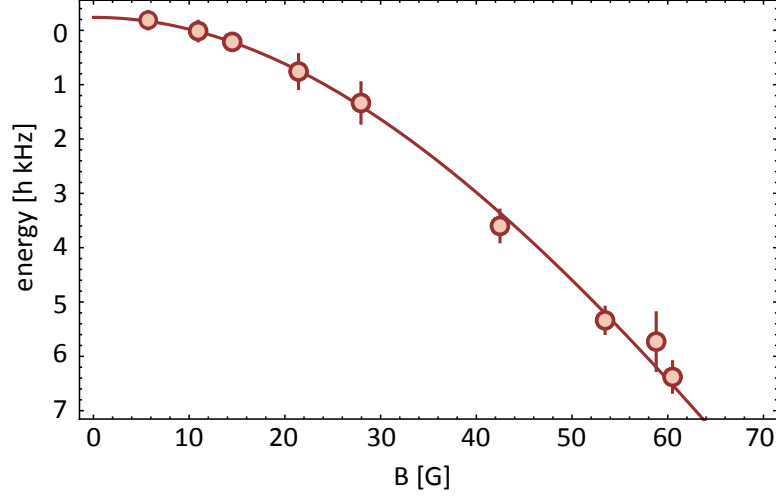
Figure 5.6: Resonant frequency of the $\left|eg^L\right\rangle$ state for a $m_F = \pm 5/2$ mixture as a function of the magnetic field B. The experimental data are fitted with Eq. (5.11) with $V - U_{gg}$ and V_{ex} as free parameters. The zero energy of the vertical axis corresponds to the center of the single particles transition, determined as the center of the $m_F = -5/2$ and $m_F = +5/2$ transitions.

Determination of the scattering lengths

The spectra in Fig. 5.5 allow not only for the identification of the peaks, but also for the determination of the scattering lengths associated to the interaction channels $\left|eg^\pm\right\rangle$ and $\left|ee\right\rangle$, as explained below.

The position of the $\left|eg^L\right\rangle$ peak at a given magnetic field is related to the difference in interaction energy $U_{eg^L} - U_{gg}$. Fig. 5.6 reports the results of a fitting procedure of the positions of the $\left|eg^L\right\rangle$ peak at different values of magnetic field with the expression of Eq. (5.26). From the fit, it is possible to determine the values of the parameters $V - U_{gg}$ and V_{ex}. The ground state interaction energy $U_{gg} = 4\pi\hbar^2 a_{gg}/2\mu \int d\mathbf{r}|w(\mathbf{r})|^4$ can be calculated using the known value $a_{gg} = 199.4\ a_0$ for ^{173}Yb [93] and exploiting the knowledge of the Wannier functions at lattice depth 30 E_r, so it can be subtracted from V. Then, from V and V_{ex} we extract the values of the interaction energies $U_{eg^\pm}$ according to Eq. (5.11). From these values of $U_{eg^\pm}$, the associated scattering lengths can be determined using the Fermi-Hubbard interaction energy:

$$U_{eg^\pm} = \frac{4\pi\hbar^2 a_{eg^\pm}}{2\mu} \int d\mathbf{r}\, w_0^4(\mathbf{r}). \qquad (5.33)$$

The resulting scattering length values are $a_{eg}^- = (215 \pm 40)a_0$ and $a_{eg}^+ = (2600 \pm 500)a_0$. The value of a_{eg}^- is compatible with the value determined in [84] of $a_{eg}^- = (219.5 \pm 2.0)a_0$. In the following sections, this more accurate value of the a_{eg}^- scattering length will be used, since it is the results of a detailed study of the

interaction energy U_{eg}^- for several spin mixtures. Regarding the scattering length a_{eg}^+, it is important to note that it exceeds the harmonic oscillator length associated to a lattice site, which of the order of $\sim 1000 a_0$ for a $s = 30$ lattice. In this regime, the Fermi-Hubbard model is no longer valid and the estimated interaction energy of $U_{eg}^+/h = 40$ kHz is incorrect. In order to properly estimate U_{eg}^+ and its scattering length an alternative theoretical model has to be developed. The simple case of two strongly interacting particles in an harmonic trap has been resolved analytically in Ref. [180]. This model will be explained and extended to the deep lattice case in the section 5.2.3.

For sake of completeness, from the position of the $|ee\rangle$ peak, that is independent on the magnetic field, it is in principle possible to determine a value for the scattering length a_{ee}. The peaks position is indeed related to the energy difference:

$$\Delta U = U_{ee} - U_{gg} = \frac{4\pi\hbar^2(a_{ee} - a_{gg})}{2\mu} \int d\mathbf{r}\, w_0^4(\mathbf{r}). \tag{5.34}$$

From this equation, using the known value of $a_{gg} = 199.4\ a_0$ and knowing the Wannier functions for a $s = 30$ lattice, it is possible to determine the scattering length a_{ee} associated to the e-e interaction channel. This has been done in Ref. [84], obtaining $a_{ee} = 306.2\ a_0$.

5.2 Interorbital spin-exchange oscillations

As we saw at the end of the previous section, incoherent spectroscopy is a valuable tool to obtain information regarding the interaction properties of the interorbital collisional channel, but it features some drawbacks. First, it is not possible to directly probe the $\left|eg^H\right\rangle$ state in symmetric spin mixtures, since this state is adiabatically connected to the $|eg^+\rangle$ state which cannot be excited in spin mixtures in which $m = -m'$. This implies that in this case all the information about the U_{eg}^+ interaction energy have to be extracted from the data relative to the $|eg^-\rangle$ channel, as explained in the previous section. With this approach, it is possible to estimate a very high scattering length a_{eg}^+, a value at which the Fermi-Hubbard model is no longer valid so that the obtained interaction energy and associated scattering length becomes unreliable. Moreover, spectroscopy experiments cannot highlight the coherent nature of the interorbital spin-exchange interaction. The possibility to coherently manipulate atoms interacting via interorbital spin-exchange could open new realistic possibilities for both quantum information processing and quantum simulation.

This section reports the first direct observation of interorbital spin-exchange oscillations [41], i.e. a process in which two atoms in different electronic orbitals and with different nuclear spin states swap their spin as a direct consequence of the spin-exchange interaction. Noticeably, this oscillatory dynamics is a demonstration of the coherent nature of the interorbital spin-exchange interaction. As will be explained later in this section, the frequency of these oscillations is directly related to the exchange energy V_{ex}, allowing for a direct measurements of the interaction
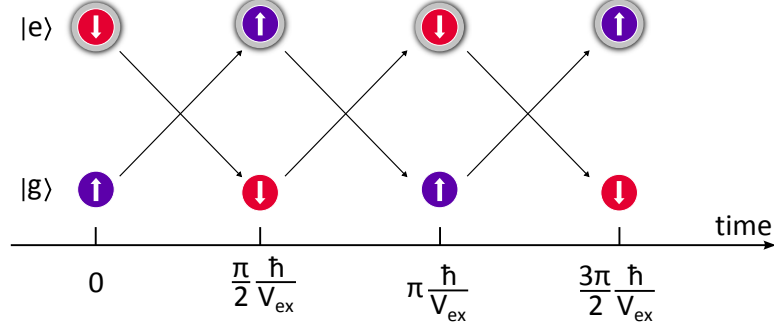
Figure 5.7: Sketch of the interorbital spin-exchange oscillation process. A pair of atoms in definite electronic and nuclear spin states periodically swap their spins at a frequency determined by the exchange interaction.

energy U_{eg}^+ even in mixtures where direct excitation is not possible. Later in this section, it will be also shown how from the measured values of the interaction energies an estimation of the a_{eg}^+ scattering length can be obtained with a theoretical model based on the model of Ref. [180], which takes into account the modification of the wavefunctions induced by the strong interaction in optical lattices.

5.2.1 Origin of interorbital spin-exchange oscillations

In order to understand the origin of the interorbital spin-exchange oscillations, let us suppose to prepare an initial state that is the superposition of $|eg^+\rangle$ and $|eg^-\rangle$, namely:

$$|\psi\rangle = \alpha\,|eg^+\rangle + \beta\,|eg^-\rangle, \tag{5.35}$$

where $|\alpha|^2 + |\beta|^2 = 1$. Since $|eg^+\rangle$ and $|eg^-\rangle$ are eigenstates of the zero field Hamiltonian, the temporal evolution of the state $|\psi\rangle$ will be given by, up to a global phase factor:

$$|\psi(t)\rangle = \alpha\,|eg^+\rangle + e^{\frac{-2iV_{ex}t}{\hbar}}\beta\,|eg^-\rangle, \tag{5.36}$$

where we remind that $2\,|V_{ex}| = U_{eg}^+ - U_{eg}^-$. Since $|eg^\pm\rangle$ are eigenstates of the Hamiltonian, the projection of $|\psi\rangle$ on $|eg^\pm\rangle$ is constant in time, but the phase evolution between the two components affects the projection on a different basis, for example influencing the probability to find an atom in a given electronic and spin state. Considering that the states $|eg^\pm\rangle$ can be written as $|eg^\pm\rangle = 1/\sqrt{2}\,(|e\uparrow, g\downarrow\rangle \pm |g\uparrow, e\downarrow\rangle)$ (see section 5.1.1), the probability to find one atom in the state $|g\uparrow\rangle$, considering for simplicity the case $\alpha = \beta = 1/2$, will be given by:

$$P(|g\uparrow\rangle) = |\langle\psi(t)|g\uparrow, e\downarrow\rangle|^2 = \left|1 - e^{+2iV_{ex}t/\hbar}\right|^2 = \frac{1}{2}\left[1 - \cos\left(\frac{2V_{ex}t}{\hbar}\right)\right], \tag{5.37}$$

featuring an oscillation at frequency $f_{osc} = 2V_{ex}/\hbar$ in which atoms in the ground and excited state periodically flip and exchange their spin with each other (see Fig. 5.7). The same can be found calculating the probability $P(|e\downarrow\rangle)$, while for $P(|g\downarrow\rangle)$ and $P(|e\uparrow\rangle)$ we obtain:

$$P(|g\downarrow\rangle) = P(|e\uparrow\rangle) = |\langle\psi(t)|e\uparrow, g\downarrow\rangle|^2 = \frac{1}{2}\left[1 + \cos\left(\frac{2V_{ex}t}{\hbar}\right)\right]. \qquad (5.38)$$

In the more general case of an unbalanced superposition of $|eg^+\rangle$ state, i.e. $\alpha \neq \beta \neq 1/\sqrt{2}$, the oscillation frequency of the probabilities (5.37) and (5.38) is unaltered, whereas the amplitude of the oscillations is reduced. In particular, $P(|g\downarrow\rangle)$ is by given by:

$$P(|g\downarrow\rangle) = \frac{1}{2}\left[1 + 2\alpha\sqrt{1 - |\alpha|^2}\cos\left(\frac{2V_{ex}t}{\hbar}\right)\right], \qquad (5.39)$$

in which the relation $\beta^2 = 1 - |\alpha|^2$ has been used. Surprisingly, the relative amplitude of the oscillation has not a strong dependence on the unbalance. For example, with a small admixture given by $\alpha^2 = 0.9$, the oscillation amplitude is already around 0.6. As a consequence, spin-exchange oscillations may be visible even with a highly unbalanced initial state.

5.2.2 Experimental observation of spin-exchange oscillations

The experimental sequence for the observation of the coherent interorbital spin-exchange dynamics is explained in Fig. 5.8. The experiment is performed on quantum degenerate Fermi gases of ^{173}Yb in the symmetric spin mixture $m = \pm 5/2$, which are produced by evaporative cooling in the crossed dipole trap at 1064 nm. At the end of the evaporation ramp, approximately 4×10^4 atoms at a temperature $T \simeq 0.15 T_F \simeq 25$ nK are left. The atomic cloud is then adiabatically loaded in a 3D optical lattice operating at the magic-wavelength $\lambda_L = 759.35$ nm[1]. In order not to induce unwanted light shift and inhomogeneous intensity broadening of the clock transition, the optical dipole trap intensity is ramped to zero during the lattice ramp up. Before the lattice loading, the dipole trap is slightly compressed in order to enhance the fraction of doubly occupied sites in the central region of the cloud. The atom number is adjusted in order to minimize the occupation of the first excited band, which would lead to spurious $|gg\rangle^* \to |eg\rangle^*$ processes. With this procedure the average filling is $0.5 \leq \bar{n} \leq 1$ atoms per lattice site per spin component.

In order to prepare the superposition of $|eg^+\rangle$ and $|eg^-\rangle$ state needed to detect spin-exchange oscillation, a possible approach is to spectroscopically excite the $|eg^L\rangle$ and $|eg^H\rangle$ states and adiabatically ramp to zero the magnetic field B. Indeed, at $B \neq 0$, the oscillation frequency $U_{eg}^H - U_{eg}^L$ also depends on the magnetic field

---

[1]We used the magic wavelength of ^{174}Yb since this experiment was carried out before the measurement of the magic wavelength for ^{173}Yb of section 4.3.1.
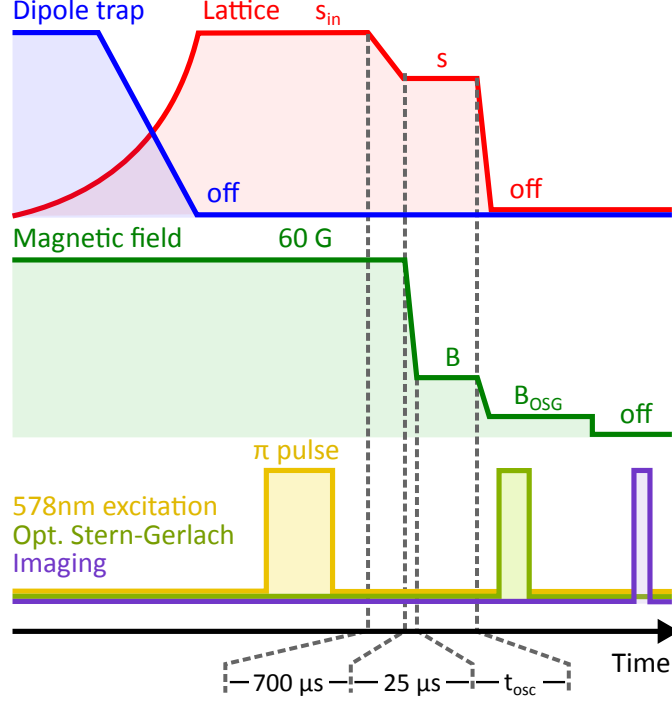
Figure 5.8: Experimental sequence for the observation of spin-exchange oscillations. The Fermi gas of $^{1}73Yb$ is prepared in a dipole trap and then loaded in a 3D optical lattice at the magic wavelength at an initial depth $s_{in} \geq 30\,s$. The $\left|eg^L\right\rangle$ state is excited with a clock laser π-pulse performed at a magnetic field of 60 G. After the excitation the lattice depth is lowered to the value s at which the oscillations will be detected. The magnetic field is then quenched to a bias (3.5 G or higher), and the system is allowed to evolve for a time t_{osc}. The field is then lowered to 3.5 G and the atom number for each spin component is measured by means of OSG technique.

(see Eq. 5.26), so "pure" spin-exchange oscillations can be observed only at $B = 0$. Hovewer, this solution is not applicable at the studied mixture, since it is not possible to directly excite the $|eg\rangle^L$ state in spin-symmetric mixtures $m = -m'$ (see section 5.1.4). The adopted method relies instead on the excitation of the $\left|eg^L\right\rangle$ state at high field values, where it is a superposition of $|eg^\pm\rangle$, followed by a quench of the magnetic field to very low values in order to populate $|eg^+\rangle$ via nonadiabatic Landau-Zener tunneling. The atoms are excited by a π-pulse of 578 nm light resonant with the $|gg\rangle \rightarrow |eg^L\rangle$ transition. The excitation is performed at a large lattice depth $s_{in} \geq 30\,s$, which grants the deep Lamb-Dicke regime. The excitation is also performed at a magnetic field of 60 G, in order to have a sizeable admixture of the spin-singlet state $|eg^+\rangle$ into the $|eg^L\rangle$ state. We note that the employed spin mixture $m_F = \pm 5/2$ grants the maximal state mixing ($|\gamma|^2 \simeq 0.75$, $|\delta|^2 \simeq 0.25$, see section 5.1.3). After the excitation pulse the magnetic field is switched off with a
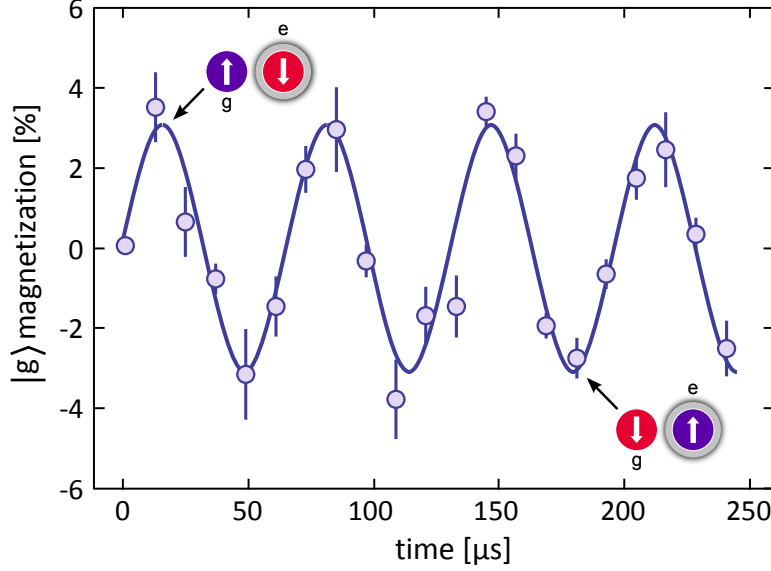
Figure 5.9: Time resolved detection of a interorbital spin-exchange oscillations at a lattice depth s = 30.8 with a bias magnetic field of 3.5 G. The points show the difference in fraction population between $|g \uparrow\rangle$ and $|g \downarrow\rangle$ atoms. The points are the result of an average over 5 acquisitions and the line is the result of a fit using a damped sinusoidal function. A common error bar based on the fit residuals has been assigned to the points.

MOSFET in a time $t_{ramp} \simeq 25 \ \mu$s, fast enough to have a significant population of the $|eg^H\rangle \simeq |eg^+\rangle$ state by nonadiabatic Landau-Zener excitation (with an initial field of 60 G, a ramp time $t_{ramp} \leq 20 \ \mu$s is necessary in order to have a $\geq 10\%$ population of the $|eg^+\rangle$ state [181]). Before the magnetic field quench, the lattice depth is ramped to a desired value of $s < s_{in}$ in 700 μs, in order to observe spin-exchange oscillations at lattice depth different than the initial value.

The magnetic field quench allows us to start the spin dynamics, which is observed by detecting the fraction of ground-state atoms in the different spin states by performing optical Stern-Gerlach (OSG) detection after different evolution times (see section 2.2.2). The bias OSG magnetic field of 3.5 G is generated with an additional coil, always operating during the entire excitation process. Clear oscillations are visible observing the ground-state magnetization

$$M = \frac{N(g \uparrow) - N(g \downarrow)}{N(g \uparrow) + N(g \downarrow)}$$

driven by the spin-exchange process. A typical oscillation is shown in Fig: 5.9. These oscillations, which are visible for hundreds of μs and are characterized by a very short period, represent a clear demonstration of the coherent nature of this interorbital spin-exchange interaction.

As stated above, the measurement of the oscillation frequency provides a direct, model-independent determination of the interaction energy, which is $2V_{ex} = h \times$
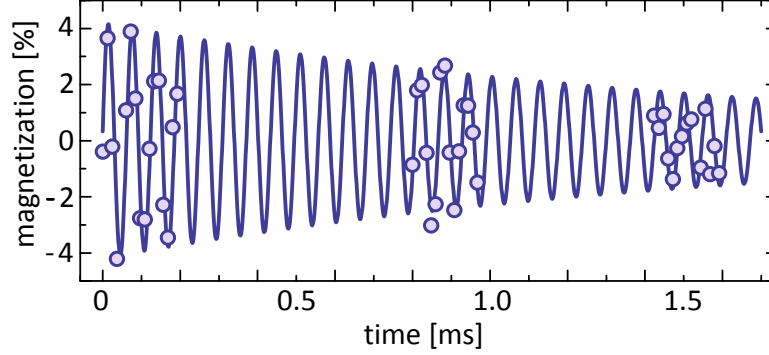
Figure 5.10: Spin-exchange oscillation at s = 35 aquired for longer hold times. A damping on timescales of the order of 2 ms is visible.

(13.9 ± 0.2) kHz for the data in Fig. 5.9. With reference to Fig. 5.16, it should be noted that the presence of the finite bias magnetic field $B \simeq 3.5$ G used for the measurement implies a slightly faster oscillation frequency than $2V_{ex}/h$ (by ~ 100 Hz). The experimental points have been offset by a constant value ($\simeq 5\%$) to take into account a slight unbalance of the spin mixture resulting from an imperfect preparation of the initial state. The oscillation in Fig. 5.9 shows an oscillation amplitude that is lower than the maximum allowed value of 100%. This can be ascribed mainly to the combination of a small initial admixture of the $|eg^+\rangle$ in the $|eg^L\rangle$ state and of a non fully diabatic quench of the magnetic field, that results in an even small admixture of the $|eg^L\rangle$ in the oscillation initial state (reasonably below 10% [181]). Moreover, the sample includes atoms lying in singly-occupied states, which do not participate to the spin-exchange dynamic but are still detected during the imaging. Finally, not all the doubly-occupied states may be properly excited to the $|eg^L\rangle$ state with the π-pulse. In order to clearly ascribe the observed oscillation to the interorbital spin-exchange interaction, we have checked that these oscillations disappear if no clock laser excitation pulse is performed and that the same holds if the magnetic field is switched off slowly instead of with an abrupt quench. We have also checked that no other nuclear spin states (different from $|\uparrow\rangle$ and $|\downarrow\rangle$) are populated during the spin-exchange dynamics.

We measure a finite lifetime of the spin-exchange oscillations, on the order of ~ 2 ms, after which the oscillation amplitude becomes comparable with the scattering of the points, as shown in Fig. 5.10. In order to investigate the origin of this damping, we have performed additional experiments in which we introduce a variable waiting time t_{wait} between the laser excitation to the $|eg^L\rangle$ state and the magnetic field quench that initiates the spin-exchange oscillations. For t_{wait} up to 30 ms (more than one order of magnitude larger than the observed damping time) we can still detect high-contrast spin-exchange oscillations. For this reason, both inelastic $|g\rangle - |e\rangle$ collisions in doubly-occupied sites and tunneling of highly mobile atoms in excited lattice bands can be ruled out as possible sources of the damping shown in Fig. 5.10. Moreover, also $|e\rangle - |e\rangle$ inelastic collisions are significatively

reduced, since only one excited atom is present in each doubly-occupied lattice sites. Excluding these fundamental mechanisms of decoherence, it seems highly plausible that the decay of the spin-exchange oscillations arises from technical imperfections, associated e.g. to the switching of the magnetic field or to an imperfect stabilization of the lattice beams intensity. Another possible source of decoherence may be the residual drift of ultranarrow laser, which during the measurement presented in this and the following sections (5.2.3 and 5.2.4) was not stabilized on the fiber link (see section 3.2.4), but only partially corrected though feed-forward (see section 3.1.5).

5.2.3 Spin-exchange oscillations versus lattice depth

As stated above, the observation of spin-exchange oscillations allows for a direct, model independent measurement of the difference between the interaction energies $U_{eg^{\pm}}$, simply measuring the oscillation frequency $2V_{ex} = U_{eg}^{+} - U_{eg}^{-}$. As seen in section 5.1.4, from a qualitative argument we expect the scattering length a_{eg}^{+} to be of the same order of magnitude of the harmonic oscillator length associated to a lattice site. In this regime, the Fermi-Hubbard models fails to properly describe the system. This is evident comparing the interaction energy $U_{eg}^{-} \sim 38$ kHz obtained with the fitting procedure of section 5.1.4 to the measured value $U_{eg}^{-} \simeq 13.8$ kHz. For this reason, in order to obtain a value for the scattering length a_{eg}^{+} from the measured interaction energies, we developed a theoretical model based of the real wavefunctions of this strongly interacting system, which can no longer be approximated by Wannier functions. The model is based on the analytic solution to the problem of two strongly interacting particles in a harmonic trap developed by Busch et al. in Ref. [180].

Let us consider the problem of two interacting particles of mass m in a lattice site. The Hamiltonian of the system will be given by:

$$\hat{H} = \frac{\mathbf{p}_1^2}{2m} + \frac{\mathbf{p}_2^2}{2m} + V_{lat}(\mathbf{r}_1) + V_{lat}(\mathbf{r}_2) + V_{int}(\mathbf{r}_1 - \mathbf{r}_2), \qquad (5.40)$$

where $V_{int}(\mathbf{r}_1 - \mathbf{r}_2)$ is the pseudo-potential defined in section 1.2.1:

$$V_{int}(\mathbf{r}) = \frac{4\pi\hbar^2}{m} a_s \frac{d}{dr} \delta(\mathbf{r}), \qquad (5.41)$$

and the $V_{lat}(\mathbf{r}_i)$ is the lattice potential of the i-th particle which is given by:

$$V_{lat}(r) = V_{lat}(x, y, z) = V_0 \sum_{x_i=\{x,y,z\}} \sin^2(k_L x_i). \qquad (5.42)$$

where $k_L = 2\pi/\lambda_L$ is the wavevector of the laser. Considering a lattice site with the minimum in the origin, the potential V_{lat} can be expanded giving:

$$\begin{aligned} V_{lat}(\mathbf{r}) &= V_0 \left((k_L x_i)^2 - \frac{1}{3}(k_L x_i)^4 + \frac{2}{45}(k_L x_i)^6 + \cdots \right) = \\ &= V_0(k_L \mathbf{r})^2 + V_{an}(\mathbf{r}) \end{aligned} \qquad (5.43)$$

where $V_{an}(\mathbf{r})$ term contains all the anharmonic corrections to the harmonic potential $V_0(k_L\mathbf{r})^2$. Let us now operate the following coordinate transformation:

$$\mathbf{R} = \frac{\mathbf{r}_1 + \mathbf{r}}{\sqrt{2}}, \quad \mathbf{r} = \frac{\mathbf{r}_1 - \mathbf{r}}{\sqrt{2}}, \tag{5.44}$$

that are similar to the usual "relative" and "center of mass" coordinates, but with different coefficients. Using these coordinates, the Hamiltonian (5.40) can be rewritten as:

$$\hat{H} = \underbrace{\frac{P^2}{2m} + \frac{1}{2}m\omega^2 R^2}_{\hat{H}_{CM}} + \underbrace{\frac{p^2}{2m} + \frac{1}{2}m\omega^2 r^2 + V_{int}(\mathbf{r})}_{\hat{H}_{rel}} + V_{an}(\mathbf{R}, \mathbf{r}), \tag{5.45}$$

which has the advantage that both the kinetic energy and the harmonic oscillator frequencies $\omega = 2\sqrt{s}E_r/\hbar = \sqrt{2V_0 k_L^2/m}$ have the same dependency on m in both the relative and center of mass (CM) terms of the Hamiltonian. The center of mass term $\hat{H}_{CM}$ of the Hamiltonian (5.45) is an harmonic oscillator whose eigenfunctions in spherical coordinates $\psi_{N,L,M}(\mathbf{R})$ are identified by the usual quantum numbers $\{N, L, M\}$ and have the form:

$$\Psi_{N,L,M}(\mathbf{R}) = A_{N,L}R^L e^{-\frac{1}{2}\left(\frac{R}{a_{ho}}\right)^2} \mathcal{L}_g Y_L^M(\theta_R, \phi_R), \tag{5.46}$$

where $A_{L,M}$ is a normalization factor, $a_{ho} = \sqrt{\hbar/m\omega}$ is the harmonic oscillator length, $\mathcal{L}_g$ are the Laguerre polynomials and $Y_L^M(\theta_R, \phi_R)$ are the spherical harmomics with quantum numbers L, M. Slightly more complex is the term related to the relative coordinate $\hat{H}_{rel}$. Since it contains an interaction term which is non-zero only in the origin, it is possible to distinguish between two different possibilities. In case the interaction term can be neglected, the Hamiltonian $\hat{H}_{rel}$ reduces to an harmonic oscillator with eigenfunctions $\psi_{n,l,m}(\mathbf{r})$ of the same form of Eq. (5.46) and identified by the quantum numbers $\{n, l, m\}$. This is a good approximation when $l \neq 0$, since the harmonic oscillator eigenfunctions have a node in the origin. For $l = 0$ instead, the point-like interaction term have to be considered and the eigenfunctions have the form of Ref. [180]:

$$\psi_{m,0,0}(\mathbf{r}) = Ae^{\left(-\frac{r^2}{2a_{ho}^2}\right)}\Gamma\left(-\frac{E}{2\hbar\omega} + \frac{3}{4}\right)\mathcal{U}\left(-\frac{E}{2\hbar\omega} + \frac{3}{4}, \frac{3}{2}, \frac{r^2}{a_{ho}^2}\right), \tag{5.47}$$

where Γ is the Euler function, $\mathcal{U}$ are the confluent hypergeometric functions, A is a normalization factor and E is the total energy, given by the solution of the equation:

$$\sqrt{2}\frac{\Gamma\left(-\frac{E}{2\hbar\omega} + \frac{3}{4}\right)}{\Gamma\left(-\frac{E}{2\hbar\omega} + \frac{1}{4}\right)} = \frac{a_{ho}}{a_s}. \tag{5.48}$$
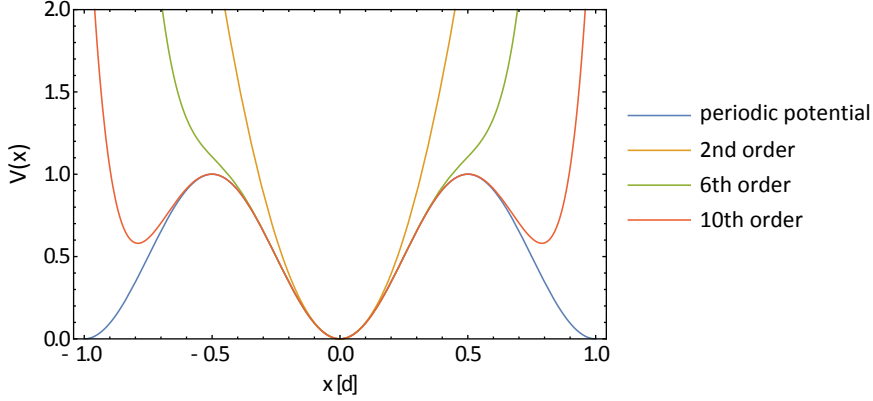
Figure 5.11: Series expansion of a lattice potential $V = \sin^2(k_L x)$ (blue) line up to different orders. The horizontal axis is in units of the lattice spacing $d = \lambda_L/2$. At the 10-th order, the expansion faithfully reproduces a lattice site.

In any case, the presence of the $V_{an}(\mathbf{r}$ in the Hamiltonian (5.45) mixes the relative and center of mass degrees of freedom, making the problem impossible to be solved analytically. In order to extend the exact results of Ref. [180] for the harmonic oscillator problem to the case of a lattice site potential, we diagonalized numerically the Hamiltonian (5.45) on the basis of the eigenstates $\Phi(\mathbf{r}, \mathbf{R})$ of $\hat{H}_{CM} + \hat{H}_{rel}$, namely

$$\Phi(\mathbf{r}, \mathbf{R}) = \Psi_Q(\mathbf{R})\psi_q(\mathbf{r}), \tag{5.49}$$

where $\Psi_Q(\mathbf{R})$ are the wavefunctions of Eq. (5.46) and $\psi_q(\mathbf{r})$ are the eigenstates of $\hat{H}_{rel}$ discussed above and $Q = \{N, L, M\}$ and $q = \{n, l, m\}$ are the quantum numbers for the center of mass and relative coordinates respectively. We evaluated the anharmonic terms on this complete basis up to the 10-th order, which is high enough to faithfully reproduce the lattice potential on the lattice site (see Fig. 5.11). An higher order expansion, approximately to the 20-th order, would be necessary in order to reproduce also the nearest neighbor sites potential and properly evaluate tunneling processes, but since the measurements are performed at high lattice depth, tunneling is not likely to occur on the experiment timescales. Moreover, we observed that the model already converges considering wavefunctions with principal quantum numbers N and n up to 4, and increasing them to 6 only yields a 10^{-4} fractional difference.

By diagonalizing the numerically calculated Hamiltonian, we derive the energy $E_0(a_s, s)$ of the ground state of two particles interacting with scattering length a_s in a lattice site of depth s. The interaction energy related to the scattering length a_s will finally be given by:

$$U_{a_s} = E_0(a_s, s) - E_0(0, s), \tag{5.50}$$

where $E_0(0, s)$ is the energy of the system of two non-interacting particles. The results are shown in Fig. 5.12, where the interaction energy is reported as a function
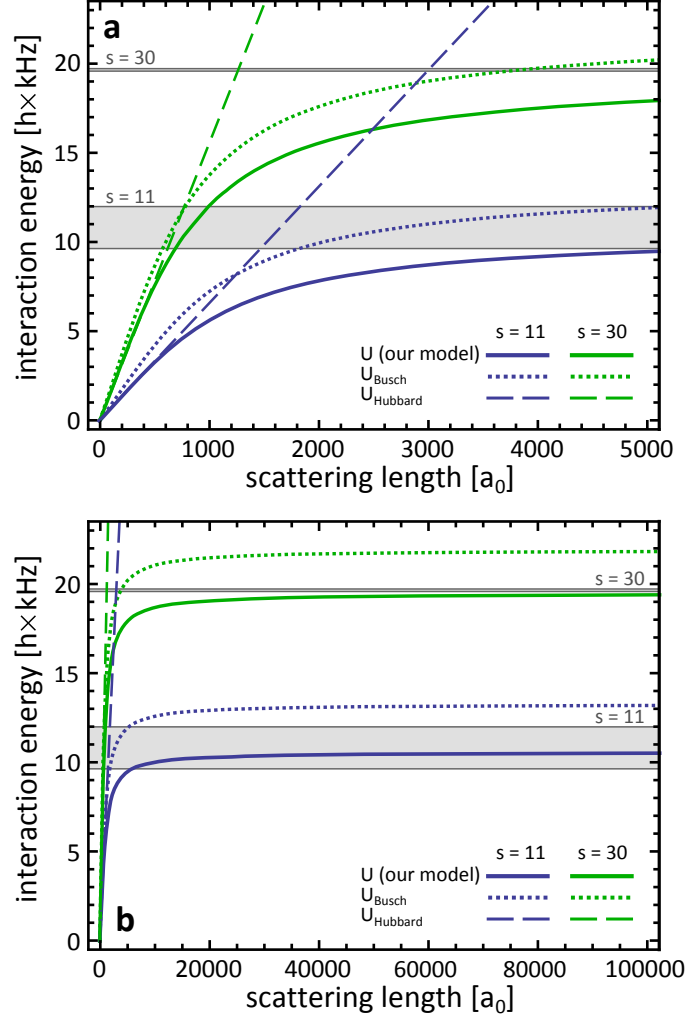
Figure 5.12: **a.** *Interaction energy of two particles in a lattice site calculated with three different models (see text) for two lattice depth values, s = 11 and s = 30. The interaction energy is well approximated by the Hubbard model only for low values of the scattering length a_s.* **b.** *The same interaction energy is plotted up to higher values a_s. The interaction energy saturates at the value of the energy separation between the ground and first excited lattice bands, represented by the gray areas.*

of the scattering length for three different models: the solid line is the interaction energy obtained with our model, in which the anharmonic corrections to the parabolic potential are considered. The dotted curve is the interaction energy calculated with in the model of Ref. [180], where the potential is quadratic with no anharmonic corrections. The dashed line is the interaction energy calculated with the Hubbard model which takes into account the full lattice potential and depends linearly on the scattering length a_s. The curves are plotted for two different lattice depths, $s = 11$ and $s = 30$. The relative energy gaps between the lowest and first excited bands
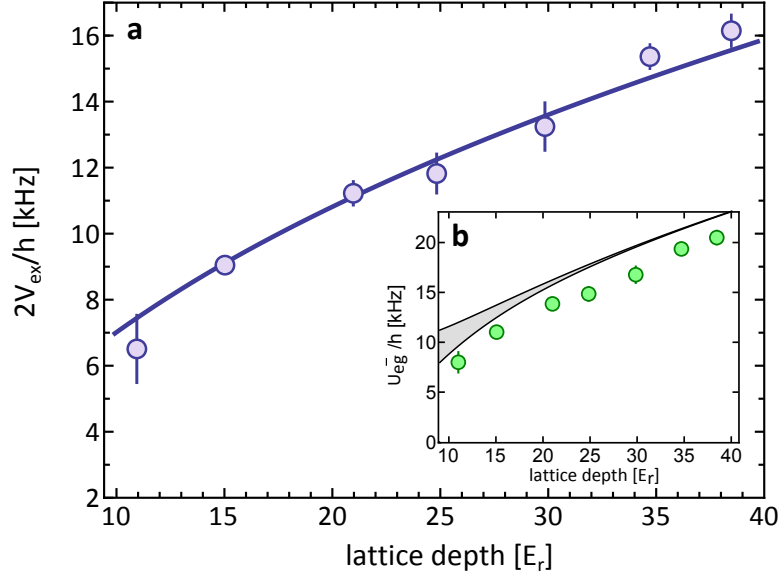
*Figure 5.13: **a.** The experimental points are the spin-exchange frequency $2V_{ex}$ measured for different values of lattice depth s. The points are corrected for the effect of the bias magnetic field of 3.5 G in order to obtain the zero field values. Each point is the average of at least three acquisition and the error bar is the statistical error. The solid line is the fit of experimental data with the theoretical model described in the text. **b.** Interaction energy U_{eg}^+ corresponding to the experimental points of the main figure calculated as the sum of the measured $2V_{ex}$ and the energy U_{eg}^- calculated for $a_{eg}^+ = 219.5$ a_0 [84]. The shaded area is the energy difference between the ground and first excited lattice band.*

are represented by the gray shaded areas (note that the gap for $s = 11$ is wider the gap for $s = 30$, due to the energy bands being wider at a lower lattice depth). From Fig. 5.12 it can be seen that the interaction energy is well approximated by the Hubbard model for scattering lengths up to a few hundreds of a_0, while at higher values the discrepancy between the two models becomes macroscopic. Moreover, Fig. (5.12)b shows that at very high values of the scattering length the interaction energy saturates at the value of the gap between the lowest and first excited bands. This behavior was expected from an extension of the model of Ref. [180], in which the interaction energy saturates at the spacing between the oscillator energy levels, to the lattice potential case.

The theoretical model we have developed is used to investigate the dependence of the interaction energy on the lattice depth. The energy difference $2V_{ex} = U_{eg}^+ - U_{eg}^-$ is obtained from the spin-exchange oscillation frequencies acquired at different values of lattice depth s (see section 5.1.4). The experimental data are then fitted with the function:

$$2V_{ex}(s) = E_0(a_{eg}^+, s) - E_0(a_{eg}^-, s), \qquad (5.51)$$

where the eigenenergies $E_0(a_s, s)$ of our model are calculated leaving a_{eg}^+ as a free
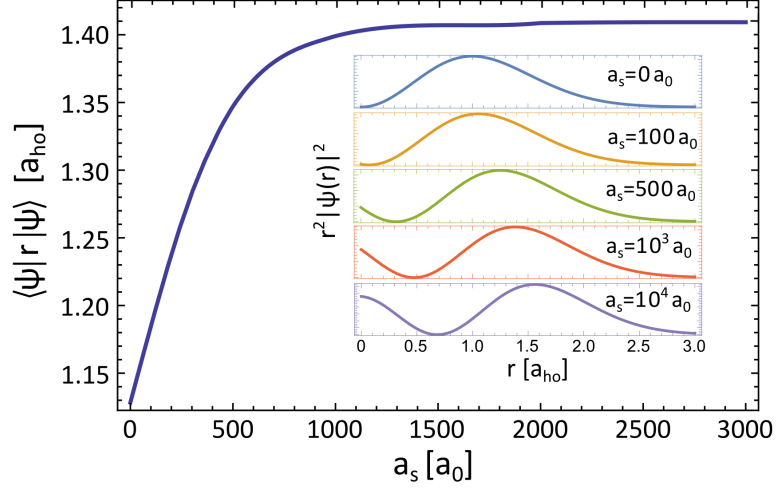
Figure 5.14: Mean inter-particle distance in the model of Ref. [180] plotted versus the scattering length. At higher interaction energies, the particles tend to stay separated within the harmonic well. The insets shows the radial probability profiles of the wavefunctions $\psi(r)$ of model [180] for increasing scattering lengths. The horizontal axis of the insets are in units of harmonic oscillator length calculated for a lattice well with $s = 30$, corresponding to $a_{ho} = 977\, a_0$.

parameter and using $a_{eg}^- = 219.5\ a_0$, as measured in Ref. [84]. In order to obtain the zero field energies, the experimental data are corrected for the contribution of the 3.5 G bias magnetic field shift, measured according to the procedure described in the following section. The result of the fit is shown in Fig. 5.13 and gives a spin-singlet scattering length $a_{eg}^+ = (3300 \pm 300)a_0$. This very large value of scattering length causes the energy U_{eg}^- to almost saturate to the energy gap as shown in the inset of Fig. 5.13, in agreement with the theoretical prediction.

5.2.4 Spin-exchange oscillations versus magnetic field

In addition to the analysis of the dependence of the spin-exchange oscillations frequency on the lattice depth, we also studied the problem related to the presence of a finite magnetic field. Understanding the dependence of the oscillation frequency on the magnetic field is useful, for instance to find out how to compensate for the presence of the bias magnetic field, which is always necessary in the experiment in order not to depolarize the sample. Importantly, also an estimation of the scattering length a_{eg}^+ may be obtained from the experimental data of oscillation frequencies measured at different magnetic fields.

At a finite B the spin-exchange oscillation shows a faster frequency, as the Zeeman energy contributes to the energy difference between $|eg^L\rangle$ and $|eg^H\rangle$ (see Fig. 5.2). In particular, according to the model of section 5.1.3, the energy difference for a spin-symmetric mixture $m = \pm 5/2$, is given by Eq. (5.26):

$$U_{eg}^H(B) - U_{eg}^L(B) = 2\sqrt{V_{ex}^2 + \Delta B^2}. \tag{5.52}$$

where we have defined $\Delta B = \frac{5}{2}\delta g \mu_B B$. However this simple model is not taking into account the fact that the two-particle spatial wavefunctions are significantly modified in case of strong interactions between the particles. In order to get the idea, let us consider the analytical wavefunctions $\psi(\mathbf{r})$ of the model of Ref. [180] for two interacting particles in a harmonic well defined in (5.47). In these wavefunctions, the maximum of the radial probability profile shifts to larger values of the interparticle distance $\mathbf{r} = \mathbf{r}_1 - \mathbf{r}_2/\sqrt{2}$ with increasing values of the scattering length a_s (see Fig. 5.14), indicating that the two particles tend to spatially separate in each lattice site [182]. Since the states $|eg^+\rangle$ and $|eg^-\rangle$ are characterized by very different scattering lengths, the spatial wavefuntion of these two states cannot be considered the same, as supposed in section 5.1.3 and the off-diagonal matrix elements of Eq. (5.22) should also take into account the spatial overlap between the two states $|eg^\pm\rangle$. The external magnetic field coupling between the two collisional channels becomes:

$$\langle\Phi^\mp|\langle eg^\mp|\hat{H}_Z|eg^\pm\rangle|\Phi^\pm\rangle = F\,\Delta B, \tag{5.53}$$

where we have introduced a *Frank-Condon* factor F between the two-particle spatial wavefunctions of the $|eg^+\rangle$ and $|eg^-\rangle$ states which mitigates the mixing induced by the external magnetic field and is given by:

$$F = \langle\Phi^\mp|\Phi^\pm\rangle = \iint d\mathbf{r}\,d\mathbf{R}\,\Phi_{eg}^{\mp*}(\mathbf{r}, \mathbf{R})\Phi_{eg}^\pm(\mathbf{r}, \mathbf{R}). \tag{5.54}$$

This overlap integral is calculated between the spin-triplet and spin-singlet wavefunctions $\Phi_{eg}^\pm(\mathbf{r}, \mathbf{R})$, which are the eigenfunctions of the Hamiltonian (5.45) in the previous section (that includes the anharmonic corrections). Fig. 5.15 shows the Franck-Condon factor $F = \langle\Phi(a_1)|\Phi(a_2)\rangle$ for several pairs of scattering lengths a_1 and a_2. As expected, $F = 1$ along the diagonal, where $a_1 = a_2$ and the two states coincide, while it drops down to ~ 0.6 if the difference between the scattering lengths a_1 and a_2 is very high. Taking into account the motional degree of freedom, the sum of the Hamiltonian $\hat{H}_0$ (5.24 and of the Zeeman Hamiltonian $\hat{H}_Z$ can then be written on the $\{|eg^+\rangle, |eg^-\rangle\}$ basis as:

$$\begin{pmatrix} U_{eg}^+ & F\Delta B \\ F\Delta B & U_{eg}^- \end{pmatrix}, \tag{5.55}$$

It should be noted that this is the same Hamiltonian shown in Eq. (5.25) in the case of $m = -m'$ with the addition of the Franck-Condon factor F. By diagonalizing the Hamiltonian (5.55), the eigenenergies E_{eg}^H and E_{eg}^L can be calculated and their difference delivers the frequency of the spin-exchange oscillation at finite magnetic field, given by:
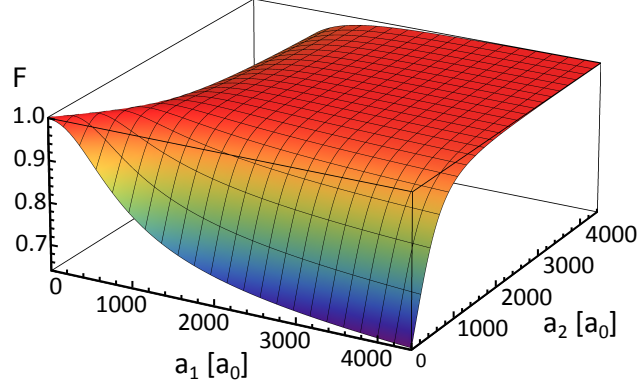
Figure 5.15: Franck-Condon factor of Eq. (5.54) describing the overlap of the spatial wavefunctions for two different scattering lengths a_1 and a_2 in units of the Bohr radius a_0.

$$\nu = \frac{E_{eg}^H(B) - E_{eg}^L(B)}{h} = \frac{2}{h}\sqrt{\left[V_{ex}\left(a_{eg}^+, a_{eg}^-\right)\right]^2 + \left[F\left(a_{eg}^+, a_{eg}^-\right)\Delta B\right]^2}, \quad (5.56)$$

where $F\left(a_{eg}^+, a_{eg}^-\right)$ is the Frank-Condon factor of Eq. (5.54) calculated for the scattering lengths a_{eg}^+ and a_{eg}^- and $V_{ex}\left(a_{eg}^+, a_{eg}^-\right) = (U_{eg}^+ - U_{eg}^-)/2$.

The circles in Fig. 5.16 are the measured spin-oscillation frequencies $(U_{eg}^H - U_{eg}^L)/h$ at lattice depth $s = 30$ at different values of magnetic field B, while the squares indicate the energy of the $|eg^L\rangle$ state determined by fitting the position of the peaks in the spectroscopic measurements (Fig. 5.4). The solid lines in Fig. 5.16 show the predictions of the model in Eq. (5.56) using the parameters $a_{eg}^- = 219.5\,a_0$ of Ref. [84] and $a_{eg}^+ = 3300\,a_0$ obtained in section 5.2.3, which determine a Franck-Condon factor $F = 0.77$ calculated by using the interacting wavefunctions described above. The agreement with the experimental data is quite good, showing the substantial validity of the Hamiltonian (5.55) in which the Frank-Condon factor F is considered in the mixing terms. Additionally, we have performed a simultaneous fit of the two datasets in Fig. 5.16 using Eq. (5.56) as fitting function with U_{eg}^+ and F as functions of the free parameter a_{eg}^+ and with $a_{eg}^- = 219.5\,a_0$. The result of this fitting procedure is also shown in Fig. 5.16 (dashed lines) and gives $a_{eg}^+ = (4400 \pm 600)\,a_0$, which differs of $\sim 2\sigma$ from the more precise value obtained with the fit of the data at different lattice depths shown in Fig. 5.13. It is important to note that the discrepancy between the results for scattering length a_{eg}^+ obtained with the two different methods may be due to the fact that in a strongly interacting regime the dependence of U_{eg}^+ on a_{eg}^+ is extremely weak, as can be seen in Fig. 5.12. In this case, even small effects, coming e.g. from experimental uncertainties or from higher-order contributions in the theory, could imply significant changes. We also note that, in presence of a strong confinement, the interpretation of the results in terms of an effective scattering length should be considered [183]. However, we stress that while the determination
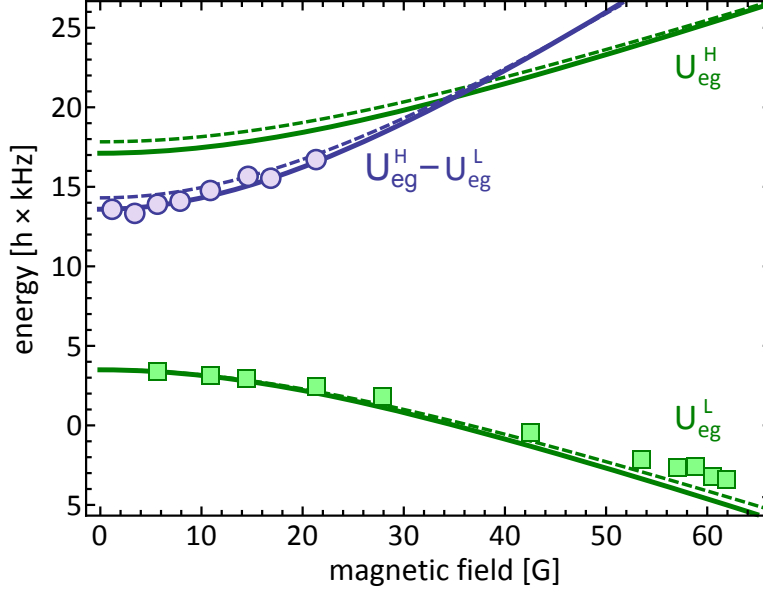
118

Figure 5.16: The blue circles are the measured spin-exchange frequencies $(U_{eg}^H - U_{eg}^L)/h$ at different values of magnetic field at $s = 30$, while the green squares are the measured energy of the $|eg^L\rangle$ state obtained from spectroscopy (Fig. 5.4). The solid lines are the predictions of the model in Eq. (5.55) with $a_{eg}^- = 219.5 \, a_0$ and $a_{eg}^+ = 3300 \, a_0$ derived in Fig. 5.13 in section 5.2.3. The dashed lines show a fit of the points with the same model leaving a_{eg}^+ as free parameter.

of the scattering length a_{eg}^+ is heavily model-dependent, the determination of the exchange interaction V_{ex} is free from any assumption and represents an accurate measurement of the spin-exchange coherent coupling in a multi-orbital system.

5.2.5   Constraints on SU(N) symmetry violation

As already mentioned in section 5.2.1, also the interorbital interactions are characterized by a SU(N) symmetry, implying that the scattering lengths $a_{eg}^\pm$ assume the same values for all the nuclear spin states m_F. However, due to the hyperfine interaction, there is a tiny admixture of the $^3P_1$ into the $^3P_0$, which implies a violation of the SU(N) symmetry leading to a relative scattering length difference $\delta a/a$, that is expected to be of the order of 10^{-3} in ^{87}Sr [26]. The interorbital spin-exchange oscillations represent a valid tool in order to investigate this violation in ^{173}Yb. The oscillations frequency $f_{ex} = 2/hV_{ex}$ is indeed directly related to the exchange energy V_{ex} (and so to the scattering lengths $a_{eg}^\pm$), and can be measured with a high degree of accuracy due to the long-lived nature of the spin-exchange oscillations.

We try to give a constraint on SU(N) symmetry violation in ^{173}Yb by measuring the difference in oscillation frequency for two different mixtures of nuclear spin states. In order to maximize the accuracy of the measurement of the oscillation frequency, we exploit the presence of the optical fiber link described in 3.2.4 to
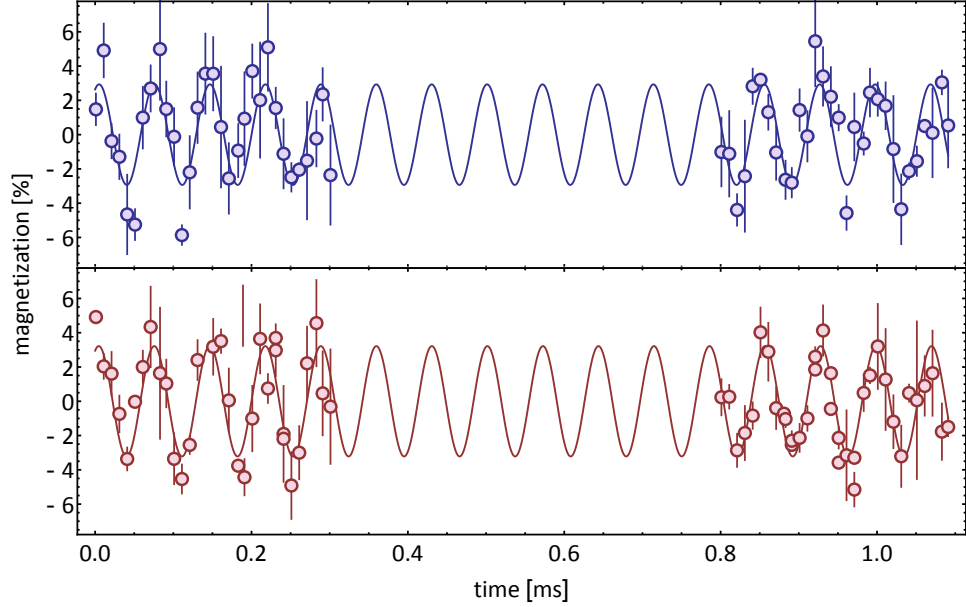
Figure 5.17: interorbital spin-exchange oscillations measured for the spin mixtures $m = -5/2$, $m' = +1/2$ and $m = -3/2$, $m' = +3/2$, respectively in blue and red. The dots represents the experimental data and the solid lines are the fit with a sinusoidal function. The measured frequencies are (14.11 ± 0.05) kHz and (14.08 ± 0.04) kHz for the blue and red curves respectively, which are compatible within the error bar.

stabilize the frequency of the 578 nm laser. This allows for a stable excitation of the transition to the two particle $\left|eg^L\right\rangle$ state for the entire day, since the laser linewidth is only limited by the short-term stability when the laser is disciplined to the remote frequency reference. Moveover, as discussed in section 5.2.3, the oscillation frequency depends on the lattice depth. For this reason, the data are taken alternating, at each experimental cycle, between the two different spin mixtures considered in the experiment. In this way, possible slow drifts in the lattice alignment lead to a common-mode effect on the global dataset for the two cases. The measurement are performed at a finite magnetic field of 3 G in order to define a quantization axis. At finite magnetic field the oscillation frequency $f_{ex} = 2/h(U_{eg}^H - U_{eg}^+)$ depends on Δm as:

$$f_{ex} = \frac{2}{h}\sqrt{V_{ex}^2 + \frac{1}{2}F\Delta m \delta g \mu_B B}, \qquad (5.57)$$

where we have also considered the Frank-Condon factor F introduced in section 5.2.4. This equation suggests that for an accurate measurement of the difference of f_{ex} in spin mixtures with different Δm, one would need to take into account a correction for the magnetic field term, which would also imply an exact knowledge of the term F. For this reason, we perform the measurement on spin mixtures with the same $\Delta m = m - m'$, so that the magnetic field correction is a common factor.

A typical result of these measurement is reported in Fig. 5.17. The measurement is performed on the spin mixtures $m = -5/2$, $m' = +1/2$ and $m = -3/2$, $m' = +3/2$, which are reported as blue and red circles, respectively. The two oscillation frequencies are determined by fitting the data with a sinusoidal function and are (14.11 ± 0.05) kHz for the blue curve and (14.08 ± 0.04) kHz for the red curve, featuring a difference of 30 ± 60 Hz. We note that the reduced amplitude of the oscillation, with respect to Fig. 5.9, is a consequence of the lower admixture of the $|eg^+\rangle$ and $|eg^-\rangle$ states in the considered mixtures with respect to the $m = -5/2$, $m' = +1/2$ case. The two frequencies are compatible within the error bar and the difference is compatible with zero. The same result is obtained for other measurements, even between other mixtures with different Δm taking in account the magnetic field correction using our experimental parameters and using the value for F found in section 5.2.4. We can conclude that no violation of the SU(N) symmetry is observed within the level of uncertainty of $\sim 4 \times 10^{-3}$ currently achievable with our experimental setup. On the other hand, these measurements do not represent a proof of the SU(N) symmetry, a task that would require a systematic investigation of all the possible spin mixture combinations. We can conclude that, an improvement of our experimental setup is needed in order to increase the accuracy of this kind of measurement.

Chapter 6

Orbital Feshbach Resonances

As already mentioned before, the presence of the metastable state and the SU(N) symmetry of interactions are peculiar features of AEL atoms. Despite these remarkable properties, two-electron atoms are, up to now, thought to lack the tunability of interactions, due to their null electronic angular momentum in the ground state, that precludes the existence of convenient magnetic Feshbach resonances at reasonable values of magnetic field. This is a fundamental tool in ultracold gases of alkali atoms [85], which allowed for breakthrough achievements, including studies of strongly interacting fermionic systems, with the demonstration of high-density molecular gases and the exploration of fermionic superfluidity at the BEC-BCS crossover [78]. It is straightforward that disposing of a similar tunability for two-electron atoms would open totally new avenues, including the study of the crossover in a two-orbital system and the investigation of topological fermionic superfluids [58]. In this direction, Optical Feshbach resonances in two-electron atoms have been proposed [184] and observed experimentally [185, 186], but their implementation presents a high degree of difficulties, such as heating and losses. For this reason, Optical Feshbach resonances are not a viable tool to be exploited for the observation of true many-body quantum physics, although novel promising schemes have been very recently investigated [187].

In this chapter we describe the first experimental observation of a new kind of Feshbach resonance, called Orbital Feshbach Resonance (OrbFR), affecting the the scattering between atoms in different electronic states, which have been recently proposed in Ref. [58]. The results of this observation are reported in Ref. [57] and are confirmed by the independent, complementary measurements reported in Ref. [188]. Exploiting this resonance, we realized a strongly interacting gas of two-electron fermionic Yb atoms with orbital degree of freedom and tunable interactions. After a short introduction to the subject of Feshbach resonances and a description of the mechanism at the basis of OrbFR, it will be shown how we could detect the OrbFR by observing a hydrodynamic expansion of the Fermi gas in the strongly interacting regime. Finally, atom losses across the resonance will be investigated, in order to determine the actual exploitability of this new kind of
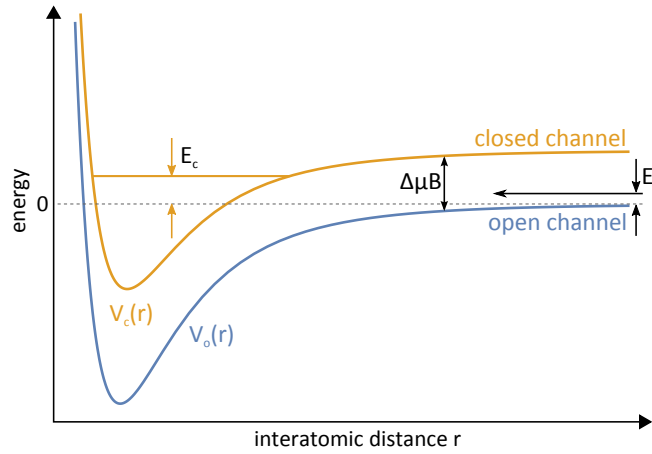
Figure 6.1: Open channel and closed channel molecular potentials. At energy E only the open channel is accessible. Tunig the magnetic field B, the position of the closed channel bound state can be adjusted and a Feshbach resonance occurs when it matches the open channel energy threshold.

scattering resonance.

6.1 Introduction to Feshbach resonances

A Feshbach resonance is a resonance of the scattering length between two atoms. The physical origin and the elementary properties of a Feshbach resonance can be understood with a simple picture. Let us consider consider a pair of colliding atoms with different internal degree of freedom. These atoms can interact in different combinations, or channels (e.g singlet and triplet channels for two atoms with spin states $|\uparrow\rangle$ and $|\downarrow\rangle$), which correspond to different molecular potentials. In particular, the lowest energy potential is asymptotically connected, at large internuclear distances r, to free ultracold atoms of the gas. In a collisional process having energy E, this potential represents the accessible "open channel", which we label as $V_o(r)$. The other potential $V_c(r)$, with asymptotic energy higher than E, is called "closed channel" and is unaccessible during the collision due to energy conservation. However, it can support the existence of a bound state with energy E_c near the threshold of the open channel (see Fig. 6.1).

A Feshbach resonance occurs when the energy of closed channel bound state E_c approaches the energy of the scattering state in the open channel. In this case, even small couplings between the two channels can lead to a strong mixing between them. In the case in which the magnetic moments of the two channels are different, the two potentials can be energetically shifted with respect to one another by means of an external magnetic field, leading to a magnetical Feshbach resonance. The aforementioned finite coupling between the open and closed channels is fundamental for the emergence of the resonance. This coupling implies that the initial state
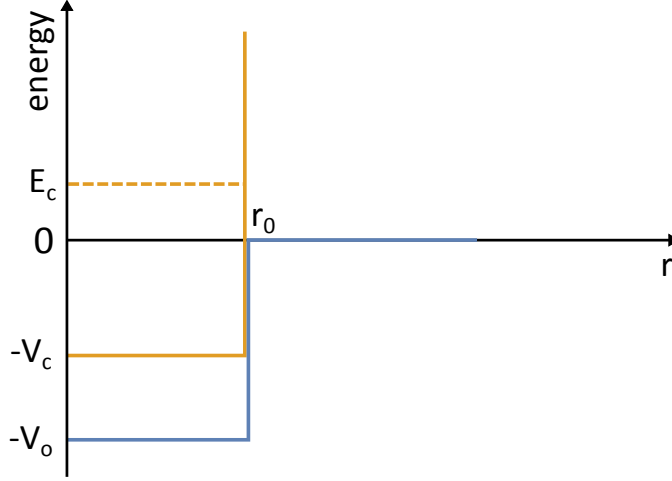
Figure 6.2: Square-well potentials of the simplified Feshbach resonance model defined in Eq. (6.1).

is no longer an eigenstate at closer internuclear distances and changes the character of the bound state, which will be an eigenstate of the total interaction Hamiltonian, different from that of the closed channel potential.

In order to clarify the main characteristics of a Feshbach resonance, let us consider a simple model in which the two molecular potentials are represented by square-well potentials, which can resolved analytically [85, 189]. The two potentials will be given by:

$$V_o(r) = \begin{cases} -V_o & \text{if } r < r_0 \\ 0 & \text{if } r > r_0, \end{cases} \qquad V_c(r) = \begin{cases} -V_c & \text{if } r < r_0 \\ +\infty & \text{if } r > r_0, \end{cases} \qquad (6.1)$$

where r_0 is the characteristic length of the potential (i.e. equivalent to the van der Waals length of a van der Waals potential). Let us also suppose that the closed channel potential can be energetically shifted by an amount $\Delta\mu B$, where $\Delta\mu > 0$ is the differential magnetic moment between the two channels and B the magnetic field. Finally let us consider a coupling potential of the type:

$$V_{oc}(r) = \begin{cases} -V_{oc} & \text{if } r < r_0 \\ 0 & \text{if } r > r_0, \end{cases} \qquad (6.2)$$

with $V_{oc} \ll |V_o - V_c|$. The coupling V_{oc} could embed different types of interactions. In magnetic Feshbach resonances between alkali atoms, open and closed channels are coupled by the hyperfine interaction, but also other mechanism are possible, as will be explained later in this chapter. The total Hamiltonian will be then given by:

$$\hat{H} = \begin{pmatrix} \dfrac{\hbar^2 k^2}{2m_r} + V_o(r) & V_{oc}(r) \\ V_{oc}(r) & \dfrac{\hbar^2 k^2}{2m_r} + V_c(r) + \Delta\mu B \end{pmatrix}, \tag{6.3}$$

where m_r is the mass of the atom pair. This Hamiltonian is valid for generic molecular potentials $V_o(r)$, $V_c(r)$, and the associated Schrödinger equation is analytically solvable for the considered case of square-well potentials. Let us first consider the case in which $V_{oc} = 0$. In this case the Hamiltonian is diagonal and the two potentials can be treated independently. In particular, for zero energy E and $B \neq 0$, only the open channel potential has a wavefunction $\psi_o(r)$ that can be described by the standard scattering theory of section 1.2, resulting in a scattering length a_{bg} which depends on the size of the box. Moreover, both $\psi_o(r)$ and a_{bg} do not depend on the value of the magnetic field. The situation is different for the closed channel potential. The magnetic field shifts the potential depth V_c and the energy of its associated bound state E_c (see Fig. 6.1), which depends linearly on B. In particular, the bound state energy will be zero at the magnetic field value B_0 for which $\Delta\mu B_0 = -E_c(B = 0)$.

The Schrödinger equation can be resolved exactly also in the case in which $V_{oc} \neq 0$, with eigenfuncitons that are combinations of exponentials and oscillating terms. For simplicity, the calculations are not carried out here and only the principal results will be discussed. For $E > 0$, the open channel wavefunction $\psi_o(r)$, will show an oscillating behavior outside the box for $r > r_0$, and a phase shift and related scattering length are introduced by imposing the boundary conditions in $r = r_0$. When $\psi_o(r)$ is coupled to the closed channel wavefuntion inside the box for $r < r_0$, the wavefunction picks up an additional resonant phase shift, due to the presence of the closed channel bound state $E_c(B)$:

$$\delta_0 = \delta_{bg} + \delta_{res}. \tag{6.4}$$

It can be shown [85] that this phase shift, which depends on the magnetic field since it is related to $E_c(B)$, induces a magnetic-field-dependent resonant feature in the scattering length, specifically:

$$a = a_{bg} \left(1 + \frac{\Delta B}{B - B_{res}} \right). \tag{6.5}$$

Several important parameters characterize the Feshbach resonance. The shape is determined by the its position B_{res}, the background scattering length a_{bg} and the width ΔB, that is defined as the difference $B_{res} - B_{zero}$, where B_{zero} is the magnetic field value at which the scattering length is zero. Another important quantity is the bound state energy. In the vicinity of the resonance position B_{res}, where the two channels are strongly coupled, for large positive values of a a "dressed" shallow molecular state exists with a binding energy [85]:
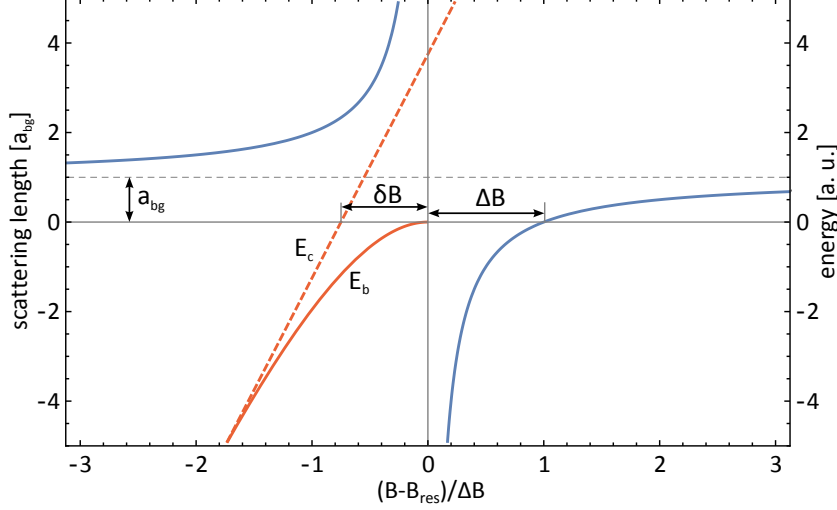
Figure 6.3: Scattering length (blue curve) and binding energy (solid red) as a function of the magnetic field B around a Feshbach resonance. The scattering length diverges at magnetic field B_{res} and has a width ΔB. On the positive scattering length side of the resonance, the bound state energy depends quadratically on the magnetic field and vanishes for $a \to +\infty$ at B_{res}. Far from the resonance, where the mixing between closed and open channel is small, the bound state energy reduces to that of the closed channel bound state E_c, represented by the dashed red line.

$$E_b = -\frac{\hbar}{2m_r a^2}, \tag{6.6}$$

and, since $a \propto B^{-1}$, with a quadratic dependence on magnetic field detuning $B - B_{res}$. This region is of particular interest due to its universal features. Here the molecular state can be well described by a single effective potential with scattering length a given by Eq. (6.5). The bound state energy E_b has a zero crossing in B_{res}, which is shifted by an amount $\delta B = B_{res} - B_0$ from the zero crossing of the unperturbed bound state E_c. In the vicinity of the resonance, where this quadratic behavior holds, the bound state projection on the open channel will be close to 1. Far from the resonance instead, where the state mixing is reduced, the bound state energy reduces to that of the closed channel bound state E_c, as shown in Fig, 6.3, and a linear dependence on the magnetic field is recovered.

In this context, it is possible to introduce the parameter Z, that is defined as the closed channel fraction of the eigenstate of total Hamiltonian and that substantially distinguishes between the shallow bound state behavior, quadratic in the magnetic field, and the linear, closed channel dominated, regime. Near the resonance, for $B \to B_{res}$ and $a \to \infty$, Z is given by [85]:

$$\lim_{a\to\infty} Z = \zeta^{-1} \left| \frac{B - B_{res}}{\Delta B} \right|, \tag{6.7}$$

where the dimensionless parameter ζ^{-1} determines the rate at which the Feshbach bound state state deviates from the open channel dominated regime when B is tuned away from B_{res}. In the case of the box-potential model it is possible to derive an analytic expression of ζ given by:

$$\zeta = \frac{\mu_B}{\hbar^2} a_{bg}^2 \Delta\mu\Delta B. \tag{6.8}$$

This expression clearly shows that the value of ζ is determined by the parameters of the potential (in this particular case, by the magnetic field sensitivity and the background scattering length, in addition to the width ΔB of the resonance). Equation (6.7) suggests that having a small closed channel fraction $Z \ll 1$ implies that $|B - B_{res}| \ll \zeta\Delta B$. If $\zeta \ll 1$ then $|B - B_{res}| \ll \Delta B$, which means that the bound state has open channel character only for a small fraction of the resonance width ΔB. Such resonances are called "closed channel dominated", or "narrow", resonances. If instead $\zeta \geq 1$ then $|B - B_{res}|$ will be of the order of ΔB, that means that the weakly bound character of the molecular state persists over a large portion of the resonance width, and the resonance is well described by Eq. (6.5). In this case, the resonance is defined as an "open channel dominated" or "broad" resonance. The broad or narrow character of the resonance can also be related to the effective range r_{eff} of the potential (see Eq. 1.33) with a similar argument. It can be shown [190] that the open channel population, i.e. the open channel fraction, is given by:

$$P_{\text{open}} = \frac{1}{\sqrt{1 + 4r_{\text{eff}}/a}}. \tag{6.9}$$

This equation implies that $P_{\text{open}} \sim 1$ if $r_{\text{eff}}/a \ll 1$. A high value of the effective range implies that $a \gg r_{\text{eff}}$ only for values of magnetic field in the vicinity of the resonance $|B - B_{res}| \ll \Delta B$, where the scattering length is very high. In this case the resonance will be closed-channel dominated. If instead r_{eff} is small, then the condition $r_{\text{eff}}/a \ll 1$ holds over a wider range of magnetic field and the resonance will be open channel dominated.

6.2 Orbital Feshbach resonances

In the previous section we saw that for a Feshbach resonance to exist, a coupling term between the two molecular potentials is needed. In alkali atoms, the electronic ground state is $^2S_{\frac{1}{2}}$ and if the nuclear spin $I \neq 0$, only two hyperfine sublevels are presents, namely $F = I \pm 1/2$. If a magnetic field is present, the states are split in a Zeeman manifold, and pairs of atoms interact through molecular potentials which depend on their Zeeman level and can be relatively shifted by varying the magnetic field. The mixing between the molecular potentials is provided by the
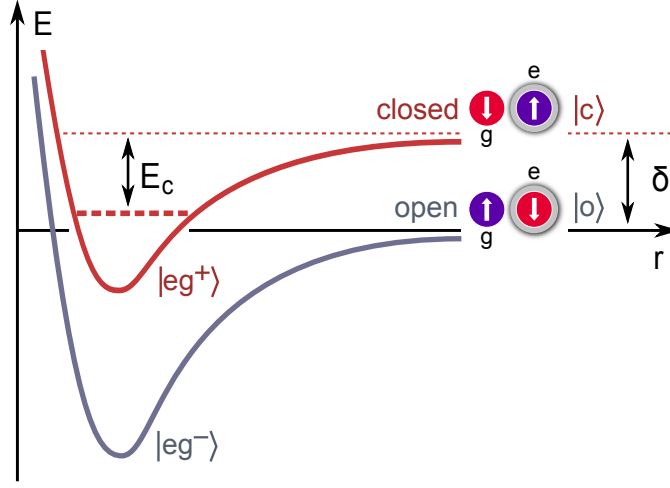
Figure 6.4: Scheme of the ^{173}Yb orbital Feshbach resonance mechanism affecting the scattering between one $|g\rangle = {}^1S_0$ atom and one $|e\rangle = {}^3P_0$ atom in two different spin states (see text for details).

hyperfine interaction, and the condition necessary for a Feshbach resonance to exist are satisfied.

In the case of AEL atoms instead, the ground state has $J = 0$, so even if fermionic atoms with opposite spins $|\uparrow\rangle$, $|\downarrow\rangle$ can interact through different singlet and triplet potentials, no hyperfine interaction is present to provide the mixing between the two, hence no magnetic Feshbach resonance can occur at realistic values of magnetic field. However, it was very recently pointed out in Ref. [58] that the AEL atoms orbital degree of freedom provided by the metastable state can be exploited in order to lead to a new type of Feshbach resonance, the OrbFR, which relies on the spin-exchange interaction described in chapter 5 as state-coupling mechanism.

In order to understand how orbital Feshbach resonances are originated, let us consider a pair of atoms in different electronic orbitals $|g\rangle$, $|e\rangle$ and in different spin states m and m' that we label $|\downarrow\rangle$ and $|\uparrow\rangle$. For large interatomic distances, when the atoms are separated, interactions between them are negligible and the eigenstates of the system are $|e\uparrow, g\downarrow\rangle$ and $|g\uparrow, e\downarrow\rangle$. These states, which are explicitly defined in Eq. (5.4), link a defined nuclear spin to a specific orbital state. At finite magnetic field, these two states have different threshold energies, separated by the differential Zeeman energy $\delta = \Delta\mu B = \delta g \Delta m \mu_B B$, with δg being the differential Landé g-factor. In particular the $|e\uparrow, g\downarrow\rangle$ state will have the higher energy. For this reason we will refer to this state as the closed channel $|c\rangle$, while $|g\uparrow, e\downarrow\rangle$ will be the open channel $|o\rangle$ (see Fig. 6.4). In the rest of the chapter, we will use the more compact notation $|o\rangle$ and $|c\rangle$ for the states $|g\uparrow, e\downarrow\rangle$ and $|e\uparrow, g\downarrow\rangle$, respectively. At lower interatomic distances, the interactions are no longer negligible, and, as showed in section 5.1.1, atoms can couple in two anti-symmetric states $|eg^{\pm}\rangle$, defined in

Eq. (5.5) as linear combinations of the states $|o\rangle$ and $|c\rangle$. The very strong inter-orbital spin-exchange interaction V_{ex}, giving rise to a coupling between $|o\rangle$ and $|c\rangle$ (see also Eq. (5.30)), becomes resonant when the Zeeman energy δ equals the binding energy E_c of the least bound state in the closed channel. This coupling mechanism is completely different from the hyperfine coupling, typical of magnetic Feshbach resonances.

A formal demonstration of the orbital Feshbach resonance can be found in Ref. [58]. The non interacting Hamiltonian in the $\{|o\rangle, |c\rangle\}$ basis is given by:

$$\hat{H}_0 = \left(\frac{\hbar^2 \nabla^2}{2m_r} + \delta\right) |c\rangle \langle c| + \left(\frac{\hbar^2 \nabla^2}{2m_r}\right) |o\rangle \langle o|, \tag{6.10}$$

where m_r is the reduced mass. As shown in section 5.1.1, the interaction potential is instead diagonal in the $|eg^\pm\rangle$ base, and in particular it is given by Eq. (5.8), that for clarity we rewrite as:

$$\hat{V} = V(|o\rangle \langle o| + |c\rangle \langle c|) + V_{ex}(|c\rangle \langle o| + |o\rangle \langle c|), \tag{6.11}$$

where V and V_{ex} are the direct and exchange pseudo-potentials (see section 5.1.1), respectively, with direct and exchange scattering lengths a_d and a_{ex} given respectively by:

$$a_d = \frac{a_{eg}^+ + a_{eg}^-}{2}, \qquad a_{ex} = \frac{a_{eg}^+ - a_{eg}^-}{2}. \tag{6.12}$$

Defining then the two-body scattering wave function as [58]:

$$|\psi\rangle = \left[e^{i\mathbf{k}\mathbf{r}} + f_o(k)\frac{e^{ikr}}{r}\right] |o\rangle + f_c(k)\frac{e^{-\sqrt{m\delta/\hbar^2 - k^2}\, r}}{r} |c\rangle, \tag{6.13}$$

where $f_{o,c}(k)$ are the scattering amplitudes for the open and closed channels, and by solving the Schrödinger equation $(\hat{H}_0 + \hat{V}) |\psi\rangle = E |\psi\rangle$ with $E = \hbar^2 k^2/2m_r$, it is possible to find an expression for the scattering amplitude $f_o(k)$, which directly leads to a magnetic field dependence of the open channel scattering length $a_s = \lim_{k \to 0} f_0(k)$. The simple result for the pseudo-potential, which we do not report here, can be easily extended to the case of a potential with finite van der Waals range r_0 [58], obtaining:

$$a_s = \frac{-a_d + \sqrt{m\delta/\hbar^2}[(a_d^2 - a_{ex}^2) - r_0 a_d]}{\sqrt{m\delta/\hbar^2}(a_d - r_0) - 1}, \tag{6.14}$$

where r_0 is the van der Waals length and in which the magnetic field dependence is contained in the term δ. It should be noted that the spin-exchange interaction term is crucial for the existence of the orbital Feshbach resonance. Indeed, in case of zero exchange interaction $V_{ex} = 0$, the exchange scattering length $a_{ex} = 0$ and the scattering length a_s becomes a constant, specifically, $a_s = a_d$. In this case, there is no mixing between open and closed channels, and the Feshbach resonance cannot
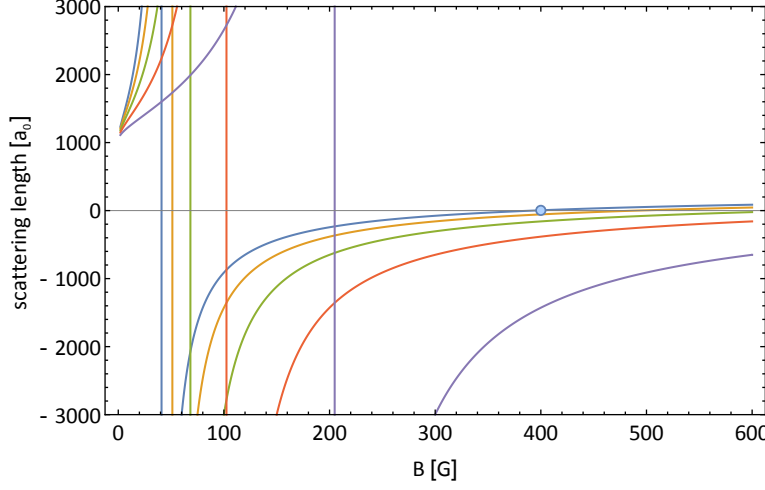
Figure 6.5: Scattering length a_s of Eq. (6.14) plotted as a function of the magnetic field for $\Delta m = 1, \cdots, 5$. The resonance positions are identified by the colored vertical lines. The resonance magnetic field is lower (~ 40 G) for $\Delta m = 5$ (blue line) and increases as Δm^{-1}. The blue circle identifies the zero crossing for the $\Delta m = 5$ mixture around 400 G.

occur. If instead $V_{ex} \neq 0$, there is a non-zero mixing between open and closed channel, allowing for the existence of the orbital Feshbach resonance, which will have a width ΔB determined by the value of the exchange scattering length a_{ex}. In particular, a stronger mixing, and thus a higher value of a_{ex} imply a higher ΔB. The resonance position will instead be determined by the direct scattering length a_d. Indeed, according to Eq. (6.14), the scattering length a_s has a divergence for:

$$\delta = \delta_{res} = \frac{\hbar^2}{m(a_d - r_0)^2},\qquad(6.15)$$

where $m = 2m_r$ is the atomic mass. This equation shows that the resonance will be located at lower values of magnetic field for higher values of the direct scattering length a_d. This is a direct consequence of the fact that a high value of a_d implies a shallow closed channel bound state $|E_c| = \hbar^2/ma_d^2$, so that the Zeeman energy δ equals the E_c for low values of magnetic field. For this reason, Ytterbium is an ideal candidate for the observation of orbital Feshbach resonances: the values of the scattering lengths $a_{eg}^{\pm}$ reported in Chapter 5 imply a direct scattering length a_d of the order of thousands of Bohr radii, meaning that the resonance is expected to be located in a very convenient range of a few tens of gauss. This is a major advantage with respect to other systems, for example ^{87}Sr in which, due to the very small inter-orbital scattering length, the OrbFR is expected to be located at magnetic field of the order of $10^3 - 10^4$ G. Another remarkable feature of OrbFR that can be deduced from Eq. (6.15) is that, since δ is proportional to Δm, the magnetic field B at which the resonance is observed scales as Δm^{-1}. This is a direct consequence of the SU(N) interaction symmetry, that causes the binding energy

E_c to be independent on Δm. As a consequence, the energy $\delta = \delta g \Delta m \mu_B B$ for which the coupling between $|o\rangle$ and $|c\rangle$ is resonant has to be the same in all the spin mixtures Δm, hence the scaling with Δm.

Finally, it is possible to identify a zero-crossing of the scattering length a_s in:

$$\delta = \delta_0 = \frac{\hbar^2}{m(a_d - r_0 - a_{ex}^2/a_d)^2}. \tag{6.16}$$

In Fig. 6.5, we show the plot of the scattering length for different spin mixture with $\Delta m = 1, \ldots, 5$, where we have used the parameters $\delta g \mu_B = 2\pi\hbar \times 113$ Hz/G, $r_0 = 84.8 \, a_0$ Ref. [33] and the value $2a_d = a_{eg}^+ + a_{eg}^- \approx 2100 \, a_0$, that we estimate from our experimental measurements (see section 6.3.2). The curve shows that the resonance position scales with Δm^{-1}. In particular, the resonance for the $\Delta m = 5$ mixtures is located at the minimum value of magnetic field (~ 40 G) and is represented by the blue curve. This curve also shows a zero crossing around 400 G, represented by the blue circle.

6.3 Observation of orbital Feshbach resonances

In this section, we discuss the experimental observation of orbital Feshbach resonances in ultracold Fermi gases of ^{173}Yb, which was very recently reported in for the first time in [57].

6.3.1 Detection of the strongly interacting regime through hydrodynamic expansion

In the experiment, we prepare different two-spin component mixtures with spin $m_\uparrow$ and $m_\downarrow$ and with $\Delta m = m_\uparrow - m_\downarrow$. The atoms are cooled in the crossed ODT at 1064 nm down to the degenerate level, obtaining a Fermi gas with a total atom number of $N_{at} \simeq 60 \times 10^4$ at $T \simeq 0.15T_F$. The gas is subsequently loaded in a second ODT operating at the magic wavelength $\lambda = 759$ nm, which traps both $|g\rangle$ and $|e\rangle$ atoms and does not shift the $|g\rangle \rightarrow |e\rangle$ transition frequency, and with beam waist $\sim 30 \, \mu$m. The ODT is superimposed to optical lattice 1 (OL1) beam (which is not used in this experiment). This beam results in a cigar-shaped trap with trapping angular frequencies $\vec{\omega} = 2\pi \times (13, 188, 138)$ Hz, which imply a peak atomic cloud density $n \simeq 2.4 \times 10^{13}$ cm^{-3} per spin component. In this way the investigated system consists in a 3D gas, in which no confinement induced resonances are present [191, 192], so that we directly probe the effect of orbital Feshbach resonances. In order to excite the atoms in the $|e\rangle$ state without imparting a momentum kick to the system, we direct the 578 nm laser beam on an alternative path, which is superimposed with (OL2). The lattice beam is slowly ramped up to $s = 30$, and the $m_\downarrow$ atoms are excited to the state $|e\rangle$ with a 400 μs pulse of 578 nm light. In this way, the excitation is performed in a deep Lamb-Dicke regime (see section 4.2.1), and the atoms are transferred in the state $|e\rangle$ with a $\geq 80\%$ efficiency
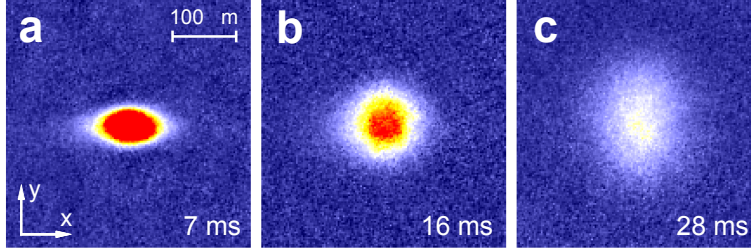
*Figure 6.6: False color absroption images of the remaining $|g\rangle$ atoms after the excitation in the open channel for different expansion times t_{tof} (**a.** 7 ms, **b.** 16 ms, **c.** 28 ms). At short time of flight the could shape is determined by the shape of the trap, while at longer t_{tof} the aspect ratio of the cloud inverts due to the higher interaction energy in the strongly confined direction.*

without imparting an optical momentum kick in order to maintain the system at equilibrium. Since the atoms are not isolated like in the case of the 3D lattice, a fast excitation pulse is important in order to minimize inelastic losses during the excitation, so the transition is power broadened in order to achieve faster Rabi frequencies (see section 4.2.2). In order to resolve the Zeeman components of the transition and only excite only one spin state, the excitation is performed at an high magnetic field B_{exc} ranging from 72 to 167 G. Moreover, at these magnetic field values the Zeeman energy is higher than the exchange energy, and the open and closed channels are the eigenstates of the Hamiltonian. In this way it is possible to excite the open channel $|o\rangle$ by exciting the $m_\downarrow$ atoms, which have a lower clock transition frequency. After the excitation, the optical lattice is ramped down to zero in 100 ms to recover a 3D atomic gas. At this point, the magnetic field intensity is changed to desired B value in $\sim$ 2 ms. Immediately after, the 759 nm trap is suddenly switched off, and the remaining ground state atoms are imaged after a time of flight t_{tof}.

In order to detect the onset of a strongly interacting regime, we keep the magnetic field at the value B during the first 5 ms of the expansion, allowing for the release of their interaction energy into kinetic energy, and we observe the evolution in time of flight of the cloud aspect ratio (AR) R_y/R_x, with R_y and R_x being the atomic cloud radii along the directions of strong and weak confinement, respectively. Under these conditions, a weakly interacting gas will expand ballistically, eventually resulting in a spherical shape (aspect ratio value of 1) for sufficiently long expansion times (much larger than the inverse trap frequencies) [193]. On the contrary, the observation of the aspect ratio inversion would represent a signature of hydrodynamic regime for the Fermi gas, which has already been observed for alkali fermionic gases close to magnetic Feshbach resonances [194]. This hydrodynamic regime occurs in presence of strong interactions, which is a necessary condition for the onset of fermionic superfluidity [195–197]. In the hydrodynamic limit, the collisional rate Γ is larger than the geometric trapping frequency $\bar\omega = (\omega_x\omega_y\omega_z)^{1/3}$, causing
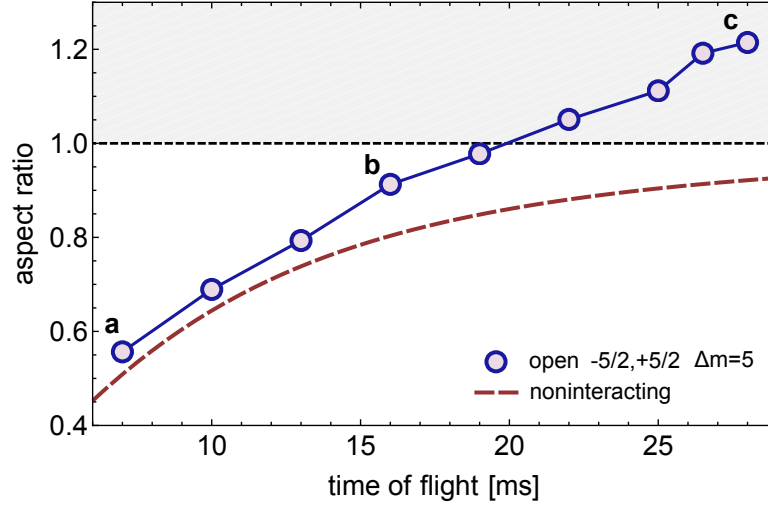
133

*Figure 6.7: Aspect ratio of a strongly interacting ^{173}Yb Fermi gas prepared in the open channel at B = 41 G as a function of the time of flight. The circles represent the experimental data, and the labels **a**, **b**, **c** refer to the images in Fig. 6.6. The long-dashed gray line represents the behvior expected from a non-interacting Fermi gas. The short-dashed black line indicates the limit above which the experimental aspect ratio gets inverted because of hydrodynamic expansion.*

a faster expansion along the tightly confined axis of the harmonic trap because of the larger density gradient. This can be clearly seen in Fig. 6.6, which shows false color absorption images of an atomic cloud with nuclear spin components $m_{\downarrow} = -5/2$ $m \uparrow = +5/2$ at magnetic field $B = 41$ G for different value of time of flight t_{tof}, that clearly show an inversion of the cloud shape from prolate to oblate. Fig. 6.7 shows instead the evolution of the aspect ratio as a function of t_{tof}, represented by the circles (the points corresponding to the images in Fig. 6.6a,b,c are labeled with the corresponding letter). The aspect ratio exceeds 1 for $t_{tof} \simeq 18$ ms and differs clearly from the long-dashed curve, which represents the aspect ratio evolution in the non-interacting case, approaching 1 in the far field limit. It should be noted that the value of the aspect ratio in the strongly interacting regime is lower than that predicted by the hydrodynamic equations of superfluids at resonant interactions (≈ 2 at our maximum expansion time) [198]. This discrepancy has been already observed in [199], and could be ascribed to the fact that the expansion does not take place entirely in the hydrodynamic regime, possibly due to a narrow character of the OrbFR [200]. Indeed, as pointed out in section 6.1, a narrow resonance implies a large effective range r_{eff}. In this case, the term depending on r_{eff} of Eq. (1.33) cannot be neglected and the scattering amplitude (1.32) features an additional dependence on k. In this case, it is possible that part of the gas is not in the hydrodynamic regime. It is anyhow important to stress that the effective range of the potential is not yet known and further theoretical investigation is necessary in order to definitively attribute a narrow or broad character to the resonance.
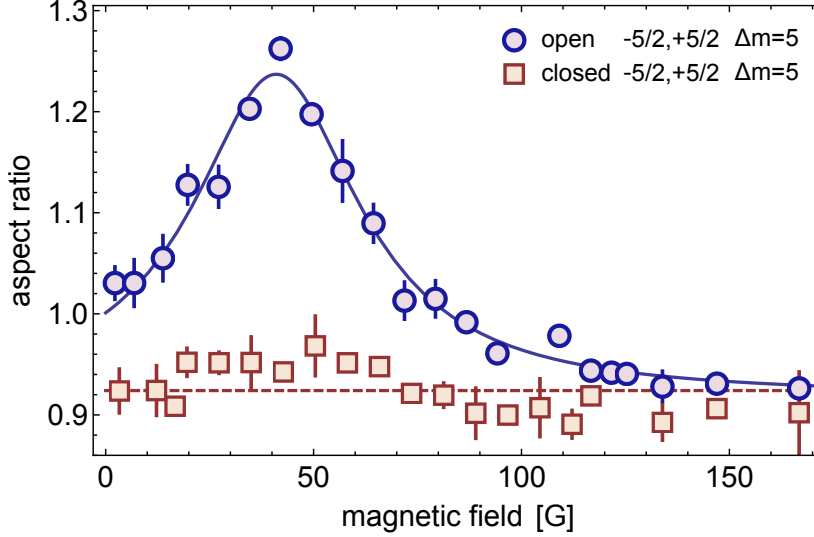
Figure 6.8: Aspect ratio of the atomic cloud after t_{tof} = 28 ms as a function of the magnetic field B for a Δm = 5 mixture. The gray squares correspond to the AR measured in a mixture prepared in the closed channel, whereas the blue circles correpond to the AR measured in a mixture prepared in the open channel. The resonant feature of the latter is fitted with a Lorentzian curve (blue solid line). The aspect ratio background signal is less than one because the expansion is not fully in the far-field limit.

6.3.2 Location of orbital Feshbach resonance

In order to detect and locate the OrbFR predicted in Ref. [58], we study the dependence of the asymptotic value of the aspect ratio as a function of the magnetic field B, after the excitation of the open channel. In this way, the anisotropy discussed in the previous section is used as a tool to detect the magnetic field values at which the onset of the strongly interacting regime occurs, as already studied in the case of alkali atoms [199]. The results of this measurement for the spin mixture with Δm = 5 at time of flight t_{tof} = 28 ms are reported in Fig. 6.8. The blue circles correspond to the excitation of the open channel, showing a maximum of the anisotropy around $B \sim 40$ G, which is a clear signal of enhancement of the elastic collisional rate at the Feshbach resonance above the hydrodynamic regime. If compared with the typical width of magnetic Feshbach resonances in alkali atoms, this resonance shows a large feature, which is anyhow not related to a broad character of the resonance itself. Indeed, this behavior a consequence of the very small magnetic sensitivity of the energy levels, which depends on the nuclear magneton and is three orders of magnitude lower than in alkalis. The data are fitted with a Lorentzian curve, which is only used to determine the center of the resonant feature. The result of the fit is represented by the solid blue line, and is centered at $B = (41 \pm 1)$ G. The grey squares represent instead the aspect ratio at t_{tof} = 28 ms after the excitation of the closed channel. No resonant feature is observed, and for all the magnetic field values, the measured aspect ratio remains
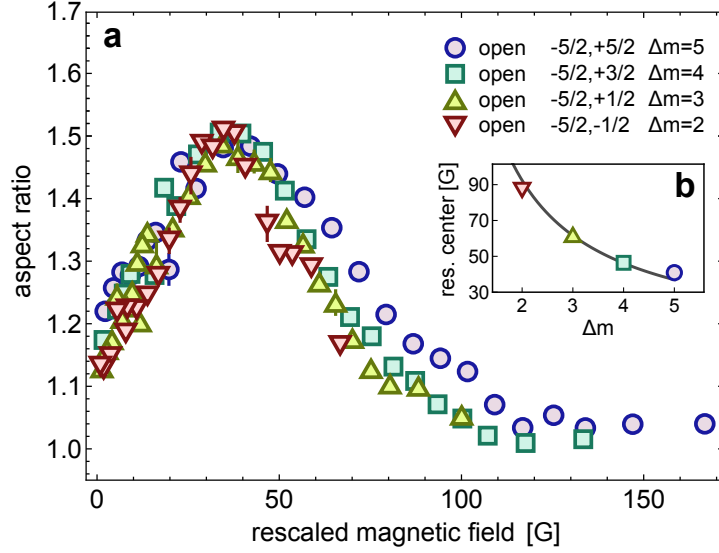
Figure 6.9: **a.** *Comparison between open channel mixtures with different* Δm, *plotted as a fuction of a rescaled magnetic field* $\bar{B} = B\Delta m/5$. *Different colors refer to different* Δm. *The different datasets collapse onto the same curve thus verifying the OrbFR scaling law, which is in turn a direct consequence of the* $SU(N)$ *symmetry of two-electron atoms.* **b.** *Resonance centers of the data shown in* **b** *before the magnetic field rescaling plotted versus* Δm. *The line is a fit with the expected* Δm^{-1} *behavior.*

constant slightly below the predicted value of 1 in the non-interacting case. The same background value is observed also for the excitation of the open channel at high values of magnetic field. This may be ascribed to the expansion non being fully in the far-field limit, so that the cloud has no time to reach the steady value of 1.

It should be noted that, while we exclude possible confinement-induced shifts due to the low trapping frequencies, the resonance position can be affected by finite energy effects. The closed channel features a bound state with energy $|E_c| = \hbar^2/ma_d^2 \sim h \times 20\,\text{kHz}$, where a_d as been defined is Eq. (6.12), only about one order of magnitude higher than the Fermi energy $k_b T_F \sim h \times 4\,\text{kHz}$, so also scattering states in the closed channel may play a role [58]. Moreover, the Fermi energy spread corresponds to a magnetic field width $k_B T_F/\Delta\mu \sim 7\,\text{G}$ for a $\Delta m = 5$ sample, which may contribute to the observed width of the resonance. Nevertheless, from the fitted position of the maximum of Fig. 6.8, by using Eq. (6.15) and a van der Waals length $r_0 = 84.8\,a_0$ Ref. [33] we obtain $2a_d = a_{eg}^+ + a_{ag}^- \approx 2200\,a_0$. It should be noted that this is only a rough estimate, also considering the aforementioned possibly narrow character of the resonance due to the tiny energy scales involved in the process. In order to determine a more precise value, additional theoretical investigations are required as well as further experimental efforts. However, with this value and by using the model in Eq. (6.14) we obtain the behavior of the scattering length as a function of the magnetic field for the $\Delta m = 5$ case, which is represented by the blue

line in Fig. 6.5. From this model it is also possible to estimate the magnetic field value at which the scattering length features a zero crossing, obtaining $B \approx 400$ G. This value lays outside the range of our experimental setup (~ 170 G), but has been confirmed in the independent measurement of Ref. [188].

We have repeated the same measurement also for mixtures with progressively smaller Δm values, finding that the resonance position is shifted towards significantly larger magnetic field values. The results of these measurement are reported in Fig. 6.9a for all the values of Δm, with the exception of $\Delta m = 1$ whose center lies outside the accessible magnetic field range. The different peak aspect ratio with respect to Fig. 6.8 is due to the different employed excitation scheme, in which the atoms are excited directly, without the application of the optical lattice, in a 3D trap with different trapping frequencies $\vec{\omega} = (22, 181, 139)$ Hz. In order to highlight the scaling with Δm, each resonance is plotted versus a rescaled magnetic field $\bar{B} = B\Delta m/5$. The different datasets clearly show a very similar dependence on $\bar{B}$, which is a distinctive feature of the OrbFR mechanism and a direct consequence of the SU(N) interaction symmetry of ^{173}Yb. In particular, the collapse of the experimental data onto the same curve verifies the scaling with Δm^{-1}, as can also be seen by Fig. 6.9b in which the resonance centers before the rescaling are plotted versus Δm and fitted with a function proportional to Δm^{-1}.

6.3.3 Inelastic losses

For future studies of many-body physics exploiting this novel experimental scheme, it is important to understand the effect of inelastic losses across the orbital Feshbach resonance. With this aim, after the two-orbital Fermi gas prepared in the open channel is loaded in the 3D dipole trap at 759 nm, we wait for a variable time t_{hold} before switching the trap beams off. After a time a flight $t_{tof} = 28$ ms we measure the aspect ratio and the residual number of atoms N_g in the $|g\rangle$ state. Fig. 6.10 shows the measured aspect ratio as a function of the holding time at $B = 60$ G in the trap, while Fig. 6.10 shows the number of atoms N_g. The aspect ratio slowly decays, with a $1/e$ lifetime $\tau \simeq 380$ ms, towards an asymptotic value slightly smaller than 1, corresponding to a weakly interacting regime as already observed in Fig. 6.8. As already mentioned in the previous section, this value of the aspect ration is lower than 1 because the expansion is not fully in the far-field limit. On the same timescale, N_g decreases towards a non-zero value. This decay can be interpreted as the result of inelastic collisions between $|g\rangle$ and $|e\rangle$ atoms progressively emptying the two states. As a consequence of the atom loss, the gas slowly becomes less and less interacting until the conditions for being in the hydrodynamic regime are abandoned. The non-zero asymptotic value of N_g can be ascribed to an unbalance in the state preparation, that causes the initial number of $|g\rangle$ atoms to be higher than that of $|e\rangle$ atoms.

We note that the smooth decay of the aspect ratio in Fig.6.10 is an evidence of the absence of shape excitations of the atomic cloud, confirming the adiabaticity of the excitation and trap loading procedures. Indeed, non-adiabatic procedures
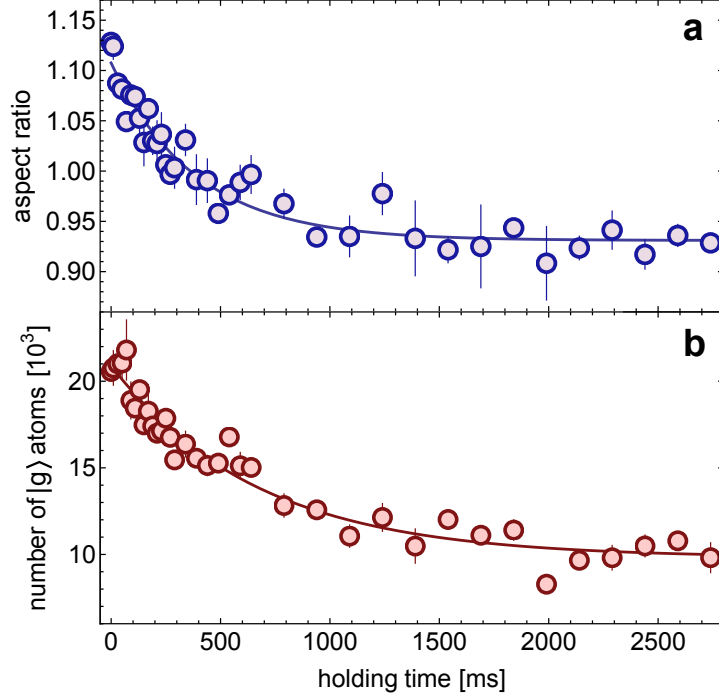
Figure 6.10: **a.** *Evolution of the aspect ratio for a* $\Delta m = 5$ *cloud, initially prepared in the open channel, after different holding times in the 759 nm trap at* $B = 60$ *G and a fixed time of flight* $t_{tof} = 28$ *ms. The asymptotic value of the aspect ratio is less than one because the expansion is not fully in the far-field limit.* **b.** *Number of atoms for the same experimental parameters as in* **a.**

would have induced oscillations on timescales of the order of the inverse trap frequencies, which instead are not observed. Moreover, we have also verified, by means of OSG nuclear spin detection, that no inter-orbital spin-exchange dynamics takes place during the experiment. This is mainly determined by the fact that the spin-exchange interaction V_{ex} is low in the 3D trap geometry employed in the experiment. This causes the open and closed channel to be well defined ($\delta \gg V_{ex}$) even for low differential Zeeman energies, and close the the Feshbach resonance we do not observe any significant repopulation of the atoms in the $|g, m_\downarrow\rangle$ state which was initially emptied during the loading of the open channel.

As a final characterization, we studied the atoms losses as a function of the magnetic field across the Feshbach resonance. The results of these measurements are reported in Fig 6.11. The lifetimes are estimated from a fit of the experimental data with a single exponential function, as in Fig. 6.10, used to globally quantify the losses. Actually, atom losses may be caused by several decay processes, including atom+dimer and dimer+dimer inelastic collisions [201, 202], but the characterization of the specific decay channels goes beyond the scope of this work and shall be investigated in future works. However, also a single exponential approximation leads to interesting insights on possible exploitability of such resonance for
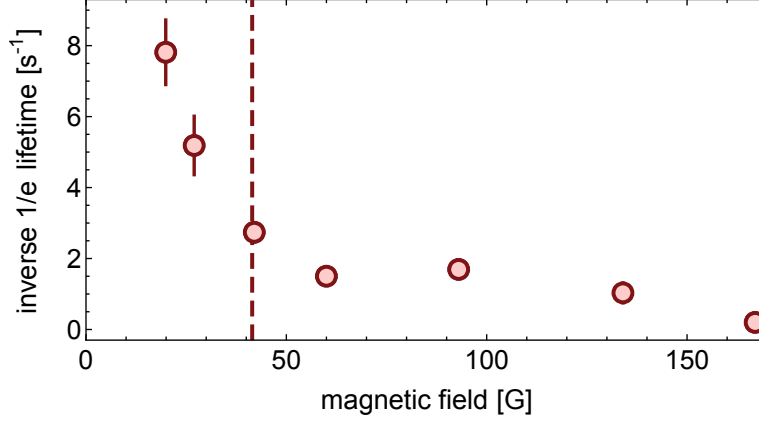
Figure 6.11: Inverse 1/e lifetime of the $\Delta m = 5$ open-channel mixture as a function of the magnetic field. On the BEC side of the resonance the losses are increased due to the presence of multiple decay channels.

many-body physics applications. Indeed, as Fig 6.11 shows, lifetime is strongly asymmetric with respect to the center of the Feshbach resonance. In particular, the loss rate increases on the BEC side (with positive scattering length) of the resonance, as a consequence of the activation of the aforementioned inelastic channels. Noticeably, however, the observed lifetime at the resonance seems to be rather long, with a $1/e$ lifetime of ≈ 350 ms measured at $B = 41$ G. For this reason, orbital Feshbach resonances represent a promising tool for future implementation of novel many-body physics simulation schemes with Ytterbium atoms.

Chapter 7

Review of other results

In this chapter we discuss further experimental results achieved during these years, regarding the investigation of the role of spin multiplicity in interacting one-dimensional systems [32] and the observation of edge physics in synthetic Hall ribbons through a hybrid 2D lattice made of a real and a synthetic dimension [203]. Since the phenomena observed in these experiments do not directly involve two-orbital physics, which is the main focus of this work, they are only concisely discussed in the following sections, for sake of briefness. The two experiments are described in details, both from the theoretical and experimental point of view, in the PhD theses of my coworkers G. Pagano [111] and M. Mancini [116], and in two related papers [32, 203].

7.1   A one-dimensional liquid of fermions with tunable spin

Correlations in systems with spin degree of freedom are at the heart of fundamental phenomena, ranging from magnetism to superconductivity. The system dimensionality strongly influences the effects of correlations, a subject which was extensively studied theoretically over the past fifty years in both fermionic and bosonic systems[204–209]. Considering the case of fermions, a 2D or 3D fermionic system can be described by the Landau-Fermi liquid theory. In this model, excitation of quasi-particles with arbitrary small energy can exists for every momentum $\mathbf{q}$, annihilating a particle below the Fermi surface and recreating it above. The presence of interactions doesn't change much with respect to the non-interacting case. The elementary particles of such a system are fermionic quasi-particles, fermions dressed by the density fluctuations around them, which behave as they were essentially free with an effective mass m^*.

In one dimension instead, a fermion that tries to propagate has to "push" the other particles because of the constraints of the direction of motion so that any single-particle excitation becomes a collective one (see Fig. 7.1). Introducing the spin degree of freedom further complicates the description, as a single fermionic excitation splits into a collective mode carrying density (or "charge") and a collective
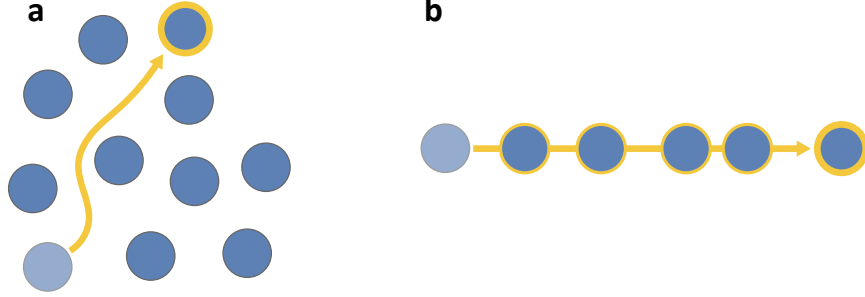
141

Figure 7.1: **a.** *In more than one dimension, quasi-particle excitations exist.* **b.** *In a one-dimensional interacting system instead, only collective excitations can exist.*

mode carrying spin. This characteristic clearly makes any attempt to describe the situation within the Fermi liquid framework unsuccesful. A one-dimensional interacting Fermi gas is instead described by the long-standing Luttinger Liquid model [204, 210, 211] in the low-q regime. In 1D, the zero range interaction g_{1D} of the type $U(x) = g_{1D}\delta(x)$ is given by the expression [212]:

$$g_{1D} = -\frac{2\hbar^2}{ma_{1D}} = \frac{2\hbar^2}{m}\frac{a_{3D}}{a_\perp}\frac{1}{1 - 1.033a_{3D}/a_\perp}, \tag{7.1}$$

where a_{3D} is the scattering length in 3D and $a_\perp = \sqrt{\hbar/m\omega_\perp}$ is the harmonic oscillator length of the external harmonic confinement, transverse to the 1D string[1]. With this definition, interactions can be parameterized with the adimensional parameter [213]:

$$\gamma = \frac{mg_{1D}}{\hbar^2 n_{1D}} = \frac{2}{a_{1D}n_{1D}}, \tag{7.2}$$

where n_{1D} is the one-dimensional density. Eq. (7.2) has the counterintuitive consequence that the role of interactions increases by decreasing the density of the sample. Following the approach of Refs. [214, 215], the Luttinger liquid model can be extended to the case of ultracold atoms, finding that the low energy physics of the system is completely described by three quantities, the charge and spin "sound" velocities v_c and v_s, respectively, and the charge Luttinger parameter $K_c = K^2$. These quantities depend non-trivially on the interaction strength parameter γ. In general, for non zero interactions ($\gamma \neq 0$) the two sound velocities are different, giving rise to the so-called spin-charge separation. The parameter K instead varies from $K = 1$ in the non-interacting case to $K = 0.5$ for $\gamma \to \infty$.

The Luttinger theory discussed up to now is valid for the case of a two-spin components system. A comprehensive model for the case of higher spin multiplicity

---

[1]The energy $\hbar\omega_\perp$ have to be the highest energy scale of the system in order to consider it truly one-dimensional.

[2]A fourth parameter, the spin Luttinger parameter K_s is identically $K_s = 1$ for a spin-rotationally invariant system, like a SU(N)-interacting gas.

is still lacking, as well as a systematic experimental investigation. Exploiting the possibility to prepare stable mixtures of SU(N) interacting atoms we investigated for the first time the physics of one-dimensional systems as a function of the number of spin components N [32, 111], in an intermediate coupling regime with $\gamma \simeq 4.8$ and $K \simeq 0.73$. In the following sections, we will see how inter-particle interactions cause static and dynamic properties of one-dimensional fermions to significantly deviate from the Luttinger theory when the sample is prepared in more than two spin states.

7.1.1 Momentum distribution

We prepare a ^{173}Yb degenerate Fermi gas trapped in an harmonic potential at $T < 0.3T_F$ and with $N_{at} \simeq 6500$ atoms per spin component. The spin population distribution is initialized using the optical pumping techniques described in section 2.2.2. The atoms are confined in one-dimensional wires by loading the Fermi gas in a two-dimensional optical lattice at 759 nm(see section 2.2.1) at $s = 40$, corresponding to a transverse trapping angular frequency $\omega_\perp \simeq 2\pi \times 25$ kHz. Since the energy $\hbar\omega_\perp$ is more than one order of magnitude larger than the Fermi energy, the occupation of excited radial modes is negligible, which makes our wires truly one-dimensional. After a 10 ms holding time, the trap is suddenly switched off in less then 10 ms. After a ballistic expansion of $t_{TOF} = 23$ ms, the sample is detected by means of absorbtion imaging (section 2.2.2), as done in previous works to measure the momentum distribution $n(k)$ of a Tonks-Girardeu gas [22]. The momentum distribution is obtained by integrating the images along the strong-confinement direction (orthogonal to the 1D wires), normalizing to the same unity area, and fitting it with the Fermi gas momentum distribution function. Due to the presence of the axial harmonic confinement, with(angular) frequency ω_x ranging from $2\pi \times 60$ Hz to $2\pi \times 100$ Hz (depending on the particular experiment), the number of atoms per tube decreases from a maximum of 20 (per spin component) in the central tube, to a vanishing occupation of the more peripheral tubes [111]. The final momentum distribution is then found by averaging over the contribution from the different independent wires.

The result of the measurement for different numbers of spin components in reported in Fig. 7.2. In the non-interacting case the data (solid blue) are very well accounted for by the theory of a trapped ideal Fermi gas (dashed blue). Increasing the number of spin components N, we observe a clear monotonic broadening of $n(k)$, with a reduction of the weight at low k and a slower decay of the large-k tails. The observed $n(k)$ broadening arises from a pure many-body effect and is not accounted for by standard mean-field physics [32]. Indeed, if we consider a mixture of spin-1/2 fermions in the limit of infinite repulsive interaction, the density-density correlation function $G_{\uparrow\downarrow}(d) = \langle \hat{n}_\uparrow(x+d)\hat{n}_\downarrow(x)\rangle$ (where $\hat{n}_\uparrow(x)$ and $\hat{n}_\downarrow(x)$ are the density operators for the two spin components) falls to zero for $d \to \infty$ as $G_{\uparrow\uparrow}(d)$ does in the case of a spin polarized gas, thus mimicking the effects of Pauli repulsion between distinguishable particles. This fermionization, restricting the effective
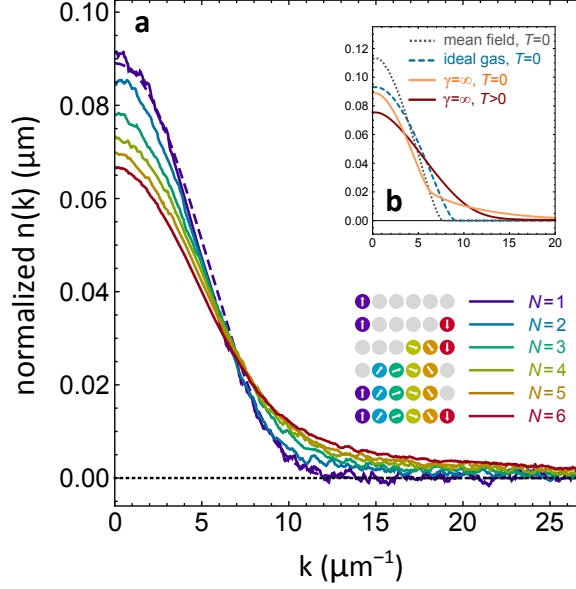
Figure 7.2: **a.** *Momentum distribution* $n(k)$ *measured with time-of-flight absorption imaging for different number of spin components N and with the same atom number* N_{at} *per spin component. Each curve results from the average of* $30 - 50$ *experimental images.* **b.** *Theoretical* $n(k)$ *for a N = 2 system derived using different models: ideal Fermi gas at* $T = 0$ *(dashed), mean-field treatment of finite interactions at* $T = 0$ *(dotted), full many-body problem for infinite interactions both for* $T = 0$ *(light solid) and* $T > 0$ *(dark solid). Only the many-body curves account for the observed broadening.*

space which is available to the particles, causes them to populate states with larger momentum [216, 217]. We note that an opposite behaviour would be predicted by a mean-field treatment of interactions: the effectively weaker confinement along the wire induced by the atom-atom repulsion would lead to more extended single-particle wavefunctions, hence to a decreased width of $n(k)$. Moreover, the details of $n(k)$ depend nontrivially on the temperature, owing to the thermal population of spin excitations. The finite temperature leads to a further broadening of the $n(k)$ (as showed in the inset of Fig. 7.2), explainable in terms of modified effective Fermi momentum [218]. This aspect is further discussed in [32, 111].

7.1.2 Excitation spectrum

A distinctive feature of 1D fermions is the existence of a well-resolved excitation spectrum at low momenta $q \ll k_F$. Number conserving excitations in the ideal 1D Fermi gas correspond to particle-hole pairs with energy $\hbar\omega = v_F \hbar q$, where v_F is the Fermi velocity. In case of an interacting gas, according to Luttinger theory excitations acquire a purely collective character and the spectrum of phononic excitations will be described by a linear dispersion $w = cq$, where $c = v_F/K$ is a renormalized sound velocity which, in a two-component mixture, is larger than the
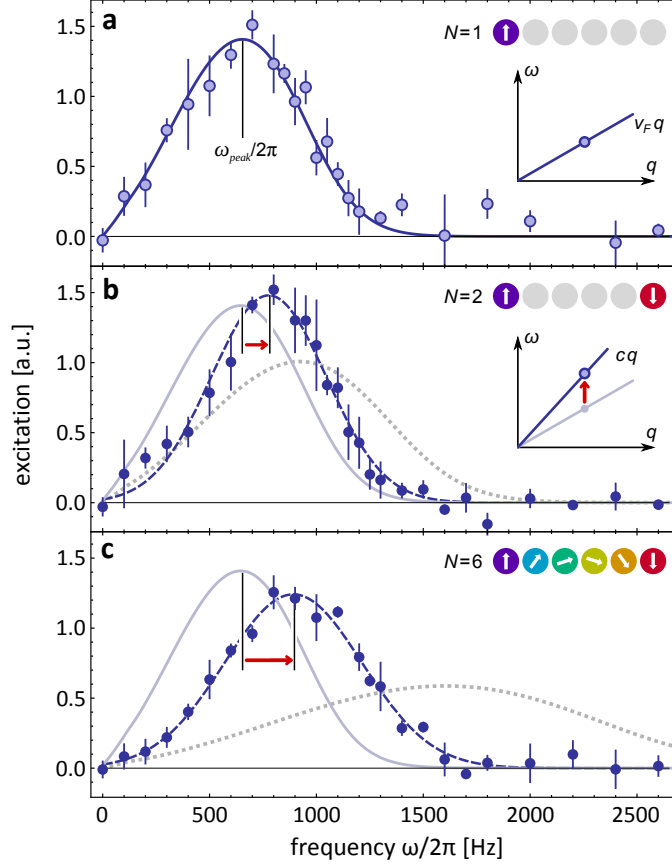
Figure 7.3: **a.** *Excitation spectra for non-interacting fermions in 1D. The points show the measured increase in atomic momentum transfer after a Bragg excitation with energy $\hbar\omega$ at a fixed momentum $q \simeq 0.2 k_F^0$ for $N = 1$. The solid line is the calculated response function for the ideal Fermi gas.* **b,c.** *Excitation spectra of the 1D interacting fermions with number of spin components $N = 2$ (**b**) and $N = 6$ (**c**). The dashed lines are Gaussian fits to the experimental points to extract the peak excitation frequency. The dotted lines represent the calculation in the limit of infinite repulsion. Both experimental and theoretical spectra have been normalized to unit area. The graphs in the inset show a sketch of the increase of the dispersion relation curve at low q passing from ideal to two-component Fermi gas. The red arrows indicate the shift in the excitation resonance.*

Fermi velocity since the Luttinger parameter K lies in the interval $0.5 < K < 1$. The excitation spectrum of the fermionic tubes is characterized by performing Bragg spectroscopy, which allows for the selective excitation of density waves with energy $\hbar\omega$ and momentum $\hbar q$ [111, 219], where $\omega = \omega_1 - \omega_2$ and $q = q_1 - q_2$ are respectively the frequency difference and momentum difference along the tubes direction between two Bragg beams. Note that we employed 759 nm light which is far-detuned with respect to any atomic transition, so the Bragg excitation acts equally on each spin components (i.e. we are only exciting charge modes). The angle between the Bragg beams is small enough to guarantee that the transferred

momentum is much lower than the Fermi momentum $q \ll kF$.

Fig. 7.3a shows the measured spectrum for $N = 1$ at low momentum transfer $q \simeq 0.2k_F^0$ (with k_F^0 being the peak Fermi wave vector in the central tube). A clear resonance is observed, in excellent agreement with the calculated response for ideal fermions (solid line, with no free parameters). For $N = 2$ the resonance is clearly shifted towards higher frequencies (Fig. 7.3b), as expected from Luttinger theory. The measured shift $(+15 \pm 4)\%$ agrees with the expected $(+10 \pm 2)\%$ shift in the sound velocity predicted on the basis of the Luttinger theory for a trapped system [213]. For $N = 6$ the spectrum shows a much larger shift $(+33 \pm 4)\%$ (Fig. 7.3c), which disagrees with the predictions for $N = 2$, signalling an increased effect of interactions. The calculated spectra for trapped fermions with infinite interactions is also plotted (Fig. 7.3b,c dotted lines), which shows how the measured spectra lie between the response of the ideal Fermi gas and that of a fermionized system.

7.1.3 Collective breathing oscillations

More insight into the physics of multicomponent 1D fermions can be obtained by studying the low-energy breathing oscillations in which the cloud radius oscillates in time. It is indeed a well known fact that in the Luttinger model the spectrum is completely built by collective excitations, as single-particle excitations are suppressed due to the reduced dimensionality. We measure the frequency of this collective mode by suddenly changing the trap frequency and measuring the time evolution of the radius. In Fig. 7.4a, we plot the measured squared ratio $\beta = (\omega_B/\omega_x)^2$ of the breathing frequency ω_B to the trap frequency ω_x as a function of the number of spin components N (squares). For $N = 1$ the measured value is in good agreement with the expected value $\beta = 4$ for ideal fermions (upper horizontal line). By increasing N our data clearly show a monotonic decrease of β, induced by the repulsive interactions in the spin mixture. Already for $N = 4$, the measured value of β lies outside the interval of possible values obtained for the $N = 2$ case [213], implying that a mixture with $N > 2$ is not simply a more interacting $N = 2$ mixture. The dependence of β on the interaction strength is remarkably non trivial already for $N = 2$, as first predicted in [213]. Indeed, $\beta = 4$ in both the limiting cases of an ideal gas ($\gamma = 0$) and a fermionized ($\gamma = \infty$) system, whereas for finite repulsion it is expected to exhibit a nonmonotonic behaviour, with a minimum at finite interaction strength. The theoretical curves in Fig. 7.4b show the expected dependence of β on the interaction parameter $\eta = N_{at}^1(a_{1D}/a_x)^2$ in which N_{at}^1 is the number of atoms per tube, a_{1D} is the 1D scattering length and a_x is the trap oscillator length. These results have been derived by our collaborators at the Swinburne University by combining a Bethe Ansatz approach with the exact solution of the hydrodynamic equations describing a 1D fermionic liquid with N components [111, 220]. As N is increased, the curves exhibit an increasingly larger redshift of β, and for $N \to \infty$ they asymptotically approach the curve for 1D spinless bosons. The circles indicate the theoretical values for the average $\eta = 0.44$ in our experiment. The agreement between experiment and theory is excellent, as shown in Fig. 7.4a.
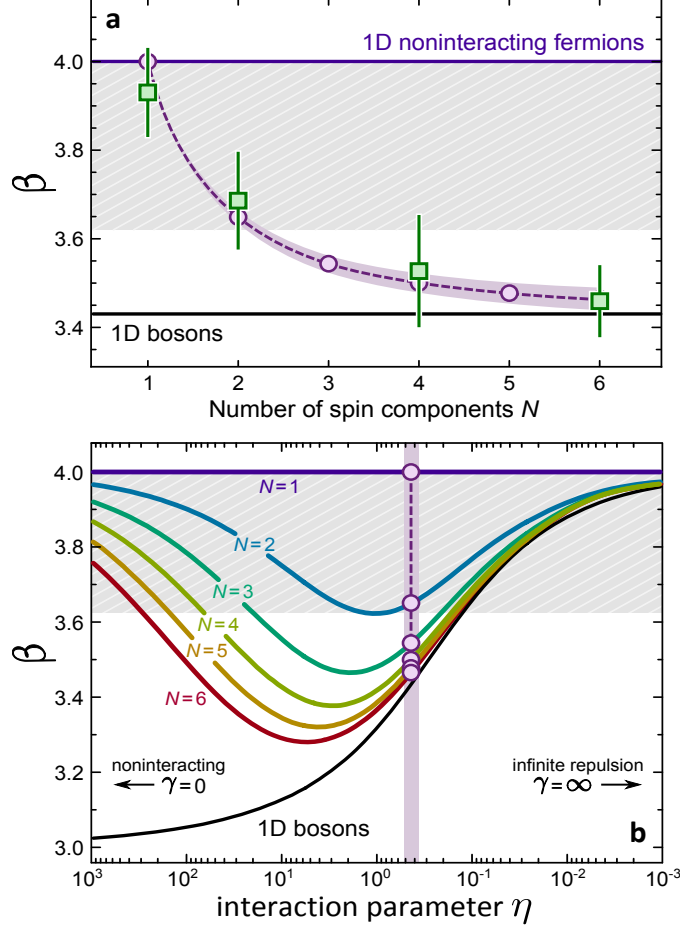
Figure 7.4: **a.** The squares represent the measured ratio $\beta = (\omega_B/\omega_x)^2$ plotted as a function of N, obtained as the weighted mean over sets of up to nine repeated measurements. The circles show the theoretical predictions for the average interaction parameter $\eta = 0.44$ for our experiment. The dashed line is a guide to the eye, while the violet shaded area around the theoretical points indicates the uncertainty on the theoretical values resulting from the experimental uncertainty $\Delta\eta = 0.08$ coming from the experimental parameters. The upper horizontal line shows the theoretical value for the non-interacting Fermi gas while the lower line shows the result for 1D spinless bosons. **b.** The lines show the theoretical dependence of β on the interaction parameter η. The circles are the predicted values for our average interaction parameter also shown in **a.** In both panels the height of the grey region shows the range of β for $N = 2$ and any possible value of the repulsion strength. Our measurements show that $N = 6$ is already compatible with the predictions for a spinless bosonic case.

147

The experimental data and the theoretical curves clearly show that the effect of a change of N are substantially different from those induced by simply changing the interaction strength in an $N = 2$ mixture. A way to see this is to note that, by increasing N, the constraints of the Pauli principle become less stringent and the number of binary-collisional partners increases, causing the system to acquire a more "bosonic" character. This bosonic limit, reported as black lines in Fig. 7.4, for $N \rightarrow \infty$ is a remarkable property of multicomponent 1D fermions that has been pointed out theoretically only very recently by C.N. Yang [221].

7.1.4 Conclusions and perspectives

With this experiment we explored for the first time the physics of one-dimensional multi-component interacting fermionic systems with tunable SU(N) symmetry. In particular the possibility to create stable mixtures with different number of spin components allowed us to study different regimes of interplay between Fermi statistics and degree of distinguishability, observing how increasing the number of spin components the system of one-dimensional fermions exhibits properties of a bosonic spinless liquid. In a quantum simulation perspective, the controlled realization of 1D multi-component fermions represents a powerful test bench for large-spin models and paves the way to the observation in ultracold atoms of elusive fundamental aspects of one-dimensional interacting systems, such as spin-charge separation, first predicted for a $N = 2$ fermionic system. This work indeed concerns exclusively charge (density) collective modes, since the excitations studied are all spin-independent. Differently, given two spin species $|\uparrow\rangle$ and $|\downarrow\rangle$, a spin-selective Bragg excitation [222, 223] should in principle allow for the comparison between the charge and spin velocities through the measurement of the charge and spin dynamical structure factors.

7.2 Observation of chiral edge states in synthetic Hall ribbons

Ultracold atoms in optical lattices represent an ideal system for studying the physics of condensed matter problems in a fully tunable and controllable environment. One of the most intriguing subjects in condensed matter is the physics of the gauge fields. These kind of systems are characterized by a so-called "topological" ordering, which was subject of intensive studies during the last decades [224–226]. A notable example is a system of electrons confined in two dimensional structures and subjected to strong magnetic fields. When placed in a large enough magnetic field, the Landau-level quantization becomes important and electrons exhibit quantized orbits. In this Hall regime, the Hall conductance is an integer in units of the quantum of conductance e^2/h, and the transport becomes dissipationless along the edges of the system [227, 228]. This is the so-called Integer Quantum Hall effect.

In presence of a vector potential $\mathbf{A}(\mathbf{r})$, a free electron moving on a plane along a closed trajectory γ will acquire an Aharonov-Bohm phase [229]:

$$\Phi = \frac{e}{\hbar} \oint_\gamma \mathbf{A}(\mathbf{r}) \cdot d\mathbf{r} = 2\pi \frac{\Phi_B}{\Phi_0}, \tag{7.3}$$

where Φ_B is the flux of the magnetic field $\mathbf{B}(\mathbf{r}) = \nabla \times \mathbf{A}(\mathbf{r})$ through the surface enclosed by the contour γ and $\Phi_0 = h/e$ is the magnetic flux quantum. In presence of a 2D lattice, the Aharonov-Bohm effect is described in terms of Peierls substitution [230], in which the (formerly real) tunneling t between two adjacent lattice sites becomes a complex number with phase $\varphi_{n,m}^k = eA_{n,m}^k/\hbar$, where n, m are the lattice site indexes and $k = \{x, y\}$ labels the tunneling direction, called Peierls phase (Fig. 7.5). The total phase acquired by a particle moving along a lattice plaquette, linked to the flux of the perpendicular magnetic field through the plaquette surface,

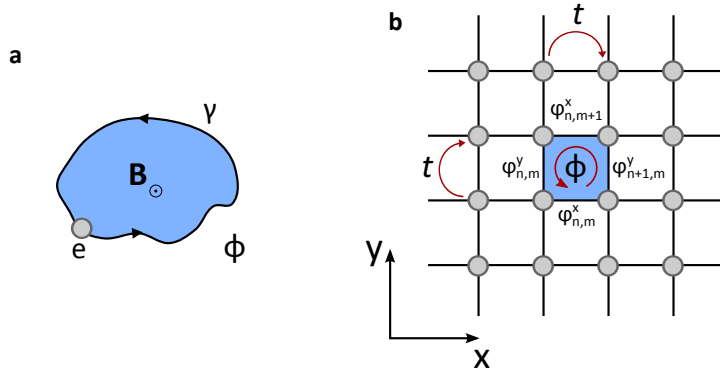
Figure 7.5: **a.** *Representation of the Aharonov-Bohm effect (see text).* **b.** *In a 2D lattice for a charged particle, the total phase is ≠ 0 and the flux through a plaquette will be given by the sum of the phases aquired along the sides.*

will then be given by, in units of Φ_0:

$$\Phi = \varphi_{n,m}^x + \varphi_{n+1,m}^y - \varphi_{n,m+1}^x - \varphi_{n,m}^y. \tag{7.4}$$

With this definition and choosing the Landau gauge $\mathbf{A} = (0, x\Phi, 0)$, the non interacting lattice Hamiltonian can be written as:

$$\hat{H} = -t \sum_{n,m} \left[\hat{a}_{n+1,m}^\dagger \hat{a}_{n,m} + e^{i\Phi n} \hat{a}_{n,m+1}^\dagger \hat{a}_{n,m} \right] + h.c., \tag{7.5}$$

in which only the tunneling along direction $\hat{y}$ is complex, whereas the tunneling along $\hat{x}$ is real. Hamiltonian (7.5) is called Harper-Hofstadter Hamiltonian [231, 232]. Solving this Hamiltonian imposing periodic boundary conditions, the single-particle energy spectrum exhibits a fractal selfsimilar structure as a function of the flux $\alpha = \Phi/2\pi$, known as Hofstadter's butterfly. The fractal structure emerges in presence of a rational flux per plaquette $\alpha = p/q$; in this case the fundamental energy band splits into q sub-bands with dispersion relations $E_\eta(k)$, with $\eta = \{1, ..., q\}$ [230]. If open boundary conditions are instead imposed, the systems features a certain number of "edge" states, which close the energy gaps present in the periodic boundary conditions case and are characterized by a density distribution localized on the edges of the system. The current of the edge states is chiral, meaning that it circulates only in one sense which depends on the edge state considered and on the sign of the magnetic flux. This type of behaviour is pictorially described in terms of skipping orbits, cyclotron orbits that are naturally truncated at the edges of the sample.

In the following sections, the emergence of chiral edge state in a system with complex tunneling will be shown [203]. The details about these experiments are extensively discussed in [116].

7.2.1 Synthetic gauge fields in synthetic dimensions

In recent years ultracold atoms have been extensively used for the quantum simulation of gauge fields physics, exploiting light-matter interaction in order to imprint the Peierls phase to the particles wavefunction [233–235]. These gauge fields, first synthesized in Bose-Einstein condensates [236], have recently allowed for the investigation of the bulk properties of topological matter with the realization of the Harper-Hofstadter Hamiltonian in ultracold bosonic two-dimensional (2D) lattice gases [237, 238].

In our work, we study instead the edge properties of fermionic ultracold gas confined in a two-dimensional system with sharp and addressable edges, implemented following Ref. [239]. The same approach was followed in Ref. [240] for the observation of edge properties in a bosonic system. We engineer a 2D lattice where one dimension is represented by the real space, while the other is encoded in the nuclear spin degree of freedom, which becomes an effective "extra-dimension", providing direct access to edge physics by means of spin selective imaging (see section 2.2.2).
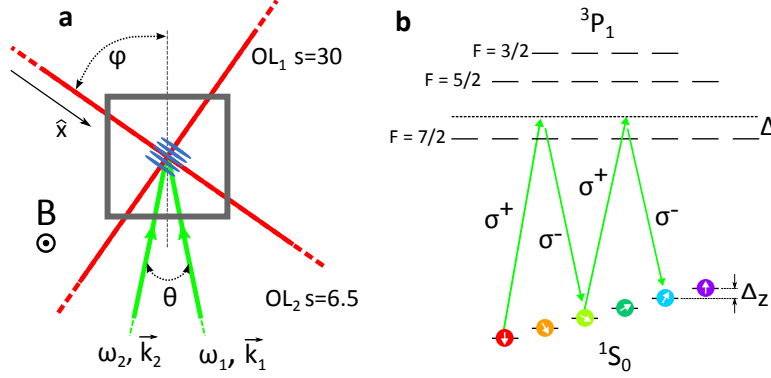
Figure 7.6: ***a.*** *Sketch of the experimental setup. The atoms are confined in 1D wires and a shallow lattice is applied along the wire direction. Two beams induce Raman transitions which also transfer a momentum to the atoms in the wire direction.* ***b.*** *Scheme of a $\sigma^+ - \sigma^-$ Raman transition. The energy difference between the beams is twice the Zeeman separation Δ_Z. The light is quasi-resonant with the intercombination transition so the atoms feel a spin-dependent light shift.*

Experimentally, the system is represented by an array of one-dimensional wires, as in the experiment described in section 7.1, with the difference that a shallow optical lattice with depth $s = 6.5$ is imposed along the wires direction $\hat{x}$, creating a real tunneling between the different lattice sites n (see Fig. 7.6a). The extra, synthetic dimension is implemented by a pair of angled beams at 556 nm of frequencies ω_1 and ω_2 and wavevectors $\mathbf{k}_1$ and $\mathbf{k}_2$, quasi-resonant with the $^1S_0 \rightarrow {}^3P_1$ transition, which induce Raman transitions between states with different nuclear spin m_F (see Fig. 7.6b). This can be seen as a tunneling in the nuclear spin "extra dimension". In particular the beams polarization is $\sigma^\pm$, so that they induce Raman transitions with $\Delta m_F = 2$. Since $|\mathbf{k}_1| \cong |\mathbf{k}_2| = k$, the transferred momentum is $q_R = 2k \sin(\theta/2) \sin\varphi$ to the atoms along direction $\hat{x}$ (see Fig. 7.6a). An atom in the lattice site n in the real dimension $\hat{x}$, tunneling in the extra dimension from the site (n, m_F) to the site $(n, m_F + 2)$ will acquire a phase:

$$q_R x = q_R n d = q_R \frac{\lambda_L}{2} n = \frac{q_R}{2k_L} 2\pi n = \Phi n \qquad (7.6)$$

with k_L being the optical lattice wavevector. Summing the phases along a plaquette, one can find the flux of the "synthetic" magnetic field through it, which is exactly given by $\Phi = 2\pi(q_R/2k_L)$ (see Fig. 7.7). Since the sign of the flux depends on q_r, the magnetic field direction can be reversed simply switching the beam frequencies. With our experimental parameters, the flux is $\Phi \simeq 0.37\pi$. Noticeably, this is the Peierls substitution corresponding to a synthetic $|B|$ values of thousands of Tesla, completely out of reach in "real" experiments. Labeling the nuclear spins $m_F = (-5/2, -1/2, +3/2)$ respectively $m = (1, 2, 3)$ The Hamiltonian of the system will be given by:
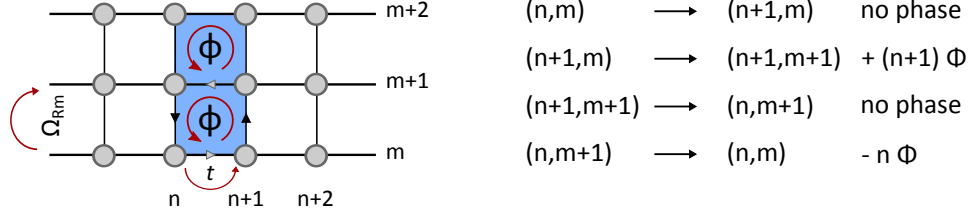
Figure 7.7: Sketch of the 2D synthetic lattice. In the real dimension (n sites) the tunneling is real and no phase is acquired by the atoms. Along the nuclear spin synthetic dimension the tunneling imprints a phase shift to the atomic wavefunction. The flux though a plaquette is given by the phase shift Φ.

$$\hat{H} = \sum_{n,m} \left[-t\hat{a}^\dagger_{n+1,m}\hat{a}_{n,m} + \mu_n\hat{n}_{n,m} + \frac{\hbar}{2}\Omega_{Rm}e^{i\Phi n}\hat{a}^\dagger_{n,m+1}\hat{a}_{n,m} + \xi_m\hat{n}_{n,m} \right] + h.c.,$$

(7.7)

where Ω_{Rm} is the Rabi coupling between the states m and $m+1$[3], μ_n represents the residual harmonic trapping and ξ_m is the spin dependent light shift induced by the quasi-resonant Raman beams (see section 1.1.3). This last term is important as it can be tuned in order to select the number of spin components (or legs) which give the "extension" of the synthetic dimension [116]. This allowed us to study two-leg (with spin components $m_F = -5/2, -1/2$) and three-leg (with spin components $m_F = -5/2, -1/2, +3/2$) ladder systems, the latter being the minimal configuration that is showing both edge and bulk states.

7.2.2 Equilibrium properties

In both the two-leg and three-leg case it can be shown that the lowest energy band of the Hamiltonian (7.7) describes the propagation of "edge states" localized in spin space at $m = (-5/2, -1/2)$ (in the two-level system) and $m = (-5/2, +3/2)$ (in three-level system): these states propagate along $\hat{x}$ in opposite directions. We detect the chiral nature of the current carried by each spin state, starting from the case of two-leg ladder. A quantum degenerate ^{173}Yb Fermi gas with 1.6×10^4 atoms, spin-polarized in the $m_F = -5/2$ state and an initial temperature $T \simeq 0.2T_F$ is prepared in one-dimensional wires by slowly ramping up the power of the lattice beams to a depth of $s = 30$, which grants a suppression of the dynamics along the transverse directions. The shallow lattice along $\hat{x}$ is ramped as well to $s = 6.5$, preparing a system in which all atoms occupy the $m = -5/2$ leg with less than one atom per (real) lattice site. Then, by controlling the intensity and frequency of the Raman beams [116], we slowly activate the tunneling between the legs so as to adiabatically load the fermionic system in the lowest band of Hamiltonian (7.7). Despite the absence of a real bulk region, this two-leg configuration is expected

---

[3]Since only three states are involved, there will be only two Rabi frequencies, Ω_{R1} coupling the $-5/2$ and $-1/2$ states, and Ω_{R2} coupling the $-1/2$ and $+3/2$ states
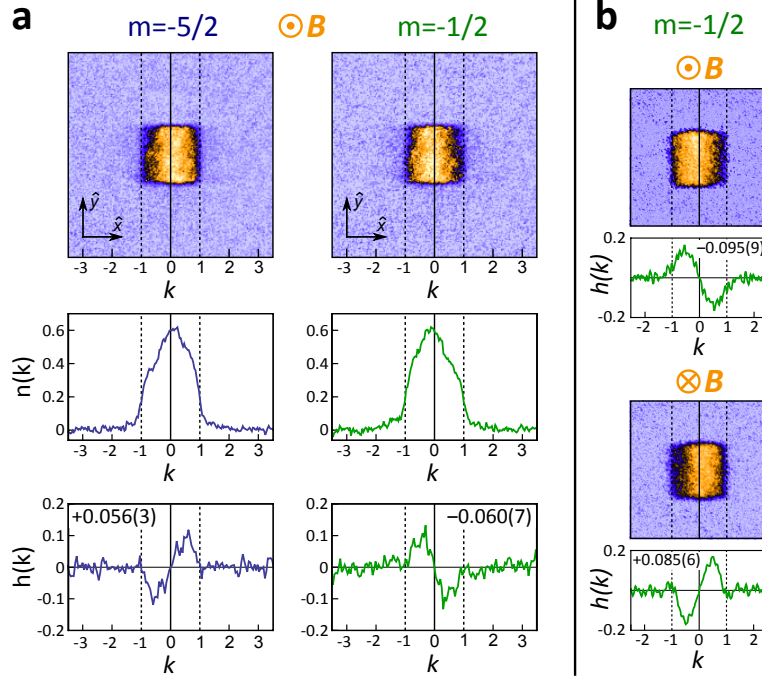
*Figure 7.8: **a.** (Top) False-color time of flight images of the atomic cloud for two different spin states, m = −5/2 and m = −1/2. The images are the result of an average over 30 aquisitions. (Middle) Integrated momentum distributions n(k). The distributions are centered at k ≠ 0, depending on the specific spin state. (Bottom) h(k) = n(k) − n(−k). The numerical plots are the momentum imbalance J (see text). **b.** Time-of-flight images and h(k) for the m = −1/2 leg and opposite directions of the synthetic magnetic field.*

to support chiral currents with atoms flowing in opposite directions along the legs as investigated recently in bosonic systems [241]. To observe this, we measured the relative motion of the atoms in the two legs by spin-selective imaging of the lattice momentum distribution, obtained by time-of-flight imaging after switching off the synthetic coupling and the optical lattice (see Fig. 7.8a). We are interested only in direction $\hat{x}$, which reflects the distribution of the lattice momenta k along the legs (in units of k_L). The lattice momentum distribution along $\hat{y}$ is a uniform square due to the presence of the strong optical lattice along the transverse (frozen) real directions. In order to quantify the current, the momentum distribution in integrated along $\hat{y}$ and normalized, and the quantity

$$h(k) = n(k) - n(-k) \tag{7.8}$$

is computed. Fig. 7.8a also reports $n(k)$ and $h(k)$. We then calculate the quantity $J = \int_0^1 h(k)\,dk$, that provides a measurement of the lattice momentum unbalance and quantifies the strength of the chiral motion of the particles along the two legs. For the images in Fig. 7.8a, obtained for $\Omega_{R1} = 2\pi \times 489$ Hz and $t = 2\pi \times 134$ Hz ($\Omega_{R1}/t = 3.65$), we obtain $J = +0.056(3)$ for $m = -5/2$ and $J = -0.060(7)$
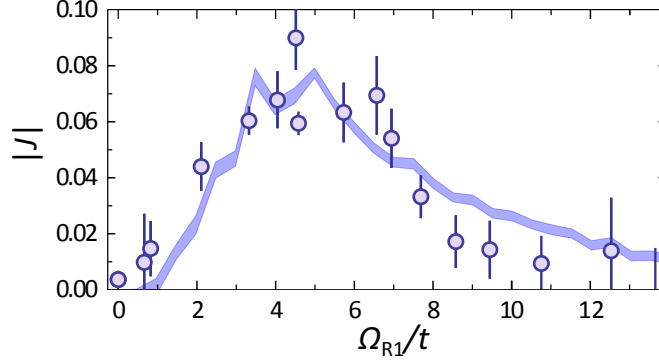
Figure 7.9: Lattice momentum unbalance |J| for the m = −5/2 leg as a function of Ω_{R1}/t for Φ = 0.37π. The circles are the experimental data and the error bars are obtained with a bootstrapping method applied on ∼ 30 different measurements. The shaded area is the result of a numerical simulation that includes thermal fluctuations [116].

for $m = -1/2$. These values are approximately equal in intensity and opposite in sign, providing direct evidence for presence of chirality in the system. In order to verify that the observed currents are direct consequence of the presence of the synthetic magnetic field, we reversed the direction of **B** and performed the same experiment. The results are reported in Fig. 7.8b, obtained for $\Omega_{R1} = 2\pi \times 394$ Hz and $t = 2\pi \times 87$ Hz ($\Omega_{R1}/t = 4.53$) and a magnetic flux $\Phi = \pm 0.37\pi$. We observe a change of sign in J, corresponding to currents circulating in the opposite direction. This behavior confirms the interpretation of our data in terms of chiral currents induced by a synthetic magnetic field in a synthetic 2D lattice.

In our system, the appearance of a chiral behavior is governed by several key parameters, including the ratio Ω_{R1}/t, the Fermi energy E_F, and the flux Φ. In particular, by varying the tunneling rates along $\hat{x}$ and $\hat{m}$ we investigate the rise and fall of the edge currents as a function of the parameter Ω_{R1}/t [241] without affecting other relevant parameters, such as E_F and the temperature. Figure 7.9 illustrates the measurement of $|J|$ as a function of Ω_{R1}/t (circles). As expected, no chirality is observed for vanishing Ω_{R1}, when the legs are decoupled. Chirality is also suppressed for large inter-edge coupling $\Omega_{R1} \gg t$. In the latter regime, the largest energy scale in the system is the effective kinetic energy along the synthetic direction and this contribution is minimized when the fermions occupy the lowest energy state on each rung, which does not exhibit any chiral behavior. The measured values of $|J|$ compare well with the results of a numerical simulation, carried out by our collaborators of IQOQI in Innsbruck, that includes thermal fluctuations (shaded area in Fig. 7.9) [203].

The same measurements were performed for the three-leg ladder, with the same experimental procedure. This is the minimal configuration that includes a bulk, the $m_F = -1/2$ state, while the $m_F = -5/2$ and $m_F = +3/2$ states represent the edges. Also in this case, we observe the onset of chiral edge currents for values of $\Omega_{R1} \gg t$ similar to those observed for the two-leg ladder [203], with the additional
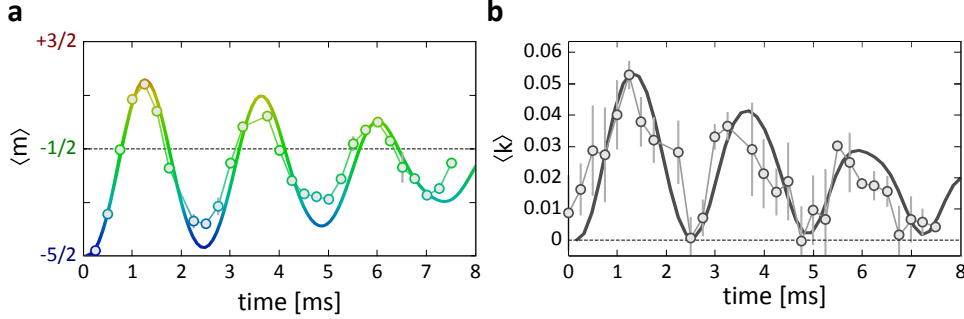
154

Figure 7.10: **a.** *Time dependence of the average nuclear spin (i.e. the average position in the extra-dimension) $\langle m \rangle$ after a quench on the Raman coupling in the synthetic direction, measured with OSG technique.* **b.** *Time dependence of the average lattice momentum $\langle k \rangle$ along the $\hat{x}$ direction, measured with time-of-flight imaging of the whole cloud. In both the imgaes the circles are the experimental data, connected by thin lines, while the thick lines are the theoretical predictions.*

feature that the bulk state $m_F = -1/2$ shows a very reduced current, in agreement to the theoretical preditcion [116]. We have then demonstrated the existence of chiral currents arising from the edge states of the system, in analogy to a Hall system.

7.2.3 Skipping orbits

Finally, exploiting the three-leg ladder configuration, we performed quench dynamics experiments that provide direct evidence of chiral transport properties along the edges. We prepared a system of lattice fermions in an initial state with zero average momentum on the lower $m_F = -5/2$ leg. The system is then quenched by suddenly activating the complex tunneling in the synthetic direction, turning on the Raman beams at resonance. The employed experimental parameters are $\Omega_{R1} = 2\pi \times 490$ Hz and $t = 2\pi \times 94$ Hz, implying a value $\Omega_{R1}/t = 5.2$ where the chiral behavior is maximum. The time dependence of the average spin $\langle m \rangle$ (or "position" in the synthetic dimension) is measured by means of OSG detection (see section 2.2.2 and is reported in Fig. 7.10a. In Fig. 7.10b instead, the time dependence of the average lattice momentum $\langle k \rangle$ along $\hat{x}$ is showed, measured by time-of-flight imaging of the whole atomic cloud. In order to reconstruct the orbit on the ribbon surface, we determine the average position in real space $\langle x \rangle$, starting from the knowledge of energy band dispersion versus lattice momentum, and then performing an integration in time [116]. In this way we obtain a plot of $\langle m \rangle$ versus the average position in real space $\langle x \rangle$, which is shown in Fig. 7.11. The dynamics displays a strong chiral character, demonstrated by the in-phase oscillations in Fig. 7.10a, b and the orbits in Fig. 7.11. Under the effect of the synthetic magnetic field, the fermions move according to cyclotron-type dynamics, which is naturally truncated by the synthetic edge, giving rise to a skipping-type orbit, as expected for a quantum Hall system [224, 242]. The experimental data are in reasonable agreement with the theoretical predictions, represented by the thick lines in Fig. 7.10a, b and Fig. 7.11. The mis-
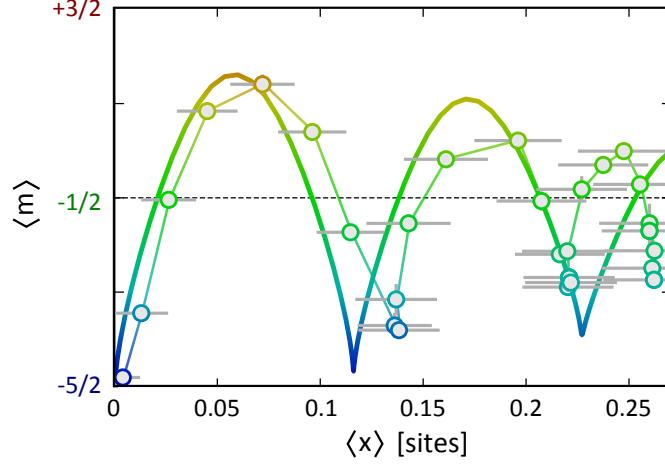
Figure 7.11: Plot of the average spin $\langle m \rangle$ versus the average position $\langle x \rangle$, representing the trajectory in the $\hat{x} - \hat{m}$ space. The circle, connected by the thin lines as a guide to the eye, are the experimental data and the thick line is the theoretical predition (see text).

match between theoretical model and experimental data after the second orbit could possibly be ascribed to an accumulation of integration error in the data analysis, which amplifies the effects of the assumptions in the model (such as not accounting for interactions). We note that both the data and the theoretical curves effectively damped, as a result of averaging over many different fermionic trajectories. This also justifies the reduction of the average orbit radius to less than one real lattice site of Fig. 7.11. This behavior is very different from the case of a noninteracting Bose gas, which would occupy a single condensed wave packet undergoing undamped oscillations [240]. Anyhow, also interactions are envisioned to play a major role, and further studies are tracking this issue [243].

7.2.4 Conclusions and perspectives

In this section we reported the observation of chiral edge states in a system of neutral fermions subjected to a synthetic magnetic field. In particular by following the innovative approach theorized in Ref. [239] we realized a system in which the nuclear spin of the atoms is used to encode a lattice structure in an extra-dimension, providing direct access to edge physics. By exploiting the high level of control in our system, we studied the onset of chirality as a function of the Hamiltonian couplings. These results are a demonstration of the feasibility of the "extra-dimension" approach for the quantum simulation of gauge fields physics, and represent the first step towards the investigation of both edge and bulk 2D topological matter. In particular, a study of the combined effect of interactions and synthetic gauge fields could lead to the observation of exotic states of matter [244] such as chiral Mott insulator states, in ladder systems. Moreover, exploiting the possibility to implement periodic boundary conditions in the synthetic dimension [245] opens

the door to the study of the topological properties of bulk physics, potentially allowing for the observation of the fractal structure of the Hofstadter spectrum, as will be discussed in the Conclusions. Also, periodic boundary conditions could also allow for the realization of the famous Laughlin pump [246], and so for the observation the quantization of the Hall conductivity.

Conclusions and perspectives

In this thesis, I have reported the experimental techniques and the the theoretical efforts that have been employed in order to investigate the emergence of two-orbital quantum physics phenomena in fermionic degenerate gases of ^{173}Yb. Most of these results are based on a narrow-line complex laser system, that i have mainly devised, characterized and realized during the three years of PhD.

In a first set of experiments [41], we studied the two-orbital spin exchange interaction arising between two atoms in different nuclear spin and electronic state, by exploiting the coherent addressing of the $^3P_0$ metastable state using an ultranarrow laser at 578 nm. The atomic samples are confined in a deep three-dimensional optical lattice, so that high-precision spectroscopy can be performed on the sample and the two-body interaction peaks of the spectrum can be resolved and individually addressed. This possibility is exploited in order to selectively excite only doubly-occupied lattice sites and study the two-orbital interaction. In our experiments, we directly measured inter-orbital spin-exchange interaction energy by observing for the first time significantly fast coherent orbital magnetization oscillations. In particular, the exchange energy V_{ex}, of the order of $\sim h \times 10$ kHz, is much larger than both the Fermi ($k_B T_F$) and the thermal ($k_B T$) energies and is only limited by the lattice band gap. From the direct measurement of V_{ex} it was possible to determine the inter-orbital scattering length a_{eg}^+ associated to the spin-singlet $|eg^+\rangle$ state, which exceeds the spin-triplet scattering length a_{eg}^-, determined with high accuracy in Ref. [84], by ≥ 10 times. The measurement and characterization of the spin-exchange interaction represents a very important step towards the quantum simulation of two-orbital many-body models ranging from the Kondo model [35, 42] to heavy-Fermi behavior [36, 43, 44] and magnetic ordering [45, 46].

The noticeably high spin-exchange energy played also a fundamental role in the observation of orbital Feshbach resonances [57], which enables the tuning of the inter-orbital scattering length. The mixing between a pair of two-orbital atoms in the open or closed channel is indeed provided by the exchange interaction V_{ex}, according to the theoretical model of Ref. [58]. In our experiments, the signature of an increased interaction strength is represented by the anisotropic expansion of the Fermi gas in time of flight. We observed the emergence of resonant interactions at very convenient values of the order tens of Gauss in different spin-mixtures, following the predicted scaling with Δm. In addition, in order to determine the effective feasibility of this interaction tuning knob, we studied the effect of inelastic
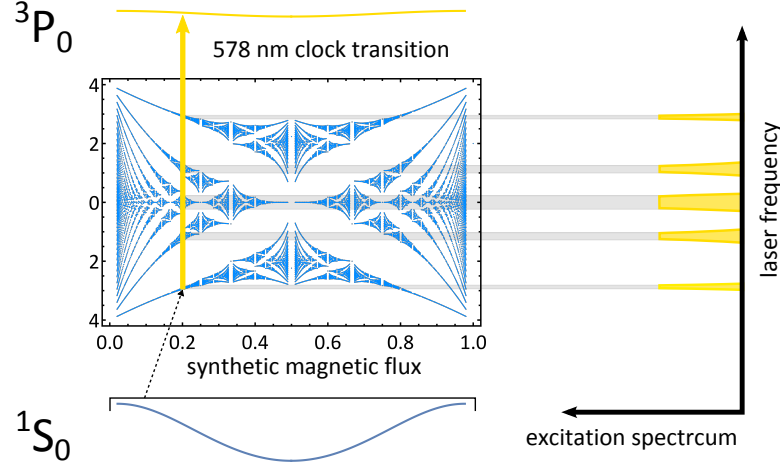
Figure A: Conceptual scheme of an experimental proposal. A 1D electronic-state-dependent optical lattice has a flat lowest band for metastable atoms and non-flat band for ground state atoms. Imposing a synthetic magnetic flux using the nuclear spin degree of freedom (see section 7.2), the ground state atoms lattice band is divided in several sub-bands, which can be probed performing high-resolution spectroscopy of the clock transition.

losses across the orbital Feshbach resonance. We found a lifetime of the order of hundreds of ms at resonance, which make orbital Feshbach resonances a promising tool for future investigations of many-body physics by using two-electron atoms. While this system still requires an accurate study also from the theoretical point of view, this observation is the starting point for a whole new range of experimental investigations, ranging from the investigation of the BEC-BCS crossover in an ultracold gas of fermions with orbital degree of freedom to the realization of two-orbital Hubbard models [26] with tunable interactions and the realization of novel forms of topological superfluids with spin-orbit coupling [58].

In another, transversal experiment [56], we demonstrate the possibility to perform precision measurements beyond the GPS level by performing high-accuracy spectroscopy of the ^{173}Yb clock transition after having disciplined our 578 nm ultranarrow laser to a 1542 nm optical reference, traced to the SI second and transferred, via a 642 nm long fiber link, from the Italian National Metrology Institute to the European Laboratory for Nonlinear Spectroscopy. Within this context, I conspicuously contributed to the realization of the "receiving station" of the link at LENS, which allows for the referencing of the local laser to the disseminated signal. By exploiting the high degree of precision and accuracy of the disciplined ultranarrow laser, we measure the absolute frequency of the $^1S_0 \rightarrow {}^3P_0$ transition in ^{173}Yb with an uncertainty of 10 Hz (2×10^{-14}), limited by our end-user laboratory systematic uncertainties, improving the known value [165] by two orders of magnitude. We demonstrate that this dissemination method enables the transfer of typical accuracies of 4×10^{-15} from primary standards to non-metrological end-users in
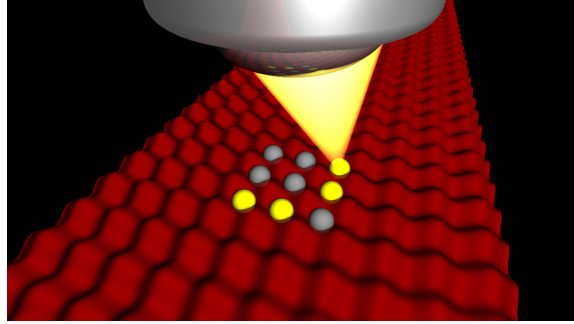
Figure B: The adoption of an high-resolution objective will allow for single-site imaging and addressing of indivual atoms.

timescales as short as few hours, overcoming the same-timescale accuracy of the GPS, nowadays the commonly used frequency and timebase dissemination method. Such a result could not only grant great benefits in a wealth of applications ranging from scientific research to industrial development and production processes, but also be exploited for the implementation of novel quantum information [26] and simulation [28–30] schemes, where the high-precision of the probe laser is of the highest importance.

In this context, this infrastructure could be exploited, in combination with the possibility to engineer electronic-state-dependent optical lattices and "extra-dimension" approach outlined in section 7.2, to study the bulk physics of a system subjected to a synthetic gauge field with periodic boundary conditions in both the real and synthetic dimension. With the appropriate choice of the lattice wavelength, it would be possible to realize an optical lattice that is shallow for ground state atoms and deep for the metastable state. Owing to the flat nature of the metastable state lattice band, it would be possible to study the structure of the ground state atoms lattice band, by performing high-precision spectroscopy of the clock transition. With our spectral resolution of the order of a few parts in 10^{-14} it would be possible to distinguish bandgaps of the order of $10-20$ Hz, possibly enlightening the fractal structure of the Hofstadter spectrum (see Fig. A) once periodic boundary conditions are imposed.

Finally, in the long-term several improvements to the experimental setup are planned. In particular, the experimental setup, with its high-optical-access glass cell, has been designed with the possibility to implement single-site imaging and addressing of Yb atoms confined in optical lattices with a high-resolution objective. In the past years, such technique has been successfully implemented in several experiments with bosons [247–250] and more recently with fermions [251–253], enlightening promising opportunities, also on the side of quantum information tasks. In our case the high numerical aperture objective, in combination with the ultranarrow laser, could grant the opportunity to encode and read-out quantum information in individually addressed atoms (see Fig. B). The adoption of these techniques in our experimental setup will require a serious and challenging technical

effort, at the same time offering the opportunity to lead to major achievements in the investigation of quantum many-body systems and to the implementation of quantum information protocols which rely on single atom addressing.

Appendix A

Ytterbium transitions and Clebsh-Gordan coefficients

Tables of Yb atomic energy levels and transitions from the $^1S_0$ and $^3P_0$ states used to compute the dipole potentials reported in Fig. 4.2 and of the Clebsch-Gordan coefficients of the $^1S_0 \to {}^3P_1$ transition.

Table A.1: Ytterbium $^1S_0$ energy levels and linewidths.

States	Energy [cm^{-1}]	λ [nm]	τ [ns]	$\Gamma/2\pi$ [MHz]	Branching Ratio
$6s6p\,(^3P_1)$	17992.007[a]	555.802	870[a]	0.1829	-
$6s6p\,(^1P_1)$	25068.222[a]	398.911	5.46[a]	29.12	-
$(7/2, 5/2)\,j = 1$	28857.014[a]	346.536	14.6[b,c]	10.90	-
$(5/2, 5/2)\,j = 1$	37414.59[a]	267.275	70[a]	2.067	-
$6s7p\,(^3P_1)$	38174.17[b,c]	261.957	120[b,c]	1.326	0.8
$6s7p\,(^1P_1)$	40563.97[a]	246.524	10[a]	15.91	0.65
$6s8p\,(^3P_1)$	43659.38[b]	229.046	140[b]	1.136	-
$6s8p\,(^1P_1)$	44017.60[b]	227.182	50[b]	3.183	-

[a] NIST atomic spectra database, [b] Ref. [254], [c] Ref. [255], [d] Ref. [256].

Table A.2: Ytterbium $^3P_0$ energy levels and linewidths.

States	Energy [cm^{-1}]	λ [nm]	τ [ns]	$\Gamma/2\pi$ [MHz]	Branching Ratio
$6s5d$ ($^3D_1$)	7200.663[b]	1388.76	380[b]	0.423	0.639
$6s7s$ ($^3S_1$)	15406.253[d]	649.087	14[d])	11.36	0.15
$6s6d$ ($^3D_1$)	22520.281[b]	444.044	21[b]	7.01	0.582
$6s8s$ ($^3S_1$)	24326.601[d]	411.073	34[d]	4.68	0.135
$6p^2$ ($^1P_1$)	26516.981[b]	377.117	15[b]	10.61	0.35
$6s7d$ ($^3P_1$)	27022.941[b]	370.056	38[b]	4.19	0.56

[a] NIST atomic spectra database, [b] Ref. [254], [c] Ref. [255], [d] Ref. [256].

Table A.3: Clebsch-Gordan coefficient for $^1S_0 \to {}^3P_1$, π transition.

m_g	-5/2	-3/2	-1/2	+1/2	+3/2	+5/2
$F' = \frac{7}{2}$	$-\sqrt{\frac{2}{21}}$	$-\frac{1}{3}\sqrt{\frac{10}{7}}$	$-\sqrt{\frac{2}{21}}$	$-\sqrt{\frac{2}{21}}$	$-\frac{1}{3}\sqrt{\frac{10}{7}}$	$-\sqrt{\frac{2}{21}}$
$F' = \frac{5}{2}$	$\sqrt{\frac{5}{21}}$	$\sqrt{\frac{3}{35}}$	$\sqrt{\frac{1}{105}}$	$-\sqrt{\frac{1}{105}}$	$-\sqrt{\frac{3}{35}}$	$-\sqrt{\frac{5}{21}}$
$F' = \frac{3}{2}$	0	$\frac{2}{3\sqrt{5}}$	$\sqrt{\frac{2}{15}}$	$\sqrt{\frac{2}{15}}$	$\frac{2}{3\sqrt{5}}$	0

Table A.4: Clebsch-Gordan coefficient for $^1S_0 \to {}^3P_1$, σ^+ transition.

m_g	-5/2	-3/2	-1/2	+1/2	+3/2	+5/2
$F' = \frac{7}{2}$	$\frac{1}{3\sqrt{7}}$	$\frac{1}{\sqrt{21}}$	$\sqrt{\frac{2}{21}}$	$\frac{1}{3}\sqrt{\frac{10}{7}}$	$\sqrt{\frac{5}{21}}$	$\frac{1}{\sqrt{3}}$
$F' = \frac{5}{2}$	$-\sqrt{\frac{2}{21}}$	$-\frac{4}{\sqrt{105}}$	$-\sqrt{\frac{6}{35}}$	$-\frac{4}{\sqrt{105}}$	$-\sqrt{\frac{2}{21}}$	0
$F' = \frac{3}{2}$	$\frac{\sqrt{2}}{3}$	$\sqrt{\frac{2}{15}}$	$\sqrt{\frac{1}{15}}$	$\frac{1}{3\sqrt{5}}$	0	0

Appendix B

Optical frequency comb

A frequency comb is a spectrum consisting of a series of discrete, equally spaced frequencies. Such frequency comb can be obtained through the stabilization of the pulse train generated by a mode-locked laser, a technique that led to the award of the Nobel Prize in Physics to John L. Hall and Theodor W. Hänsch in 2005.

In the following years an intense effort has been made to develop this technique, leading to the realization of highly reliable fiber-based devices, and making frequency combs invaluable tools is many fields of experimental physics. Frequency combs are used to perform absolute measurements of CW lasers by "transferring" the optical frequencies into the RF domain, as well as to "bridge" different optical frequencies, due to their extremely broad spectrum. Here we very briefly describe the principle of operation of an optical frequency comb, how it can used to measure optical frequencies and the techniques used to stabilize its main parameters. For additional details we refer to Ref. [257].

A frequency comb is based on a mode-locked pulsed laser, characterized in the time domain by gaussian pulses of FWHM duration δt, with distance ΔT between the wavefronts and a carrier-envelope phase shift $\Delta \phi$ between two consecutive pulses (see Fig. B.1). The correspondent spectrum in the frequency domain is a series of frequencies equally spaced by a quantity determined by time between consecutive pulses as:

$$ f_{RR} = \frac{1}{\Delta T}, \tag{B.1} $$

that is called "repetition rate" frequency. The carrier-envelope phase shift is instead related to a second quantity, called the "carrier-envelope offset" (CEO) frequency f_0, which represents the offset of the entire frequency spectrum and is defined as:

$$ f_0 = \frac{\Delta \phi}{2\pi \Delta T}. \tag{B.2} $$

With typical pulsed laser parameters, both f_{RR} and f_0 lie in the RF domain. For example, the comb employed in our setup (Menlo Systems FC1500-250-WG) has
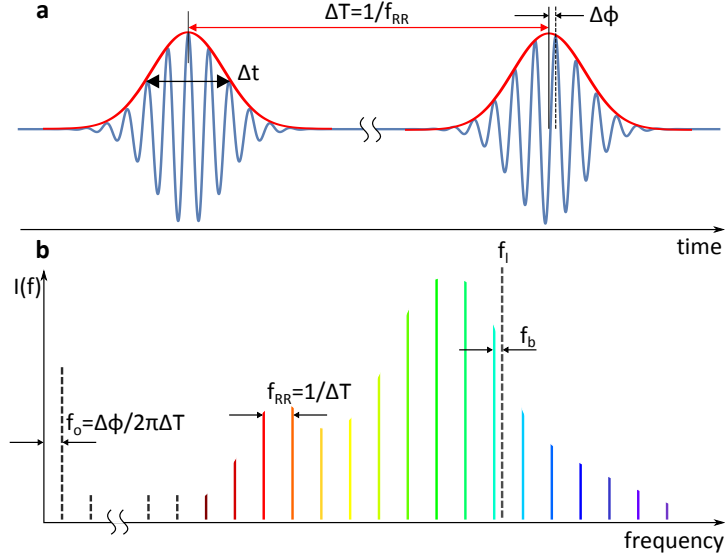
Figure B.1: **a.** *Emission of mode-locked laser in time.* **b.** *Corresponding spectrum in the frequency domain. The distance f_{RR} between the peaks and the initial frequency f_0 are determined by the parameters ΔT and $Delta\phi$ of the temporal evolution. The beatnote between an unknown laser (grey dashed line) with frenquency f_l and the nearest comb tooth will have frequency f_b.*

$f_{RR} \simeq 250$ MHz and $f_0 \simeq 20$ MHz. Finally, the parameter δt will determined the width of the Gaussian envelope of the frequency spectrum as:

$$\Delta f = \frac{1}{2\sqrt{2\ln 2}\Delta t} \tag{B.3}$$

However, in real frequency comb systems, the spectrum envelope will be mainly determined by the laser medium gain curve, and this parameter substantially only defines the extension of the comb spectrum but not its real shape. With these definitions, the frequency of every tooth of the frequency comb will be determined by the parameters f_{RR} and f_0 as:

$$f_n = nf_{RR} + f_0, \tag{B.4}$$

where n is the tooth number. This property can be exploited to measure the frequency of a unknown CW laser by beating it with the frequency comb and measure the resulting beatnote frequency f_b. The laser frequency will then be given by:

$$f_l = n'f_{RR} + f_0 + f_b \tag{B.5}$$

where n' is the number of the comb tooth closest to the CW laser frequency. Supposing to be able to measure the unknown laser frequency independently with an accuracy $< f_{RR}$, then n' is univocally determined and the laser frequency can be

166

found if the comb parameters f_{RR} and f_0 and the beatnote f_b are known. However, the precision and accuracy of a frequency measurement is limited by the uncertainty that affects the comb parameters. In a pulsed laser indeed, the repetition rate and CEO are subject to fluctuations, implying that both f_{RR} and f_0 have to be stabilized in order to fix the position of the frequency comb teeth. Typically, f_{RR} and f_0 are stabilized on external frequency references and, depending on the type of available reference, two different methods can be used to lock the comb parameters in our comb setup.

RF lock technique

The RF lock technique is used if only a RF absolute frequency reference is available. In our laboratory, such reference is a GPS-stabilized quartz oscillator.

In order to stabilized the CEO frequency, the commonly employed method is the "f-$2f$" technique, which relies on the stabilization of the beatnote between two comb teeth at frequency f and $2f$. For this reason, an octave spanning frequency comb is necessary, so non-linear media as birefringent crystals or micro-structured optical fibers are used to broaden the mode-locked laser spectrum, which is typically only a few tens of nm. The lower frequency part of the spectrum at frequency $f = f_0 + n_i f_{RR}$ is then independently frequency-doubled obtaining $2f = 2f_0 + 2n_i f_{RR}$ and compared to the higher frequency part of the spectrum at frequency $f' = f_0 + m_i f_{RR}$. The heterodyne signal between the two will be given by a series of beatnotes with frequencies:

$$\delta f_i = 2(n_i f_{RR} + f_0) - (m_i f_{RR} + f_0) = (2n_i - m_i) f_{RR} + f_0. \qquad (B.6)$$

With the aid of a low pass filter, it is possible to retain only the lowest frequency beatnote, i.e. with $n_i = 2m_i$, and obtain exactly f_0. This frequency can be then stabilized over the external RF reference with a Phase Locked Loop (PLL), typically acting on the laser pump power. With common RF references it is possible to easily achieve a relative uncertainty of the order of 10^{-10}, corresponding to an uncertainty Δf_0 of the order of the mHz.

The repetition rate is instead stabilized by directly measuring it with a photodiode, fast enough to clearly detect two consecutive laser pulses. This signal, or one of its harmonic, is then directly locked to the RF reference with a PLL which actively stabilizes the repetition rate by controlling the cavity length of the frequency comb laser, typically acting on a piezo-mounted mirror. The repetition rate is commonly stabilized with an uncertainty Δf_{RR} of the order of the mHz, corresponding to a fractional uncertainty of 10^{-10}.

With both f_0 and f_{RR} stabilized on the RF external reference, the measurement of an unknown CW laser frequency f_l given by Eq. (B.5) will have an uncertainty given by:

$$\Delta f_l = n\Delta f_{RR} + \Delta f_0 + \Delta f_b \qquad (B.7)$$

where Δf_b is the uncertainty of the beatnote frequency, which is typically dominated by the worse between the comb tooth and laser frequency uncertainty. Considering that $f_{RR} \approx 10^8$ Hz (250 MHz for our comb) and the frequency range of visible and near infrared lasers of the order of 10^{14}, then the comb tooth n is of the order of 10^6. As a consequence, an uncertainty $\Delta f_{RR} \sim 1$ mHz would result in an uncertainty of the order of 1 kHz on Δf_l. This uncertainty represents the ultimate limit of the frequency measurement, which compromises the accuracy level of frequency measurements of ultrastable laser sources, as that described in chapter 3.

Optical lock technique

The "optical lock" technique relies on the presence of an optical frequency reference in addition to the aforementioned RF reference. While the CEO frequency is stabilized on the RF reference with the same technique described before, the repetition rate is not stabilized directly, but the beatnote between the optical reference and the comb is stabilized to fix the comb teeth positions. Being f_r the optical reference frequency, measuring it with the frequency comb will imply:

$$f_r = n_r f_{RR} + f_0 + f_{br}, \qquad (B.8)$$

where n_r is the the closest tooth with respect to f_r and f_{br} the beatnote between the frequency comb and the optical reference. In the optical lock scheme, the beatnote f_{br} is stabilized on the RF reference with a PLL. Being f_0 already stabilized, the PLL acts on the repetition rate in order to fix the position of the tooth n_r and keep the beatnote f_{br} constant. This is done adjusting the frequency comb laser cavity length with a fast actuator, which is typically an intra-cavity EOM, achieving an uncertainty Δf_{br} of the order of mHz. Since f_r is known, Eq. (B.8) can be inverted to evaluate f_{RR} and the unknown laser frequency f_l will be given by:

$$f_l = n f_{RR} + f_0 + f_b = \frac{n}{n_r}(f_r - f_o - f_{br}) + f_o + f_b, \qquad (B.9)$$

with an uncertainty:

$$\Delta f_l = \frac{n}{n_r}\Delta f_r + \left(1 + \frac{n}{n_r}\right)\Delta f_0 + \frac{n}{n_r}\Delta f_{br} + \Delta f_b \sim \frac{n}{n_r}\Delta f_r + \Delta f_b. \qquad (B.10)$$

From this expression it is clear that the uncertainty of the frequency reference determines the frequency measurement uncertainty with a multiplication factor $n/n_r \simeq 1$ instead of 10^6 as in the RF lock case. Eq. B.10 substantially shows that, as a consequence of the locking procedure, the stability of the optical reference is transferred directly to the comb teeth, resulting in a measurement uncertainty simply limited by the worse between the reference and the unknown laser. It is also clear that if the beatnote between the comb and the unknown laser is in turn stabilized over an RF reference, as described in section 3.2.4, then the stability of the optical reference will also be inherited, through the frequency comb, by the unknown laser.

Appendix C

Power Spetral Density and Allan variance

In this appendix we briefly review some basic facts about the two main statistical quantities used in frequency metrology: the phase noise power spectrum and the Allan deviation. These subjects are extensively discussed in many textbooks, like [258].

Let us consider a time-dependent quantity $x(t)$, e.g. an oscillator's instantaneous phase or frequency. The power spectral density (PSD) of $x(t)$ is defined as the Fourier transform of the autocorrelation function $R(\tau)$ of $x(t)$ defined as [258]:

$$R(\tau) = \int_{-\infty}^{+\infty} x(t + \tau) x^s tar(t) \, dt, \tag{C.1}$$

in which we have assumed that the noise is stationary, i.e. that $R(\tau)$ does not depend on t. The PSD will then by given by:

$$S_x(f) = \int_{-\infty}^{+\infty} R(\tau) e^{-i2\pi f \tau} \, d\tau. \tag{C.2}$$

If we introduce the relative frequency variation

$$y = \frac{\delta \nu}{\nu}, \tag{C.3}$$

then the PSD $S_y(f)$ of $y(t)$ is an extremely useful quantity to investigate the noise in oscillators, as different type of noise correspond to polynomials $S_y(f) \propto f^i$ with different exponents i (for example $i = 0$ for withe noise and $i = -1$ for flicker noise). In a more complex system, where more than one typical kind of noise is present, the PSD also allows for the identification of other peculiar features, like electronic or mechanical resonant frequencies.

When an oscillator frequency is measured directly with a frequency counter, this measurement never corresponds to the "instantaneous" frequency, but rather to an averaged frequency over a period of time t_a (in frequency counters for example

the averaging time t_a is the gate time). Hence, the relative frequency variation measured at an arbitrary time t_k will be given by:

$$y(t_k) = \int_{t_k - t_a}^{t_k} y(t) \, dt. \tag{C.4}$$

If we assume a stationary noise, then $\langle y(t_k) \rangle = 0$ and the variance will be given by:

$$\sigma^2 = \langle y(t_k)^2 \rangle = \left\langle \left| \int_{-\infty}^{+\infty} y(t) h(t - t_k) \, dt \right|^2 \right\rangle, \tag{C.5}$$

where $h(t)$ is defined as:

$$h(t) = \begin{cases} 1/t_a & \text{if } 0 < t < t_a \\ 0 & \text{elsewhere.} \end{cases} \tag{C.6}$$

Being $H(f)$ the Fourier transform of $h(t)$m, it can be shown that [258];

$$\sigma^2 = \int_{-\infty}^{+\infty} S_y(f) |H(f)|^2 \, df, \tag{C.7}$$

where $|H(f)|^2 = \frac{\sin^2(2\pi f t_a)}{(2\pi f t_a)^2}$. It can be seen that the expression (C.7) of the classical variance does not converge for some noise processes. For this reason, in frequency metrology the classical variance has to be replaced with another statistical estimator. Let us then define the N-sample variance:

$$\sigma^2(N, t_a) = \left\langle \frac{1}{N-1} \left(\sum_{k=1}^{N} y(t_k)^2 - \frac{1}{N} \sum_{j=1}^{N} y(t_j) \right)^2 \right\rangle, \tag{C.8}$$

where N is the number of samples of the full measurement of duration T. From Eq. (C.8) it is possible to define the 2-sample variance, also called Allan variance, as [259]:

$$\sigma_y^2(t_a) = \frac{1}{2} \langle (y(t_k) - y(t_{k+1}))^2 \rangle. \tag{C.9}$$

This expression has the advantage that its transfer function $|H_A(f)|^2 = \frac{\sin^4(2\pi f t_a)}{(2\pi f t_a)^2}$ acts as a second-order high-pass filter at low frequencies, making it convergent for all the type of noise that can affect the oscillator. Starting from Eq. (C.8), other statistical estimators, like the modified Allan variance [146], can be defined, with a low-frequency behavior depending on the needs of the particular analysis. However, the ultimately correct estimator of an oscillator stability, recommended by the IEEE, is the Allan deviation, defined as the square root of the Allan variance defined in Eq. (C.9).

Bibliography

[1] R. P. Feynman. *Simulating physics with computers*. Int. J. of Theor. Phys. **21**, 467–488 (1982).

[2] I. Buluta and F. Nori. *Quantum Simulators*. Science **326**, 108–111 (2009).

[3] R. Blatt and C. F. Roos. *Quantum simulations with trapped ions*. Nat Phys **8**, 277–284 (2012).

[4] A. Aspuru-Guzik and P. Walther. *Photonic quantum simulators*. Nat Phys **8**, 285–291 (2012).

[5] A. A. Houck, H. E. Tureci, and J. Koch. *On-chip quantum simulation with superconducting circuits*. Nat Phys **8**, 292–299 (2012).

[6] I. Bloch, J. Dalibard, and S. Nascimbene. *Quantum simulations with ultra-cold quantum gases*. Nat Phys **8**, 267–276 (2012).

[7] H. Metcalf and P. van der Straten. *Laser cooling and trapping*. Spinger (1999).

[8] M. H. Anderson, J. R. Ensher, M. R. Matthews, C. E. Wieman, and E. A. Cornell. *Observation of Bose-Einstein Condensation in a Dilute Atomic Vapor*. Science **269**, 198–201 (1995).

[9] K. B. Davis, M. O. Mewes, M. R. Andrews, N. J. van Druten, D. S. Durfee, D. M. Kurn, and W. Ketterle. *Bose-Einstein Condensation in a Gas of Sodium Atoms*. Phys. Rev. Lett. **75**, 3969–3973 (1995).

[10] B. DeMarco and D. S. Jin. *Onset of Fermi Degeneracy in a Trapped Atomic Gas*. Science **285**, 1703–1706 (1999).

[11] I. Bloch, J. Dalibard, and W. Zwerger. *Many-body physics with ultracold gases*. Rev. Mod. Phys. **80**, 885–964 (2008).

[12] D. Jaksch, C. Bruder, J. I. Cirac, C. W. Gardiner, and P. Zoller. *Cold Bosonic Atoms in Optical Lattices*. Phys. Rev. Lett. **81**, 3108–3111 (1998).

[13] M. Greiner, O. Mandel, T. Esslinger, T. W. Hänsch, and I. Bloch. *Quantum phase transition from a superfluid to a Mott insulator in a gas of ultracold atoms*. Nature **415**, 39–44 (2002).

[14] R. Jordens, N. Strohmaier, K. Gunter, H. Moritz, and T. Esslinger. *A Mott insulator of fermionic atoms in an optical lattice*. Nature **455**, 204–207 (2008).

[15] U. Schneider, L. Hackermüller, S. Will, T. Best, I. Bloch, T. A. Costi, R. W. Helmes, D. Rasch, and A. Rosch. *Metallic and Insulating Phases of Repulsively Interacting Fermions in a 3D Optical Lattice*. Science **322**, 1520–1525 (2008).

[16] G. Roati, C. D'Errico, L. Fallani, M. Fattori, C. Fort, M. Zaccanti, G. Modugno, M. Modugno, and M. Inguscio. *Anderson localization of a non-interacting Bose-Einstein condensate*. Nature **453**, 895–898 (2008).

[17] J. K. Chin, D. E. Miller, Y. Liu, C. Stan, W. Setiawan, C. Sanner, K. Xu, and W. Ketterle. *Evidence for superfluidity of ultracold fermions in an optical lattice*. Nature **443**, 961–964 (2006).

[18] S. Fölling, S. Trotzky, P. Cheinet, M. Feld, R. Saers, A. Widera, T. Muller, and I. Bloch. *Direct observation of second-order atom tunnelling*. Nature **448**, 1029–1032 (2007).

[19] S. Trotzky, P. Cheinet, S. Fölling, M. Feld, U. Schnorrberger, A. M. Rey, A. Polkovnikov, E. A. Demler, M. D. Lukin, and I. Bloch. *Time-Resolved Observation and Control of Superexchange Interactions with Ultracold Atoms in Optical Lattices*. Science **319**, 295–299 (2008).

[20] D. Greif, T. Uehlinger, G. Jotzu, L. Tarruell, and T. Esslinger. *Short-Range Quantum Magnetism of Ultracold Fermions in an Optical Lattice*. Science **340**, 1307–1310 (2013).

[21] T. Kinoshita, T. Wenger, and D. S. Weiss. *Observation of a One-Dimensional Tonks-Girardeau Gas*. Science **305**, 1125–1128 (2004).

[22] B. Paredes, A. Widera, V. Murg, O. Mandel, S. Fölling, I. Cirac, G. V. Shlyapnikov, T. W. Hänsch, and I. Bloch. *Tonks-Girardeau gas of ultracold atoms in an optical lattice*. Nature **429**, 277–281 (2004).

[23] M. Takamoto, F.-L. Hong, R. Higashi, and H. Katori. *An optical lattice clock*. Nature **435**, 321–324 (2005).

[24] M. A. Cazalilla, A. F. Ho, and M. Ueda. *Ultracold gases of ytterbium: ferromagnetism and Mott states in an SU(6) Fermi system*. New Journal of Physics **11**, 103033 (2009).

[25] M. Hermele, V. Gurarie, and A. M. Rey. *Mott Insulators of Ultracold Fermionic Alkaline Earth Atoms: Underconstrained Magnetism and Chiral Spin Liquid*. Phys. Rev. Lett. **103**, 135301 (2009).

[26] A. V. Gorshkov, M. Hermele, V. Gurarie, C. Xu, P. S. Julienne, J. Ye, P. Zoller, E. Demler, M. D. Lukin, and A. M. Rey. *Two-orbital SU(N) magnetism with ultracold alkaline-earth atoms*. Nat. Phys. **6**, 289–295 (2010).

[27] A. J. Daley, M. M. Boyd, J. Ye, and P. Zoller. *Quantum Computing with Alkaline-Earth-Metal Atoms*. Phys. Rev. Lett. **101**, 170504 (2008).

[28] K. Shibata, S. Kato, A. Yamaguchi, S. Uetake, and Y. Takahashi. *A scalable quantum computer with ultranarrow optical transition of ultracold neutral atoms in an optical lattice*. Applied Physics B **97**, 753–758 (2009).

[29] A. V. Gorshkov, A. M. Rey, A. J. Daley, M. M. Boyd, J. Ye, P. Zoller, and M. D. Lukin. *Alkaline-Earth-Metal Atoms as Few-Qubit Quantum Registers*. Phys. Rev. Lett. **102**, 110503 (2009).

[30] A. J. Daley. *Quantum computing and quantum simulation with group-II atoms*. Quantum Inf. Process. **10**, 865–884 (2011).

[31] S. Taie, R. Yamazaki, S. Sugawa, and Y. Takahashi. *An SU(6) Mott insulator of an atomic Fermi gas realized by large-spin Pomeranchuk cooling*. Nat. Phys. **8**, 825–830 (2012).

[32] G. Pagano, M. Mancini, G. Cappellini, P. Lombardi, F. Schäfer, H. Hu, X.-J. Liu, J. Catani, C. Sias, M. Inguscio, and L. Fallani. *A one-dimensional liquid of fermions with tunable spin*. Nat. Phys. **10**, 198–201 (2014).

[33] X. Zhang, M. Bishof, S. L. Bromley, C. V. Kraus, M. S. Safronova, P. Zoller, A. M. Rey, and J. Ye. *Spectroscopic observation of SU(N)-symmetric interactions in Sr orbital magnetism*. Science **345**, 1467–1473 (2014).

[34] M. A. Cazalilla and A. M. Rey. *Ultracold Fermi gases with emergent SU(N) symmetry*. Rep. Progr. Phys. **77**, 124401 (2014).

[35] M. Foss-Feig, M. Hermele, and A. M. Rey. *Probing the Kondo lattice model with alkaline-earth-metal atoms*. Phys. Rev. A **81**, 051603 (2010).

[36] M. Foss-Feig, M. Hermele, V. Gurarie, and A. M. Rey. *Heavy fermions in an optical lattice*. Phys. Rev. A **82**, 053624 (2010).

[37] F. Gerbier and J. Dalibard. *Gauge fields for ultracold atoms in optical superlattices*. New Journal of Physics **12**, 033007 (2010).

[38] N. Hinkley, J. A. Sherman, N. B. Phillips, M. Schioppo, N. D. Lemke, K. Beloy, M. Pizzocaro, C. W. Oates, and A. D. Ludlow. *An Atomic Clock with 10^{-18} Instability*. Science **641**, 1215–1218 (2013).

[39] B. J. Bloom, T. L. Nicholson, J. R. Williams, S. L. Campbell, M. Bishof, X. Zhang, W. Zhang, S. L. Bromley, and J. Ye. *An optical lattice clock with accuracy and stability at the 10^{-18} level*. Nature **506**, 71–75 (2014).

[40] I. Ushijima, M. Takamoto, M. Das, T. Ohkubo, and H. Katori. *Cryogenic optical lattice clocks*. Nat. Photon. **9**, 185–189 (2015).

[41] G. Cappellini, M. Mancini, G. Pagano, P. Lombardi, L. Livi, M. S. de Cumis, P. Cancio, M. Pizzocaro, D. Calonico, F. Levi, C. Sias, J. Catani, M. Inguscio, and L. Fallani. *Direct Observation of Coherent Interorbital Spin-Exchange Dynamics*. Phys. Rev. Lett. **113** (2014).

[42] S. Doniach. *The Kondo lattice and weak antiferromagnetism*. Physica B+C **91**, 231 – 234 (1977).

[43] G. R. Stewart. *Heavy-fermion systems*. Rev. Mod. Phys. **56**, 755–787 (1984).

[44] P. Gegenwart, Q. Si, and F. Steglich. *Quantum criticality in heavy-fermion metals*. Nat. Phys. **4**, 186–197 (2008).

[45] H. v. Löhneysen, A. Rosch, M. Vojta, and P. Wölfle. *Fermi-liquid instabilities at magnetic quantum phase transitions*. Rev. Mod. Phys. **79**, 1015–1075 (2007).

[46] M. A. Ruderman and C. Kittel. *Indirect Exchange Coupling of Nuclear Magnetic Moments by Conduction Electrons*. Phys. Rev. **96**, 99–102 (1954).

[47] A. D. Ludlow, X. Huang, M. Notcutt, T. Zanon-Willette, S. M. Foreman, M. M. Boyd, S. Blatt, and J. Ye. *Compact, thermal-noise-limited optical cavity for diode laser stabilization at 1×10−15*. Opt. Lett. **32**, 641–643 (2007).

[48] J. Alnis, A. Matveev, N. Kolachevsky, T. Udem, and T. W. Hänsch. *Subhertz linewidth diode lasers by stabilization to vibrationally and thermally compensated ultralow-expansion glass Fabry-Pérot cavities*. Phys. Rev. A **77**, 053809 (2008).

[49] Y. Y. Jiang, A. D. Ludlow, N. D. Lemke, R. W. Fox, J. A. Sherman, L.-S. Ma, and C. W. Oates. *Making optical atomic clocks more stable with 10^{-16}-level laser stabilization*. Nat. Photon. **5**, 158–161 (2011).

[50] G. Cappellini, P. Lombardi, M. Mancini, G. Pagano, M. Pizzocaro, L. Fallani, and J. Catani. *A compact ultranarrow high-power laser system for experiments with 578 nm ytterbium clock transition*. Rev. Sci. Instrum. **86**, 073111 (2015).

[51] D. Calonico, E. K. Bertacco, C. E. Calosso, C. Clivati, G. A. Costanzo, M. Frittelli, A. Godone, A. Mura, N. Poli, D. V. Sutyrin, G. Tino, M. E.

Zucco, and F. Levi. *High-accuracy coherentopt frequency transfer over a doubled 642-km fiber link*. Appl. Phys. B **117**, 979–986 (2014).

[52] A. Yamaguchi, M. Fujieda, M. Kumagai, H. Hachisu, S. Nagano, Y. Li, T. Ido, T. Takano, M. Takamoto, and H. Katori. *Direct Comparison of Distant Optical Lattice Clocks at the 10 -16 Uncertainty*. Applied Physics Express **4**, 082203 (2011).

[53] C. Lisdat, G. Grosche, N. Quintin, C. Shi, S. M. F. Raupach, C. Grebing, D. Nicolodi, F. Stefani, A. Al-Masoudi, S. Dörscher, S. Häfner, J.-L. Robyr, N. Chiodo, S. Bilicki, E. Bookjans, A. Koczwara, S. Koke, A. Kuhl, F. Wiotte, F. Meynadier, E. Camisard, M. Abgrall, M. Lours, T. Legero, H. Schnatz, U. Sterr, H. Denker, C. Chardonnet, Y. L. Coq, G. Santarelli, A. Amy-Klein, R. L. Targat, J. Lodewyck, O. Lopez, and P.-E. Pottie. *A clock network for geodesy and fundamental science*. arXiv:1511.07735 (2015).

[54] H. Margolis, R. Godun, P. Gill, L. Johnson, S. Shemar, P. Whibberley, D. Calonico, F. Levi, L. Lorini, M. Pizzocaro, P. Delva, S. Bize, J. Achkar, H. Denker, L. Timmen, C. Voigt, S. Falke, D. Piester, C. Lisdat, U. Sterr, S. Vogt, S. Weyers, J. Gersl, T. Lindvall, and M. Merimaa. *International timescales with optical clocks (ITOC)*. In *European Frequency and Time Forum International Frequency Control Symposium (EFTF/IFC), 2013 Joint*, pages 908–911 (2013).

[55] C. Clivati, G. Costanzo, M. Frittelli, F. Levi, A. Mura, M. Zucco, R. Ambrosini, C. Bortolotti, F. Perini, M. Roma, and D. Calonico. *A coherent fiber link for very long baseline interferometry*. IEEE Trans. Ultrason. Ferroelectr. Freq. Contr. **62**, 1907–1912 (2015).

[56] C. Clivati, G. Cappellini, , L. Livi, F. Poggiali, M. Siciliani de Cumis, M. Mancini, G. Pagano, M. Frittelli, A. Mura, G. A. Costanzo, F. Levi, D. Calonico, L. Fallani, J. Catani, and M. Inguscio. *Measuring absolute frequencies beyond the GPS limit via long-haul optical frequency dissemination*. arXiv:1511.08485 (2015).

[57] G. Pagano, M. Mancini, G. Cappellini, L. Livi, C. Sias, J. Catani, M. Inguscio, and L. Fallani. *Strongly Interacting Gas of Two-Electron Fermions at an Orbital Feshbach Resonance*. Phys. Rev. Lett. **115**, 265301 (2015).

[58] R. Zhang, Y. Cheng, H. Zhai, and P. Zhang. *Orbital Feshbach Resonance in Alkali-Earth Atoms*. Phys. Rev. Lett. **115**, 135301 (2015).

[59] C. Cohen-Tannoudji. *Atomic motion in laser light*. Les Houches session LIII (1992).

[60] D. A. Steck. *Quantum and Atom optics*. (2007).

[61] R. Grimm, M. Weidemüller, and Y. B. Ovchinnikov. *Optical Dipole Traps for Neutral Atoms*. Volume 42 of *Adv. At. Mol. Opt. Phys.*, pages 95 – 170. Academic Press (2000).

[62] S. Chu, J. E. Bjorkholm, A. Ashkin, and A. Cable. *Experimental Observation of Optically Trapped Atoms*. Phys. Rev. Lett. **57**, 314–317 (1986).

[63] D. M. Stamper-Kurn, M. R. Andrews, A. P. Chikkatur, S. Inouye, H.-J. Miesner, J. Stenger, and W. Ketterle. *Optical Confinement of a Bose-Einstein Condensate*. Phys. Rev. Lett. **80**, 2027–2030 (1998).

[64] N. L. Smith, W. H. Heathcote, G. Hechenblaikner, E. Nugent, and C. J. Foot. *Quasi-2D confinement of a BEC in a combined optical and magnetic potential*. J. Phys. B **38**, 223 (2005).

[65] L. Corman, L. Chomaz, T. Bienaimé, R. Desbuquois, C. Weitenberg, S. Nascimbène, J. Dalibard, and J. Beugnon. *Quench-Induced Supercurrents in an Annular Bose Gas*. Phys. Rev. Lett. **113**, 135302 (2014).

[66] A. L. Gaunt, T. F. Schmidutz, I. Gotlibovych, R. P. Smith, and Z. Hadzibabic. *Bose-Einstein Condensation of Atoms in a Uniform Potential*. Phys. Rev. Lett. **110**, 200406 (2013).

[67] C. Becker, P. Soltan-Panahi, J. Kronjäger, S. Dörscher, K. Bongs, and K. Sengstock. *Ultracold quantum gases in triangular optical lattices*. New J. Phys. **12**, 065025 (2010).

[68] P. Soltan-Panahi, J. Struck, P. Hauke, A. Bick, W. Plenkers, G. Meineke, C. Becker, P. Windpassinger, M. Lewenstein, and K. Sengstock. *Multicomponent quantum gases in spin-dependent hexagonal lattices*. Nat. Phys. **7**, 434–440 (2011).

[69] L. Tarruell, D. Greif, T. Uehlinger, G. Jotzu, and T. Esslinger. *Creating, moving and merging Dirac points with a Fermi gas in a tunable honeycomb lattice*. Nature **483**, 302–305 (2012).

[70] G.-B. Jo, J. Guzman, C. K. Thomas, P. Hosur, A. Vishwanath, and D. M. Stamper-Kurn. *Ultracold Atoms in a Tunable Optical Kagome Lattice*. Phys. Rev. Lett. **108**, 045305 (2012).

[71] N. Ashcroft and N. Mermin. *Solid State Physics*. Saunders College Publishing, Fort Worth, TX (1976).

[72] M. Greiner, I. Bloch, O. Mandel, T. W. Hänsch, and T. Esslinger. *Exploring Phase Coherence in a 2D Lattice of Bose-Einstein Condensates*. Phys. Rev. Lett. **87**, 160405 (2001).

[73] M. Köhl, H. Moritz, T. Stöferle, K. Günter, and T. Esslinger. *Fermionic Atoms in a Three Dimensional Optical Lattice: Observing Fermi Surfaces, Dynamics, and Interactions*. Phys. Rev. Lett. **94**, 080403 (2005).

[74] G. F. Gribakin and V. V. Flambaum. *Calculation of the scattering length in atomic collisions using the semiclassical approximation*. Phys. Rev. A **48**, 546–553 (1993).

[75] J. Dalibard. *Collisional dynamics of ultra-cold atomic gases*. In *Proceedings of the International School of Physics "E. Fermi", Course CLXI*, pages 321–349. IOS Press, Amsterdam (1999).

[76] V. A. Dzuba and A. Derevianko. *Dynamic polarizabilities and related properties of clock states of the ytterbium atom*. Journal of Physics B **43**, 074011 (2010).

[77] L. D. Landau and E. M. Lifshitz. *Quantum Mechanics*. Pergamon Press, Oxford (1977).

[78] W. Ketterle and M. W. Zwierlein. *Making, probing and understanding ultracold Fermi gases*. In *Proceedings of the International School of Physics "E. Fermi", Course CLXIV*, pages 95–287. IOS Press, Amsterdam (2006).

[79] K. Huang. *Statistical Mechanics*. John Wiley & Sons (1987).

[80] K. Huang and C. N. Yang. *Quantum-Mechanical Many-Body Problem with Hard-Sphere Interaction*. Phys. Rev. **105**, 767–775 (1957).

[81] A. Rapp, G. Zaránd, C. Honerkamp, and W. Hofstetter. *Color Superfluidity and "Baryon" Formation in Ultracold Fermions*. Phys. Rev. Lett. **98**, 160405 (2007).

[82] D. Banerjee, M. Bögli, M. Dalmonte, E. Rico, P. Stebler, U.-J. Wiese, and P. Zoller. *Atomic Quantum Simulation of $U(N)$ and $SU(N)$ Non-Abelian Lattice Gauge Theories*. Phys. Rev. Lett. **110**, 125303 (2013).

[83] F. Scazza. *Probing SU(N)-symmetric orbital interactions with ytterbium Fermi gases in optical lattices*. PhD thesis, Ludwig-Maximilians-Universität, München (2015).

[84] F. Scazza, C. Hofrichter, M. Hofer, P. C. De Groot, I. Bloch, and S. Folling. *Observation of two-orbital spin-exchange interactions with ultracold SU(N)-symmetric fermions*. Nat Phys **10**, 779–784 (2014).

[85] C. Chin, R. Grimm, P. Julienne, and E. Tiesinga. *Feshbach resonances in ultracold gases*. Rev. Mod. Phys. **82**, 1225–1286 (2010).

[86] D. M. Stamper-Kurn and M. Ueda. *Spinor Bose gases: Symmetries, magnetism, and quantum dynamics*. Rev. Mod. Phys. **85**, 1191–1244 (2013).

[87] T.-L. Ho. *Spinor Bose Condensates in Optical Traps*. Phys. Rev. Lett. **81**, 742–745 (1998).

[88] S.-K. Yip and T.-L. Ho. *Zero sound modes of dilute Fermi gases with arbitrary spin*. Phys. Rev. A **59**, 4653–4656 (1999).

[89] A. Widera, F. Gerbier, S. Fölling, T. Gericke, O. Mandel, and I. Bloch. *Coherent Collisional Spin Dynamics in Optical Lattices*. Phys. Rev. Lett. **95**, 190405 (2005).

[90] A. Widera, F. Gerbier, S. Fölling, T. Gericke, O. Mandel, and I. Bloch. *Precision measurement of spin-dependent interaction strengths for spin-1 and spin-2 87 Rb atoms*. New J. Phys. **8**, 152 (2006).

[91] J. S. Krauser, J. Heinze, N. Flaschner, S. Gotze, O. Jurgensen, D.-S. Luhmann, C. Becker, and K. Sengstock. *Coherent multi-flavour spin dynamics in a fermionic quantum gas*. Nat. Phys. **8**, 813–818 (2012).

[92] J. S. Krauser, U. Ebling, N. Fläschner, J. Heinze, K. Sengstock, M. Lewenstein, A. Eckardt, and C. Becker. *Giant Spin Oscillations in an Ultracold Fermi Sea*. Science **343**, 157–160 (2014).

[93] M. Kitagawa, K. Enomoto, K. Kasa, Y. Takahashi, R. Ciuryło, P. Naidon, and P. S. Julienne. *Two-color photoassociation spectroscopy of ytterbium atoms and the precise determinations of s-wave scattering lengths*. Phys. Rev. A **77**, 012719 (2008).

[94] J.-C. G. de Marignac. *Oeuvres complétes: Mémoires et critiques. 1860-1887*. Ch. Eggimann et Cie (1902).

[95] J. Miao, J. Hostetter, G. Stratis, and M. Saffman. *Magneto-optical trapping of holmium atoms*. Phys. Rev. A **89**, 041401 (2014).

[96] A. Frisch, K. Aikawa, M. Mark, A. Rietzler, J. Schindler, E. Zupanič, R. Grimm, and F. Ferlaino. *Narrow-line magneto-optical trap for erbium*. Phys. Rev. A **85**, 051401 (2012).

[97] M. Lu, S. H. Youn, and B. L. Lev. *Spectroscopy of a narrow-line laser-cooling transition in atomic dysprosium*. Phys. Rev. A **83**, 012510 (2011).

[98] R. Maruyama. *Optical trapping of ytterbium atoms*. PhD thesis, University of Washington, Washington (2003).

[99] M. Berglund and M. E. Wieser. *Isotopic compositions of the elements 2009 (IUPAC Technical Report)*. Pure Appl. Chem. **83**, 397–410 (2011).

[100] W. C. M. J. E. Sansonetti. *Handbook of basic atomic spectroscopic data*. J. Phys. Chem. Ref. Data **34**, 1559–2260 (2005).

[101] A. Yamaguchi. *Metastable State of Ultracold and Quantum Degenerate Ytterbium Atoms*. PhD thesis, Kyoto University (2008).

[102] D. Das, S. Barthwal, A. Banerjee, and V. Natarajan. *Absolute frequency measurements in Yb with* 0.08 ppb *uncertainty: Isotope shifts and hyperfine structure in the* 399-nm $^1S_0 \to^1 P_1$ *line*. Phys. Rev. A **72**, 032506 (2005).

[103] K. Pandey, A. K. Singh, P. V. K. Kumar, M. V. Suryanarayana, and V. Natarajan. *Isotope shifts and hyperfine structure in the 555.8-nm* $^1S_0 \to {}^3P_1$ *line of Yb*. Phys. Rev. A **80**, 022518 (2009).

[104] M. Borkowski, R. Ciuryło, P. S. Julienne, R. Yamazaki, H. Hara, K. Enomoto, S. Taie, S. Sugawa, Y. Takasu, and Y. Takahashi. *Photoassociative production of ultracold heteronuclear ytterbium molecules*. Phys. Rev. A **84**, 030702 (2011).

[105] T. Fukuhara, S. Sugawa, Y. Takasu, and Y. Takahashi. *All-optical formation of quantum degenerate mixtures*. Phys. Rev. A **79**, 021601 (2009).

[106] S. Sugawa, K. Inaba, S. Taie, R. Yamazaki, M. Yamashita, and Y. Takahashi. *Interaction and filling-induced quantum phases of dual Mott insulators of bosons and fermions*. Nat. Phys. **7**, 642–648 (2011).

[107] S. Taie, Y. Takasu, S. Sugawa, R. Yamazaki, T. Tsujimoto, R. Murakami, and Y. Takahashi. *Realization of a* SU(2) × SU(6) *System of Fermions in a Cold Atomic Gas*. Phys. Rev. Lett. **105**, 190401 (2010).

[108] A. D. Ludlow, N. D. Lemke, J. A. Sherman, C. W. Oates, G. Quéméner, J. von Stecher, and A. M. Rey. *Cold-collision-shift cancellation and inelastic scattering in a Yb optical lattice clock*. Phys. Rev. A **84**, 052724 (2011).

[109] N. D. Lemke, J. von Stecher, J. A. Sherman, A. M. Rey, C. W. Oates, and A. D. Ludlow. *p-Wave Cold Collisions in an Optical Lattice Clock*. Phys. Rev. Lett. **107**, 103902 (2011).

[110] A. D. Ludlow, M. M. Boyd, J. Ye, E. Peik, and P. O. Schmidt. *Optical atomic clocks*. Rev. Mod. Phys. **87**, 637–701 (2015).

[111] G. Pagano. *Many-body physics with Ytterbium Fermi gases in optical lattices: from one-dimensional systems to orbital magnetism*. PhD thesis, Scuola Normale Superiore, Pisa (2015).

[112] G. Pagano. *Raffreddamento e intrappolamento di atomi di Itterbio*. Master's thesis, Università "La Sapienza" (2011).

[113] B. Zimmermann, T. Müller, J. Meineke, T. Esslinger, and H. Moritz. *High-resolution imaging of ultracold fermions in microscopically tailored optical potentials*. New J. Phys. **13**, 043007 (2011).

[114] T. L. Gustavson, A. P. Chikkatur, A. E. Leanhardt, A. Görlitz, S. Gupta, D. E. Pritchard, and W. Ketterle. *Transport of Bose-Einstein Condensates with Optical Tweezers*. Phys. Rev. Lett. **88**, 020401 (2001).

[115] S. Schmid, G. Thalhammer, K. Winkler, F. Lang, and J. H. Denschlag. *Long distance transport of ultracold atoms using a 1D optical lattice*. New J. Phys. **8**, 159 (2006).

[116] M. Mancini. *Quantum simulation with Ytterbium atoms in synthetic dimensions*. PhD thesis, Università di Firenze (2015).

[117] M. Mancini. *Realizzazione sperimentale di un gas quantistico degenere di atomi di Itterbio*. Master's thesis, Università di Milano (2012).

[118] T. W. Hänsch and B. Couillaud. *Laser frequency stabilization by polarization spectroscopy of a reflecting reference cavity*. Opt. Commun. **35**, 441–444 (1980).

[119] B. Fröhlich, T. Lahaye, B. Kaltenhäuser, H. Kübler, S. Müller, T. Koch, M. Fattori, and T. Pfau. *Two-frequency acousto-optic modulator driver to improve the beam pointing stability during intensity ramps*. Rev. Sci. Intrum. **78**, 043011 (2007).

[120] E. D. Black. *An introduction to Pound-Drever-Hall laser frequency stabilization*. Am. J. Phys. **69** (2001).

[121] S. Dörscher, A. Thobe, B. Hundt, A. Kochanke, R. Le Targat, P. Windpassinger, C. Becker, and K. Sengstock. *Creation of quantum-degenerate gases of ytterbium in a compact 2D-/3D-magneto-optical trap setup*. Rev. Sci. Instrum. **84** (2013).

[122] W. D. Phillips and H. Metcalf. *Laser Deceleration of an Atomic Beam*. Phys. Rev. Lett. **48**, 596–599 (1982).

[123] T. E. Barrett, S. W. Dapore-Schwartz, M. D. Ray, and G. P. Lafyatis. *Slowing atoms with σ^- polarized light*. Phys. Rev. Lett. **67**, 3483–3486 (1991).

[124] C. Fort. *Intrappolamento e raffreddamento di atomi di cesio tramite luce laser: misure spettroscopiche*. PhD thesis, Università di Firenze (1995).

[125] G. Insero. *Realizzazione di un Apparato Sperimentale per il rallentamento di un fascio atomico di Itterbio*. (2010).

[126] T. Kuwamoto, K. Honda, Y. Takahashi, and T. Yabuzaki. *Magneto-optical trapping of Yb atoms using an intercombination transition*. Phys. Rev. A **60**, R745–R748 (1999).

[127] K.-A. Suominen. *Theories for cold atomic collisions in light fields*. J. Phys. B **29**, 5981 (1996).

[128] J. Weiner, V. S. Bagnato, S. Zilio, and P. S. Julienne. *Experiments and theory in cold and ultracold collisions*. Rev. Mod. Phys. **71**, 1–85 (1999).

[129] L. F. Livi. *Trasporto ottico di atomi freddi a lunga distanza*. (2012).

[130] Y. B. Ovchinnikov, J. H. Müller, M. R. Doery, E. J. D. Vredenbregt, K. Helmerson, S. L. Rolston, and W. D. Phillips. *Diffraction of a Released Bose-Einstein Condensate by a Pulsed Standing Light Wave*. Phys. Rev. Lett. **83**, 284–287 (1999).

[131] B. Hundt. *Momentum-resolved optical lattice modulation spectroscopy on Bose-Fermi mixtures*. Master's thesis, Universität Hamburg (2011).

[132] W. Ketterle, D. Durfee, and D. M. Stamper-Kurn. *Making, probing and understanding Bose-Einstein condensates*. In *Proceedings of the International School of Physics "E. Fermi", Course CXL*, pages 67–176. IOS Press, Amsterdam (1999).

[133] S. Stellmer, R. Grimm, and F. Schreck. *Production of quantum-degenerate strontium gases*. Phys. Rev. A **87**, 013611 (2013).

[134] R. V. P. Drever, J. L. Hall, F. V. Kowalski, J. Hough, G. M. Ford, A. J. Munley, and H. Ward. *Laser phase and frequency stabilization using an optical resonator*. Appl. Phys. B **31**, 97–105 (1983).

[135] R. W. Fox, C. W. Oates, and L. W. Hollberg. *Stabilizing diode lasers to high-finesse cavities*. Experimental Methods in the Physical Sciences, Cavity-Enhanced Spectroscopies **40**, 1–46 (2003).

[136] S. A. Webster, M. Oxborrow, S. Pugla, J. Millo, and P. Gill. *Thermal-noise-limited optical cavity*. Phys. Rev. A **77**, 033847 (2008).

[137] C. W. Oates, Z. W. Barber, J. E. Stalnaker, C. W. Hoyt, T. M. Fortier, S. A. Diddams, and L. Hollberg. *Stable Laser System for Probing the Clock Transition at 578 nm in Neutral Ytterbium*. In *IEEE Int. Frequency Control Symp.-21st European Frequency and Time Forum*, pages 1274–1277 (2007).

[138] M. Pizzocaro, G. A. Costanzo, A. Godone, F. Levi, A. Mura, M. Zoppi, and D. Calonico. *Realization of an ultrastable 578-nm laser for an Yb lattice clock*. IEEE Trans. on Ultrason. Ferroelectr. Freq. Control **59**, 426–431 (2012).

[139] N. Kolachevsky, J. Alnis, C. G. Parthey, A. Matveev, R. Landig, and T. W. Hänsch. *Low phase noise diode laser oscillator for 1S-2S spectroscopy in atomic hydrogen*. . Lett. **36**, 4299–4301 (2011).

[140] L. Ricci, M. Weidemüller, T. Esslinger, A. Hemmerich, C. Zimmermann, V. Vuletic, W. König, and T. W. Hänsch. *A Compact Grating-stabilized Diode Lased System for Atomic Physics*. . Commun. **117** (1995).

[141] K. M. Jones, E. Tiesinga, P. D. Lett, and P. S. Julienne. *Ultracold photoassociation spectroscopy: Long-range molecules and atomic scattering*. Rev. Mod. Phys. **78** (2006).

[142] D. Z. Anderson, J. C. Frisch, and C. S. Masser. *Mirror reflectometer based on optical cavity decay time*. Appl. Opt. **23**, 1238–1245 (1984).

[143] J. Bergquist, W. Itano, and D. Wineland. *Laser Stabilization to a Single Ion*. In *Proceedings of the International School of Physics "E. Fermi", Course CXX*, pages 359–376. North-Holland (1992).

[144] G. D. Domenico, S. Schilt, and P. Thomann. *Simple approach to the relation between laser frequency noise and laser line shape*. Appl. . **49**, 4801–4807 (2010).

[145] E. A. Whittaker, M. Gehrtz, and G. C. Bjorklund. *Residual amplitude modulation in laser electro-optic phase modulation*. J. Opt. Soc. Am. B **2**, 1320–1326 (1985).

[146] C. Clivati. *Realization of a phase-coherent fiber link for the comparison of remote atomic clocks*. PhD thesis, Politecnico di Torino (2014).

[147] B. Guinot and E. F. Arias. *Atomic time-keeping from 1955 to the present*. Metrologia **42**, S20 (2005).

[148] T. E. Parker. *Long-term comparison of caesium fountain primary frequency standards*. Metrologia **47**, 1 (2010).

[149] M. Lombardi. *The Use of GPS Disciplined Oscillators as Primary Frequency Standards for Calibration and Metrology Laboratories*. NCSLI Measure (2008).

[150] F. Levi, C. Calosso, D. Calonico, L. Lorini, E. Bertacco, A. Godone, G. A. Costanzo, B. Mongino, S. R. Jefferts, T. P. Heavner, and E. A. Donley. *Cryogenic fountain development at NIST and INRIM: preliminary characterization*. IEEE Trans. Ultrason. Ferroelectr. Freq. Contr. **57**, 600–605 (2010).

[151] S. Droste, F. Ozimek, T. Udem, K. Predehl, T. W. Hänsch, H. Schnatz, G. Grosche, and R. Holzwarth. *Optical-Frequency Transfer over a Single-Span 1840 km Fiber Link*. Phys. Rev. Lett. **111**, 110801 (2013).

[152] O. Lopez, A. Haboucha, B. Chanteau, C. Chardonnet, A. Amy-Klein, and G. Santarelli. *Ultra-stable long distance optical frequency distribution using the Internet fiber network*. Opt. Express **20**, 23518–23526 (2012).

[153] A. Bauch, J. Achkar, S. Bize, D. Calonico, R. Dach, R. Hlavać, L. Lorini, T. Parker, G. Petit, D. Piester, K. Szymaniec, and P. Uhrich. *Comparison*

between frequency standards in Europe and the USA at the 10^{-15} uncertainty level. Metrologia **43**, 109 (2006).

[154] A. Matveev, C. G. Parthey, K. Predehl, J. Alnis, A. Beyer, R. Holzwarth, T. Udem, T. Wilken, N. Kolachevsky, M. Abgrall, D. Rovera, C. Salomon, P. Laurent, G. Grosche, O. Terra, T. Legero, H. Schnatz, S. Weyers, B. Altschul, and T. W. Hänsch. *Precision Measurement of the Hydrogen 1S-2S Frequency via a 920-km Fiber Link*. Phys. Rev. Lett. **110**, 230801 (2013).

[155] S. Droste, C. Grebing, J. Leute, S. M. F. Raupach, A. Matveev, T. W. Hänsch, A. Bauch, R. Holzwarth, and G. Grosche. *Characterization of a 450 km baseline GPS carrier-phase link using an optical fiber link*. New J. Phys. **17**, 083044 (2015).

[156] B. Argence, B. Chanteau, O. Lopez, D. Nicolodi, M. Abgrall, C. Chardonnet, C. Daussy, B. Darquié, Y. Le Coq, and A. Amy-Klein. *Quantum cascade laser frequency stabilization at the sub-Hz level*. Nat. Photon. **9**, 456–460 (2015). Article.

[157] O. Lopez, A. Haboucha, F. Kéfélian, H. Jiang, B. Chanteau, V. Roncin, C. Chardonnet, A. Amy-Klein, and G. Santarelli. *Cascaded multiplexed optical link on a telecommunication network for frequency dissemination*. Opt. Express **18**, 16849–16857 (2010).

[158] H. Jiang, F. Kéfélian, S. Crane, O. Lopez, M. Lours, J. Millo, D. Holleville, P. Lemonde, C. Chardonnet, A. Amy-Klein, and G. Santarelli. *Long-distance frequency transfer over an urban fiber link using optical phase stabilization*. J. Opt. Soc. Am. B **25**, 2029–2035 (2008).

[159] P. A. Williams, W. C. Swann, and N. R. Newbury. *High-stability transfer of an optical frequency over long fiber-optic links*. J. Opt. Soc. Am. B **25**, 1284–1293 (2008).

[160] F. Levi, D. Calonico, A. Mura, M. Frittelli, C. Calosso, M. Zucco, C. Clivati, G. Costanzo, R. Ambrosini, G. Galzerano, P. De Natale, D. Mazzotti, N. Sutyrin, and G. Tino. *LIFT-the Italian link for time and frequency*. In *European Frequency and Time Forum International Frequency Control Symposium (EFTF/IFC), 2013 Joint*, pages 477–480 (2013).

[161] S. T. Dawkins, J. J. McFerran, and A. N. Luiten. *Considerations on the measurement of the stability of oscillators with frequency counters*. IEEE Trans. Ultrason. Ferroelectr. Freq. Contr. **54**, 918–925 (2007).

[162] F. Poggiali. *Ultranarrow laser stabilization with long-distance optical fiber link for experiments with Ytterbium ultracold gases*. Master's thesis, Università di Firenze (2015).

[163] N. Poli, Z. W. Barber, N. D. Lemke, C. W. Oates, L. S. Ma, J. E. Stalnaker, T. M. Fortier, S. A. Diddams, L. Hollberg, J. C. Bergquist, A. Brusch, S. Jefferts, T. Heavner, and T. Parker. *Frequency evaluation of the doubly forbidden* $^1S_0 \to {}^3P_0$ *transition in bosonic* ^{174}Yb. Phys. Rev. A **77**, 050501 (2008).

[164] N. D. Lemke, A. D. Ludlow, Z. W. Barber, T. M. Fortier, S. A. Diddams, Y. Jiang, S. R. Jefferts, T. P. Heavner, T. E. Parker, and C. W. Oates. *Spin-1/2 Optical Lattice Clock*. Phys. Rev. Lett. **103**, 063001 (2009).

[165] C. W. Hoyt, Z. W. Barber, C. W. Oates, T. M. Fortier, S. A. Diddams, and L. Hollberg. *Observation and Absolute Frequency Measurements of the* $^1S_0 \to {}^3P_0$ *Optical Clock Transition in Neutral Ytterbium*. Phys. Rev. Lett. **95**, 083003 (2005).

[166] M. M. Boyd, T. Zelevinsky, A. D. Ludlow, S. Blatt, T. Zanon-Willette, S. M. Foreman, and J. Ye. *Nuclear spin effects in optical lattice clocks*. Phys. Rev. A **76**, 022510 (2007).

[167] S. G. Porsev and A. Derevianko. *Hyperfine quenching of the metastable* $^3P_{0,2}$ *states in divalent atoms*. Phys. Rev. A **69**, 042506 (2004).

[168] S. G. Porsev, A. Derevianko, and E. N. Fortson. *Possibility of an optical clock using the* $6^1S_0 \to 6^3P_0^o$ *transition in* ^{171,173}Yb *atoms held in an optical lattice*. Phys. Rev. A **69**, 021403 (2004).

[169] A. V. Taichenachev, V. I. Yudin, C. W. Oates, C. W. Hoyt, Z. W. Barber, and L. Hollberg. *Magnetic Field-Induced Spectroscopy of Forbidden Optical Transitions with Application to Lattice-Based Optical Atomic Clocks*. Phys. Rev. Lett. **96**, 083001 (2006).

[170] Z. Barber. *Ytterbium Optical Lattice Clock*. PhD thesis, University of Colorado (2007).

[171] A. D. Ludlow. *The Strontium Optical Lattice Clock: Optical Spectroscopy with Sub-Hertz Accuracy*. PhD thesis, University of Colorado (2008).

[172] D. Leibfried, R. Blatt, C. Monroe, and D. Wineland. *Quantum dynamics of single trapped ions*. Rev. Mod. Phys. **75**, 281–324 (2003).

[173] Z. W. Barber, J. E. Stalnaker, N. D. Lemke, N. Poli, C. W. Oates, T. M. Fortier, S. A. Diddams, L. Hollberg, C. W. Hoyt, A. V. Taichenachev, and V. I. Yudin. *Optical Lattice Induced Light Shifts in an Yb Atomic Clock*. Phys. Rev. Lett. **100**, 103002 (2008).

[174] F. Levi, D. Calonico, C. E. Calosso, A. Godone, S. Micalizio, and G. A. Costanzo. *Accuracy evaluation of ITCsF2: a nitrogen cooled caesium fountain*. Metrologia **51**, 270 (2014).

[175] J. A. Sherman, N. D. Lemke, N. Hinkley, M. Pizzocaro, R. W. Fox, A. D. Ludlow, and C. W. Oates. *High-Accuracy Measurement of Atomic Polarizability in an Optical Lattice Clock*. Phys. Rev. Lett. **108**, 153002 (2012).

[176] D. Calonico, A. Cina, I. H. Bendea, F. Levi, L. Lorini, and A. Godone. *Gravitational redshift at INRIM*. Metrologia **44**, L44 (2007).

[177] A. V. Taichenachev, V. I. Yudin, V. D. Ovsiannikov, and V. G. Pal'chikov. *Optical Lattice Polarization Effects on Hyperpolarizability of Atomic Clock Transitions*. Phys. Rev. Lett. **97**, 173601 (2006).

[178] M. Anderlini, P. J. Lee, B. L. Brown, J. Sebby-Strabley, W. D. Phillips, and J. V. Porto. *Controlled exchange interaction between pairs of neutral atoms in an optical lattice*. Nature **448**, 452–456 (2007).

[179] R. H. Dicke. *Coherence in Spontaneous Radiation Processes*. Phys. Rev. **93**, 99–110 (1954).

[180] T. Busch, B.-G. Englert, K. Rzazewski, and M. Wilkens. *Two Cold Atoms in a Harmonic Trap*. Foundations of Physics **28**, 549–559 (1998).

[181] L. F. Livi. *Generation of coherent atomic states through forbidden transitions in ultracold Fermi gases*. Master's thesis, Università di Firenze (2015).

[182] G. Zürn, F. Serwane, T. Lompe, A. N. Wenz, M. G. Ries, J. E. Bohn, and S. Jochim. *Fermionization of Two Distinguishable Fermions*. Phys. Rev. Lett. **108**, 075303 (2012).

[183] E. L. Bolda, E. Tiesinga, and P. S. Julienne. *Effective-scattering-length model of ultracold atomic collisions and Feshbach resonances in tight harmonic traps*. Phys. Rev. A **66**, 013403 (2002).

[184] R. Ciuryło, E. Tiesinga, and P. S. Julienne. *Optical tuning of the scattering length of cold alkaline-earth-metal atoms*. Phys. Rev. A **71**, 030701 (2005).

[185] S. Blatt, T. L. Nicholson, B. J. Bloom, J. R. Williams, J. W. Thomsen, P. S. Julienne, and J. Ye. *Measurement of Optical Feshbach Resonances in an Ideal Gas*. Phys. Rev. Lett. **107**, 073202 (2011).

[186] K. Enomoto, K. Kasa, M. Kitagawa, and Y. Takahashi. *Optical Feshbach Resonance Using the Intercombination Transition*. Phys. Rev. Lett. **101**, 203201 (2008).

[187] S. Taie, S. Watanabe, T. Ichinose, and Y. Takahashi. *Feshbach-Resonance-Enhanced Coherent Atom-Molecule Conversion with Ultra-Narrow Photoassociation Resonance*. preprint arXiv:1509.01830 (2015).

[188] M. Höfer, L. Riegger, F. Scazza, C. Hofrichter, D. R. Fernandes, M. M. Parish, J. Levinsen, I. Bloch, and S. Fölling. *Observation of an Orbital Interaction-Induced Feshbach Resonance in* ^{173}*Yb*. Phys. Rev. Lett. **115**, 265302 (2015).

[189] E. Wille. *Preparation of an Optically Trapped Fermi-Fermi Mixture of* ^{6}*Li and* ^{40}*K Atoms and Characterization of the Interspecies Interactions by Feshbach Spectroscopy*. PhD thesis, Universität Innsbruck (2009).

[190] D. S. Petrov. *The few-atoms problem*. arxiv:1206.5752v2 (2012).

[191] E. Haller, M. J. Mark, R. Hart, J. G. Danzl, L. Reichsöllner, V. Melezhik, P. Schmelcher, and H.-C. Nägerl. *Confinement-Induced Resonances in Low-Dimensional Quantum Systems*. Phys. Rev. Lett. **104**, 153203 (2010).

[192] H. Moritz, T. Stöferle, K. Günter, M. Köhl, and T. Esslinger. *Confinement Induced Molecules in a 1D Fermi Gas*. Phys. Rev. Lett. **94**, 210401 (2005).

[193] S. Giorgini, L. P. Pitaevskii, and S. Stringari. *Theory of ultracold atomic Fermi gases*. Rev. Mod. Phys. **80**, 1215–1274 (2008).

[194] K. M. O'Hara, S. L. Hemmer, M. E. Gehm, S. R. Granade, and J. E. Thomas. *Observation of a Strongly Interacting Degenerate Fermi Gas of Atoms*. Science **298**, 2179–2182 (2002).

[195] M. Greiner, C. A. Regal, and D. S. Jin. *Emergence of a molecular Bose-Einstein condensate from a Fermi gas*. Nature **426**, 537–540 (2003).

[196] S. Jochim, M. Bartenstein, A. Altmeyer, G. Hendl, S. Riedl, C. Chin, J. Hecker Denschlag, and R. Grimm. *Bose-Einstein Condensation of Molecules*. Science **302**, 2101–2103 (2003).

[197] M. W. Zwierlein, C. A. Stan, C. H. Schunck, S. M. F. Raupach, S. Gupta, Z. Hadzibabic, and W. Ketterle. *Observation of Bose-Einstein Condensation of Molecules*. Phys. Rev. Lett. **91**, 250401 (2003).

[198] C. Menotti, P. Pedri, and S. Stringari. *Expansion of an Interacting Fermi Gas*. Phys. Rev. Lett. **89**, 250402 (2002).

[199] C. A. Regal and D. S. Jin. *Measurement of Positive and Negative Scattering Lengths in a Fermi Gas of Atoms*. Phys. Rev. Lett. **90**, 230404 (2003).

[200] E. L. Hazlett, Y. Zhang, R. W. Stites, and K. M. O'Hara. *Realization of a Resonant Fermi Gas with a Large Effective Range*. Phys. Rev. Lett. **108**, 045304 (2012).

[201] D. S. Petrov, C. Salomon, and G. V. Shlyapnikov. *Scattering properties of weakly bound dimers of fermionic atoms*. Phys. Rev. A **71**, 012708 (2005).

[202] Z. Shizhong and T.-L. Ho. *Atom loss maximum in ultra-cold Fermi gases.* New J. of Phys. **13**, 055003 (2011).

[203] M. Mancini, G. Pagano, G. Cappellini, L. Livi, M. Rider, J. Catani, C. Sias, P. Zoller, M. Inguscio, M. Dalmonte, and L. Fallani. *Observation of chiral edge states with neutral fermions in synthetic Hall ribbons.* Science **349**, 1510–1513 (2015).

[204] T. Giamarchi. *Quantum physics in one dimension.* Clarendon Press (2003).

[205] C. N. Yang. *Some Exact Results for the Many-Body Problem in one Dimension with Repulsive Delta-Function Interaction.* Phys. Rev. Lett. **19**, 1312–1315 (1967).

[206] B. Sutherland. *Further Results for the Many-Body Problem in One Dimension.* Phys. Rev. Lett. **20**, 98–100 (1968).

[207] G. A. Fiete. *Colloquium : The spin-incoherent Luttinger liquid.* Rev. Mod. Phys. **79**, 801–820 (2007).

[208] E. H. Lieb and W. Liniger. *Exact Analysis of an Interacting Bose Gas. I. The General Solution and the Ground State.* Phys. Rev. **130**, 1605–1616 (1963).

[209] M. D. Girardeau. *Permutation Symmetry of Many-Particle Wave Functions.* Phys. Rev. **139**, B500–B508 (1965).

[210] F. D. M. Haldane. *"Luttinger liquid theory" of one-dimensional quantum fluids. I. Properties of the Luttinger model and their extension to the general 1D interacting spinless Fermi gas.* J. Phys. C **14**, 2585 (1981).

[211] H. J. Schulz, G. Cuniberti, and P. Pieri. *Field theories for low-dimensional condensed matter systems*, Chapter *Fermi liquids and Luttinger liquids.* Springer (2000).

[212] M. Olshanii. *Atomic Scattering in the Presence of an External Confinement and a Gas of Impenetrable Bosons.* Phys. Rev. Lett. **81**, 938–941 (1998).

[213] G. E. Astrakharchik, D. Blume, S. Giorgini, and L. P. Pitaevskii. *Interacting Fermions in Highly Elongated Harmonic Traps.* Phys. Rev. Lett. **93**, 050402 (2004).

[214] A. Recati, P. O. Fedichev, W. Zwerger, and P. Zoller. *Spin-Charge Separation in Ultracold Quantum Gases.* Phys. Rev. Lett. **90**, 020401 (2003).

[215] A. Recati, P. O. Fedichev, W. Zwerger, and P. Zoller. *Fermi one-dimensional quantum gas: Luttinger liquid approach and spin-charge separation.* J. Opt. B **5**, S55 (2003).

[216] M. Ogata and H. Shiba. *Bethe-ansatz wave function, momentum distribution, and spin correlation in the one-dimensional strongly correlated Hubbard model*. Phys. Rev. B **41**, 2326–2338 (1990).

[217] V. V. Cheianov, H. Smith, and M. B. Zvonarev. *Low-temperature crossover in the momentum distribution of cold atomic gases in one dimension*. Phys. Rev. A **71**, 033610 (2005).

[218] A. E. Feiguin and G. A. Fiete. *Spectral properties of a spin-incoherent Luttinger liquid*. Phys. Rev. B **81**, 075108 (2010).

[219] J. Stenger, S. Inouye, A. P. Chikkatur, D. M. Stamper-Kurn, D. E. Pritchard, and W. Ketterle. *Bragg Spectroscopy of a Bose-Einstein Condensate*. Phys. Rev. Lett. **82**, 4569–4573 (1999).

[220] X.-J. Liu and H. Hu. *Collective mode evidence of high-spin bosonization in a trapped one-dimensional atomic Fermi gas with tunable spin*. Annals of Physics **350**, 84 – 94 (2014).

[221] C. N. Yang and Y. Yi-Zhuang. *One-Dimensional w-Component Fermions and Bosons with Repulsive Delta Function Interaction*. Chinese Phys. Lett. **28**, 020503 (2011).

[222] I. Carusotto. *Bragg scattering and the spin structure factor of two-component atomic gases*. J. Phys. B **39**, S211 (2006).

[223] S. Hoinka, M. Lingham, M. Delehaye, and C. J. Vale. *Dynamic Spin Response of a Strongly Interacting Fermi Gas*. Phys. Rev. Lett. **109**, 050403 (2012).

[224] M. Z. Hasan and C. L. Kane. *Colloquium : Topological insulators*. Rev. Mod. Phys. **82**, 3045–3067 (2010).

[225] J. E. Moore. *The birth of topological insulators*. Nature **464**, 194–198 (2010).

[226] D. J. Thouless, M. Kohmoto, M. P. Nightingale, and M. den Nijs. *Quantized Hall Conductance in a Two-Dimensional Periodic Potential*. Phys. Rev. Lett. **49**, 405–408 (1982).

[227] K. v. Klitzing, G. Dorda, and M. Pepper. *New Method for High-Accuracy Determination of the Fine-Structure Constant Based on Quantized Hall Resistance*. Phys. Rev. Lett. **45**, 494–497 (1980).

[228] B. I. Halperin. *Quantized Hall conductance, current-carrying edge states, and the existence of extended states in a two-dimensional disordered potential*. Phys. Rev. B **25**, 2185–2190 (1982).

[229] Y. Aharonov and D. Bohm. *Significance of Electromagnetic Potentials in the Quantum Theory*. Phys. Rev. **115**, 485–491 (1959).

[230] B. A. Bernevig and T. L. Hughes. *Topological Insulators and Topological Superconductors*. Princeton University Press (2013).

[231] P. G. Harper. *Single Band Motion of Conduction Electrons in a Uniform Magnetic Field*. Proceedings of the Physical Society. Section A **68**, 874 (1955).

[232] D. R. Hofstadter. *Energy levels and wave functions of Bloch electrons in rational and irrational magnetic fields*. Phys. Rev. B **14**, 2239–2249 (1976).

[233] D. Jaksch and P. Zoller. *Creation of effective magnetic fields in optical lattices: the Hofstadter butterfly for cold neutral atoms*. New J. Phys. **5**, 56 (2003).

[234] J. Dalibard, F. Gerbier, G. Juzeliunas, and P. Öhberg. *Colloquium: Artificial gauge potentials for neutral atoms*. Rev. Mod. Phys. **83**, 1523–.–1543 (2011).

[235] N. Goldman, G. Juzeliunas, P. Öhberg, and I. B. Spielman. *Light-induced gauge fields for ultracold atoms*. Rep. Prog. in Phys. **77**, 126401 (2014).

[236] Y.-J. Lin, R. L. Compton, K. Jimenez-Garcia, J. V. Porto, and I. B. Spielman. *Synthetic magnetic fields for ultracold neutral atoms*. Nature **462**, 628–632 (2009).

[237] M. Aidelsburger, M. Atala, M. Lohse, J. T. Barreiro, B. Paredes, and I. Bloch. *Realization of the Hofstadter Hamiltonian with Ultracold Atoms in Optical Lattices*. Phys. Rev. Lett. **111**, 185301 (2013).

[238] H. Miyake, G. A. Siviloglou, C. J. Kennedy, W. C. Burton, and W. Ketterle. *Realizing the Harper Hamiltonian with Laser-Assisted Tunneling in Optical Lattices*. Phys. Rev. Lett. **111**, 185302 (2013).

[239] A. Celi, P. Massignan, J. Ruseckas, N. Goldman, I. B. Spielman, G. Juzeliunas, and M. Lewenstein. *Synthetic Gauge Fields in Synthetic Dimensions*. Phys. Rev. Lett. **112**, 043001 (2014).

[240] B. K. Stuhl, H.-I. Lu, L. M. Aycock, D. Genkina, and I. B. Spielman. *Visualizing edge states with an atomic Bose gas in the quantum Hall regime*. Science **349**, 1514–1518 (2015).

[241] M. Atala, M. Aidelsburger, M. Lohse, J. T. Barreiro, B. Paredes, and I. Bloch. *Observation of chiral currents with ultracold atoms in bosonic ladders*. Nat. Phys. **10**, 588–593 (2014). Article.

[242] R. E. Prange and S. M. Girvin. *The Quantum Hall Effect*. Springer, New York (1990).

[243] S. Barbarino, L. Taddia, D. Rossini, L. Mazza, and R. Fazio. *Synthetic gauge fields in synthetic dimensions: Interactions and chiral edge modes.* arXiv:1510.05603 (2015).

[244] S. Barbarino, L. Taddia, D. Rossini, L. Mazza, and R. Fazio. *Magnetic crystals and helical liquids in alkaline-earth fermionic gases.* Nat. Commun. **6** (2015). Article.

[245] O. Boada, A. Celi, J. Rodríguez-Laguna, J. I. Latorre, and M. Lewenstein. *Quantum simulation of non-trivial topology.* New J. Phys. **17**, 045007 (2015).

[246] R. B. Laughlin. *Quantized Hall conductivity in two dimensions.* Phys. Rev. B **23**, 5632–5633 (1981).

[247] W. S. Bakr, A. Peng, M. E. Tai, R. Ma, J. Simon, J. I. Gillen, S. Fölling, L. Pollet, and M. Greiner. *Probing the Superfluid–to–Mott Insulator Transition at the Single-Atom Level.* Science **329**, 547–550 (2010).

[248] J. F. Sherson, C. Weitenberg, M. Endres, M. Cheneau, I. Bloch, and S. Kuhr. *Single-atom-resolved fluorescence imaging of an atomic Mott insulator.* Nature **467**, 68–72 (2010).

[249] C. Weitenberg, M. Endres, J. F. Sherson, M. Cheneau, P. Schausz, T. Fukuhara, I. Bloch, and S. Kuhr. *Single-spin addressing in an atomic Mott insulator.* Nature **471**, 319–324 (2011).

[250] M. Miranda, R. Inoue, Y. Okuyama, A. Nakamoto, and M. Kozuma. *Site-resolved imaging of ytterbium atoms in a two-dimensional optical lattice.* Phys. Rev. A **91**, 063414 (2015).

[251] E. Haller, J. Hudson, A. Kelly, D. A. Cotta, B. Peaudecerf, G. D. Bruce, and S. Kuhr. *Single-atom imaging of fermions in a quantum-gas microscope.* Nat Phys **11**, 738–742 (2015). Letter.

[252] L. W. Cheuk, M. A. Nichols, M. Okan, T. Gersdorf, V. V. Ramasesh, W. S. Bakr, T. Lompe, and M. W. Zwierlein. *Quantum-Gas Microscope for Fermionic Atoms.* Phys. Rev. Lett. **114**, 193001 (2015).

[253] M. F. Parsons, F. Huber, A. Mazurenko, C. S. Chiu, W. Setiawan, K. Wooley-Brown, S. Blatt, and M. Greiner. *Site-Resolved Imaging of Fermionic* ^{6}Li *in an Optical Lattice.* Phys. Rev. Lett. **114**, 213002 (2015).

[254] K. Blagoev and V. Komarovskii. *Lifetimes of Levels of Neutral and Singly Ionized Lanthanide Atoms.* Atomic Data and Nuclear Data Tables **56**, 1 – 40 (1994).

[255] C. J. Bowers, D. Budker, E. D. Commins, D. DeMille, S. J. Freedman, A.-T. Nguyen, S.-Q. Shang, and M. Zolotorev. *Experimental investigation*

of excited-state lifetimes in atomic ytterbium. Phys. Rev. A **53**, 3103–3109 (1996).

[256] M. Baumann, M. Braun, A. Gaiser, and H. Liening. *Radiative lifetimes and g J factors of low-lying even-parity levels in the Yb I spectrum*. Journal of Physics B: Atomic and Molecular Physics **18**, L601 (1985).

[257] J. Ye and S. T. Cundiff. *Femtosecond optical frequency comb: principle, operation and applications*. Springer (2005).

[258] E. Rubiola. *Phase Noise and Frequency Stability in Oscillators*. Cambridge University Press (2009).

[259] D. W. Allan. *Statistics of Atomic Frequency Standards*. Proceedings of the IEEE **54**, 221–230 (1966).